

# **Photosensitive device application using Inorganic and Organic semiconducting nano-composites and unique approach of Crystalline Silicon selective emitter solar cell**

**A Dissertation submitted to  
Jadavpur University, Kolkata**



*In partial fulfillment of the requirements for the degree of*  
**DOCTOR OF PHILOSOPHY (Ph.D.) in SCIENCE**

**By**

**Baishakhi Pal**

**Department of Physics**

**Jadavpur University**

**Kolkata-700032**

**India**

**May 2024**





## CERTIFICATE FROM THE SUPERVISOR(S)

This is to certify that the dissertation entitled “**Photosensitive device application using Inorganic and Organic semiconducting nano-composites and unique approach of Crystalline Silicon selective emitter solar cell**” submitted by **Ms. Baishakhi Pal**, who got her name registered on **16.11.2016** (Registration Index No. 200/16/Phys./25) for the award of Ph.D. (Science) degree of **Jadavpur University**, is a bonafide record absolutely based upon her own work under our supervision and that neither this dissertation nor any part of it has been submitted for either any degree/diploma, fellowship or any other academic award anywhere before.

*Partha Pratim Ray*  
14/5/24



**Dr. Partha Pratim Ray**  
Professor  
Department of Physics  
Jadavpur University



*Utpal Gangopadhyay* 14/05/2024

**Prof. (Dr.) Utpal Gangopadhyay**  
Professor  
Meghnad Saha Institute of Technology  
Nazirabad, Kolkata - 700150

(Signature with seal)

Prof. (Dr.) Partha Pratim Ray

Professor, Dept. of Physics,  
Jadavpur University,  
Kolkata-700032, India

(Signature with seal)

Prof. (Dr.) Utpal Gangopadhyay

Professor, Dept. of Physics,  
Meghnad Saha Institute of Technology,  
Kolkata-700150, India





*This dissertation is dedicated  
to  
my Family & my Teachers,  
who installed in me  
the virtues of devotion & willpower  
and  
inexorably encouraged me to  
endeavour for excellence*



# Table of Contents

<b>Declaration .....</b>	<b>i</b>
<b>Acknowledgement .....</b>	<b>ii</b>
<b>Preface .....</b>	<b>v</b>
<b>Chapter 1: Introduction to Inorganic and Organic semiconducting nano-composites and Schottky Barrier Diode .....</b>	<b>1</b>
1.1. Introduction .....	2
1.2. Transition Metal Dichalcogenides: Properties, Structures and Applications .....	4
1.3. Methods for Synthesis of Transition Metal Dichalcogenides .....	4
1.3.1. Exfoliation .....	5
1.3.2. Laser Ablation .....	5
1.3.3. Arc Discharge .....	5
1.3.4. Microwave plasma .....	6
1.3.5. Hydrothermal Method .....	6
1.3.6. Vapor Phase Epitaxy (VPE) .....	7
1.3.7. Metal Organic Chemical Vapor Deposition (MOCVD) .....	7
1.3.8. Molecular Beam Epitaxy (MBE) .....	8
1.3.9. Bridgman and Gradient Freezing (GF) Method .....	8
1.3.10. The Travelling Heater Method (THM) .....	8
1.4. Application of Transition Metal Dichalcogenides .....	9
1.4.1. Electronics .....	9
1.4.2. Sensing .....	9
1.5. Molybdenum Tungsten Disulfide .....	9
1.6. Organic Semiconductor: its Revolution and Schottky Challenge .....	10
1.7. Metal-Organic Gels (Metallogels) & Properties .....	11
1.8. Metallogels Synthesis Method & Challenges .....	12
1.9. Innovative Applications of Metallogels .....	13
1.9.1. Electronic Devices .....	13
1.9.2. Electrolytic Material & Energy Devices .....	13
1.9.3. Multi-Stimuli Sensor .....	13
1.9.4. Catalysis .....	14
1.10. Schottky Diodes Overview: Metal- Semiconductor Interface .....	14
1.10.1. Technological Development of Metal-Semiconductor Interface .....	15

1.10.2. Theoretical Modeling of Metal-Semiconductor Interface .....	16
1.10.3. Schottky-Mott Theory and Energy-Band Diagram .....	17
1.10.4. Modifications to Schottky-Mott Theory .....	21
1.11. Metal-Semiconductor Interface Categorization .....	23
1.12. Contacts with Surface States and an Insulating Interfacial Layer .....	24
1.13. Fabrication Process of Schottky Diodes .....	25
1.13.1. Aluminium in Device Fabrication .....	26
1.13.2. Glass Substrate Coated with Indium Tin Oxide (ITO).....	27
1.13.3. Metal Deposition .....	27
1.14. Electrical studies of Schottky barrier diodes .....	28
1.14.1. Techniques for determining the series resistance, barrier height and ideality factor .....	28
1.14.2. Estimation of Mobility and Transit Time .....	32
1.14.3. Capacitance-Voltage Measurements .....	33
1.14.4. Photoelectric Measurements .....	34
1.15. Applications of Schottky Barrier Diode .....	35
1.16. Outline of the Thesis .....	35
References .....	38

## **Chapter 2: Improvement of charge kinetics of MoS<sub>2</sub> nano-petal based Schottky device by incorporation of W: A comparative study of structural, optical, and electrical properties ..... 45**

Abstract.....	46
2.1. Introduction .....	47
2.2. Experimental Section .....	48
2.2.1. Material preparation .....	48
2.2.2. Synthesis of Molybdenum Di-Sulfide.....	48
2.2.3. Synthesis of Molybdenum Tungsten Di-Sulfide .....	49
2.2.4. Thin Film Device fabrication .....	49
2.2.5. Capacitance-Frequency measurement .....	50
2.2.6. Material characterization .....	50
2.3. Results and discussions.....	51
2.3.1. Structural analysis .....	51
2.3.2. Optical analysis .....	57
2.3.3. Thermal stability analysis of MoS <sub>2</sub> and MoWS <sub>2</sub> nano-composites and BET characterization .....	60
2.3.4. Electrical study of Al/Compound/ITO Schottky diode .....	62

2.3.5. Impedance Spectroscopy analysis .....	72
2.4. Conclusions .....	75
References .....	76

**Chapter 3: Investigating charge transportation and photo-responsive outcome of a Schottky diode fabricated by 2-amino terephthalic acid directed supramolecularMn(II)-metallogel..... 79**

Abstract .....	80
3.1. Introduction .....	81
3.2. Experimental section .....	82
3.2.1. Materials .....	82
3.2.2. Characterizations .....	83
3.2.3. Synthesis of Mn-ATA .....	83
3.2.4. Minimum critical gelation concentration (MGC) of the synthesized Mn-ATA metallogel .....	84
3.2.5. Testing gel-forming ability of different solvents in producing stable Mn-ATA .....	85
3.3. Results and discussions .....	86
3.3.1. Morphological and elemental study .....	86
3.3.2. Rheological study .....	87
3.3.3. FT-IR spectroscopic study.....	89
3.3.4. ESI mass analysis .....	90
3.3.5. Optical study.....	91
3.3.6. Fabrication of indium tin oxide (ITO)/gel compound/aluminum (Al)-based Schottky barrier diode .....	92
3.3.7. Analysis of electrical characteristics .....	93
3.4. Conclusions .....	100
References .....	101

**Chapter 4: Comparative outcomes of the voltage-dependent current density, charge transportation and rectification ratio of electronic devices fabricated using mechanically flexible supramolecular networks..... 105**

Abstract .....	106
4.1. Introduction .....	108
4.2. Experimental section .....	110
4.2.1. Materials .....	110
4.2.2. Characterizations .....	110

4.2.3. Synthesis method of Mn-BDA and Cd-BDA metallogels.....	111
4.2.4. Minimum critical gelation (MCG) concentration of Mn-BDA and Cd-BDA metallogels .....	112
4.2.5. Inspecting the trend of Mn-BDA, and Cd-BDA metallogel formation in diverse solvent media .....	113
4.2.6. Device Fabrication and Characterization .....	115
4.3. Results and discussion.....	115
4.3.1. FESEM Microstructural and EDAX Elemental Studies.....	115
4.3.2. Rheological characterizations of Mn-BDA, and Cd-BDA metallogels.....	118
4.3.3. FT-IR spectroscopic study of the synthesized Mn-BDA, and Cd-BDA metallogels .....	120
4.3.4. ESI Mass Analyses .....	121
4.3.5. Electrical characterization .....	124
4.4. Conclusions.....	130
References.....	132

<b>Chapter 5: A Semiconducting Supramolecular novel Ni(II)-Metallogel derived from 5-aminoisophthalic acid low molecular weight gelator: An Efficient Schottky Barrier Diode Application.....</b>	<b>137</b>
Abstract .....	138
5.1. Introduction.....	139
5.2. Experimental .....	141
5.2.1. Materials.....	141
5.2.2. Apparatus and measurements .....	141
5.2.3. Synthetic Procedure of Ni(II)-metallogel (Ni@5AIA).....	142
5.2.4. Stability of the Ni@5AIA metallogel in different pH media .....	143
5.3. Results and discussions.....	144
5.3.1. Rheological Analysis.....	144
5.3.2. Microstructural Study .....	145
5.3.3. FT-IR analysis of Ni@5AIA metallogel .....	146
5.3.4. Fabrication of thin film Device .....	146
5.3.5. Optical characterization.....	147
5.3.6. Electrical Characterization of Device.....	148
5.4. Conclusions.....	151
References.....	152

<b>Chapter 6: Introduction to Crystalline Silicon selective emitter solar cell.....</b>	<b>158</b>
6.1. Introduction.....	159
6.2. Energy Scenario .....	159
6.3. Utilization of Solar Energy .....	160
6.4. A Brief History of Solar Cell .....	160
6.5. Solar Cell: Basics .....	162
6.5.1. Creation of Charge Carriers through Photon Absorption in Junction-Forming Materials .....	162
6.5.2. Sequential Segregation of the Photo-Induced Charge Carriers within the Junction.....	164
6.5.3. Gathering the Photo-generated Charge Carriers at the Terminals of the Junction .....	164
6.6. Crystalline Silicon Solar Cell: PV market overview .....	165
6.7. Selective Emitter Solar cell: efficient Solar cell design .....	166
6.8. Fabrication of selective emitter using different techniques.....	167
References .....	172
 <b>Chapter 7: Novel Technique for Fabrication of n-type Crystalline Silicon Selective Emitter for Solar Cell Processing.....</b>	<b>175</b>
Abstract .....	176
7.1. Introduction.....	177
7.2. Experimental details .....	179
7.3. Results and Discussions .....	182
7.3.1. Texturization and spectral response .....	182
7.3.2. Formation of homogeneously doped emitter & sheet resistance measurement.....	183
7.3.3. Stability of paste in HF solution & stripping of paste .....	184
7.3.4. Formation of rear side diffusion as well as front side selective emitter & sheet resistance measurement.....	185
7.4. Conclusions .....	187
References .....	188
 <b>Chapter 8: Optimizing front contact Selective Emitter doping in n-substrate Solar Cells: simulation modeling and experimental application .....</b>	<b>190</b>
Abstract .....	191
8.1. Introduction .....	192
8.2. Modeling and Design of Selective Emitter .....	193
8.2.1. Device Structure.....	193
8.2.2. Device simulation.....	194

8.2.3. Simulation Result .....	194
8.3. Solar cell fabrication with simulated result .....	201
8.3.1. Experimental methods .....	201
8.3.1.1. Cleaning and Texturization .....	201
8.3.2. Experimental results .....	202
8.3.2.1. Front emitter and rear surface diffusion .....	202
8.3.2.2. Dielectric film deposition.....	204
8.3.2.3. Lifetime measurement.....	205
8.3.2.4. Deposition of anti-reflection coating .....	205
8.3.2.5. Metallization and Co-firing .....	206
8.3.2.6. Fabrication of Selective emitter solar cell.....	207
8.4. Conclusions.....	209
References.....	211

**Chapter 9: Conclusion, Novelty and Scope of future work ..... 213**

9.1. Conclusion .....	214
9.2. Novelty .....	217
9.3. Scope of future work.....	218

**List of Publications ..... 218**

**Conferences, Symposiums & Short-term Courses Attended ..... 223**

**Workshops & Hands-on Training Programme Attended ..... 224**

**Certificates..... 225**



# DECLARATION

I hereby declare that the dissertation entitled “**Photosensitive device application using Inorganic and Organic semiconducting nano-composites and unique approach of Crystalline Silicon selective emitter solar cell**” submitted to the Department of Physics, Jadavpur University, Kolkata in partial fulfillment for the award of the degree of DOCTOR OF PHILOSOPHY and that the dissertation has not previously formed the basis for the award of any other degree, diploma, fellowship or other title.

*Baishakhi Pal*  
*15/05/2024*

---

Ms. Baishakhi Pal

*(Registration Index No. 200/16/Phys./25)*

Department of Physics,

Jadavpur University,

Kolkata-700032

India



## *Acknowledgement*

I would like to take this opportunity to convey my sincere gratitude towards all those people who have extended their valuable assistance and contributed indispensably to this thesis in one way or other.

First and foremost, I would like to express my deepest appreciation to my research supervisor, Prof. (Dr.) Partha Pratim Ray and Prof. (Dr.) Utpal Gangopadhyay for their enthusiasm, guidance, inspiration and support throughout the course of this research. I want to thank them for giving me this excellent opportunity to work and sharing their immense knowledge. Without their guidance and persistent help, this dissertation would not have been possible.

Besides my advisor, I would like to extend my gratitude to Prof. Hiranmoy Saha (SAMGESS, IEST) and Prof. Raghunath Bhattacharya (SAMGESS, IEST) for providing invaluable suggestions, motivation. I would like to thank Dr. Mukul Kumar Das (IIT (ISM) Dhanbad), Dr. Biswajit Dey (Visva-Bharati University) and Dr. Bidyut Saha (Burdwan University) for their valuable support in my research.

I am highly grateful to my senior Dr. Joydeep Datta, Dr. Arka Dey, Dr. Mrinmay Das, Dr. Rajkumar Jana, Dr. Soumi Halder, Dr. Sayantan Sil and Dr. Joydeep Dhar for their invaluable support and guidance to plan and complete my entire work. It was really great experience to work in their association.

I would like to thank the group members in our laboratory, Dr. Animesh Layek, Dr. Jitendra Saha, Mr. Animesh Biswas, Ms. Pubali Das, Mr. Dhananjoy Das, Mr. Mainak Das, Mr. Ramjan SK and Mr. Supravat Ghosh for providing with a healthy and good working environment. Special thank goes to Ms. Pubali Das for her continuous help and support I received while working together. I have

learnt a lot from all of you and all of you have provided me with some really memorable moments in this tenure. Without all of yours support this research work would have been difficult.

My sincere thanks go to Dr. Sukhendu Jana and Dr. Soma Ray in research centre at Meghnad Saha Institute of Technology (MSIT), Kolkata, for facilitating me whenever I felt clueless about my work. From the very first day Dr. Soma Ray who is also like my elder sister has rendered her help whenever required. I have learnt a lot from her starting from handling of instruments to fabrication procedure. In spite of her hectic schedule she was always ready to share her knowledge and experience which guided me in my research to a great extent.

My special thanks go to Dr. Subhendu Dhibar and Dr. Santanu Majumder for providing me an opportunity to work in collaboration with all of them. I express my deepest gratitude to them.

Special appreciation is extended to SAMGESS (IEST), IIT (ISM) Dhanbad, IACS Kolkata, Visva-Bharati University, Burdwan University for providing facility of material processing and characterizations.

I also take this opportunity to thank the former and present head, and all the professors of Physics Department for providing all type of support whenever required. Also all the office staffs of Physics department, Research section and PhD section are acknowledged for their cooperation in all administrative works related to my research.

My parents deserve special mention for their inextricable love, prayers, blessings and moral support throughout the life. I don't have words to justify their importance in my life. I don't know how to thank them. So, I dedicate this thesis to them. I would like to express my heartfelt recognition especially my mother Chaina Pal, I must say that I could not have been able to establish in this

position without her continuous support and strength that she gives me. They always cherished me in every valuable moment and supported when I badly needed them. I want to mention my lovely sister Dr Preyasi Pal for her encouragement and supportive nature. I also extend my gratitude to my in-laws whose encouragement and support also helped me to complete my work.

Finally all my acknowledgements go to my beloved husband Mr. Abhisek Chowdhury, whom I consider my best friend. There are lots of ups and downs in this tenure but he has made me felt amazed by warm endearment, his extreme support in the tough phases of my life. Whenever I lost my patience and felt disappointed he used to always encourage me which brought back my confidence every time. He acted as a frustration reliever during my entire research period and aggravated my research interests indirectly. Without your love, constant moral support and inspiration I could never complete this work. Thank you for being with me always.

I would like to express my heartfelt gesture to my precious 3-month-old baby [Akansha] for bringing joy, love, and inspiration into my life throughout the process of completing this dissertation. Your innocent presence has been a constant source of motivation, reminding me of the importance of balance and resilience. Though you may be too young to understand now, know that your presence has made a profound impact on this journey.

Finally I would like to gratefully acknowledge the Department of Science & Technology (DST), Government of India, for providing the INSPIRE Ph.D. fellowship. Without their financial support, this Ph.D. work would not have been possible.

Again, thanks to all.

Baishakhi Pal  
15/05/2024



## *Preface*

Inorganic and organic semiconductor materials have garnered significant attention due to their distinctive structural, optical, electrical, and magnetic properties. Over the past decade, substantial efforts have been devoted to comprehending the chemistry and physics of two-dimensional transition metal dichalcogenides (TMDs). While much research has centred on exploring the electrical and magnetic behaviours of these materials, there remains a scarcity of studies on the electrical properties of Schottky devices constructed from metal dichalcogenides. TMDs have emerged as promising materials for next-generation researchers interested in electronics, energy, and other fields, owing to their fascinating properties. Among the various TMDs available, Molybdenum Disulphide ( $\text{MoS}_2$ ) has been extensively investigated due to its unique optical, electronic, and mechanical characteristics. However, the combination of  $\text{MoS}_2$  with  $\text{WS}_2$  to form  $\text{Mo}_{1-x}\text{W}_x\text{S}_2$  composites holds great importance for enhancing properties, as it harnesses the potential of both materials, resulting in excellent characteristics. This composite material holds promise for applications in energy storage, supercapacitors, and photosensitive devices. Therefore, the exploration of  $\text{Mo}_{1-x}\text{W}_x\text{S}_2$  composites in Schottky Barrier Diodes (SBDs) is encouraged to uncover its potential in the technology sector. The metal-semiconductor (MS) interface serves as the foundation for various semiconductor devices, including SBDs, necessitating detailed study for insights into future prospects. Fabricating diodes should be accompanied by the determination of various device parameters such as photosensitivity, detectivity, conductivity, and mobility. Consequently, gaining an understanding of charge transport phenomena and the behaviour of metal-semiconductor junctions has become a primary objective for researchers. Therefore, this thesis focuses on the synthesis, characterization, and potential applications of different inorganic and organic materials, alongside conducting charge transport investigations through current-voltage characteristics and Impedance Spectroscopy analysis.

As the global population grows alongside industrialization, there has been a rapid increase in energy demand worldwide. This surge, coupled with the finite resources of fossil fuels and the consequent escalation of environmental pollution, has spurred efforts to explore alternative and new sources of energy generation. Consequently, research into renewable energies and their integration into modern life play a crucial role in fostering sustainable development across environmental, economic, and societal domains. Among the array of available renewable energy options, solar energy emerges as one of the most promising

solutions to address the mounting energy consumption. Solar energy conversion primarily encompasses two technologies: solar thermal and photovoltaic (PV). The conversion of sunlight into electricity through photovoltaic offers a clean, low-carbon solution. Despite advancements, the PV market remains predominantly dominated by crystalline silicon (c-Si) solar cells, posing challenges in the realms of energy, environment, and ecology.

Hence, this thesis concentrates mainly on creating various organic and inorganic materials and using them in thin film Schottky barrier diodes. Detailed examinations were conducted on the photo response and charge transport characteristics. Furthermore, an endeavour was made to construct a solar cell with a selectively doped emitter passivated with  $\text{Al}_2\text{O}_3$ , followed by an assessment of its operational efficiency. The thesis structure comprises 10 chapters, each covering specific aspects of the research, outlined briefly below.

**Chapter 1** serves as an introduction to the fundamental role of Schottky barrier diodes in electronics, covering both their historical context and the underlying physics governing their formation. The chapter explores research on inorganic nano-composites and organic semiconductors, emphasizing their applications in Schottky barrier diodes and techniques for measuring barrier height. Specific attention is given to 2D materials, particularly Transition Metal Dichalcogenides, including discussions on synthesis methods and applications. Additionally, the chapter highlights the growing importance of organic semiconductors in electronic devices, with a focus on metallogels.

**Chapter 2** focuses on comparing the structural, optical, and electrical characteristics of Schottky diodes made from the  $\text{MoS}_2$  &  $\text{Mo}_{1-x}\text{W}_x\text{S}_2$  -alloy composite, determining various device parameters. It details the synthesis of the  $\text{MoS}_2$  and  $\text{MoWS}_2$  composite through a hydrothermal method and thoroughly characterizes both materials. Analyzing charge transport via impedance spectroscopy and current-voltage studies enhances comprehension of the composite material's device performance, with impedance data simulation achievable through appropriate equivalent circuit.

Apart from studying inorganic semiconductors, I've also delved into organic semiconductor research. Therefore, in chapters 3 to 5 of my thesis, I synthesized diverse supramolecular metallogels and analyzed their gel properties. The determination of band gap values signifies their semiconducting nature, while opto-electronic investigations unveiled their potential utility in photosensitive devices.



**Chapter 3** presents the synthesis of a supramolecular Mn (II) metallogel, showcasing its robust mechanical properties and viscoelastic parameters through rheology-based experiments. The microstructure was analyzed using FESEM, while infrared spectrum analysis helped in understanding Mn-ATA formation. Electrospray ionization mass investigation confirmed the presence of various metallogel components contributing to its structure. Diode parameters were assessed, revealing its semiconductor characteristics, with non-linear rectifying J–V characteristics indicating Schottky diode behaviour. The device demonstrated enhanced rectifying properties under illumination, suggesting photo-responsive behaviour.

**Chapter 4** illustrates the synthesis of two unique supramolecular metallogels, Mn-BDA and Cd-BDA, with rheological parameters investigating their mechanical flexibility. Both metallogels exhibit notable mechanical stability, with FESEM providing morphological visualizations. FT-IR and ESI-mass spectroscopic analyses confirm potential non-covalent supramolecular interactions. Additionally, Schottky diodes (SDs) comprising ITO/Cd-BDA/Al and ITO/Mn-BDA/Al configurations are fabricated, showcasing significant semiconductor characteristics with nonlinear J–V curve.

**Chapter 5** introduces the creation of a supramolecular Ni(II)-metallogel, investigating its mechanical properties through rheological studies. FESEM analysis reveals flake-like morphological patterns, while FT-IR spectroscopy examines the metallogel formation approach. Thin film devices based on the metallogel demonstrate electrical conductivity in metal-semiconductor junctions, with a focus on evaluating semiconductor properties such as Schottky barrier diode behaviour to assess device quality.

**Chapter 6** offers an overview of solar energy's potential as a renewable resource. It includes an introduction to energy and the importance of seeking renewable alternatives. Additionally, it delves into the early developments of photovoltaic, particularly the emergence of Silicon solar cells. The chapter highlights the importance of emitter design in improving the performance of crystalline silicon solar cells and examines the advantages and disadvantages of selective emitter solar cells compared to homogeneous emitter ones.

Selective emitter technology, also known as selectively doped emitter, shows promise in photovoltaics by effectively managing contact resistance and surface recombination velocity, thereby enhancing solar cell efficiency. Various methods exist for creating selective emitter doping profiles, such as double diffusion with photolithography, reactive ion etching (RIE),

electrochemical etching (i.e., etch back method), laser doped selective emitter (LDSE), and laser over-doping treatment. In this thesis, I propose a new technique for forming selective emitters (detailed in Chapter 7) offering an alternative to traditional approaches. Beside that, among all of the conventional technique mentioned above, laser over-doping stands out in solar cell applications due to its affordability, simple fabrication process, and effective optical confinement (discussed in Chapter 8). Following diffusion, before metal contacts are applied, the surface undergoes laser treatment where the grid structure will be formed, eliminating the need for double diffusion.

**Chapter 7** showcases a novel approach to create a selective emitter in crystalline silicon is presented, involving the concurrent development of both the front side selective emitter and the rear back surface field (BSF) layer during the rear side diffusion step. This chapter introduces a unique method for attaining a selective emitter, characterized by a highly diffused region with low sheet resistance and in the remaining portion, a lightly diffused region with higher sheet resistance. The outcomes indicate that the selective emitter can be produced in a single diffusion process without the need for additional heat treatment or chemical etching, rendering this approach cost-effective.

**Chapter 8** delves into crafting n-type crystalline silicon selective emitter solar cells, showcasing the optimization of parameters like the dielectric passivation layer, doping profile, and etching parameters through simulation techniques. Drawing from these simulations, the chapter presents a cost-effective, batch process-compatible  $\text{Al}_2\text{O}_3$ -passivated n-type c-Si selective emitter solar cell achieved via laser overdoping, boasting an efficiency of 17.2%. Additionally, it conducts a comparative analysis between conventional homogeneous doping emitter solar cells and selectively doping emitter solar cells treated with laser over-doping, noting identical process parameters including cleaning, texturization, rear side diffusion (BSF), front and rear surface dielectric passivation, ARC coating, and metallization for contact formation for both cell types.

**Chapter 9** contains conclusion and novelty of the entire work and scope of future work.

All references in this thesis are formatted as follows:

**[Citation format]:** Initial and surname of authors, Journal name, Volume (Year) Page No.

Example: B. Pal, P. Das, J. Datta, U. Gangopadhyay, P.P. Ray, Material Science and Semiconductor Processing, 162 (2023) 107535.

**[Book]:** Author, Title, Publisher, Place Published, Year.

Example: S. M. Sze and K. K. Ng, Physics of semiconductor devices, John wiley & sons, 2006.

Baishakhi Pal  
15/05/2024

\*\*\*





*"Imagination is more important than knowledge. For knowledge is limited, whereas imagination embraces the entire world, stimulating progress, giving birth to evolution"*

- *Albert Einstein*



# Chapter 1

---

**Introduction to Inorganic and Organic  
semiconducting nano-composites and Schottky Barrier  
Diode**

## 1.1. Introduction

Throughout human history, the accumulation of scientific knowledge and technological advancements has exhibited a consistent pattern of slightly exponential and self-reinforcing growth. The technological revolution, widely praised, has notably intensified in recent decades, marking the twentieth century as the onset of the electronic age. The term "semiconducting" was introduced by Alessandro Volta in 1782, as noted by G. Busch [1]. Michael Faraday's observation in 1833 revealed the negative temperature coefficient of  $\text{Ag}_2\text{S}$  (Silver Sulfide) [2, 3], while Humphrey Davy observed a decrease in the electrical conductivity of metals with rising temperature. Johann Hittorf's publication in 1851 provided a comprehensive investigation into the relationship between temperature and the electrical conductivity of  $\text{Ag}_2\text{S}$  and  $\text{Cu}_2\text{S}$  [1]. In 1874, Karl Ferdinand Braun observed rectification and conduction in metal sulfides through the use of a metal point (whisker) [4]. In the same year, Arthur Schuster made a significant discovery in rectification while experimenting with a circuit composed of copper wires and screws [5]. The initial observation of photoconductivity in solids was credited to Willoughby in 1873, who noted a rapid decrease in resistance (selenium resistors) when exposed to light [6, 7]. In 1906, Pochettino made a significant discovery by determining the photoconductivity of anthracene, marking it as the inaugural organic compound to exhibit this property [8]. Following this, in 1913, Volmer further contributed to the understanding of anthracene's photoconductivity [9]. Johan Koenigsberger, in 1914, categorized solid-state materials into metals, insulators, and variable conductors based on their conductivity [10]. Walter Schottky validated the presence of a barrier through experimentation in a metal-semiconductor interface in 1931 [11]. In 1939, Neville F. Mott, Walter Schottky, and Boris Davydov proposed a theoretical model introducing the concept of a surface barrier formed between metals and semiconductors with different work functions, later named the Schottky barrier in honor of Walter Schottky. Allan Wilson, in 1931, formulated a successful semiconductor behavior theory grounded in advanced quantum theory [12], known as the "band theory" of solids, elucidating the mechanism of impurity doping [13]. The semiconductor landscape saw further strides in 2000 with the Nobel Prize awarded to Hebert Kroemer, Zhores Alferov, and Jack Kilby for their contributions to the development of semiconductor heterostructures used in high-speed devices and optoelectronics. Post-World War II, the focus on basic semiconductor physics research shifted, emphasizing the pivotal role of elemental



semiconductors in scientific and technological progress. Today, semiconductor material science stands as the cornerstone of technological advancement, with ongoing research shaping the future of semiconducting materials. Hans Albrecht Bethe got the Nobel Prize in 1967 for his research conducted in 1942 on the thermionic emission of electrons through the barrier potential between metal and semiconductor materials [14].

In the 21<sup>st</sup> century, we find ourselves in a technological era capable of manipulating materials at the nanometer scale, yielding extraordinary outcomes such as innovative tools and advancements that were previously inconceivable. This progress is exemplified by applications ranging from nano-material-based cancer treatments [15] to the development of high-performance composites [16-18]. Consequently, nanotechnology is opening up new frontiers for innovation in diverse fields, including electronics, material science, and energy [19, 20]. Concurrently, technological advancements have led to the emergence of a distinctive class of lower-dimensional systems, marking the evolution of nano-science. This classification includes zero-dimensional (0D) polymer dots and up-conversion nano-particles, one-dimensional (1D) nano-fibers, nano-rods, and nano-filaments, two-dimensional (2D) layered metal oxides, transition metal dichalcogenides, nano-films, and three-dimensional (3D) nano-cones, pyramids, and nano-balls [21]. Notably, the dimensionality of these nanostructures is a key distinguishing factor, elucidating both the atomic structure and governing the properties to a significant extent [22]. Among these structures, 2D materials been extensively studied because of their unique physical properties and their crucial roles in diverse applications such as in electronics, sensors, and storage.

Transition metal dichalcogenides (TMDs) stand out as a extensively examined class of 2D materials, representing a prevalent system for layering van der Waals solids. TMDCs exhibit a range of intriguing properties, including both direct and indirect band gaps, mechanical strength, electrochemical behavior, and more. These characteristics have propelled TMDCs into the spotlight in the 21<sup>st</sup> century, finding diverse applications in thermoelectric devices [23], hydrogen production [24, 25], semiconductors [26], nano-electronics, optoelectronic devices, energy harvesting, and beyond [27-30].

Within TMDCs, the transition metal assumes octahedral coordinates, observed in d0, d3, and a few d1 metals. In contrast, in 1T and 2H crystals, the transition metal adopts trigonal prismatic

coordinates, present in d2 and d1 metals. These coordinates share common edges with adjacent neighbors in each layer, forming a hexagonal honeycomb structure [31, 32].

### 1.2. Transition Metal Dichalcogenides: Properties, Structures and Applications

Transition Metal Dichalcogenides (TMDs), a crucial subset within the 2D family, have garnered significant attention in the realm of photovoltaic in recent years owing to their notable light-absorbing capabilities [33-34] and heightened conversion efficiency [35]. In the past decade, substantial efforts have been dedicated to unraveling the chemical and physical intricacies of TMDs. These semiconductors are atomically thin and follow the general formula  $\text{MX}_2$ , where M denotes a transition metal atom such as W or Mo, and X represents a chalcogen atom like S, Te, or Se. A single layer of M atoms is sandwiched between two X layers, bonded covalently by weak Van der Waals forces. The crystal structure exhibits a three-fold symmetry in a honeycomb hexagonal lattice, featuring an inversion center. However, in a monolayer, the inversion center may be absent. Bulk TMDs possess an indirect band gap at the center of the Brillouin zone, whereas the monolayer exhibits a direct band gap located at the K-points due to its absence of an inversion center [36, 37]. The spin-orbit coupling in TMDs' monolayer induces spin-orbit splitting [38] in the valence band and conduction band, resulting in regulation over electron spin through the adjustment of excitation laser photon energy and handedness [39]. Typically, a single layer of TMDs demonstrates exceptional behavior, absorbing approximately 20% of incident light. Photon absorption by the TMD monolayer with sufficient energy leads to electron creation in the conduction band, and the resultant missing electron in the valence band is compensated by a positively charged quasi-particle known as a hole. Subsequently, the Coulomb force between the positively charged hole and negatively charged electron forms a bound state called an exciton, offering intriguing properties for diverse applications.

### 1.3. Methods for Synthesis of Transition Metal Dichalcogenides

In the upcoming section, we will explore diverse growth mechanisms and synthesis procedures applicable to Transition Metal dichalcogenides:

### 1.3.1. Exfoliation

The exfoliation technique, also known as the top-down strategy, involves mechanical methods and remains the preferred approach for producing new monolayer 2D material from bulk crystals. This method is widely favored due to its simplicity, resulting in products with high crystal quality and superior electronic and optical properties compared to 2D materials obtained through alternative means. In this process, the TMD crystal is rubbed against another surface, and adhesive tape is applied to the bulk TMD material during the rubbing process. Subsequently, the tape, containing tiny flakes of the TMD bulk material, is transferred onto a substrate. Upon removing the adhesive tape from the substrate, monolayer and multilayer flakes of TMD are obtained.

### 1.3.2. Laser Ablation

One established method for creating  $C_{60}$  involves utilizing laser ablation on an appropriate material for the target. Following the successful synthesis of  $NiCl_2$  nano-tubes (NTs) and fullerene-like particles through laser ablation [40, 41], Parilla et al. employed a similar approach to generate nano-octahedral of  $MoS_2$ , later extending the technique to  $MoSe_2$  [42]. Subsequently, a few years later, Sen et al. achieved the production of metal-filled and hollow inorganic fullerene (IF)-like particles of  $MoS_2$  and  $WS_2$  [43]. Recently, Schuffenhauer et al. employed laser ablation on  $TaS_2$  under Ar and  $CS_2$  to obtain filled  $TaS_2$  fullerene-like particles [44]. Hexagonal  $WS_2$  nano-particles were formed through laser ablation in water [45]. Hong et al. successfully synthesized faceted IFs comprising  $SnS_2$  and  $SnS$  using the laser ablation technique [46].

### 1.3.3. Arc Discharge

An alternate method employed for the production of carbon onions and nano-tubes involves the use of an arc discharge technique. In 2000, Chhowalla et al. were pioneers in utilizing this approach with the same equipment, conducting it at high pressure. They successfully employed the method to fabricate  $MoS_2$ -IFs, forming a thin film with remarkable lubricating properties [47, 48]. Another variation of this method was adopted by Alexandrou, who employed the extreme conditions of an electric arc to generate  $MoS_2$  core shell particles [49]. Another variation includes performing arc discharge in a vacuum chamber filled with water, where an arc is

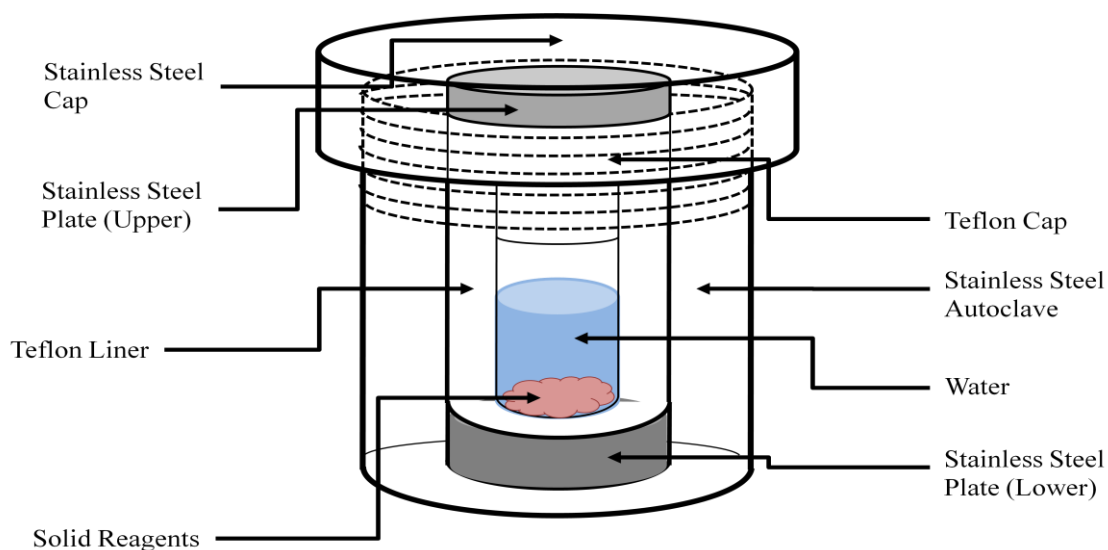
generated between a carbon cathode and a Mo hollow rod anode filled with  $\text{MoS}_2$  powder in its interior.

### 1.3.4. Microwave Plasma

In this method, a quartz tube functions as a mono-mode microwave cavity. Vollath and Szabo successfully produced nano-clusters of  $\text{MQ}_2$  ( $\text{M}=\text{Mo}, \text{W}$ ;  $\text{Q}=\text{S}, \text{Se}$ ), including some adopting a fullerene-like structure [50, 51], using the precursor  $\text{M}(\text{CO})_6$  with  $\text{H}_2\text{S}$  or  $\text{SeCl}_4$  in argon. The synthesis process involved a generator operating at frequencies of 0.915 or 2.45 GHz. Additionally, similar arrangements led to the establishment of nano-clusters for  $\text{SnS}_2$  and  $\text{ZrS}_2$ . Brooks et al. achieved the formation of  $\text{WS}_2$  and  $\text{HfS}_2$ -IFs, along with  $\text{ZrS}_2$  NTs and nano-rods, by employing  $\text{WO}_3$  nano-particles,  $\text{ZrS}_3$  or  $\text{HfS}_3$ , in microwave-induced plasmas containing  $\text{H}_2\text{S}$  and  $\text{N}_2/\text{H}_2$  [52].

### 1.3.5. Hydrothermal Method

The hydrothermal method involves crystal growth in an aqueous solvent [53], as illustrated in Fig. 1.1 depicting hydrothermal technique. This approach allows for crystal growth at relatively low temperatures (above  $100^\circ\text{C}$ ). The resulting compounds are influenced by factors such as pH, duration, temperature, and pressure in the closed system.



**Fig. 1.1: Figure depicting a steel autoclave with Teflon lining used in the hydrothermal synthesis process.**

Hydrothermal crystal growth offers several advantages: (1) it facilitates control over oxidation and enables conditions for synthesizing phases that may be challenging through alternative methods, (2) crystal growth occurs with lower thermal strain, potentially leading to a reduced dislocation density compared to melt-grown crystals with significant thermal gradients, (3) it proves valuable for synthesizing phases at low temperatures (4) it is suitable for synthesizing various materials on a large scale such as piezoelectric, magnetic, optic, and clay, and (5) hydrothermal synthesis promotes fast convection and effective solute transfer, resulting in the swift growth of larger, purer, and defect free crystals.

### **1.3.6. Vapor Phase Epitaxy (VPE)**

In the process of vapor phase epitaxy (VPE), thin film deposition occurs through the vapor phase. Two distinct methods are employed to transport the source materials: physical vapor deposition (PVD), involving no chemical vapor deposition (CVD) and chemical reaction, wherein the film formation results from a chemical reaction among the precursors at the substrate. Both chemical vapor transport (CVT) and physical vapor transport (PVT) offer advantages such as enabling growth at lower temperatures, preventing phase transition, and avoiding undesirable contamination. VPE, widely utilized in semiconductor epitaxial growth, relies on critical process parameters, including vacuum pressure, carrier gas flow rate, deposition temperature and temperature ramp. These parameters play a crucial role in determining the crystal structure, growth rate, orientation of the grown film, composition, surface morphology, and electronic properties.

### **1.3.7. Metal Organic Chemical Vapor Deposition (MOCVD)**

MOCVD, alternatively referred to as MOVPE, represents advancement over the conventional Vapor Phase Epitaxy (VPE) and stands out as one of the most accessible and widely recognized techniques for synthesizing Transition Metal Dichalcogenides (TMD). Since its inception in 1968 [54], this method has gained prominence as a preferred approach for the the process of growing compound semiconductors epitaxially, in both production and research settings. To initiate the process, precursors such as transition metal oxide and pure chalcogen are introduced into a furnace containing a substrate. The material formation occurs in the presence of an inert

gas, particularly Ar or N<sub>2</sub>, while the furnace is heated to temperatures ranging from 650 to 1000 °C [55]. The key factors contributing to the popularity of MOCVD include the ability to produce high-quality epitaxial films with a consistent film thickness.

### **1.3.8. Molecular Beam Epitaxy (MBE)**

MBE was created in the early 1970s with the aim of producing high-purity compound semiconductor epitaxial layers on specific substrates [56, 57]. Over time, it has evolved into a crucial method for producing nearly all semiconductor epi-layers. MBE functions as a vacuum evaporation apparatus, maintaining chamber pressure at approximately below  $\sim 10^{-11}$  Torr. Several advantageous features of MBE contribute to the growth of semiconducting films. Notably, the growth temperature remains exceptionally low, minimizing undesirable thermally activated processes like diffusion. Additionally, the thickness of the epi-layer can be precisely controlled at the atomic layer level. Introducing various vapor components to alter alloy composition and regulate doping concentration is easily accomplished by incorporating specific beam chambers equipped with appropriate shutters. These characteristics play a significant role, particularly in the fabrication of structures such as junctions.

### **1.3.9. Bridgman and Gradient Freezing (GF) Method**

In the realm of commercial production, achieving large single crystals is most efficiently accomplished through melt growth. The vapour phase epitaxy (VPE) growth process, although utilized, has limitations regarding both crystallite size and productivity. Bridgman's growth process involves the gradual movement of molten material through a temperature gradient at a slow pace, solidifying as the temperature drops below the material's melting point. This growth method is commonly referred to as the gradient freezing (GF) method [58], as it involves a gradual reduction of temperature while maintaining a constant temperature gradient at the interface.

### **1.3.10. The Travelling Heater Method (THM)**

The method known as the traveling heater (THM) involves a growth process in which polycrystalline feed material, possessing a consistently uniform structure, is systematically melted using a temperature gradient. Subsequently, the molten material is deposited in a single-

crystal form onto a seed with an identical composition [59]. THM proves particularly advantageous in the advancement of ternary and binary semiconductor compounds, such as CdZnTe and CdTe, demonstrating its applicability in this context [60].

## 1.4. Applications of Transition Metal Dichalcogenides

### 1.4.1. Electronics

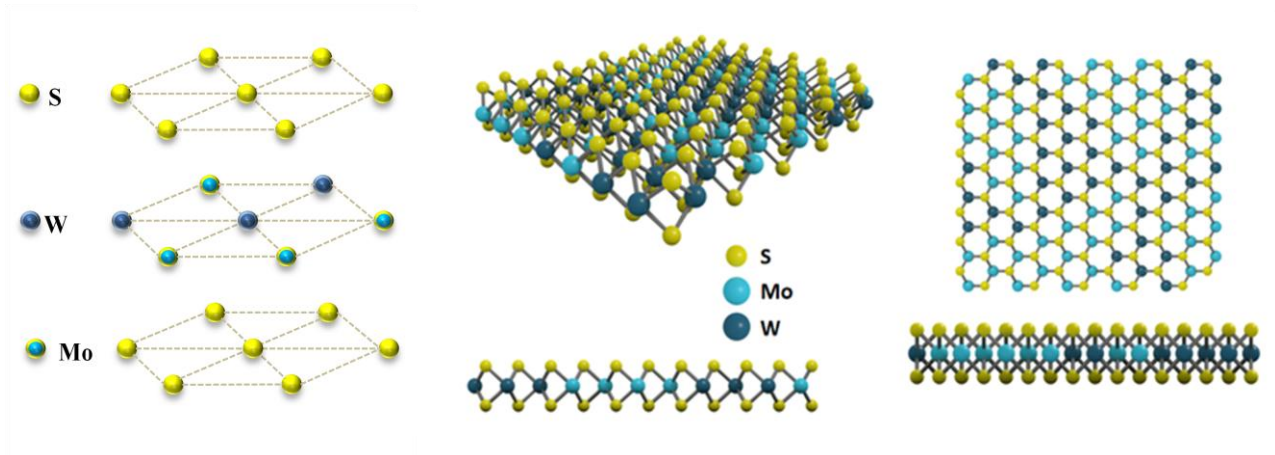
Several recognized applications exist for TMDs, such as the pioneering use of monolayer MoS<sub>2</sub> in the creation of the first Field Effect Transistor (FET) in 2011. This FET demonstrated an exceptional on/off ratio of 10<sup>8</sup>, attributed to its electrostatic regulation of the 2D layer. Subsequent FET developments involved materials like WS<sub>2</sub>, MoSe<sub>2</sub>, and WSe<sub>2</sub>. Their characteristics including electron mobility, band gap, and ultrathin structure, render them well-suited for applications in this domain [61, 62].

### 1.4.2. Sensing

The existence of a band gap positions TMDs as highly promising substitutes for graphene in the development of atomically thin sensors, spanning from gases to liquids to biological membranes. FET-based biosensors rely on receptors affixed to TMD monolayers. Alterations in current flow across the transistor occur as target molecules bind to these receptors [63].

## 1.5. Molybdenum Tungsten Disulfide

Molybdenum tungsten disulfide (MoWS<sub>2</sub>) is categorized as a Transition Metal Dichalcogenide (TMD) alloy. In recent times, the effective modulation of band gap, carrier mobility, and effective mass in 2D TMDs through alloying has been demonstrated both theoretically and experimentally [64-67]. The favorable thermodynamic stability at room temperature is indicated by negative mixing enthalpy values [67-69]. Altering the Mo and W ratio gives rise to various MoWS<sub>2</sub> alloys denoted by the chemical formula Mo<sub>x</sub>W<sub>(1-x)</sub>S<sub>2</sub>, each with distinct alloy ratios represented by the variable x. The stacking of 2H-MoS<sub>2</sub> and 2H-WS<sub>2</sub> layers occurs through van der Waals interactions, allowing for the exfoliation of thin 2D layers. Similar to MoS<sub>2</sub> and WS<sub>2</sub>, MoWS<sub>2</sub> exhibits a hexagonal crystal structure. Each monolayer is composed of an S-MoW-S layer, with one MoW plane sandwiched between two S planes.



**Fig. 1.2: The crystal structure of molybdenum tungsten disulfide ( $\text{MoWS}_2$ ) [adapted from Wikipedia]**

Fig. 1.2 depicts the crystal structure of  $\text{MoWS}_2$ . It is classified among the group-VI TMDs and, with its tunable band gap, band edge position, and effective mass of carriers, thin-layer nano-sheets of  $\text{MoWS}_2$  find applications in optoelectronic devices.

## 1.6. Organic Semiconductor: its Revolution and Schottky Challenge

In the early 21<sup>st</sup> century, a new era in electronics is underway, driven by the development and comprehension of a distinct category of active materials designed for electronic and optoelectronic purposes, commonly referred to as organic semiconductors. The remarkable advancements in this domain are fueled by the prospect of innovative applications, including expansive, versatile lighting solutions, and screens, economically produced manufactured integrated circuits, and photovoltaic cells derived from such materials. In contrast to traditional inorganic semiconductors, typically employed in a single-crystalline state, organic semiconductors, comprised of oligomer or polymer chain molecules, are typically applied as thin films over extensive areas, resulting in amorphous or polycrystalline structures. The use of flexible and transparent substrates in organic electronics opens up numerous possibilities for applications and integration. As an interdisciplinary field, organic semiconductors draw on contributions from chemistry, physics, and engineering. They hold significant potential as active matrices in the development of next-generation optoelectronic devices, including photovoltaic



cells, sensors, field-effect transistors, light-emitting diodes, thermo-electrics, and spin valves [70-74].

Organic semiconductors exhibit strong  $\pi$ -conjugation made of hydrogen and carbon atoms, along with hetero-atoms like oxygen, sulfur and nitrogen. Consequently, thin films of these molecules readily facilitate the support and transportation of carriers. The true potential of organic semiconductors lies in their capacity to design electronic and material properties to a greater extent than achievable with inorganic semiconductors. This opens up virtually limitless opportunities for precise customization of materials and devices.

These semiconductors form solids bonded by van der Waals forces, featuring much weaker intermolecular bonding in contrast to semiconductors bonded through covalent bonds."This results in altered mechanical and thermodynamic properties, leading to reduced hardness (soft materials), lower melting points, and narrower energy bands. Optical properties are marked by high absorption and emission rates, driven by polarizable  $\pi$ -electronic systems and substantial electron-hole correlation, resulting in exciton binding energies of approximately 0.5 eV.

The challenge with organic semiconductors in Schottky diodes stems from the absence of metallurgical ohmic contact and limited success in doping [75]. Consequently, the efficiency of current injection from metal electrodes to organic semiconductors becomes crucial for organic devices [76]. Achieving an effective Schottky junction necessitates addressing fundamental issues: (i) Electronic energy levels of the organic molecule relevant for injection and transport through the materials, relative to the work function of metal electrodes [77, 78]; (ii) Chemical and electronic interactions between organic semiconductors and metal electrodes [79]; and finally, (iii) Band bending at metal/organic interfaces within devices [80].

## 1.7. Metal-Organic Gels (Metallogels) & Properties

In the early twentieth century, the scientific community focused on an antiquated form of gel known as organogel, which garnered attention for its potential applications in diverse fields, including optoelectronic materials. Initially derived from high molecular weight gelators, the interest shifted over the last decade towards low molecular weight gelators (LMWGs) as the preferred candidates for global gel synthesis. The appeal lies in their small structures, facilitating

the straightforward prediction of the gelation mechanism. The involvement of small gelator molecules in synthesis allows the creation of stimuli-responsive materials through reversible weak interactions between these molecules [81]. Gels incorporating metal as an essential structural component for formation are termed metallogels, representing an expanding category within Supramolecular chemistry, these gels are formed through non-covalent interactions like hydrophobic interactions,  $\pi$ - $\pi$  interactions, and hydrogen bonding, play crucial roles for their assembly from small molecules. The primary driving factor behind the formation of metallogels typically involves strong metal-ligand coordination, where the metal coordinates with the gelator molecule (ligand). Introducing a metal to organic gels can impart additional intriguing properties, including color, charge transfer, fluorescence, rheological characteristics, magnetism, helicity, stimuli responsiveness, nanofabrication, conductance, and catalysis. Over time, metallogels have found diverse applications in interdisciplinary fields such as catalysis, electronics, and sensors. The main challenge lies in designing metallogelators, which limits their broad range of applications. Generally, scientists leverage their expertise in designing organic gelators to modify and adapt them for metallogelators, incorporating metal binding sites and adding metals through various methodologies.

## 1.8. Metallogels Synthesis Method & Challenges

The characteristics of gels are contingent upon the specific non-covalent interactions involved, with the metal-ligand interaction providing both thermodynamic stability and kinetic susceptibility. Typically, the synthesis of gels involves heating a solution containing the metal ion under investigation and the ligand responsible for forming the metallogel, along with additional compounds creating optimal reaction conditions [82]. The process continues until all added solids are dissolved in the solvent, followed by cooling to facilitate self-assembly and proper gel formation [83]. However, this conventional method has demonstrated limited success with certain transition metals and lanthanides in an acetonitrile solution of the ligand. Controlled heating and cooling, combined with the addition of transition metals and lanthanide ions to the ligand-containing solution, resulted in stable gels that successfully passed the inversion test [84]. The self-assembly is driven by non-covalent interactions, leading to linear compounds that can further organize into columnar, helical structures and eventually aggregate into fiber bundles [85].

Another alternative for creating functional nano-material gels involves the bottom-up method of subcomponent self-assembly [86], aiming to conserve resources, reduce synthesis time, and broaden the range of available gels through rapid exchange of reaction components [87].

## **1.9. Innovative Applications of Metallogels**

### **1.9.1 Electronic Devices**

Because of the existence of metal ions, metallogels typically exhibit self-healing and electrically conductive properties, making them potentially valuable in electronic devices like diodes, transistors, and solar cells [88]. Researchers led by Huo created a metallogel using  $\text{Fe}^{2+}$  coordination-driven complexation with trimesic acid as the gelator. This metallogel was subsequently employed in the application of dye-sensitized solar cells (DSSCs) as an electrolyte [89].

### **1.9.2. Electrolytic Material & Energy Devices**

Metallogels, serving as electrolytes, find crucial applications in supercapacitors, solid oxide fuel cells (SOFCs), and batteries [90]. Given the challenges associated with liquid electrolytes, such as leakage, internal corrosion, and volatilization, metallogel-based electrolytes have garnered significant attention for addressing these issues [91]. In a recent study, Bhattacharjee and colleagues synthesized a metallogel using 1-2-(3,5-ditert-butyl-2-hydroxybenzyl amino)-succinic acid with  $\text{ZnSO}_4$  and effectively applied it in supercapacitors [92]. Additionally, Kurungot and team proposed the use of metallogel solid electrolytes as proton conductors, utilizing xerogel pellets derived from metallogel in fuel cells to establish the electrical circuit between electrodes [93].

### **1.9.3. Multi-Stimuli Sensor**

The ability of metallogels to respond to multiple stimuli makes them well-suited for application as sensors, especially as both chemo-sensors and biosensors [92]. Mukhopadhyay and colleagues have documented the use of cobalt-induced metallogels for detecting L-Tryptophan within a group of amino acids [94].

### 1.9.4. Catalysis

The synthesized metallogel was reported to be useful for controlled oxidation of benzyl alcohol to benzaldehyde in good yield. Metallogel as a catalytic material shows recyclability with moderate loss in catalytic activity possibly due to the remaining amount of benzaldehyde in the gel network.

Metallogels, as intelligent materials, find applications in catalyzing significant transformations of organic molecules. In a study by Yamada et al., a novel metallogel was formed through the coordination of a tripodal ligand with Pd metal, resulting in a self-assembly process [95]. This newly created metallogel demonstrated active catalytic properties in the Suzuki-Miyaura coupling reaction involving aryl boronic and aryl halides acids. Xing et al. first reported the use of metallogel as a catalytic material in 2002 [96], where a coordination polymeric metallogel was produced by mixing Pd-salt with a tripodal ligand in dimethylsulfoxide. This synthesized metallogel proved effective in the controlled oxidation of benzyl alcohol to benzaldehyde, yielding good results. The recyclability of metallogel as a catalytic material was observed, albeit with a moderate decline in catalytic activity, possibly attributed to the residual amount of benzaldehyde within the gel network.

## 1.10. Schottky Diodes Overview: Metal- Semiconductor Interface

Metal-semiconductor (MS) contacts play a crucial role within semiconductor device structures as they establish connectivity with external elements. The pivotal feature of MS contacts lies in the barrier potential formed involving the metal's Fermi level and the semiconductor's band edge occupied by majority carriers at their junction. Typically, two categories of MS junctions are integral to semiconductor device construction. The first type, termed Ohmic contact, denotes a non-rectifying contact, while the second type, termed Schottky contact, represents a rectifying contact.

In Ohmic contact, the semiconductor undergoes heavy doping; resulting in a low resistance junction where current can flow effectively in both biasing directions. The Schottky contact, also known as Schottky-barrier diode (SBD) or surface-barrier diode is crucial in semiconductor devices as it always transitions to a metal conductor. This junction creates a barrier because of the energy-band mismatch at the interface, leading to injected carriers possessing surplus energy. This configuration is also termed as a hot-electron diode or hot-carrier diode. Unlike Ohmic

contact, Schottky contacts enable current flow in one direction while blocking it in the opposite direction, resulting in a very high resistance to current flow. Due to its rectifying properties and relatively simple fabrication process, SBDs are integral in modern semiconductor device technology [97]. The widespread adoption of Schottky barrier diodes (SBDs) can be attributed primarily to their avoidance of minority carrier effects, such as extended reverse recovery time and diffusion capacitance, commonly found in p-n junction devices. SBDs serve as fundamental components in various devices including solar cells, photo-detectors, transistors, varactors, and integrated circuits [98]. Enhancing the performance of Schottky junctions can consequently enhance the overall functionality of these devices. The formation of Schottky barriers occurs at metal-semiconductor junctions, with commonly used metals including aluminum, gold, or platinum.

This chapter provides an overview of metal-semiconductor interfaces, starting with the historical evolution of the technology and the theory behind metal-semiconductor contacts (paragraph 1.10.1 & 1.10.2). It then introduces the operational principles of such heterojunctions (paragraph 1.10.3) and discusses methods for measuring barrier height (paragraph 1.14.1), as well as the applications of Schottky barrier height (paragraph 1.15). Given the focus of this thesis on inorganic (2D materials) and organic material-based Schottky diodes, the importance of materials such as TMDs and metal-organic gels in Schottky diodes are discussed in the concluding section of the chapter (paragraph 1.16).

### **1.10.1. Technological Development of Metal-Semiconductor Interface**

The metal-semiconductor configuration is one of the earliest semiconductor devices. F. Braun introduced the rectifying property of metal-semiconductor conduction in 1874 [99], observing its dependence on voltage polarity and surface conditions [100]. However, it wasn't until 1904 that the first applications of point contact rectifiers emerged. Wilson employed band theory of solids in 1931 to develop semiconductor transport theory [101], extended to metal-semiconductor contacts. Schottky et al. observed the barrier potential at the metal-semiconductor junction in 1931 [102], with Schottky and Mott later specifying a model for barrier shape and height [103, 104]. By 1938, it was proposed that the potential barrier arises due to consistent electric charges contained within the semiconductor alone, leading to the term "Schottky barrier" [103]. The theoretical understanding of metal-semiconductor rectifiers lagged behind technological

advancements until around 1950 due to poor semiconductor quality. Metal-semiconductor diodes were replaced by p-n junctions in the 1950s due to their unreliability. Research on metal-vacuum interfaces also contributed to understanding metal-semiconductor interfaces. The 1960s saw significant progress in Schottky diode research [105], driven by factors such as the planar process invention [106] and the proposal of metal base bipolar transistors [107]. Low-temperature silicide formation [108, 109] and the availability of planar Schottky diodes led to various new applications. The 1970s marked the commercialization of Schottky diodes for high-frequency and fast-switching devices, particularly in computer circuits and microwave communication systems. This summary provides an overview of Schottky formation and its charge transport mechanism.

### **1.10.2. Theoretical Modeling of Metal-Semiconductor Interface**

As far back as 1914, Schottky proposed that an applied electric field could reduce the barrier height at a metal-vacuum interface [110]. However, it took fifty years for the accurate determination of its impact on metal-semiconductor rectifiers [111]. In 1921, Richardson introduced the concept of thermionic emission to explain electron emissions from hot metal cathodes [112]. Bethe later developed a theory in 1942, building upon Richardson's work, to explain metal-semiconductor rectification based on thermionic emission over an energy barrier [113]. Fowler explained the photo-response in 1931 [114], which is now utilized for precise measurement of metal-semiconductor barrier heights [115]. In the same year, Wilson proposed a quantum mechanical tunneling theory for metal-semiconductor diodes [116]. Stratton suggested rectification reversal due to tunneling dominance after thirty years [117]. In the late 1930s, Schottky and Spenke devised a rectification theory based on carrier diffusion over an energy barrier [118], which aligned with observed rectification polarity but lacked correct temperature dependence. Schottky made several significant theoretical contributions, including the concept of the depletion layer barrier and the relationship between barrier height and work function difference. Bardeen later proposed fixing barrier height through pinning of surface states in covalent semiconductors in 1947 [119]. In the early 1960s, Conley et al. and Stratton described field emission tunneling, while subsequent studies explored tunneling of thermally excited carriers [120, 121]. Crowell and Sze integrated Bethe's thermionic emission theory and Schottky's diffusion theory into a unified thermionic diffusion model [122].

### 1.10.3. Schottky-Mott Theory and Energy-Band Diagram

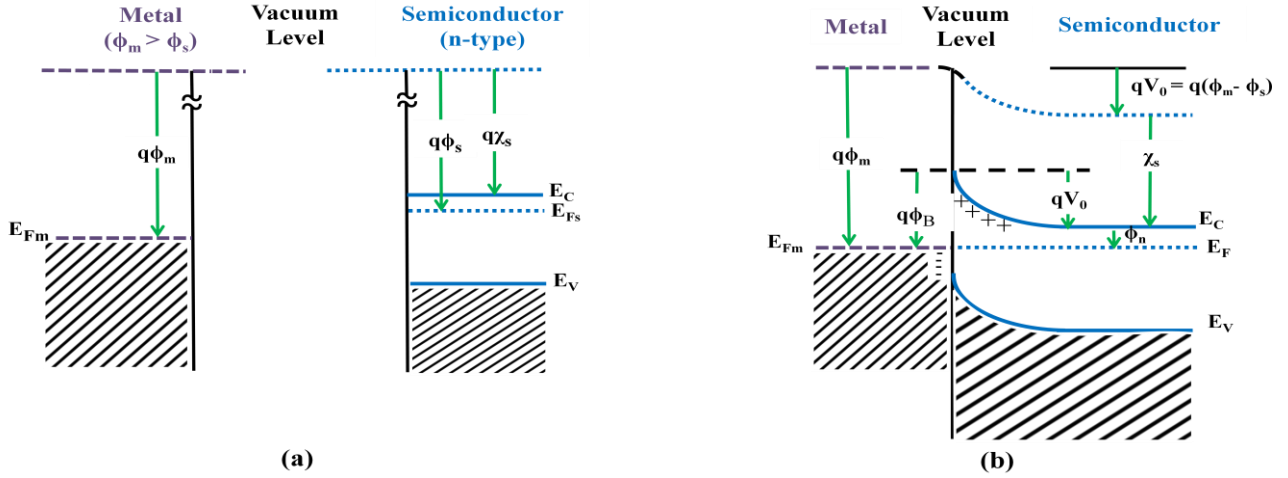
According to Schottky and Mott, the rectifying behavior observed in metal-semiconductor (MS) contacts results from the development of a barrier potential between the semiconductor and metal. This barrier arises because of the disparity in the work functions of the metal and semiconductor, assuming the semiconductor to be devoid of conduction electrons in the depletion region. Consequently, the creation of space charge in this area occurs due to uncompensated donor ions. If the space charge is evenly spread throughout the depletion region, the electric field strength increases linearly as one approach the metal from the edge of the depletion region. Consequently, the electrostatic potential increases quadratically, resulting in the formation of a parabolic potential barrier known as a Schottky barrier. The Schottky-Mott approximation defines the barrier height in the MS contact as,

$$\Phi_B = qV_i + E_c - E_F = \Phi_m - \chi_s \quad (1.1)$$

Where,  $\chi_s = \Phi_s - (E_c - E_F)$  represents the difference of energy between the bottom of the conduction band and the vacuum level, known as the electron affinity of the semiconductor. The degree of band bending is determined by the variance between the semiconductor work function ( $\Phi_s$ ) and the metal work function ( $\Phi_m$ ) and expressed as  $V_d$  (diffusion potential)  $= \Phi_m - \Phi_s$ . In the case of an n-type semiconductor, if  $\Phi_m > \Phi_s$ , the contact exhibits rectifying behavior, whereas if  $\Phi_m < \Phi_s$ , the contact is non-rectifying, i.e., ohmic. The scenario is opposite for a metal p-type semiconductor configuration.

#### (a) Rectifying Contacts

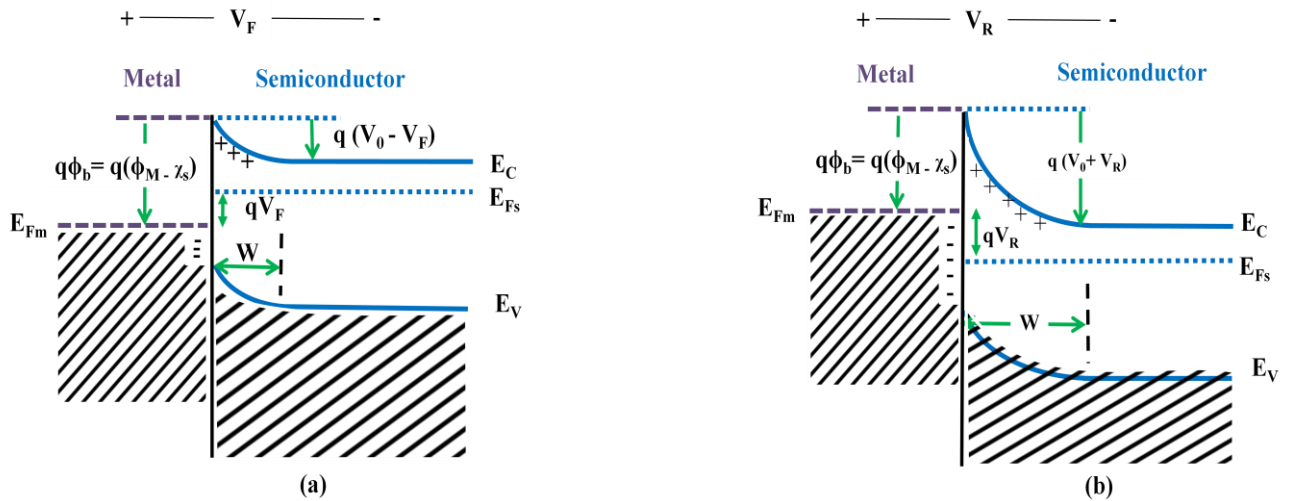
Fig. 1.3 illustrates the energy-level diagram of a specific metal and n-type semiconductor, both prior and after contact. The vacuum level serves as the reference point, with parameters  $\Phi_m$  representing the work function of metal and  $\Phi_s$  denoting the work function of semiconductor, while  $\chi$  signifies the electron affinity. Initially, when  $\Phi_m$  exceeds  $\Phi_s$  for an n-type semiconductor pre-contact, the semiconductor's Fermi level surpasses that of the metal. To attain thermal equilibrium, electrons migrate from the semiconductor to the metal's lower-energy states, leaving positively charged donor atoms behind and establishing a space charge region.



**Fig. 1.3: (a) Energy-level diagram of a metal and n-type semiconductor prior to contact, (b) after contact for  $\Phi_m > \Phi_s$**

The Schottky barrier height,  $\Phi_B$ , characterizes the barrier potential of electrons attempting to traverse into the semiconductor flowing from the metal, expressed ideally as

$$\Phi_B = \Phi_m - \chi \quad (1.2)$$



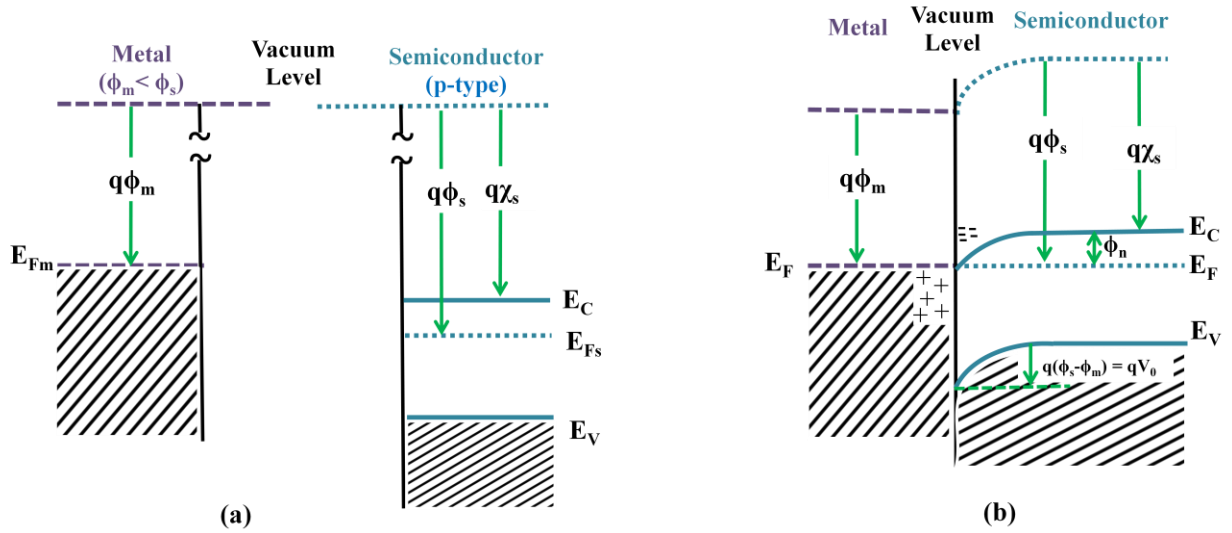
**Fig. 1.4: Optimal energy-level diagram of a metal and an n-type semiconductor junction during (a) forward bias and (b) reverse bias.**



On the semiconductor side,  $V_{bi}$  represents the built-in potential barrier encountered by electrons in the conduction band moving towards the metal, defined as

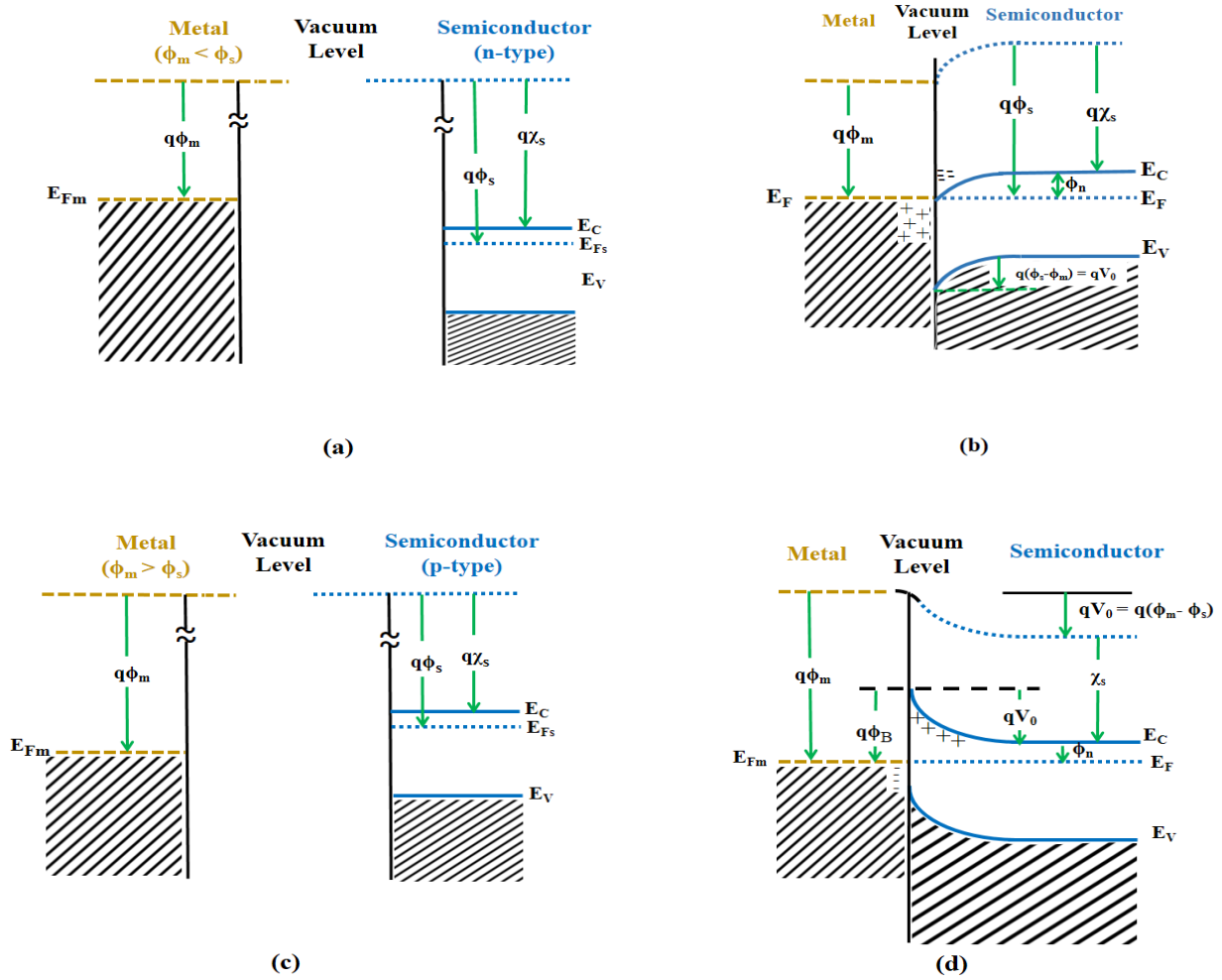
$$V_{bi} = \Phi_B - \Phi_n \quad (1.3)$$

Two scenarios arise: forward bias, where a positive voltage is enforced to the metal relative to the semiconductor, reducing the semiconductor-to-metal barrier while keeping  $\Phi_B$  constant (Fig. 1.4(a)), and reverse bias, where a positive voltage is enforced to the semiconductor compared to the metal, increasing the semiconductor-to-metal barrier (Fig. 1.4(b)). Schottky barrier diodes (SBD) primarily operate via majority carrier conduction, exhibiting improved high-frequency characteristics and switching speed compared to conventional p-n junctions. When  $\Phi_m < \Phi_s$  for a p-type semiconductor, as depicted in Fig. 1.5, a Schottky barrier forms, with the alignment of Fermi levels resulting in a depletion region  $W$ , where ionized acceptors remain uncompensated, creating a potential barrier against hole diffusion from the semiconductor to the metal, defined as  $\Phi_s - \Phi_m$ . Other scenarios involving metal-semiconductor contacts where  $\Phi_m < \Phi_s$  for an n-type semiconductor and  $\Phi_m > \Phi_s$  for a p-type semiconductor yield non-rectifying contacts.



**Fig. 1.5: (a) Energy-level diagram of a metal and p-type semiconductor prior to contact, (b) after contact for  $\Phi_m < \Phi_s$**

## (b) Non-rectifying or Ohmic Contacts



**Fig. 1.6: Ideal energy-band diagram (a) before contact, (b) after contact of metal and n-type semiconductor for  $\Phi_m < \Phi_s$ ; Ideal energy-band diagram (a) before contact, (b) after contact of metal and p-type semiconductor for  $\Phi_m > \Phi_s$**

Fig. 1.6 illustrates the energy band arrangement at the junction of metal and semiconductor, both in n-type and p-type configurations, before and after contact is established. When the metal's work function ( $\Phi_m$ ) is lower than that of the semiconductor ( $\Phi_s$ ) in the metal-n-type semiconductor interface, electron transfer from the metal to the semiconductor occurs to achieve

thermal equilibrium, resulting in an excess of electrons on the semiconductor surface, making it more n-type. Application of a positive voltage to the semiconductor relative to the metal causes electron flow to the semiconductor from the metal, leading to the formation of an Ohmic or non-rectifying contact. Conversely, applying a positive voltage to the metal relative to the semiconductor allows electrons to move easily from the semiconductor to the metal [123].

Similarly, considering the non-rectifying contact between a p-type semiconductor and a metal with  $\Phi_m > \Phi_s$ , during contact formation [Fig. 1.6 (c, d)], electrons from the semiconductor move into the metal until thermal equilibrium is reached, leaving behind more holes at the surface, making it more p-type. Consequently, electrons from the metal can readily move into the semiconductor's empty states. This charge movement corresponds to holes flowing from the semiconductor into the metal, establishing an Ohmic contact.

#### 1.10.4. Modifications to Schottky-Mott Theory

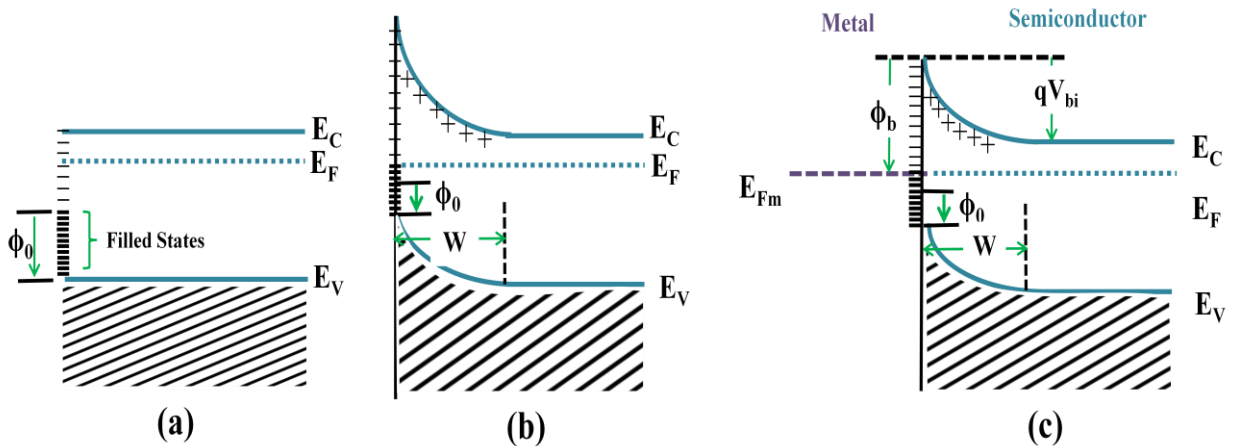
It is practically observed that the metal semiconductor interfaces do not always follow the expected behaviour as discussed above. This happens because Schottky-Mott theory neglected the contribution of the surface dipole to the electron affinity of the semiconductor and the metallic work function during the development of the MS contact. But in the real case, the surface dipole layers are very active and arise at the surface of the interface. It generates a distortion in the electron clouds of surface atoms. It avoids the overlapping of the center belonging to the positive and negative charge distribution. As per equation (1.2) the barrier height  $\Phi_B$  should increase linearly with metallic work function  $\Phi_m$ , however this dependence is observed mostly in ionic semiconductor in contrast to covalent semiconductor where the dependence is almost negligible.

In, 1947, Bardeen [119] first elucidated the surface dipoles and pointed out the nonlinear dependence of  $\Phi_B$  on  $\Phi_m$  as the localized surface state has an important role in the barrier formation in case of covalent semiconductors. In a covalent crystal, the surface atoms to make covalent bonds only with neighboring semiconductor atoms; on the vacuum part, there are no neighboring atoms available for bonding.

Consequently, each surface atom possesses one broken covalent bond, where one electron is attached while the other is absent, termed as dangling bonds [124, 125]. These dangling bonds create localized energy states within the semiconductor's surface, positioned within the forbidden

energy gap. These surface states typically distribute uniformly throughout the band gap and are defined by a neutral level  $\Phi_0$ . The placement of this neutral level ensures that when there is no band bending, the states are occupied by electrons up to  $\Phi_0$ , rendering the surface electrically neutral. States below  $\Phi_0$  act as donors when occupied and are positively charged when vacant, while states above  $\Phi_0$  exhibit acceptor-like behavior. On pristine surfaces of covalent semiconductors, the density of surface states matches the density of surface atoms. However, layers of adsorbed foreign atoms can substantially decrease this density by filling the broken covalent bonds.

Surface states alter the charge within the depletion region, thereby influencing the barrier height. Illustrated in Fig. 1.7(a) is the electron energy band diagram of an n-type semiconductor under flat band condition. This scenario represents a state of non-equilibrium, transitioning to equilibrium when electrons from the semiconductor adjacent to the surface occupy states above  $\Phi_0$ , aligning the Fermi level at the surface with that in the bulk. Consequently, the surface becomes negatively charged, leading to the formation of a depletion layer comprising ionized donors near the semiconductor surface. Because of this dipole formation, a potential barrier looking from the surface towards the semiconductor is created even in the absence of a metal contact as depicted in Fig. 1.7(b).



**Fig. 1.7:** Electron energy band representations of an n-type semiconductor with surface states. The representations illustrate (a) the flat band at the surface, (b) the surface in thermal equilibrium with the bulk, and (c) the semiconductor in contact with a metal.

When a metal is now brought in near the semiconductor to establish the contact by attaining equilibrium, the Fermi level within the semiconductor needs to adjust in accordance with the contact potential, facilitating charge exchange with the metal. When the density of surface states at the semiconductor surface is very large, the charge exchange primarily occurs at a larger level between the metal and these surface states, leaving the space charge within the semiconductor relatively unchanged. Consequently, the height of the potential barrier in Fig. 1.7(c) becomes independent of the metal work function and is mathematically given by

$$\Phi_B = E_g - \Phi_0 \quad (1.4)$$

In this scenario, the barrier height is described as being "pinned" by surface states. Equation (1.4) will be referred to as the Bardeen limit.

## 1.11. Metal-Semiconductor Interface Categorization

Interfaces between metals and non-metals can be categorized into four main types based on the resulting atomic arrangement at the interface:

**Type a:** In this category, the non-metal functions as an insulator or semiconductor, and the metal is physisorbed onto its surface. Such interfaces demonstrate an ideal Schottky barrier contact, where the barrier height correlates directly with the metal's work function.

**Type b:** Here, the non-metal is a highly polarizable semiconductor, like silicon, with a dielectric constant ( $\epsilon_r$ ) exceeding 7. The metal establishes a weak chemical bond with the semiconductor surface, without forming a bulk compound. These interfaces resemble a "Bardeen barrier," assuming surface states spread throughout the semiconductor, allowing for a potential drop across this region. In decent contacts of this kind, the barrier height is expected to show a slight dependence on the metal's work function ( $\Phi_m$ ).

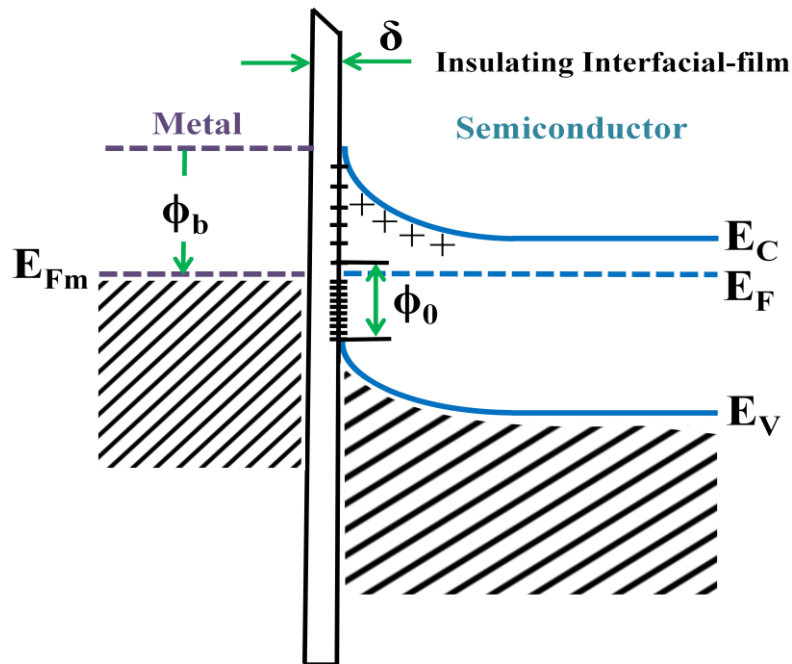
**Type c:** Type III interfaces involve a highly polarizable semiconductor undergoing a chemical reaction with the metal, resulting in the creation of one or more chemical compounds. This scenario signifies strong chemical bonding between the metal and the semiconductor, with the

barrier height influenced by factors related to chemical or metallurgical reactions occurring at the interface.

**Type d:** This type encompasses the formation of a thin native oxide film during the surface preparation of a highly polarizable semiconductor. This film serves as an interfacial layer, obstructing close contact between the metal and the semiconductor. Such interfaces are commonly encountered in practical metal-semiconductor devices, with further discussion provided in subsequent sections.

## 1.12. Contacts Involving Surface States and an Insulating Interface Layer

In most metal-semiconductor connections, the semiconductor surface is typically cleaned chemically prior to metal deposition, resulting in the formation of a thin insulating oxide layer on its surface. The thickness of this interfacial layer depends on the method of surface preparation and, for optimal Schottky contacts should ideally be kept below about 20 Å. The energy band diagram illustrating a contact with such an interfacial oxide layer is shown in Fig. 1.8.



**Fig. 1.8:** Diagram depicting the energy bands of a metal-semiconductor junction featuring surface states and an interfacial layer.

As previously explained, the Fermi level remains constant throughout the system, and the vacuum level maintains continuity along the interface. The potential drops linearly across the interfacial oxide layer, assuming it behaves as an ideal insulator with no charge. It is also assumed that the bottom edge of the conduction band in the insulator lies below the vacuum level. When the interfacial layer is sufficiently thin (i.e.,  $<20 \text{ \AA}$ ), the potential drop across it is negligibly small compared to that in the semiconductor depletion region. This thin region allows electrons to tunnel through it in both directions, making it electron-transparent. Consequently,  $\Phi_B$  and  $V_{bi}$  remain largely unaffected by the presence of this thin interfacial layer.

Contacts with a thin insulating layer between the metal and semiconductor are more conducive to theoretical understanding and analysis compared to those with thicker or stronger interfaces. This is because the insulating layer acts as a separator, allowing the metal and semiconductor to be treated as distinct systems. Thus, interface states can be considered as a characteristic of the specific semiconductor-insulator combination, without considering any changes in the surface dipole contributions to the work functions of the metal and semiconductor. Such simplifications are not applicable when dealing with clean contacts.

### 1.13. Procedure for Schottky Diodes Fabrication

**Selection of Materials:** The choice of metal in Schottky diode fabrication is critical and varies based on the type of semiconductor. For n-type semiconductors, Aluminum (Al) or Platinum (Pt) is commonly favored to establish rectifying contacts. While Silver (Ag) boasts excellent electrical conductivity, its susceptibility to oxidation limits its suitability in metal-semiconductor junctions. In thin film applications, Indium Tin Oxide (ITO) on a glass substrate is chosen for its resilience at high temperatures. Specific orientation, thickness, and resistivity of Silicon wafers are carefully considered for silicon-based Schottky diodes.

**Cleaning:** To ensure pristine surfaces, ITO-coated wafers undergo thorough cleaning with trichloroethylene, acetone, and methanol solvents. The final cleaning step involves using a 30-40% HF etching solution [126].

**Rinsing:** Wafers undergo multiple rinses in de-ionized (DI) water before subsequent deposition procedures.

**Semiconducting Materials Deposition:** Semiconducting layers are deposited onto the ITO coated glass substrate using Spin coating units with controlled rotation speed. Alternatively, other Physical Vapor Deposition (PVD) methods, such as electron beam evaporation, may be employed for deposition.

**Formation of Ohmic Contact:** Ohmic contacts on the backside of silicon wafers are established for efficient electrical connections to semiconductor regions. High-purity aluminium or the chosen metal is deposited using vacuum coating units, maintaining constant low pressure for uniformity up to several tens of nanometers. Annealing optimizes temperature, duration, and pressure, facilitating inter-diffusion and forming well-defined Ohmic contacts.

**Schottky Contacts:** Prior to metal deposition, silicon wafers are cleaned and etched in a 40% HF solution to remove the native oxide layer. A thin layer of the chosen metal is then applied to the semiconductor surface using deposition techniques such as sputtering or evaporation, with thickness controlled for desired electrical characteristics. Optional steps may include:

**Photolithography:** Defining the Schottky contact area through photolithography involves applying photoresist, exposing it to UV light through a mask, and developing the pattern through chemical processing.

**Etching:** Precision etchants selectively remove metal in exposed regions, defining the final geometry of the Schottky diode.

**Passivation:** Optionally, a passivation layer is deposited over the Schottky diode to enhance long-term stability and shield it from environmental factors.

### 1.13.1. Utilization of Aluminium in Device Fabrication

Aluminium, the most abundant metal on Earth, is distinguished by its outstanding malleability, ductility, and lightweight properties. It is relatively soft compared to many other metals. In addition to its mechanical characteristics, aluminium exhibits commendable electrical and thermal conductivity while retaining good resistance to corrosion. Notably eco-friendly, it can be recycled without losing any of its inherent qualities. In contrast, platinum, a heavier and more



expensive metal, possesses a higher work function of 5.65 eV, contrasting sharply with aluminium's lower work function of 4.2 eV.

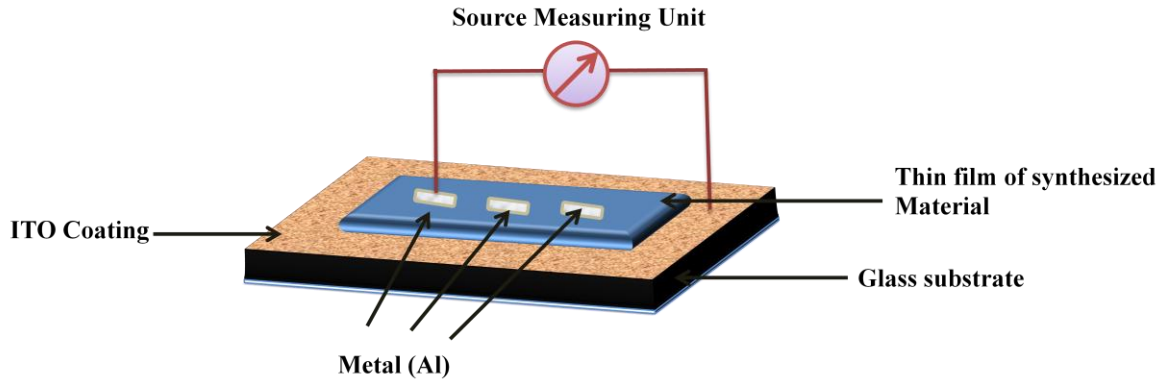
### 1.13.2. Indium Tin Oxide (ITO) Coating on Glass Substrates

Indium Tin Oxide (ITO) is a compound comprising indium (In), tin (Sn), and oxygen (O), with a composition of 74% In, 18% Sn, and 8% O. Renowned for its unique blend of electrical conductivity, optical transparency, ease of deposition as a thin layer, and resistance to moisture, ITO stands as one of the most widely used transparent conducting oxides. Typically, thin layers of indium tin oxide are applied onto glass surfaces using physical vapor deposition techniques. These films boast optical transparency exceeding 80% for thin layers, coupled with a low electrical resistivity of just  $10^{-4}$  ohm-cm [127].

### 1.13.3. Metal Deposition

The creation of metal-semiconductor junctions adopts a vertical sandwich configuration, specifically Al/synthesized material/ITO, chosen for its simplicity in junction formation. The initial step involves thorough cleaning of the ITO substrate, which undergoes a sequential cleaning process involving ultrasonication with a mild basic water solution (containing a small amount of sodium hydroxide in DI water), followed by rinsing with acetone, ethanol, and distilled water. Subsequently, the synthesized material is dispersed or dissolved in a suitable medium under ultrasonication and spin-coated onto the pre-cleaned ITO substrate at a specified rpm for multiple cycles. The resulting films are then dried in a vacuum chamber for several hours.

The subsequent stage entails depositing aluminium metal onto the thin film of the material through thermal evaporation. This process utilizes an electron gun within the vacuum coating unit, maintaining low pressure, typically at  $10^{-6}$  mbar. To precisely define the metal-semiconductor interface, a shadow mask is employed during metal deposition, ensuring an effective junctional area of  $7.065 \times 10^{-6}$  m<sup>2</sup>. The schematic structure of the fabricated Schottky diode is depicted in Fig. 1.9.



**Fig. 1.9: Illustration depicting the constructed MS junction Schottky diode.**

## **1.14. Electrical studies of Schottky barrier diodes**

### **1.14.1 Techniques for determining the series resistance, barrier height and ideality factor**

After the successful creation of the device, it's crucial to assess different parameters of the Schottky diode. Multiple methods exist for measuring key Schottky diode characteristics, such as the series resistance, ideality factor and Schottky barrier height. These parameters will be elaborated upon in the subsequent section.

The primary mode of current transport in a metal-semiconductor junction primarily involves the movement of majority carriers, rather than minority carriers as seen in a pn junction. The essential mechanism within a rectifying contact with an n-type semiconductor relies on the transport of majority carriers (electrons) across the potential barrier, resulting in the characteristic I-V curve, which can be illustrated by the theory of thermionic emission. This theory assumes that the height of the potential barrier significantly exceeds  $kT$ , allowing for the application of the Maxwell-Boltzmann approximation, and that thermal equilibrium remains unaffected by this process. According to the thermionic emission theory governing the movement of electrons across the barrier, the current density through a well-formed Schottky

barrier diode (SBD) constructed on high mobility semiconductors like Si and GaAs under forward bias voltage is expressed as follows:

$$J = J_0 \left[ \exp \left( \frac{qV}{\eta K T} \right) - 1 \right] \quad (1.5)$$

Where the current density denoted as  $J$  and the reverse saturation current density  $J_0$  is expressed as follows:

$$J_0 = A^* T^2 \exp \left( - \frac{q\Phi_B}{KT} \right) \quad (1.6)$$

Where,  $q$  represents the charge of electron,  $V$  denotes the tested voltage across the junction,  $\eta$  stands for ideality factor of the diode (a dimensionless parameter),  $K$  represents Boltzmann's constant,  $T$  signifies the absolute temperature in Kelvin scale,  $\Phi_B$  denotes the effective barrier potential height,  $A^*$  is calculated as  $4\pi q m^* k^2 / h^3$  which represents the modified Richardson's constant for the semiconductor.

We can reconfigure equation (1.6) for the reverse saturation current to determine the value of  $\Phi_B$ , which remains unaffected by bias, by expressing it as:

$$\Phi_B = \frac{KT}{q} \ln \left( \frac{A^* T^2}{J_0} \right) \quad (1.7)$$

To ascertain the value of  $J_0$ , a semilog graph of  $J$  vs.  $V$  is constructed (for forward values of  $V$  exceeding  $3kT/q$ ), yielding a linear relationship. Extrapolating the semilog of  $J$  for  $V = 0$  allows for the determination of  $J_0$ . Given the knowledge of  $A^*$ , along with the saturation current density  $J_0$  and the temperature  $T$ , the barrier height  $\Phi_B$  can be calculated. This value, obtained through this method, represents the barrier height at zero-bias and incorporates the barrier lowering  $\Delta\Phi_B$  due to image force.

Even in the absence of knowledge regarding the  $A^*$  value, the height of the potential barrier can still be determined by plotting the  $J$ - $V$  curve across a temperature range and deriving  $J_0$  for each temperature. This involves creating a linear plot of  $\ln (J_0/T^2)$  against  $1/T$ . The slope and intercept values on the vertical axis ( $J_0/T^2$ ) are then utilized to ascertain both  $\Phi_B$  and  $A^*$ .

$$\ln (J_0/T^2) = \ln (A^*) - \frac{q\Phi_B}{KT} \quad (1.8)$$

Typically, this equation yields the barrier height at 0K, which tends to be slightly higher than the barrier height observed at room temperature.

In practical Schottky devices, the ideality factor often surpasses unity, indicating non-ideal behavior attributed to barrier inhomogeneities. Such deviations may stem from a high likelihood of electron-hole recombination in the depletion region, tunneling current, or the presence of an interfacial layer [128]. When current levels are high, the series resistance ( $R_S$ ) arising from the metal, semiconductor, and their interface becomes critical in reducing the effective voltage applied to the contact point.

$$V_{\text{eff}} = V - I R_S \quad (1.9)$$

Cheung's method [129] is employed to evaluate the ideality factor and series resistance. The bias voltage can be reformulated by rearranging equation (1.5).

$$J = J_0 \left[ \exp \left( \frac{q(V - I R_S)}{\eta K T} \right) - 1 \right] \quad (1.10)$$

Under specific conditions such as forward bias ( $V \geq 3KT/q$ ) and  $V \gg I R_S$ , and by differentiating the voltage with respect to  $\ln J$ , equation (1.10) can be expressed as shown [130].

$$\frac{dV}{d \ln J} = A J R_S + \frac{\eta K T}{q} \quad (1.11)$$

Equation (1.11) is utilized to perform linear regression analysis on the plot of  $\frac{dV}{d \ln J}$  vs.  $J$ , from which the slope and intercept values are obtained to derive  $R_S$  and  $\eta$ .

In 1986, Cheung et al. proposed a model to determine the barrier height ( $\Phi_B$ ) and provide a secondary assessment of the series resistance ( $R_S$ ) through current-voltage analysis. According to their model, the voltage-dependent Cheung's function  $H(J)$  is expressed as [129].

$$H(J) = V - \frac{\eta K T}{q} \ln \left( \frac{J}{A^* T^2} \right) = A J R_S + \eta \Phi_B \quad (1.12)$$

An issue arises when trying to extract accurate barrier height values in cases where there is substantial series resistance. This situation limits the linear part of the  $\ln J$  versus  $V$  plot and complicates the accurate extrapolation to  $V = 0$ . In 1979, Norde [131] introduced an alternative method to ascertain the series resistance and barrier height of the metal semiconductor junction, particularly in scenarios where thermionic emission is predominant, termed the Norde function.

$$F(V) = \frac{V}{a} - \frac{1}{\beta} \ln \left( \frac{J}{A^* T^2} \right) \quad (1.13)$$

Where  $J$  represents the current density derived from the  $J$ - $V$  curve, 'a' is a constant greater than the ideality factor of the diode (i.e.,  $\geq 2$ , assuming  $\eta=1$ ) [132],  $\beta=q/KT$ , and other parameters are as mentioned previously. Assuming the diode includes a series resistance  $R$ ,

$$J = J_0 \left[ \exp \left( \frac{q(V - IR)}{K T} \right) - 1 \right] \quad (1.14)$$

The voltage dependence of  $\Phi_B$  is disregarded. When the voltage across the diode exceeds  $3kT/q$ , the given equation can be combined with Equation (1.13) to derive:

$$F(V) = \Phi_B + IR - \frac{V}{a} \quad (1.15)$$

For small  $V$  values (but surpassing  $3kT/q$ ), the term  $IR$  is negligible, resulting in a linear  $F(V)$  versus  $V$  plot with a slope of  $-\frac{1}{2}$ . The intercept at  $V = 0$  provides  $\Phi_B$ , although the linear range may not be extensive enough for accurate determination. Conversely, for larger  $V$  values, the current is predominantly determined by  $R$ , leading to  $I = V/R$  and  $F(V)$  approaching a straight line with a slope of  $+1/2$ .

$$F(V) = \frac{V}{a} - \frac{1}{\beta} \ln \left( \frac{V}{R A A^* T^2} \right) \quad (1.16)$$

Thus, the slope of the  $F(V)$  versus  $V$  graph transitions from  $-\frac{1}{2}$  to  $+\frac{1}{2}$ , and  $F(V)$  reaches a minimum between the two limits, as Norde demonstrated that this minimum corresponds to a specific value of  $F(V)$  satisfying the relationship.

$$F(V_{\min}) = \frac{V_{\min}}{a} - \frac{1}{\beta} \ln \left( \frac{I_{\min}}{A A^* T^2} \right) \quad (1.17)$$

The Norde function facilitates the determination of barrier height ( $\Phi_B$ ) and series resistance ( $R_S$ ).

$$\Phi_B = F(V_{\min}) + \frac{V_{\min}}{a} - \frac{1}{\beta} \quad (1.18)$$

And,

$$R_S = \frac{a - \eta}{\beta I_{\min}} \quad (1.19)$$

Where  $I_{\min}$  represents the forward current value at the voltage  $V_{\min}$ , where  $F(V)$  exhibits its minimum.

### 1.14.2. Estimation of Mobility and Transit Time

The J-V characteristics can be further explored by analyzing the mobility ( $\mu_{\text{eff}}$ ) and lifetime ( $\tau$ ) of charge carriers using the space-charge limited current (SCLC) theory, which helps to understand the charge transport mechanism for various photo-induced applications [133]. When plotting  $\log(J)$  against  $\log(V)$  for positive voltages, distinct linear regions emerge, indicating different conduction mechanisms. In metal-semiconductor junctions, interfacial trap states significantly affect charge carrier conduction, altering the J-V characteristic curves. Initially, at low bias, Ohmic behavior ( $J \propto V$ ) with a near unity slope is observed, suggesting predominant conduction by intrinsic charge carriers [134]. As the slope increases, typically reaching 2, injected carriers from the contacts start to dominate over intrinsic carriers for intermediate potential values, establishing a spatially distributed charge field. Mobility mainly governs quadratic current ( $J \propto V^2$ ) in this region [133, 135]. Eventually, at higher applied voltages, the device surpasses the trap-filled limit, leading to conduction primarily through 'trap-free space-charge limited current' characterized by power-law behavior ( $J \propto V^n$ , where  $n > 2$ ), corresponding to region III [135]. The electron mobility is estimated from the slope of the J vs.  $V^2$  plot using the Mott-Gurney equation [135].

$$J = \frac{9 \mu_{\text{eff}} \epsilon_0 \epsilon_r}{8} \left( \frac{V^2}{d^3} \right) \quad (1.20)$$

where,  $\epsilon_0$ ,  $\epsilon_r$  and  $d$  stand for the free space permittivity, the dielectric constant of materials and the thickness of the diode, respectively.

The dielectric constant ( $\epsilon_r$ ) of the synthesized materials can be estimated from the capacitance (C) vs. frequency (f) plot obtained from impedance analyzer measurements.

$$\epsilon_r = \frac{1}{\epsilon_0} \frac{C_{\text{sat}} d}{A} \quad (1.21)$$

where,  $C_{\text{sat}}$  is the saturated capacitance [136].

Additionally, the transient time ( $\tau$ ) of charge carriers can be deduced using a specific equation [137].

$$\tau = \frac{9\epsilon_0\epsilon_r}{8d} \left( \frac{V}{J} \right) \quad (1.22)$$

### 1.14.3. Capacitance-Voltage Measurements

The capacitance of the Schottky barrier diode's depletion region is linked to its width and is assessed by varying the tested reverse bias voltage. If AC voltage of a few millivolts is tested to the reverse-biased diode, the capacitance ( $C$ ) of the depletion region for a non-degenerate semiconductor under reverse bias voltage ( $V_R$ ) is described as follows:

$$C = S \left[ \frac{\epsilon_s q N_d}{2 \{ V_i + V_R - (\frac{KT}{q}) \}} \right]^{\frac{1}{2}} \quad (1.23)$$

In the provided equation,  $S$  represents the cross-sectional area of contact,  $\epsilon_s$  denotes the permittivity of the semiconductor, and all other symbols maintain their conventional meanings. This equation assumes that the diode lacks a significant interfacial oxide layer and that the n-type semiconductor possesses a uniform donor concentration  $N_d$ . If  $\Phi_B$  remains unaffected by the applied reverse bias voltage ( $V_R$ ), plotting  $1/C^2$  against  $V_R$  should result in a linear relationship, with an intercept  $V_o = (V_i - \frac{KT}{q})$  on the horizontal voltage axis, equivalent to  $[\Phi_B - \Phi_n - (\frac{KT}{q})]$ , where  $\Phi_n$  signifies the disparity in energy between the bottom of the conduction band and the Fermi level in the semiconductor. The slope of this line,  $\frac{2}{A^2 \epsilon_s \epsilon_0 q N_d}$ , facilitates the determination of the carrier concentration  $N_d$ , with  $A$  representing the effective diode area and  $\epsilon_0$  denoting the permittivity of free space. As  $qV_i = (\Phi_B - \Phi_n)$ , the barrier height  $\Phi_B$  can be calculated as follows:

$$\Phi_B = qV_o + \Phi_n + KT \quad (1.24)$$

The  $kT$  term originates from the dominant carrier's impact on the space charge, and Equation (1.20) does not incorporate the reduction in the barrier due to the image force.  $\Phi_n$  can be determined using the formula,

$$\Phi_n = \frac{KT}{q} \ln \left( \frac{N_c}{N_d} \right) \quad (1.25)$$

where  $N_c$ , conduction band's effective density of states, is provided by the equation,

$$N_c = 2 \left( \frac{2\pi m^* KT}{h^2} \right)^{3/2} \quad (1.26)$$

where  $m^*$  denotes the effective mass of electrons, equivalent to 0.22 times  $m_0$ , the rest mass of an electron, which is  $9.11 \times 10^{-31}$  kg.

#### 1.14.4. Photoelectric Measurements

Photoelectron spectroscopy, also known as photoelectric emission, stands as one of the pivotal and dependable techniques for examining solid surfaces and serves as a direct means to ascertain  $\Phi_B$ . When monochromatic light of a specific wavelength is directed onto a metal in contact with a semiconductor, and the photon energy  $h\nu$  exceeds the barrier height yet falls short of the semiconductor's band gap, the incident photons prompt a few electrons to traverse the barrier from the metal. As per the Fowler theory, the resulting photocurrent in the external circuit,  $I_{ph}$  under the condition where  $(h\nu - \Phi_B) \gg 3kT$ , is given by the equation

$$I_{ph} = B (h\nu - \Phi_B)^2 \quad (1.27)$$

Where,  $B$  represents a constant of proportionality. Plotting  $I_{ph}$  against  $h\nu$  yields a linear relationship, and the intercept on the  $h\nu$  axis directly yields the barrier height  $\Phi_B$ .

Modern-day photoelectron spectrometers gauge the energy distribution of emitted electrons rather than the total photocurrent. These spectrometers provide insight into the number of emitted electrons at various kinetic energy levels, ranging from zero up to a maximum value



determined by the energy of the incident photons. In numerous spectrometers, X-ray sources emit the photons, leading to the method being termed X-ray photoelectron spectroscopy or XPS.

## 1.15. Applications of Schottky Barrier Diode

Schottky diodes possess several advantageous characteristics compared to conventional p–n junctions, including a low forward voltage drop, higher current drive capacity, and, depending on the Schottky barrier height (SBH), a larger saturation current, rendering them suitable for various applications. Serving as a versatile rectifier, they find utility as both half-wave and full-wave rectifiers in circuits. Their non-linear I-V behavior makes them ideal as varistors. It can be used as varactors due to the variation in depletion-layer capacitance under reverse bias. Schottky photodiodes exhibit notable speed, making them suitable for optical devices. With their high-frequency capability, Schottky Barrier Diodes (SBDs) are particularly valuable as detectors and microwave mixers among all rectifiers. They serve as foundational components in numerous photosensitive devices such as solar cells, metal-base transistors, photodetectors, and MESFETs. Additionally, they function as clamping diodes in transistor-transistor logic circuits and integrated injection logic circuits. Their low loss, characterized by a low voltage drop in forward bias conditions, makes them prevalent in power electronics, particularly in low-voltage, high-current power supplies. Moreover, Schottky diodes lack minority carriers, thus circumventing limitations associated with minority carrier recombination time inherent in p–n junctions, resulting in significantly faster operation and suitability for use in digital logic circuits as rapid switches.

Furthermore, metal-semiconductor contacts play vital roles as gate electrodes in field-effect transistors, the third terminal in transferred-electron devices, drain and source contacts in MOSFETs and electrodes for high-power IMPATT oscillators.

## 1.16 Outline of the Thesis

The thesis covered on the synthesis, characterization and study of charge transport mechanism of inorganic and organic nano-composites. Lots of studies about the structural and electric properties of MoWS<sub>2</sub> have been carried out many researchers. Schottky barrier diodes, on the other hand, are a very important part to the next generation technologies as well due to its frequent occurrence in numerous electronic devices such as transistors, photodetectors and solar

cells. Extensive research has unveiled typical electronic and charge transport characteristics of molybdenum tungsten disulfide ( $\text{Mo}_{1-x}\text{W}_x\text{S}_2$ ) with the change in ratio of tungsten amount. The simple material synthesis and photovoltaic device fabrication procedure has encouraged researchers to investigate its electrical properties in a greater depth. In this regard, different organic materials have been synthesized, characterized and their device application has been studied in detail during this research work. A brief discussion of the following chapters is given below.

The first chapter introduces the importance of Schottky barrier diodes in electronics, covering their historical context and the physics of Schottky junction formation. It also discusses research on inorganic nano-composites including 2D materials like Transition Metal Dichalcogenides, organic semiconductors, emphasizing their synthesis, applications, and the superiority of organic semiconductors in electronic devices, with a focus on metallogels. The second chapter conducts comparative analyses on Schottky diodes made from  $\text{MoS}_2$  and  $\text{Mo}_{1-x}\text{W}_x\text{S}_2$ -alloy composite, investigating structural, optical, and electrical properties while determining various device parameters. It details the hydrothermal synthesis of  $\text{MoS}_2$  and  $\text{MoWS}_2$  composite, followed by comprehensive material characterization, including impedance spectroscopy and current-voltage studies to assess device performance, with impedance data simulation using suitable equivalent circuits. In third to fifth chapter, I synthesized and characterized various organic supramolecular metallogels, highlighting their semiconducting properties through band gap values and their potential application in photosensitive devices via opto-electronic analysis. The third chapter details the synthesis of a supramolecular Mn (II) metallogel, showcasing its mechanical strength and viscoelastic properties through rheological experiments, micro-structural analysis via FESEM, and infrared spectrum analysis for Mn-ATA formation. Electrospray ionization mass investigation confirms metallogel components, while diode parameter measurements reveal its semiconductor nature. The Mn-ATA-based device exhibits Schottky diode behavior, with enhanced rectifying properties under illumination, indicating photo-responsive characteristics. The fourth chapter outlines the synthesis of two distinct supramolecular metallogels, Mn-BDA and Cd-BDA, highlighting their mechanical flexibility via rheological experiments and significant mechanical stability. Morphological observations through FESEM, along with FT-IR and ESI-mass spectroscopic analyses, validate non-covalent supramolecular interactions. Additionally, two Schottky diodes (SDs) fabricated with ITO/Cd-BDA/Al and ITO/Mn-BDA/Al

configurations exhibit significant semiconductor characteristics with nonlinear J–V curve. The fifth chapter details the synthesis of a supramolecular Ni(II)-metallogel and investigates its mechanical properties through rheological studies, with FESEM revealing flake-like morphological patterns. FT-IR spectroscopy is employed to examine the formation of the metallogel, while thin film devices demonstrate electrical conductivity in metal-semiconductor junctions, evaluating their semiconductor properties such as Schottky barrier diode behaviour. The sixth chapter outlines solar energy's potential as a renewable source, discussing early photovoltaic developments and the importance of emitter design in crystalline silicon solar cells. It compares selective emitter cells' advantages and disadvantages to homogeneous emitter cells. Selective emitter technology in photovoltaic aims to balance contact resistance and surface recombination velocity, boosting solar cell efficiency. Various fabrication methods, including laser over-doping, are explored, with a novel technique proposed in the seventh chapter. Laser over-doping emerges as a cost-effective and straightforward approach, eliminating the need for double diffusion. The seventh chapter introduces a novel method for creating a selective emitter in n type crystalline silicon solar cells, combining the formation of both the front side selective emitter and rear back surface field (BSF) layer in a single rear side diffusion step. This innovative technique achieves a selective emitter with varying levels of diffusion, demonstrating cost-effectiveness by eliminating the need for additional heat treatments or chemical etching processes. The eighth chapter focuses on creating n-type crystalline silicon selective emitter solar cells via laser over-doping, optimizing parameters such as dielectric passivation layer, doping profile, and etching through simulation methods. It introduces a low-cost, industrially feasible  $\text{Al}_2\text{O}_3$  passivated n-type c-Si selective emitter solar cell with an efficiency of 17.2%, comparing it with conventional homogeneous doping emitter solar cells. All process parameters remain consistent between the two cell types, ensuring a fair comparative study. The ninth chapter summarizes the key findings and contributions of the study, outlining future research directions.

## References

- [1] G. Busch, *European Journal of Physics*, 10 (1989) 254-263.
- [2] J. Kärger, T. Binder, C. Chmelik, F. Hibbe, H. Krautscheid, R. Krishna & J. Weitkamp, *Nature materials*, 13 (2014) 333-343.
- [3] M. Faraday, *Experimental researches in electricity*, Read Books Ltd, Dover, New York, 1965, pp. 122-125.
- [4] S. Y. R. Hui, W. Zhong, & C. K. Lee, *IEEE Transactions on Power Electronics*, 29 (2013) 4500-4511.
- [5] J. Orton, *Semiconductors and the Information Revolution: Magic Crystals that Made IT Happen*. Amsterdam: Academic Press/Elsevier, 2009, 35-36.
- [6] W. Lu, Z. Li, M. Feng, H. J. Yan, B. Yan, L. Hu, ... & D. J. Xue, *Science China Chemistry*, 65 (2022) 2197-2204.
- [7] R. Niranjana & N. Padma, *Results in Optics*, 13 (2023) 100533.
- [8] A. Pochettino, *Acad. Lincei Rend.*, 15 (1906) 355.
- [9] M. Volmer, *Annalen der Physik*, 40 (1913) 775.
- [10] S. M. Sze and K. K. Ng, *Physics of semiconductor devices*, John Wiley & sons, 2006.
- [11] W. Schottky, R. Stormer, F. Waibel & Z. Hoch, *Frequenztechnik*, 37 (1931) 162.
- [12] A.H. Wilson, *Proceedings of the Royal Society of London, Series A*, 133 (1931) 458-491.
- [13] A.H. Wilson, *Proceedings of the Royal Society of London, Series A*, 134 (1931) 277-287.
- [14] C. T. Sah, *Fundamentals of Solid-State Electronics*, World Scientific publishing company limited, 73, Lynton Mead, Totteridge, London N20 8DH, England, (1991).
- [15] Y. Yao, Y. Zhou, L. Liu, Y. Xu, Q. Chen, Y. Wang, ... & A. Shao, *Frontiers in molecular biosciences*, 7 (2020) 193.
- [16] M. AhadiParsa, A. Dehghani, M. Ramezanzadeh & B. Ramezanzadeh, *Advances in Colloid and Interface Science*, 307 (2022) 102730.
- [17] A. Nieto, A. Agarwal, D. Lahiri, A. Bisht & S. R. Bakshi, *Carbon nanotubes: reinforced metal matrix composites*, CRC press, Boca Raton, 2021.
- [18] Gupta, T. Sakthivel & S. Seal, *Progress in Materials Science*, 73 (2015) 44-126.
- [19] M. P. Nikolova & M. S. Chavali, *Biomimetics*, 5(2020) 27.
- [20] S. Liang, H. Wang, Y. Li, H. Qin, Z. Luo, B. Huang, ... & L. Chen, *Sustainable Energy & Fuels*, 4 (2020) 3825-3847.

- [21] Z. Yu, L. Tetard, L. Zhai & J. Thomas, *Energy & Environmental Science*, 8 (2015) 702-730.
- [22] Z. Dai, L. Liu & Z. Zhang, *Advanced Materials*, 31 (2019) 1805417.
- [23] X. L. Shi, J. Zou & Z. G. Chen, *Chemical reviews*, 120 (2020) 7399-7515.
- [24] J. D. Benck, T. R. Hellstern, J. Kibsgaard, P. Chakthranont & T. F. Jaramillo, *American Chemical Society Catalysis*, 4 (2014) 3957-3971.
- [25] Q. Lu, Y. Yu, Q. Ma, B. Chen & H. Zhang, *Advanced Materials*, 28 (2016) 1917-1933.
- [26] K. F. Mak & J. Shan, *Nature Photonics*, 10 (2016) 216-226.
- [27] D. Jariwala, V. K. Sangwan, L. J. Lauhon, T. J. Marks, M. C. Hersam, *American Chemical Society Nano*, 8 (2014) 1102– 1120.
- [28] G. Fiori, F. Bonaccorso, G. Iannaccone, T. Palacios, D. Neumaier, A. Seabaugh, S. K. Banerjee, L. Colombo, *Nature Nanotechnology*, 9 (2014) 768– 779.
- [29] W. Wu, L. Wang, Y. Li, F. Zhang, L. Lin, S. Niu, D. Chenet, X. Zhang, Y. Hao, T. F. Heinz, J. Hone, Z. L. Wang, *Nature*, 514 (2014) 470.
- [30] S. Manzeli, D. Ovchinnikov, D. Pasquier, O. V. Yazyev, A. Kis, *Nature Reviews Materials*, 2 (2017) 17033.
- [31] W. Choi, N. Choudhary, G. H. Han, J. Park, D. Akinwande & Y. H. Lee, *Materials Today*, 20 (2017) 116-130.
- [32] S. Manzeli, D. Ovchinnikov, D. Pasquier, O. V. Yazyev & A. Kis, *Nature Reviews Materials*, 2 (2017) 1-15.
- [33] M. B. Askari, P. Salarizadeh, P. Veisi, E. Samiei, H. Saeidfirozeh, M. T. Tourchi Moghadam, & A. Di Bartolomeo, *Micromachines*, 14 (2023) 691.
- [34] A. M. Wiltrout, N. J. Freymeyer, T. Machani, D. P. Rossi & K. E. Plass, *Journal of Materials Chemistry*, 21 (2011) 19286-19292.
- [35] Rockett and R. Birkmire, *Journal of Applied Physics*, 70 (1991) R81–R97.
- [36] Splendiani, L. Sun, Y. Zhang, T. Li, J. Kim, C. Y. Chim, G. Galli, F. Wang, *Nano Letters*, 10 (2010) 1271-5.
- [37] K. F. Mak, C. Lee, J. Hone, J. Shan, T. F. Heinz, *Physical Review Letters*, 105 (2010) 136805.
- [38] J. A. Reyes-Retana, F. Cervantes-Sodi, *Scientific Reports*, 6 (2016) 24093.

- [39] G. Sallen, L. Bouet, X. Marie, G. Wang, C. R. Zhu, W. P. Han, P. Lu, P. H. Tan, T. Amand, B. L. Liu, B. Urbaszek, *Physical Review B*, 86 (2012) 3–6.
- [40] Y. R. Hacoheh, E. Grunbaum, R. Tenne, J. Sloand and J. L. Hutchison, *Nature*, 395 (1998) 336-337.
- [41] Y. R. Hacoheh, R. Popovitz-Biro, Y. Prior, S. Gemming, G. Seifert and R. Tenne, *Physical Chemistry Chemical Physics*, 5 (2003) 1644-1651.
- [42] P. A. Parilla, A. C. Dillon, K. M. Jones, G. Riker, D. L. Schulz, D. S. Ginley & M. J. Heben, *Nature*, 397 (1999) 114.
- [43] R. Sen, A. Govindaraj, K. Suenaga, S. Suzuki, H. Kataura, S. Iijima & Y. Achiba, *Chemical Physics Letters*, 340 ( 2001) 242-248.
- [44] Schuffenhauer, B. A. Parkinson, N. Y. Jin-Phillipp, L. Joly-Pottuz, J. M. Martin, R. Popovitz-Biro & R. Tenne, *Small*, 1 (2005) 1100-1109.
- [45] J. J. Hu, J. S. Zabinski, J. H. Sanders, J. E. Bultman & A. A. Voevodin, *The Journal of Physical Chemistry B*, 110 (2006) 8914-8916.
- [46] S. Y. Hong, R. Popovitz-Biro, Y. Prior & R. Tenne, *Journal of the American Chemical Society*, 125 (2003) 10470-10474.
- [47] N. Sano, H. Wang, M. Chhowalla, I. Alexandrou, G. A. J. Amaratunga, M. Naito & T. Kanki, *Chemical Physics Letters*, 368 (2003) 331-337.
- [48] M. Chhowalla, G. A. Amaratunga, *Nature*, 407 (2000) 164–167.
- [49] Alexandrou, N. Sano, A. Burrows, R. Meyer, H. Wang, A. Kirkland, C. Kiely, G. Amaratunga, *Nanotechnology*, 14 (2003) 913.
- [50] Vollath & D. V. Szabo, *Acta Materialia*, 48 (2000) 953-967.
- [51] Vollath & D. V. Szabo, *Material Letters*, 35 (1998) 236-244.
- [52] J. Brooks, R. E. Douthwaite, R. Brydson, C. Calvert, M. G. Measures & A. Watson, *Nanotechnology*, 17 (2006) 1245.
- [53] K. Byrappa, *Hydrothermal Growth of Crystal*, ed. by K. Byrappa, Pergamon:Oxford, 1991.
- [54] H. M. Manasevit, *Applied Physics Letters*, 12 (1968) 156-159.
- [55] S.Y. Kim, J. Kwak, C. V. Ciobanu, S. Y. Kwon, *Advanced Materials*, 31 (2019) 1804939.
- [56] A. Cho, *Journal of Vacuum Science & Technology*, 8 (1971) S31-S38.
- [57] B. T. Foxon, *Journal of Crystal Growth*, 251 (2003) 1-8.

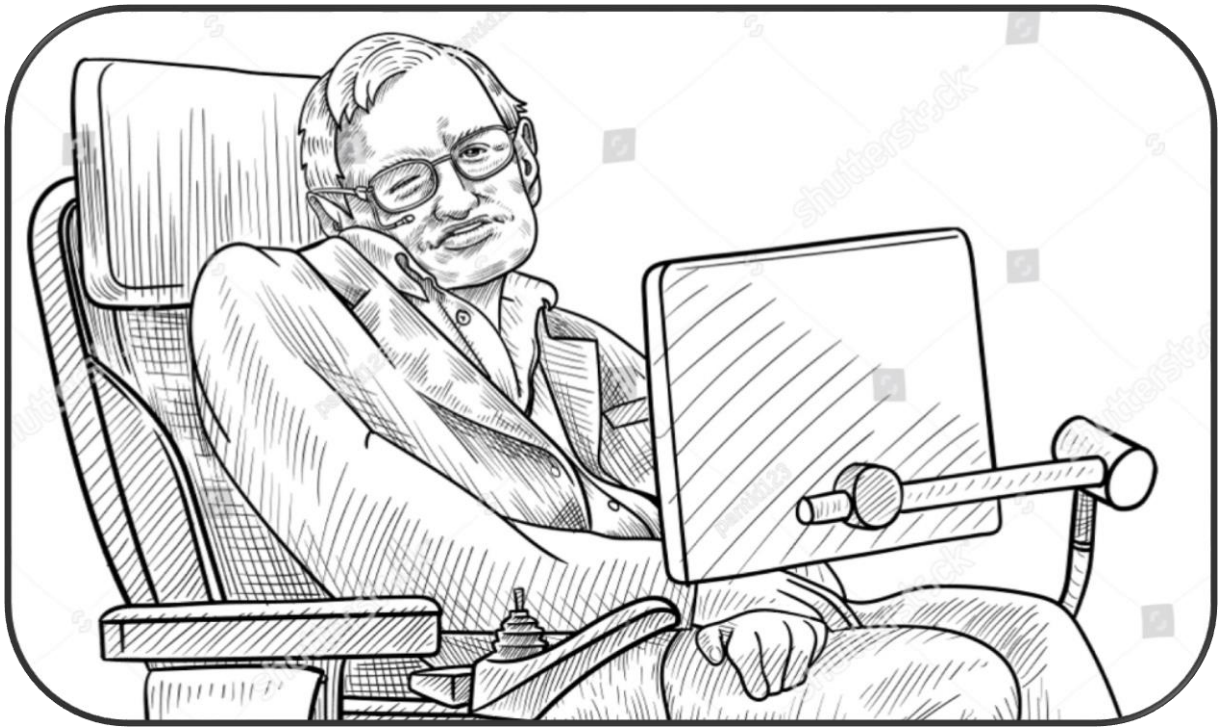
- [58] P. Höschl, Yu. M. Ivanov, E. Belas, J. Franc, R. Grill, D. Hlidek, P. Moravec, M. Zvara, H. Sitter & A. Toth, *Journal of Crystal Growth*, 184/185 (1998) 1039-1043.
- [59] M. Ohmori, Y. Iwase & R. Ohno, *Materials Science & Engineering: B*, 16 (1999) 283-290.
- [60] R. Triboulet, *physica status solidi C*, 2 (2005) 1556-1565.
- [61] Radisavljevic, A. Radenovic, J. Brivio, V. Giacometti, A. Kis, *Nature Nanotechnology*, 6 (2011) 147–50.
- [62] W. Choi, N. Choudhary, G. H. Han, J. Park, D. Akinwande, Y. H. Lee, *Materials Today*, 20 (2017) 116–130.
- [63] Y. C. Syu, W. E. Hsu, C. T. Lin, *ECS Journal of Solid State Science and Technology*, 7 (2018) 3196– 3207.
- [64] J. G. Song, G. H. Ryu, S. J. Lee, S. Sim, C. W. Lee, T. Choi, H. Jung, Y. Kim, Z. Lee, J. M. Myoung, C. Dussarrat, C. Lansalot-Matras, J. Park, H. Choi, H. Kim, *Nature Communication*, 6 (2015) 7817.
- [65] Y. Chen, J. Xi, D. O. Dumcenco, Z. Liu, K. Suenaga, D. Wang, Z. Shuai, Y. S. Huang, L. Xie, *American Chemical Society Nano*, 7 (2013) 4610– 4616.
- [66] J. Park, M. S. Kim, B. Park, S. H. Oh, S. Roy, J. Kim, W. Choi, *American Chemical Society Nano*, 12 (2018) 6301– 6309.
- [67] H. P. Komsa, A. V. Krashennnikov, *The Journal of Physical Chemistry Letters*, 3 (2012) 3652– 3656.
- [68] T. L. Tan, M. F. Ng, G. Eda, *The Journal of Physical Chemistry C*, 120 (2016) 2501– 2508.
- [69] M. Pandey, K. W. Jacobsen, K. S. Thygesen, *The Journal of Physical Chemistry C*, 120 (2016) 23024– 23029.
- [70] M. Ohmori, Y. Iwase & R. Ohno, *Materials Science & Engineering: B*, 16 (1999) 283-290.
- [71] R. Triboulet, *physica status solidi C*, 2 (2005) 1556-1565.
- [72] Yasemin, C. Mujdat, I. Saliha & A. Aytunc, *Journal of Physics D: Applied Physics*, 42 (2009) 065421.
- [73] H. Tang, S. He & C. Peng, *Nanoscale Research Letters*, 12 (2017) 410.
- [74] Z. Shi & A. H. Jayatissa, *Materials*, 11 (2018) 729.
- [75] S. Braun, W. R. Salaneck, M. Fahlman, *Advanced Materials*, 21 (2009) 1450.
- [76] Natali, M. Caironi, *Advanced Materials*, 24 (2012) 11.

- [77] Cahen, A. Kahn, *Advanced Materials*, 15 (2003) 271.
- [78] S. M. Sze, *Physics of Semiconductor Devices*, 2nd ed.; Wiley, New York, (1981).
- [79] M. A. Baldo, S. R. Forrest, *Physical Review B*, 64 (2001) 85201.
- [80] Lange, J. Blakesley, J. Frisch, A. Vollmer, N. Koch, D. Neher, *Physical Review Letters*, 106 (2011) 216402.
- [81] D. K. Smith, *Royal Society of Chemistry*, 20 (2024) 10-70.
- [82] J. Owens, R. K. Singh, F. Foroutan, M. Alqaysi, C. M. Han, C. Mahapatra, H. W. Ki, J. C. Knowles, *Progress in Materials Science*, 77 (2016) 1-79.
- [83] Bunzen & E. Kolehmainen, *Molecules*, 18 (2013) 3745-3759.
- [84] D. E. Barry, D. F. Caffrey, T. Gunnlaugsson, *Chemical Society Reviews*, 45 (2016) 3244-3274.
- [85] L. Liao, X. Jia, H. Lou, J. Zhong, H. Liu, S. Ding, ... & X. Luo, *Royal Society of Chemistry advances*, 11 (2021) 11519-11528.
- [86] A. E. Danks, S. R. Hall & Z. Schnepf, *Materials Horizons*, 3 (2016) 91-112.
- [87] D. Bokov, A. T. Jalil, S. Chupradit, W. Suksatan, , M. J. Ansari, I. H. Shewael,... & E. Kianfar, *Advances in Materials Science and Engineering*, 2021 (2021) 1-21.
- [88] J. Chen, T. Wang & M. Liu, *Inorganic Chemistry Frontiers*, 3 (2016) 1559-1565.
- [89] Iftikhar, G. G. Sonai, S. G. Hashmi, ... A. F., Nogueira, & P. D. Lund, *Materials*, 12 (2019) 1998.
- [90] S. Dwivedi, *International Journal of Hydrogen Energy*, 45 (2020) 23988-24013.
- [91] Wu, Z. Lan, J. Lin, M. Huang, S. Hao, T. Sato & S. Yin, *Advanced Materials*, 19 (2007), 4006-4011.
- [92] Picci, C. Caltagirone, A. Garau, V. Lippolis, J. Milia, J. W. Steed, *Coordination Chemistry Reviews*, 492 (2023) 215225.
- [93] B. Aiyappa, S. Saha, P. Wadge, R. Banerjee & S. Kurungot, *Chemical science*, 6 (2015) 603-607.
- [94] N. Malviya, C. Sonkar, R. Ganguly & S. Mukhopadhyay, *Inorganic chemistry*, 58 (2019) 7324-7334.
- [95] Huang, L. He, J. Zhang, L. Chen & C. Y. Su, *Journal of Molecular Catalysis A: Chemical*, 317 (2010) 97-103.
- [96] Xing, M. F. Choi, & B. Xu, *Chemistry—A European Journal*, 8 (2002) 5028-5032.



- [97] S. M. Sze, *Semiconductor Devices: Physics and Technology*, John Wiley, (1985).
- [98] A. Di Bartolomeo, *Physics Reports*, 606 (2016) 1.
- [99] F. Braun, *Annals of Physics*, 229 (1875) 556-563.
- [100] S. Kim, C. R. Lee, J. H. Im, K. B. Lee, T. Moehl, A. Marchioro, S. J. Moon, R. Humphry-Baker, J. H. Yum, J. E. Moser, M. Graätzel & N. G. Park, *Science Report*, 2 (2012) 591.
- [101] S. M. Sze, K. K. Ng, *Physics of semiconductor devices*, John wiley & sons, 2006.
- [102] W. Schottky, R. Stormer, F. Waibel, Z. Hoch, *Frequenztechnik*, 37 (1931) 162.
- [103] W. Schottky, *Naturwissenschaften*, 26 (1938) 843-843.
- [104] N. F. Mott, *Mathematical Proceedings of the Cambridge Philosophical Society*, 34 (2008) 568-572.
- [105] A. H. Agajanian, V. L. Rideout, A bibliography on metal-semiconductor (Schottky barrier) contacts, IBM Technology, Report TR22-1745, March 4, 1974.
- [106] U. S. Patent 3,025,589 (March 20, 1962), to J. A. Hoerni.
- [107] R. Crowell, S. M. Sze, *Journal of Applied Physics*, 37 (1966) 2683.
- [108] Kahng, M. P. Lepselter, *The Bell System Technical Journal*, 44 (1965) 1525.
- [109] M. P. Lepselter, S. M. Sze, *The Bell System Technical Journal*, 47 (1968) 195.
- [110] W. Schottky, *Physikalische Zeitschrift*, 15 (1914) 872.
- [111] S. M. Sze, C. R. Crowell, D. Kahng, *Journal of Applied Physics*, 35 (1964) 2534.
- [112] O. W. Richardson, *the Emission of Electricity from Hot Bodies*, Longmans Green, Harlow, Essex, (1921).
- [113] A. Bethe, Massachusetts Institute of Technology, Radiation Laboratory, Report 43-12, 1942.
- [114] R. H. Fowler, *Physical Review*, 38 (1931) 45.
- [115] C. R. Crowell, W. G. Spitzer, L. E. Howarth, E. E. Labate, *Physical Review*, 127 (1962) 2006.
- [116] A. H. Wilson, *A Proceedings of the Royal Society of London, Series A*, 136 (1932) 487.
- [117] R. Stratton, *Physical Review*, 125 (1962) 67.
- [118] W. Schottky, E. Spenke, *Wiss. Veroff, Siemens-Werken* 18 (1939) 225.
- [119] Bardeen, *Physical Review*, 71 (1947) 717.
- [120] W. Conley, C. B. Duke, G. D. Mahan, J. J. Tiemann, *Physical Review*, 150 (1966) 466.

- [121] R. Stratton, Physical Review, 125 (1962) 67.
- [122] C. R. Crowell, S. M. Sze, Solid-State Electron, 9 (1966) 1035.
- [123] A. Neamen, Semiconductor physics and devices, New York: McGraw-Hill, 2007, 304-323.
- [124] H. Rhoderick & R. H. Williams, Current Transport Mechanism in Metal semiconductor contacts, 2nd ed., Oxford: Clarendon, 1988, 94-100.
- [125] E. H. Rhoderick, IEE Proceedings - Part I: Solid-State and Electron Devices, 129 (1982) 1-14.
- [126] R. Kumar & S. Chand, Solid State Science, 58 (2016) 115.
- [127] Hass, R. Feng, T. Li, X. Li, Z. Zong, W. A. De Heer, P. N. First, E. H. Conrad, C. A. Jeffrey & C. Berger, Applied Physics Letters, 89 (2006) 143106.
- [128] Campos, L. d. S. Bulhoses & C. A. Lindino, Sensors and Actuators A: Physical, 87 (2000) 67- 71.
- [129] S. K. Cheung and N. W. Cheung, Applied Physics Letters, 49 (1986) 85-87.
- [130] R. Chauhan, A. Kumar, R. P. Chaudhary, Applied Surface Science, 270 (2013) 655-660.
- [131] Norde, Journal of Applied Physics, 50 (1979) 5052-5053.
- [132] V. Aubry & F. Meyer, Journal of Applied Physics, 76 (1994) 7973-7984.
- [133] Ullah, M. Shah, M. Khan, and F. Wahab, Journal of Electronic Materials, 45 (2016) 1175.
- [134] Taşçioğlu, U. Aydemir, and Ş. Altındal, Journal of Applied Physics, 108 (2010) 064506.
- [135] Soylu and B. Abay, Physica E: Low-Dimensional System and Nanostructures, 43 (2010) 534.
- [136] C. Kao, Dielectric Phenomena in Solids, Elsevier, 2004.
- [137] S. Sil, A. Dey, J. Datta, M. Das, R. Jana, S. Halder, J. Dhar, D. Sanyal, and P. P. Ray, Materials Research Bulletin, 106 (2018) 337.



*"Real science can be far stranger than science fiction and much more satisfying"*

- Stephen Hawking



# Chapter 2

---

**Improvement of charge kinetics of MoS<sub>2</sub> nano-petal based Schottky device by incorporation of W: A comparative study of structural, optical, and electrical properties**

## Abstract

Molybdenum Tungsten Di-Sulphide is a semiconducting alloy of different TMD (transition metal dichalcogenide) materials that has enormous tunable structural, optical, and electrical attributes. In this chapter, we have performed the hydrothermal synthesization of  $\text{Mo}_{1-x}\text{W}_x\text{S}_2$  nanocomposites with different molar concentration of tungsten (i.e.  $x=0, 0.1, 0.2, 0.3$ ) and fabricated Al/  $\text{Mo}_{1-x}\text{W}_x\text{S}_2$ /ITO structured Schottky Barrier diodes. Characterization of their structural, optical, and charge transport attributes are compared. In this alloy formation, the amount of W (tungsten) concentration has a great impact on the particle size of composites. The transportation of charges via the metal-semiconductor junction is the basis for the superiority of thin film semiconductor devices like the Schottky diode. The diode parameters as well as charge transfer characteristics were analyzed by Impedance Spectroscopy and the theory of SCLC (space charge limited current). The calculated mobility and transit time for the  $\text{Mo}_{0.8}\text{W}_{0.2}\text{S}_2$  device are  $5.65 \times 10^{-4} \text{ m}^2 \text{ V}^{-1} \text{ s}^{-1}$  and 1.59 ns respectively. These results are better than the rest of the devices. Dramatic conductivity enhancement for the  $\text{Mo}_{0.8}\text{W}_{0.2}\text{S}_2$ -based Schottky device is observed. As a result, this chapter not only investigates Al/ $\text{MoWS}_2$  interface in detail but also explains the faster and better charge transport of the  $\text{Mo}_{0.8}\text{W}_{0.2}\text{S}_2$ -based device from a structural perspective.

## 2.1. Introduction

Many 2D and 3D materials have been tremendously explored in recent years due to their distinctive traits illustrating considerable optical characteristics along with incredibly quick recovery times [1], mechanical flexibility [2], substantially greater modulation depths [3], and even high electrical conductivity [4]. The distinct properties of 2D and 3D materials turn them very appealing to use in optoelectronic devices. Among these materials, one of the varieties of 2D material, transition metal dichalcogenides (TMDs) are like  $\text{MX}_2$  form, M denotes Mo and W type transition metal, and X indicates S, Se, Te type dichalcogenide. They have a vast quantity of applications in capacitors, electrochemical devices, solid lubricants, electronic and photo-sensing components like ultrasensitive and ultraresponsive photodetector that are very thin, flexible, and almost transparent [5-10].

Currently, alloying different TMD materials are highly exciting because of aspects like greater thermal stability, extended optical absorption [11], and an elevated layer-dependent feature [12-14]. TMD alloy development can activate the inert basal planes of TMD materials [15]. Furthermore, doping heavy atoms makes electron injection easier. The quantity of electrons injected is determined by the level of doping. Tungsten (W) is a transition metal with the same physical and chemical characteristics as Mo and high electron density. Furthermore,  $\text{WS}_2$  has a comparable crystal structure and lattice constants to  $\text{MoS}_2$  [16]. As a result, we may hypothesize that even after being doped with W, the crystal structure of  $\text{MoS}_2$  can remain stable.

$\text{MoS}_2$  and  $\text{WS}_2$  together yield a mixed TMDs compound with the chemical formula  $\text{Mo}_{1-x}\text{W}_x\text{S}_2$ . Such promising substances ( $\text{MoWS}_2$ ) have substantial performance enhancements, especially to their structural characteristics and band gap tunability [17] because the dimensions of the constituent elements differ intrinsically.  $\text{WS}_2/\text{MoS}_2$  composite comprised of two S layers with a sandwiched W/Mo layer in between (S-W-S or S-Mo-S) by Vander Walls interactions [18-20]. Despite the fact that a lot of studies have been undertaken for the  $\text{WS}_2/\text{MoS}_2$ -based composites, there haven't been any reports of the utilization of semiconducting  $\text{MoWS}_2$  composite material in the context of the metal-semiconductor junction as Schottky Barrier Diode (SBD) applications yet. There is possibility of tuning the work function of different semiconductor materials by modifying their bandgap purely by optical means, so there are some possibility for creation of different metal-semiconductor junctions which provide better conduction [21, 22].

In this chapter, I have discussed the synthesis process of the novel MoS<sub>2</sub> and mixed TMDs Mo<sub>1-x</sub>W<sub>x</sub>S<sub>2</sub> (x=0.1, 0.2, 0.3) composites using a feasible and highly productive hydrothermal method. Due to the unique structure and electronic composition of Mo<sub>1-x</sub>W<sub>x</sub>S<sub>2</sub>, the fabricated Mo<sub>0.8</sub>W<sub>0.2</sub>S<sub>2</sub> compound illustrated an organized architecture with enormous nano-petals with the smallest crystallite size. X-Ray diffractometer (XRD), field emission scanning electron microscopy (FESEM), UV-VIS spectroscopy as well as Raman spectroscopy were used to systematically characterize the samples, along with that, N<sub>2</sub> gas adsorption investigation using the BET method and Thermo gravimetric analysis (TGA) have been performed to decide the nature of the nanosheets. After Schottky devices are fabricated with these materials, I explored the impedance behavior and mobile charge dynamics of the Al/MoWS<sub>2</sub> interfacial region by utilizing Impedance Spectroscopy (IS).

Studying the charge carrier transit process in both semiconductor devices and solar cells has become a popular technique in modern times. To investigate the charge transfer process, I have examined the J-V characteristics and computed the Schottky diode specifications including Mobility, Transit Time, Barrier Height, and Ideality Factor.

Briefly, the derived results fairly explain the cause of the synthesized Mo<sub>0.8</sub>W<sub>0.2</sub>S<sub>2</sub> nano-composite structure revealing a superior conductivity and high rectification ratio in the Schottky diode switching application. It has great potential in the upcoming metal-semiconductor junction-based research domain.

## 2.2. Experimental Section

### 2.2.1. Material preparation

Sodium Tungsten Di-Hydrate (Na<sub>2</sub>WO<sub>4</sub>·2H<sub>2</sub>O), Sodium Molybdate (Na<sub>2</sub>MoO<sub>4</sub>·2H<sub>2</sub>O), Thio-urea/Thio-carbamide (CN<sub>2</sub>H<sub>4</sub>S), Oxalic Acid (H<sub>2</sub>C<sub>2</sub>O<sub>4</sub>) and Hydroxylamine hydrochloride (HONH<sub>3</sub>Cl) were purchased from Merck and utilized as precursors without any additional filtration.

### 2.2.2. Synthesis of Molybdenum Di-Sulfide

The Molybdenum Di-Sulfide compound was synthesized by hydrothermal method. For the synthesis of pure MoS<sub>2</sub>, 0.001 M of Na<sub>2</sub>MoO<sub>4</sub>·2H<sub>2</sub>O was first taken in 40 ml of deionized water



in a beaker and then stirred vigorously for 15 minutes to make a homogeneous solution. Then 0.002 M of  $\text{CN}_2\text{H}_4\text{S}$ ,  $\text{H}_2\text{C}_2\text{O}_4$ , and  $\text{HONH}_3\text{Cl}$  were mixed one after another into another beaker in separate 40 ml DI water to make the 2<sup>nd</sup> solution. After that, the 2<sup>nd</sup> solution was mixed drop-wise with the prepared 1<sup>st</sup> solution drop-wise under stirring conditions. Then, the mixture of 80 ml solution (1<sup>st</sup> solution and 2<sup>nd</sup> solution) was poured into a 100 ml Teflon lined autoclave and heated for 48 hours at 180°C. Having naturally cooled, a bluish-black precipitate was formed as the resulting product which was washed using centrifugal force repeatedly with DI water and ethanol sequentially to eliminate contaminants and non-reacting components originating both in the solvent and from the precursors. Precipitation was then vacuum-dried at 60°C and gathered as bluish-black powder.

### 2.2.3. Synthesis of Molybdenum Tungsten Di-Sulfide

Molybdenum Tungsten Di-Sulfide compounds with different molar ratios were also synthesized by hydrothermal method.  $\text{Mo}_{1-x}\text{W}_x\text{S}_2$  of different molar concentration of tungsten (i.e.  $x=0.1, 0.2, 0.3$ ) were synthesized, by replacing  $\text{Na}_2\text{MoO}_4 \cdot 2\text{H}_2\text{O}$  with  $\text{Na}_2\text{WO}_4 \cdot 2\text{H}_2\text{O}$ . The subsequent steps are identical to the preparation of pure  $\text{MoS}_2$ .

### 2.2.4. Thin Film Device fabrication

To fabricate different Metal-Semiconductor (MS) junction devices i.e. Schottky devices with the synthesized compounds, four glass substrates with Indium Tin Oxide (ITO) coatings were rinsed primarily in iso-propanol using ultrasonication for 15 minutes. Afterward, they were thoroughly washed in acetone and DI water successively one after another with ultrasonication for 10 minutes and then vacuum-dried in a chamber. In N-N-Dimethyl Formaldehyde (DMF), the samples were well dispersed until homogenous dispersions were produced. Using the SCU-2007 spin coating unit under vacuum, these dispersions of the synthesized materials were spin-coated for 30 seconds at 1200 rpm onto the pre-cleaned ITO glass. The final step was carried out 4 times to get the uniform thin films of respective composites. The films were subsequently dried in a vacuum chamber. Using a surface profiler, the thicknesses of all the respective films were obtained as 1  $\mu\text{m}$ . Aluminum (Al) metal was finally deposited onto the films through the use of a shadow mask utilizing an electron gun of e-beam vapor deposition Unit (HINDHIVAC) at a base pressure of  $10^{-6}$  Torr to get sandwich structures. Thus, an MS interface has been generated and

the active diode area has been retained as  $(7.065 \pm 0.063) \times 10^{-2} \text{ cm}^2$  by the shadow mask of 3 mm diameter.

### 2.2.5. Capacitance-Frequency measurement

Before Aluminium metallisation in the device fabrication process dried-films are ready for capacitance versus frequency measurement. For this one connection (high) is taken from the film and other connection (low) is taken from the ITO. The changes of capacitance with frequency is measured by using a 50 mV oscillating voltage and a frequency regime of 40 Hz to 5 MHz at zero bias voltage.

### 2.2.6. Material characterization

Through the utilization of Bruker manufactured D8 X-Ray Diffractometer with Cu K $\alpha$  radiation (wavelength  $\lambda = 0.15418 \text{ nm}$ ), scanned within the span  $10^\circ - 70^\circ$ , I was able to get the information needed to determine the phase and structure from the Powder X-ray Diffraction (XRD) experiment. The morphology of the as-synthesized sulfide nanostructures was assessed by FEI-built Field Emission Scanning Electron Microscope (FESEM) (Inspect F50) image. To determine the material constituent, EDAX (Energy dispersive X-ray Analysis) characterization was carried out. Raman spectra analyses of the synthesized samples were obtained by a Horiba-Jobin-Yvon LabRAM HR Raman spectrometer (Excitation: 532 nm Green Laser). Optical spectra of UV-Vis absorbance were recorded using a Perkin Elmer Lambda 365 UV/VIS Spectrophotometer (Shimadzu, 2401PC UV/Visible PC) to study the light adsorption property of the materials. For BET measurement, N<sub>2</sub> gas adsorption research has been carried out at 77K using a Quanta chrome Autosorb-iQ adsorption device. This investigation had been performed with the desolvated state of pure MoS<sub>2</sub> and various MoWS<sub>2</sub> composites retained by a liquid-nitrogen bath in varying pressures of 0 to 1 bar range. Without any additional purification, N<sub>2</sub> in its purest form (99.9999 %) is used to experiment. Thermo gravimetric analysis (TGA) was conducted by METTLER TOLEDO TGA/SDTA- 851-e. Agilent 4294A device was used to acquire the capacitance versus frequency data of the material and the Impedance Spectroscopy (IS) results of the Schottky diode. To perform the electrical study utilizing the current density-voltage (J-V) characteristics, the Keithley 2635B source meter interfaced with a computer had been used. All aforementioned experiment was done at room temperature.

## 2.3. Results and discussions

### 2.3.1. Structural analysis

The crystalline phase and crystallite size of nanoparticles can be detected using X-ray diffraction analysis. The obtained powder XRD patterns (PXRD) of the synthesized pure  $\text{MoS}_2$  and various  $\text{Mo}_{1-x}\text{W}_x\text{S}_2$  ( $x = 0, 0.1, 0.2, 0.3$ ; where  $x$  refers to the variations in Tungsten sourced precursor molar concentration for synthesis) composite structures have been compared which indicates good crystallinity in Fig. 2.1. For pristine  $\text{MoS}_2$  pattern, the observed diffraction peaks can be seen at Bragg's angle  $13.717^\circ$ ,  $33.693^\circ$ , and  $58.927^\circ$  respectively correspond to (002), (101), and (110) planes of the hexagonal  $\text{MoS}_2$  primitive lattice (JCPDS Card No. 77-1716). The lack of any secondary phase verifies the pure and single-phase  $\text{MoS}_2$  nanoparticle synthesis.

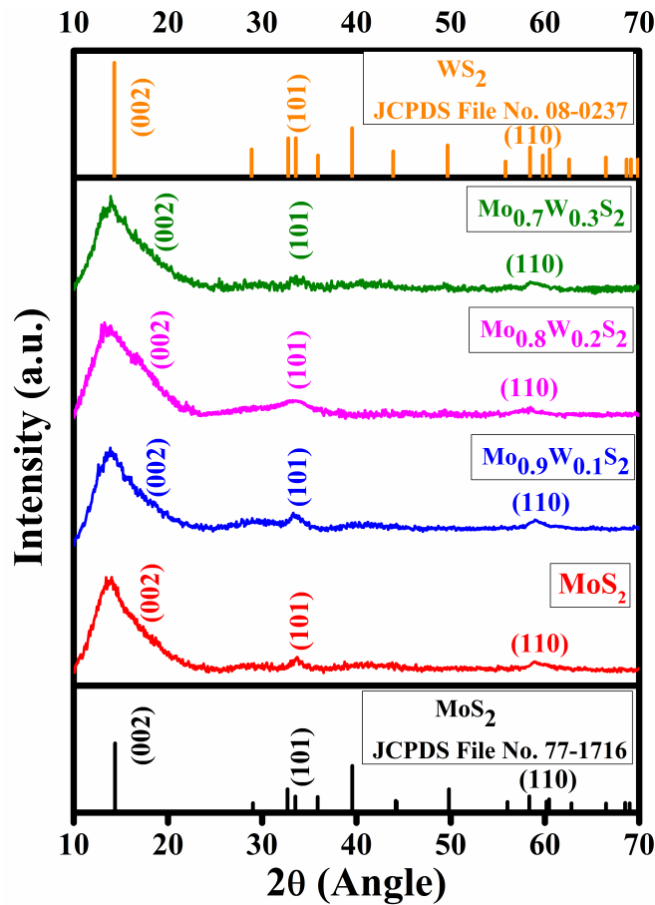


Fig. 2.1: XRD spectra of  $\text{MoS}_2$ ,  $\text{Mo}_{0.9}\text{W}_{0.1}\text{S}_2$ ,  $\text{Mo}_{0.8}\text{W}_{0.2}\text{S}_2$ , and  $\text{Mo}_{0.7}\text{W}_{0.3}\text{S}_2$ .

The diffraction peaks for MoWS<sub>2</sub> composites are equally sharp and precise, indicating a top level of crystallinity for these hydrothermally synthesized compounds. For reference JCPDS file no. 77-1716 (for pure MoS<sub>2</sub>) and JCPDS file no. 08-0237 (for pure WS<sub>2</sub>) are inserted in Fig. 2.1. According to Bragg's equation,

$$2d\sin\theta = n\lambda \quad (2.1)$$

Where  $\theta$ ,  $d$ ,  $\lambda$ , and  $n$  respectively represent diffraction angle, interplanar spacing, X-ray wavelength, and diffraction series. MoS<sub>2</sub> and WS<sub>2</sub> each have a typical diffraction peak along (002) at 14.398° and 14.319°, respectively. Other than the primary peak there are two more distinct peaks for 101 planes and 110 planes found in all synthesized compounds. For the  $x = 0.1, 0.2$ , and  $0.3$  alloys, there is no sign of individual MoS<sub>2</sub> or WS<sub>2</sub>, indicating that the material is a pure alloy.

Using the Debye-Scherrer formula [23], I determined the size of the crystallites from XRD information.

$$D = \frac{\kappa\lambda}{\beta\cos\theta} \quad (2.2)$$

Here,  $\lambda$  denotes X-ray wavelength (0.15418 nm),  $D$  defines the size of crystallite,  $\kappa$  indicates the shape factor, and  $\beta$  represents full width at half maxima (FWHM) in radian. In this case, the accepted standard value of  $\kappa$  is 0.9. The calculated crystallite sizes from PXRD for relevant compounds are listed in Table 2.1.

The observed increment of FWHM for composites with 10% and 20% alloying highlights the reduction of crystallite size as shown in Table 2.1. While for composite with 30% alloying the FWHM decreases and the crystallite size increases again. Using the following formula [24], the micro strains ( $\eta$ ) in the samples are determined.

$$\eta = \frac{\beta\cos\theta}{4} \quad (2.3)$$

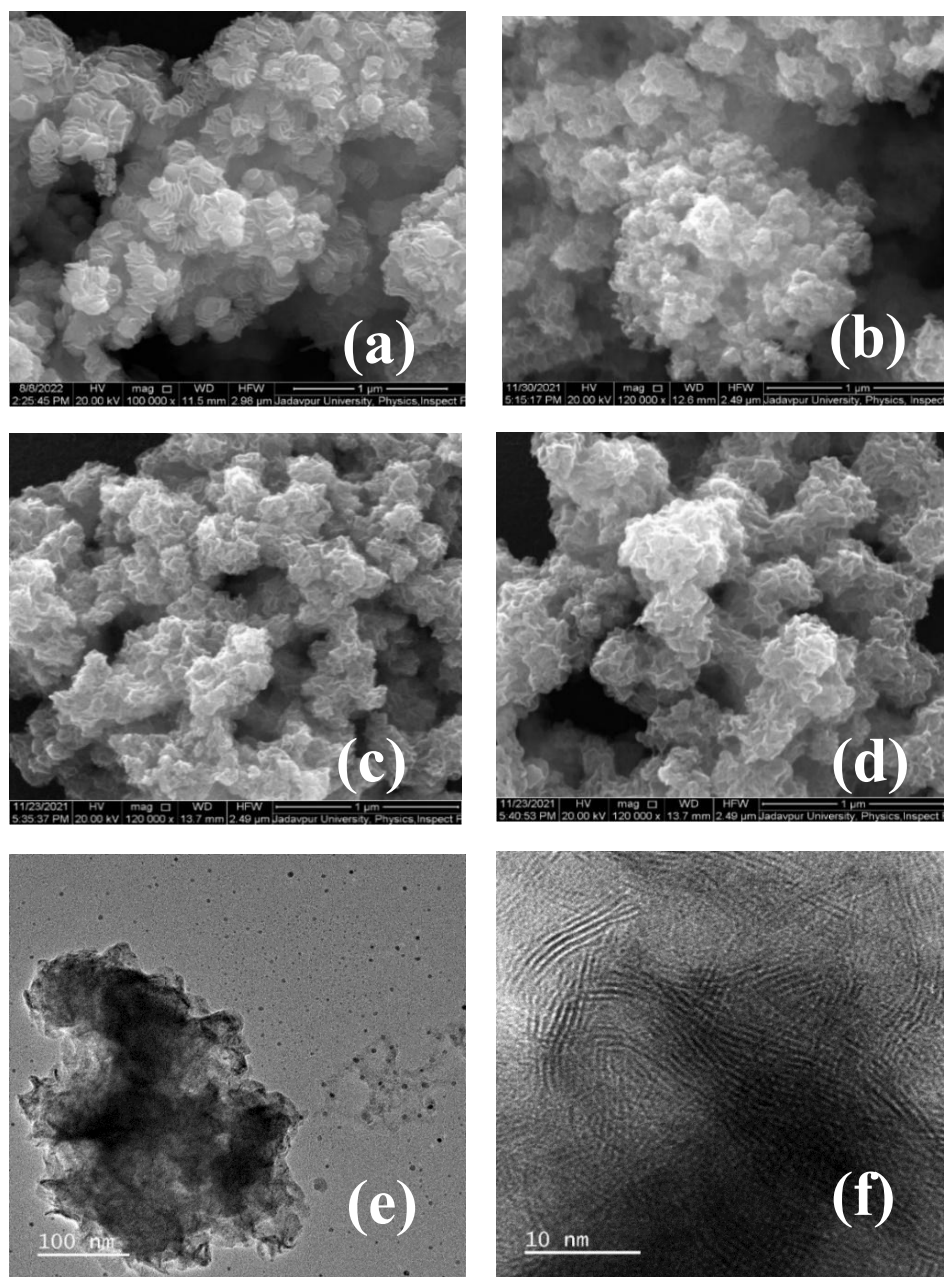
Table 2.1: XRD analysis parameters

Molybdenum Amount	Position of Peak (2 $\theta$ )	FWHM ( $\beta$ ) (°)	d-spacing (Å)	(hkl) crystal system	Lattice Parameter (a=b, c) (Å)	Crystallite Size (D) (nm)	Micro strain ( $\eta$ ) $\times (10^3)$
<b>1</b>	13.717	4.65	6.387	002	a=b=3.10	1.72	20.152
	33.693	1.11	2.654	101	c=12.77	7.47	4.641
	58.927	3.01	1.550	110		3.04	11.386
<b>0.9</b>	13.837	4.68	6.419	002	a=b=3.11	1.71	20.278
	33.393	1.65	2.695	101	c=12.84	5.02	6.899
	59.023	3.23	1.556	110		2.83	12.247
<b>0.8</b>	13.217	5.98	6.419	002	a=b=3.13	1.34	25.912
	33.313	2.96	2.695	101	c=12.84	2.80	12.385
	58.547	3.86	1.564	110		2.36	14.661
<b>0.7</b>	14.097	5.20	6.646	002	a=b=3.19	1.54	22.548
	32.693	2.91	2.727	101	c=13.29	2.84	12.182
	58.527	3.79	1.595	110		2.40	14.468

Images obtained from the Field Emission Scanning Electron Microscope (FESEM) of hydrothermally synthesized  $\text{Mo}_{1-x}\text{W}_x\text{S}_2$  nanoparticles are presented in Fig. 2.2 (a-d) where  $x = 0, 0.1, 0.2,$  and  $0.3$  respectively. It is observed that the surface morphology of all the samples has a typical 3D spherical Camellia flower-like structure and looks more or less similar. Individual  $\text{MoS}_2$  sphere has an average diameter of  $0.2 \mu\text{m}$ , as shown in Fig. 2.2 (a).

The surface of this spherical morphology is mostly made up of tightly stacked 2D curved nano petals which originate in a randomly crosswise manner. It also demonstrates that the highly scattered 2D nano-petals can develop towards the right angle to the surface, leading to the eventual formation of the spherical architecture. Fig. 2.2 (b, c, and d) show FESEM images of

the W-doped  $\text{MoS}_2$  composites. Overall, they generally correlate with the pure structure, indicating that each of these composite structures with increasing doping of tungsten tends to be larger and show 0.25, 0.3, and 0.4  $\mu\text{m}$  averaged diameter respectively.



**Fig. 2.2:** SEM images of (a)  $\text{MoS}_2$ , (b)  $\text{Mo}_{0.9}\text{W}_{0.1}\text{S}_2$ , (c)  $\text{Mo}_{0.8}\text{W}_{0.2}\text{S}_2$  and (d)  $\text{Mo}_{0.7}\text{W}_{0.3}\text{S}_2$ ; (e) The TEM image of  $\text{Mo}_{0.8}\text{W}_{0.2}\text{S}_2$  composite; (f) HRTEM image of individual  $\text{Mo}_{0.8}\text{W}_{0.2}\text{S}_2$  nano petals.

Fig. 2.2 (e) represents the image of TEM for the  $\text{Mo}_{0.8}\text{W}_{0.2}\text{S}_2$  compound. The encompassing areas of this composite are encased by semi-transparent substances attributed to nano petals. Fig. 2.2 (f) shows the HRTEM image of individual nano petals of  $\text{Mo}_{0.8}\text{W}_{0.2}\text{S}_2$  composite, which can be utilized to further examine its nanostructures.

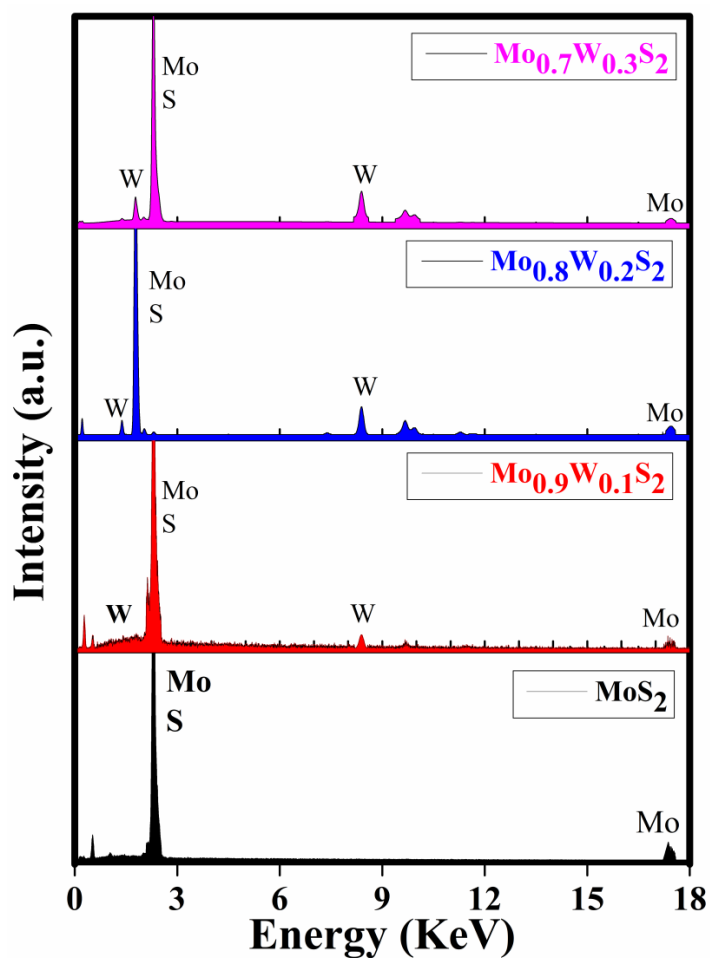
The layered growing nature of the composite has been seen in the overall HRTEM images, and the structure of the fabricated nano-petals is oriented to stack with roughly 0.75 nm spacing in a very dense manner. The crystallographic properties of the nanocomposite are vividly suggested by this sharp-edged HRTEM image, which also conclusively indicates the typical hexagonal structure. Conclusively, the thorough SEM and TEM studies of pure  $\text{MoS}_2$  and  $\text{MoWS}_2$  composites shown above, strongly demonstrate the development of the appropriate 3D hierarchical nano-petal structure. The hydrothermal environment has a significant impact on the  $\text{MoS}_2/\text{MoWS}_2$  nano-petal structure formation process. During the primary hydrothermal reaction stage, the amorphous  $\text{MoS}_2/\text{WS}_2$  would initially be developed below  $200^\circ\text{C}$ . These initial amorphous nanoparticles can roll up freely to construct a sphere with dense surface curls during the subsequent dilution method from  $\text{Na}_2\text{MoO}_4 \cdot 2\text{H}_2\text{O}/\text{Na}_2\text{WO}_4 \cdot 2\text{H}_2\text{O}$  to  $\text{MoS}_2/\text{WS}_2$  in order to remove dangling bonds and decrease the whole energy. Afterward, these initial structures spontaneously assemble into spheres as a result of the layered 2D behavior of  $\text{MoS}_2/\text{WS}_2$ . As the lattice constants of  $\text{WS}_2$  and  $\text{MoS}_2$  are precisely matched, the hydrothermal environment would cause the composite structures to also develop into curls, which would ultimately support the confined development of such a hierarchical structure without major modification.

From Fig. 2.3, the EDAX (Energy dispersive X-ray Analysis) spectrum of  $\text{Mo}_{1-x}\text{W}_x\text{S}_2$  ( $x = 0, 0.1, 0.2, 0.3$ ) are displayed and information on their constituent (at.% and wt.%) are provided in Table 2.2.

EDAX spectra for the layers were prepared, which represent the coexistence of Mo and S elements in  $\text{MoS}_2$  and Mo, W, and S elements in  $\text{MoWS}_2$  without any additional contaminates from the precursor.

Table 2.2: Composition data from EDAX analysis

Composite	Weight%			Atomic%		
	Mo	W	S	Mo	W	S
$\text{MoS}_2$	59.23	-	40.77	32.70	-	67.30
$\text{Mo}_{0.9}\text{W}_{0.1}\text{S}_2$	58.94	7.50	33.56	36.10	2.39	61.51
$\text{Mo}_{0.8}\text{W}_{0.2}\text{S}_2$	53.18	13.86	32.96	33.44	4.55	62.01
$\text{Mo}_{0.7}\text{W}_{0.3}\text{S}_2$	48.92	16.63	34.45	30.44	5.41	64.15

Fig. 2.3: EDAX spectrum of  $\text{Mo}_{1-x}\text{W}_x\text{S}_2$  ( $x = 0, 0.1, 0.2, 0.3$ ) nano-crystals.



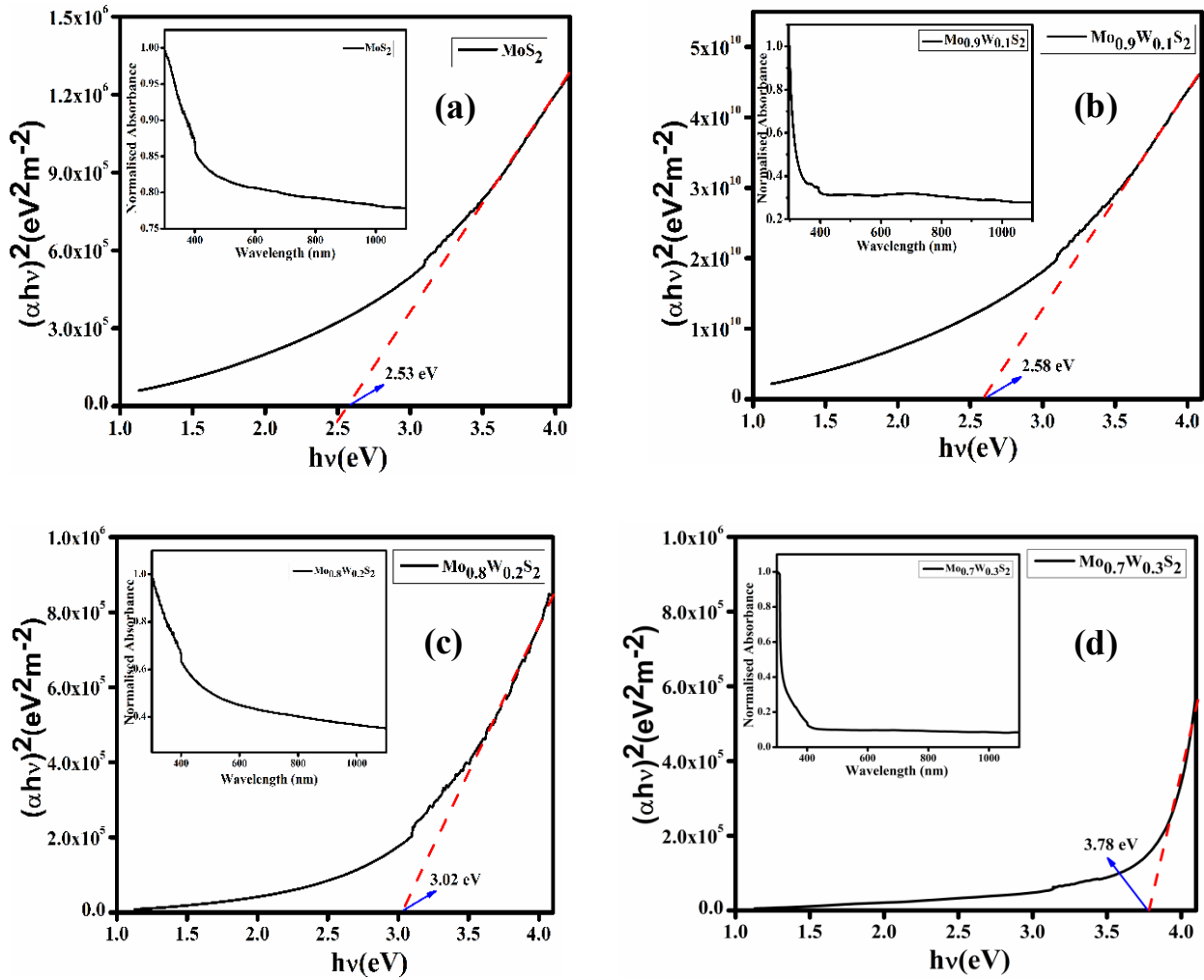
### 2.3.2. Optical analysis

UV-Vis spectroscopy is used to analyze the sample's chemical composition. To quantify the optical band gap corresponding to the excitation of electrons towards the conduction band from the valance band, the spectra of optical absorbance of the synthesized composites in the 300-1100 nm wavelength range are captured. The absorption spectra (inset) of  $\text{Mo}_{1-x}\text{W}_x\text{S}_2$  ( $x = 0, 0.1, 0.2, 0.3$ ) nanocomposites for different W concentrations are represented in Fig. 2.4. I experienced that the excitonic peaks obtained of  $\text{MoS}_2$  moved to the blue region with variation in Mo/W molar ratios. This small blue shift can be attributed to the escalating electron density of the synthesized particle as a result of the new bonds formed by introducing the W atoms into the Mo-S atomic matrix [25].

The optical band gaps of  $\text{Mo}_{1-x}\text{W}_x\text{S}_2$  ( $x = 0, 0.1, 0.2, 0.3$ ) nanocomposite were estimated with the help of Tauc's equation [26]:

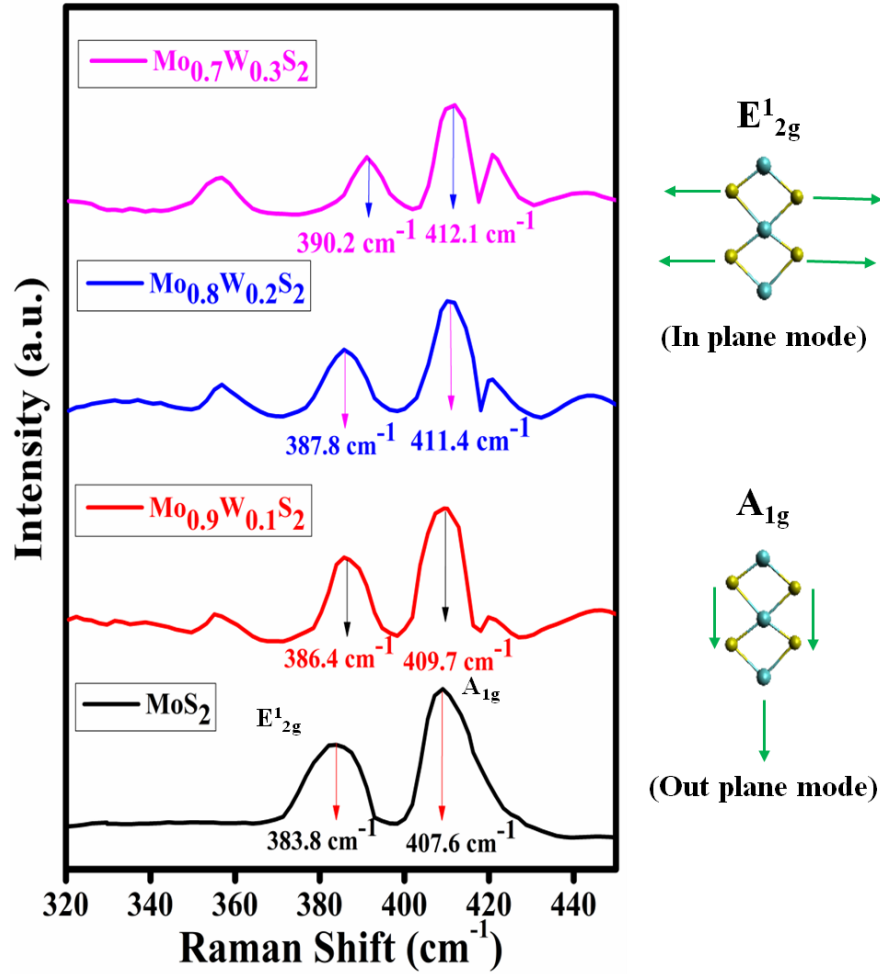
$$\alpha h\nu = A(h\nu - E_g)^{1/2} \quad (2.4)$$

Where  $\alpha$  defines the absorption coefficient,  $h\nu$  represents photon energy,  $E_g$  denotes the band gap energy,  $A$  is a constant, and for permitted direct transition, the value of  $n$  is  $1/2$ . Here, Tauc's plot is represented in Fig. 2.4. where the linear component of plots of  $(\alpha h\nu)^2$  vs.  $h\nu$  is extrapolated to  $(\alpha h\nu)^2 = 0$  to estimate the band gap. The estimated band gap energy for  $\text{MoS}_2$  is 2.53 eV, however, it changes to 2.58 eV, 3.02 eV, and 3.78 eV after 10%, 20%, and 30% alloying of W respectively. The degrees of lattice misfit, interconnectedness, and hetero-interface nature between  $\text{MoS}_2$  and  $\text{WS}_2$  have a significant impact on the optical characteristics of  $\text{Mo}_{1-x}\text{W}_x\text{S}_2$ .



**Fig. 2.4:  $(\alpha h\nu)^2$  versus  $h\nu$  curves of Mo<sub>1-x</sub>W<sub>x</sub>S<sub>2</sub> ( $x = 0, 0.1, 0.2$  and  $0.3$ ), UV-vis absorption spectra (inset) were determined with the help of Tauc's equation.**

Raman spectroscopy has been conducted to learn more about the atomic composition as well as atomic vibration of the as-prepared nanomaterials. Fig. 2.5 displays the Raman spectra of pristine MoS<sub>2</sub> and Mo<sub>1-x</sub>W<sub>x</sub>S<sub>2</sub> ( $x=0.1, 0.2, 0.3$ ) alloy composites with the laser excitation of 532 nm (1800 grating, 1mW power). The two prominent peaks of the characteristics band achieved at  $383.8\text{ cm}^{-1}$  and  $407.6\text{ cm}^{-1}$  for MoS<sub>2</sub> correspond to the  $E_{2g}^1$  and  $A_{1g}$  modes and construct the hexagonal-shaped MoS<sub>2</sub> crystal [27].



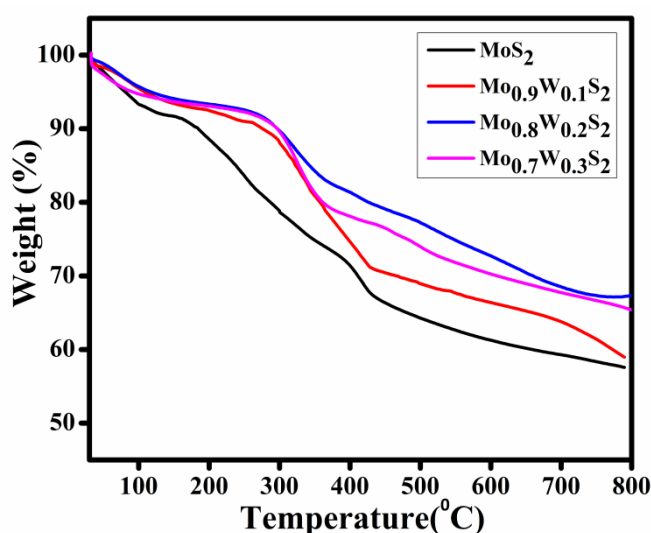
**Fig. 2.5:** Raman spectra of various vibrational modes for pure  $\text{MoS}_2$  and  $\text{MoWS}_2$  composites.

The vibration direction of the  $\text{A}_{1g}$  mode aligned with the c-axis correlates to the in-layer (out-of-plane) displacements of Mo and S atoms and the vibration orientation of  $\text{E}_{2g}^1$  mode lies inside the basal plane [28]. The blue shifts of the  $\text{E}_{2g}^1$  and  $\text{A}_{1g}$  peaks appear for the  $\text{MoWS}_2$  composite after continuous W-doping, attributing to the Vander Waals force in  $\text{MoWS}_2$  which causes a greater atomic vibrational force constant. The Raman spectral of  $\text{Mo}_{1-x}\text{W}_x\text{S}_2$  ( $x=0.1, 0.2, 0.3$ ) portray two strong prominent peaks at ( $\sim 386.4 \text{ cm}^{-1}$ ,  $\sim 409.7 \text{ cm}^{-1}$ ), ( $\sim 387.8 \text{ cm}^{-1}$ ,  $\sim 411.4 \text{ cm}^{-1}$ ) and ( $\sim 390.2 \text{ cm}^{-1}$ ,  $\sim 412.1 \text{ cm}^{-1}$ ) respectively. With increasing W content two more peaks with

increasing intensities occur in the characteristics band at  $\sim 357 \text{ cm}^{-1}$  ( $E_{2g}^1$ ) and  $\sim 418 \text{ cm}^{-1}$  ( $A_{1g}$ ) corresponding to  $\text{WS}_2$  [29].

### 2.3.3. Thermal stability analysis of $\text{MoS}_2$ and $\text{MoWS}_2$ nano-composites and BET characterization

The purpose of this thermal weight loss measurement is to analyze the stability of the composites with temperature. Fig. 2.6 depicts TGA curves of  $\text{MoS}_2$  [30] and  $\text{Mo}_{1-x}\text{W}_x\text{S}_2$  composites ( $x=0.1, 0.2, 0.3$ ) in the range of temperatures from  $30^\circ\text{C}$  to  $800^\circ\text{C}$  in the  $\text{N}_2$  atmosphere.  $\text{MoS}_2$  shows a weight loss of about 6% in the range of RT to  $100^\circ\text{C}$ , while the curve for  $\text{MoWS}_2$  composites shows  $<5\%$  weight loss in this temperature range due to loss of absorbed water [31].

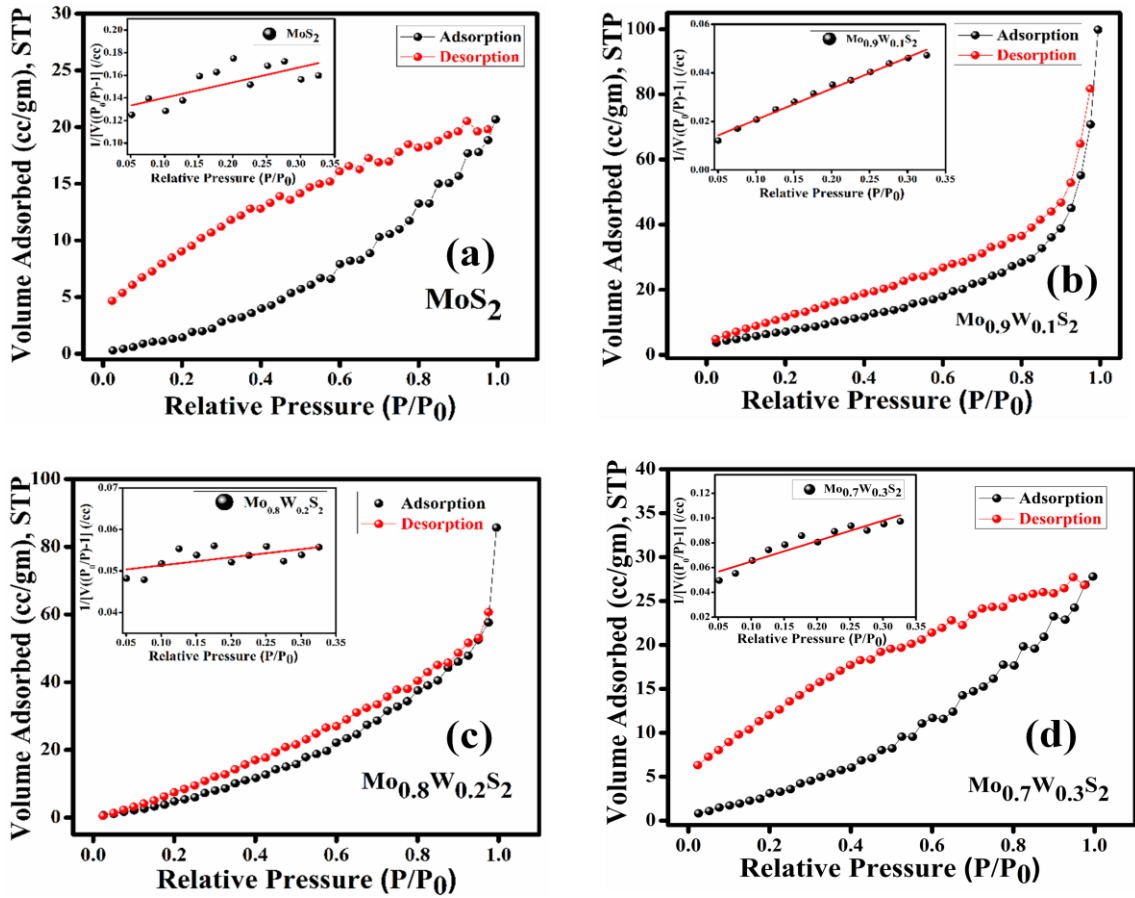


**Fig. 2.6: Thermo gravimetric analysis (TGA) curves at  $5^\circ\text{C min}^{-1}$  for the thermal decomposition in the  $\text{N}_2$  atmosphere of  $\text{MoS}_2$  and  $\text{MoWS}_2$  composites.**

From the analysis, it is concluded that  $\text{MoS}_2$  has a sharp weight loss after  $200^\circ\text{C}$  and  $\text{MoWS}_2$  composites show sharp weight loss after  $300^\circ\text{C}$  indicating that the addition of W to the  $\text{MoS}_2$  composite can increase the samples' thermal stability. This weight loss is due to adsorbed moisture in  $\text{MoS}_2$  and  $\text{MoWS}_2$  powder and is caused by the oxidation of  $\text{MoS}_2$  to  $\text{MoO}_3$  [31, 32].

The remaining weights of 57.6%, 58.9%, 67.3%, and 65.4% at 800°C were found for the MoS<sub>2</sub> and MoWS<sub>2</sub> nanocomposites with the molar concentration of 10%, 20%, and 30% respectively.

The electrical conductivity of a nanomaterial is linked to its pore size and porosity [33]. For the MoS<sub>2</sub> and MoWS<sub>2</sub> composites, the Brunauer-Emmett-Teller (BET) technique is utilized to



**Fig. 2.7:** N<sub>2</sub> adsorption-desorption isotherm for (a) MoS<sub>2</sub> (b) Mo<sub>0.9</sub>W<sub>0.1</sub>S<sub>2</sub> (c) Mo<sub>0.8</sub>W<sub>0.2</sub>S<sub>2</sub> and (d) Mo<sub>0.7</sub>W<sub>0.3</sub>S<sub>2</sub>; in inset 1/V(P<sub>0</sub>/P-1) variation with relative pressure (P/P<sub>0</sub>).

determine pore size by adsorption analysis with N<sub>2</sub> at 77K. The N<sub>2</sub> adsorption and desorption isotherms' hysteresis loops of MoS<sub>2</sub> composites with 0%, 10%, 20%, and 30% W alloying are shown in Fig. 2.7 (a, b, c, and d) using a relative pressure range of 0.02-1 respectively. The plots show an isotherm of type III with a hysteresis loop of type H3, implying solely surface

adsorption. Often, a type H<sub>3</sub> hysteresis loop is interrelated with distributed parallel plate-shaped pores with varying widths and thicknesses. This type of pore is produced by the loose bounding of flaky particles [34]. In the inset of all figures in Fig. 2.7,  $1/[V\{(P_0/P)-1\}]$  vs.  $P/P_0$  graphs are provided, which are in the relative pressure interval of  $0.05 < P/P_0 < 0.35$ , obtained using the BET equation, where the adsorption isotherm rose progressively.

The surface area derived from the linear fitting of this graph is 16.60 m<sup>2</sup>/g (for MoS<sub>2</sub>), 31.96 m<sup>2</sup>/g (for Mo<sub>0.9</sub>W<sub>0.1</sub>S<sub>2</sub>), 63.15 m<sup>2</sup>/g (for Mo<sub>0.8</sub>W<sub>0.2</sub>S<sub>2</sub>), and 20.38 m<sup>2</sup>/g (for Mo<sub>0.7</sub>W<sub>0.3</sub>S<sub>2</sub>), with pore sizes of 4.98 μm, 12.49 μm, 5.43 μm, and 5.45 μm respectively.

At increasing W doping the surface area initially rises and then reaches a maximum level with 20% alloying, after which the surface area decreases with increasing W doping. Thus, the surface area of the Mo<sub>0.8</sub>W<sub>0.2</sub>S<sub>2</sub> composite rises to a good extent, resulting in greater interfacial contact. Pores are also larger in MoWS<sub>2</sub> composites than pure MoS<sub>2</sub> because of defects produced due to alloying structure, but it is highly reduced for Mo<sub>0.8</sub>W<sub>0.2</sub>S<sub>2</sub> composite, which shows its greater effectiveness.

#### 2.3.4. Electrical study of Al/Compound/ITO Schottky diode

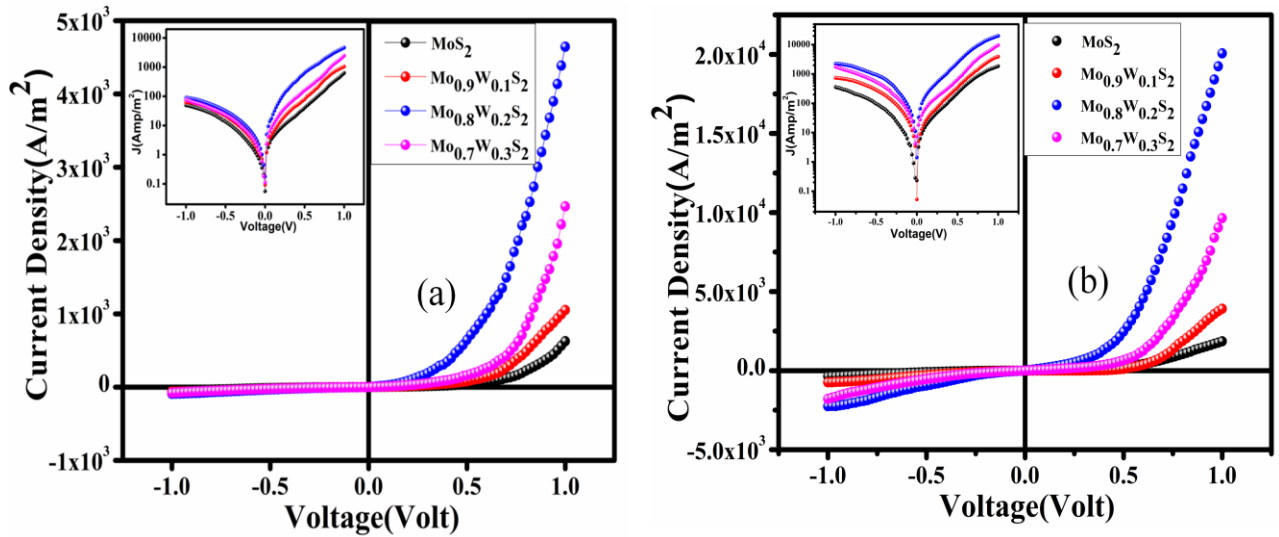
The achieved J-V characteristics ( $J=I/A$ , here A denotes the active diode area regarded as  $7.065 \times 10^{-6}$  m<sup>2</sup>) of the fabricated thin film MS junction devices based on MoS<sub>2</sub>, Mo<sub>0.9</sub>W<sub>0.1</sub>S<sub>2</sub>, Mo<sub>0.8</sub>W<sub>0.2</sub>S<sub>2</sub> and Mo<sub>0.7</sub>W<sub>0.3</sub>S<sub>2</sub> composites in the applied bias voltage range -1 V to +1 V maintained at room temperature are illustrated in Fig. 2.8 (a) with the log J vs. V graph (inset). The Schottky behavior of MS junction devices is revealed by the nonlinear rectifying nature of the graph. It is noticed that the MoWS<sub>2</sub> composites-based diodes showed enhanced Schottky behavior with higher forward currents and better-rectifying properties compared to the MoS<sub>2</sub>-based diode. The rectification ratio has been found to be 12.57 for MoS<sub>2</sub> which got enhanced to 16.95, 51.52, 31.92 for Mo<sub>1-x</sub>W<sub>x</sub>S<sub>2</sub> (x=0.1, 0.2, 0.3) respectively. The best performance was provided by the Mo<sub>0.8</sub>W<sub>0.2</sub>S<sub>2</sub>-based Schottky Barrier Diode. The conductivity has been evaluated as  $5.24 \times 10^{-5}$  S/m for MoS<sub>2</sub> at room temperature, which tremendously improved to  $1.18 \times 10^{-4}$  S/m,  $8.35 \times 10^{-4}$  and  $2.18 \times 10^{-4}$  S/m with the inclusion of Tungsten within MoS<sub>2</sub> by 10%, 20% and 30% alloying respectively.

I utilized the thermionic emission theory [35] to determine diode parameters by examining the  $J$  vs.  $V$  graph, and it can be represented as,

$$J = J_0 \left[ \exp \left( \frac{qV}{\eta K T} \right) - 1 \right] \quad (2.5)$$

Here  $J$  stands for the forward bias current density,  $J_0$  indicates reverse saturation current density,  $V$  denotes the applied bias voltage,  $q$  represents the electronic charge,  $K$  indicates the Boltzmann constant,  $T$  is the absolute temperature, and  $\eta$  is the ideality factor.

$$J_0 = A^* T^2 \exp \left( -\frac{q\Phi_B}{KT} \right) \quad (2.6)$$



**Fig. 2.8: Characteristic curve of current density-voltage (J-V) (a) under dark: (b) under illumination**

Where  $A^*$  and  $\Phi_B$  stands for Richardson constant (with value considered as  $1.2 \times 10^6 \text{ AK}^{-2} \text{ m}^{-1}$ ), and Schottky barrier height respectively.

To examine the different Schottky parameters, such as barrier height, series resistance, ideality factor, etc., and to compare the nature of  $\text{MoS}_2$  and  $\text{MoWS}_2$ -based materials, the provided set of Cheung's equations has been used [36]. Typically, a series combination of resistance and diode is

used in the construction of a basic model of the device. As a result, the voltage drop across a series combination of a resistor and a diode can take the place of the voltage drop across the diode., and this is known as  $V-IR_S$  ( $R_S$ =series resistance). Thus, for  $V_D > 3kT/q$ , the revised Eq. (2.5) can be represented as [36]

$$J = J_0 \left[ \exp \left( \frac{q (V - I R_S)}{\eta K T} \right) \right] \quad (2.7)$$

Substituting the value of saturation current density into equation (2.7), and with differentiation of  $V$  w.r.t.  $\ln J$ , Eq. (2.7) can be stated as,

$$\frac{dV}{d \ln J} = A J R_S + \frac{\eta K T}{q} \quad (2.8)$$

For the fabricated diodes,  $dV/d \ln J$  vs. the current density ( $J$ ) has been plotted and shown in Fig. 2.9(a) which represents a straight line. The value of  $\eta kT/q$  is given by the intercept of that straight line to the y-axis, and  $R_S A$  is calculated using the slope. The ideality factor value is highly crucial since it will illustrate the formation of an ideal metal-semiconductor junction. The computed value of  $\eta$  for each diode is reported in Table 2.3, where it is observed that the generated MS junctions were not perfectly ideal. The divergence from optimal behavior could be caused by the existence of interface states, series resistance at the junction, and inhomogeneities of Schottky barrier height that were created at the time of Aluminium deposition on the thin film of synthesized composites [37]. However, the  $Mo_{0.8}W_{0.2}S_2$  compound diode has a lesser value of  $\eta$  than other diodes, indicating that it forms Schottky contacts more effectively.

A different set of equations for obtaining the barrier height ( $\Phi_B$ ) is utilized which is given below [36].

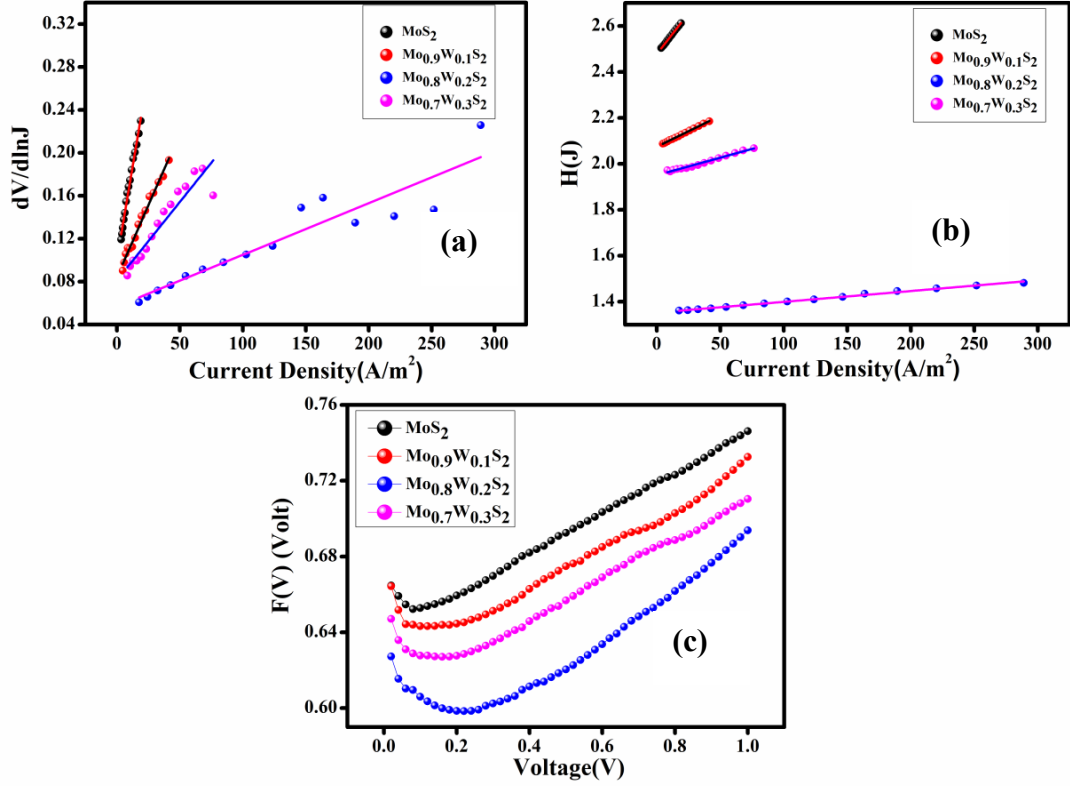
$$H(J) = V - \frac{\eta K T}{q} \ln \left( \frac{J}{A^* T^2} \right) = A J R_S + \eta \Phi_B \quad (2.9)$$

Barrier height and series resistance have been derived by the linear fitting of the  $H(J)$  vs.  $J$  graph using the intercept and slope of this model respectively as displayed in Fig. 2.9(b) and values are listed in Table 2.3.

In another way using Norde's equation [37], I derived the barrier height ( $\Phi_B$ ), and series resistance ( $R_S$ ). Norde presents the voltage-dependent parameter  $F(V)$  [38], which is,



$$F(V) = \frac{V}{a} - \frac{1}{\beta} \ln \left( \frac{J}{A^* T^2} \right) \quad (2.10)$$



**Fig. 2.9: (a)  $dV/d\ln J$  versus current density; (b)  $H(J)$  versus current density; (c)  $F(V)$  versus  $V$  plot for MoS<sub>2</sub>, Mo<sub>0.9</sub>W<sub>0.1</sub>S<sub>2</sub>, Mo<sub>0.8</sub>W<sub>0.2</sub>S<sub>2</sub> and Mo<sub>0.7</sub>W<sub>0.3</sub>S<sub>2</sub> fabricated diode.**

Where  $\beta = q/KT$  and 'a' is chosen as an arbitrary constant value that must be higher than the ideality factor ( $\eta$ ). Fig. 2.9(c) shows a plot of  $F(V)$  against the applied forward bias voltage. From the following equation,  $\Phi_B$  and  $R_s$  (displayed in Table 2.3) can be derived using the  $F(V)$  vs.  $V$  plot,

$$\Phi_B = F(V_{min}) + \frac{V_{min}}{a} - \frac{1}{\beta} \quad (2.11)$$

$$\text{and, } R_s = \frac{a - \eta}{\beta A J_{min}} \quad (2.12)$$

$F(V_{\min})$  indicates the  $F(V)$  value at the minimal voltage based on the graph in Fig. 2.9(c). The  $V_{\min}$  and  $J_{\min}$  are the voltage and current density correspond to  $F(V_{\min})$  respectively.

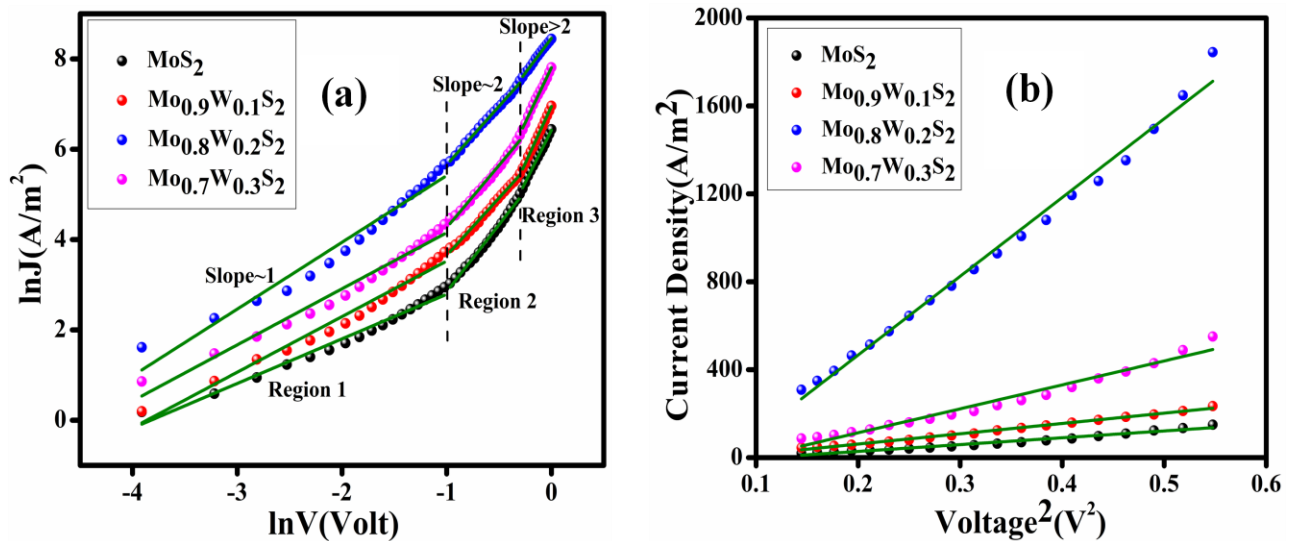
$\text{Al/Mo}_{0.8}\text{W}_{0.2}\text{S}_2$  compound junction has a lower barrier height than the other material. Due to higher on-currents and improved sub-threshold behavior provided by lower barrier height, it has very important for the Schottky diode implementation. For all of the diodes, the resistance values generated from the  $H(J)$  vs.  $J$  graph and the estimated series resistance ( $R_s$ ) value from the  $dV/d\ln J$  against the  $J$  graph correspond well. It is very much interesting that the  $\text{Mo}_{0.8}\text{W}_{0.2}\text{S}_2$  compound-based device has a lower  $R_s$  than the other device. As it can be seen in Fig. 2.8, the decreased series resistance of the  $\text{Al/Mo}_{0.8}\text{W}_{0.2}\text{S}_2/\text{ITO}$  diode indicates an increase in current density.  $\text{Mo}_{0.8}\text{W}_{0.2}\text{S}_2$ -based SBD exhibited a rectification ratio of 51.52, which is an improvement of 309% compared to the 12.57 of pristine  $\text{MoS}_2$ -based diode. Most amazingly, the conductivity has been enormously increased by 1493%. The increased charge transfer capabilities across the Schottky junction are indicated by the improved diode parameters for the  $\text{Mo}_{0.8}\text{W}_{0.2}\text{S}_2$  compound-based diode.

**Table 2.3: Schottky Diode Parameters**

Sample	Rectification Ratio	Ohmic Conductivity ( $\sigma$ ) (S/m)	Ideality factor	Series Resistance ( $R_s$ )			Potential Barrier Height ( $\phi_B$ )	
				From $dV/d\ln J$ Vs $J$ curve (K $\Omega$ )	From $H$ Vs $J$ curve (K $\Omega$ )	From $F(V)$ Vs $V$ curve (K $\Omega$ )	From $H$ vs $J$ curve (eV)	From $F(V)$ Vs $V$ curve (eV)
<b><math>\text{MoS}_2</math></b>	12.57	$0.52 \times 10^{-4}$	3.83	0.985	1.001	0.614	0.647	0.646
<b><math>\text{Mo}_{0.9}\text{W}_{0.1}\text{S}_2</math></b>	16.95	$1.18 \times 10^{-4}$	3.22	0.379	0.382	0.492	0.644	0.642
<b><math>\text{Mo}_{0.8}\text{W}_{0.2}\text{S}_2</math></b>	51.52	$8.35 \times 10^{-4}$	2.17	0.068	0.067	0.066	0.623	0.627
<b><math>\text{Mo}_{0.6}\text{W}_{0.4}\text{S}_2</math></b>	31.92	$2.18 \times 10^{-4}$	3.11	0.207	0.215	0.171	0.628	0.640

In order to get a deeper understanding of the charge transit processes, the  $J$  vs.  $V$  curves for each device are plotted in logarithmic scale under the forward bias as shown in Fig. 2.10 (a). The plot

displays three distinct regions for the devices with various slopes, where Region-I represents the slope near to unity ( $m \sim 1$ ) and here conduction is controlled by the Ohmic behavior at low bias. The thermionic emission in that region results in a current density that is directly proportional to voltage because the thermally produced free carriers are greater than the injected charges during this conduction. Therefore, tunneling is the primary contributing element, according to the J-V curve [39]. Under the SCLC hypothesis, a Schottky diode's current is said to follow the power law relationship with the applied voltage, such as  $I \sim V^m$ . Based on this procedure, a shallow trap dominates the SCLC mechanism in Region II since the slope ( $m$ ) is close to 2. The SCLC in Region III is controlled by exponentially distributed traps [39]. Typically, semiconductor often contains several localized defect states in their forbidden energy gap, trapping the injected charges from the electrode [39]. The quantity of injected charges grows as the applied bias voltage rises. The single or shallow traps are initially filled. Afterward, because of the exponential trap distribution for additional bias voltage, the current density is rapidly enhanced. The Fermi level grows up above the trapping level of an electron during this phase and comes closer to the conduction band edge [39]. As a result, a trap-free space charge region is generated and consequently, each of the localized traps is covered.



**Fig. 2.10: (a) a logarithmic plot of current density versus voltage; (b) to determine the effective mobility Current density versus Voltage<sup>2</sup> plot**

From Region II, the effective carrier mobility( $\mu_{\text{eff}}$ ), transit time, conductivity, and density of states close to the Fermi level have been determined following the SCLC model. The Mott-Gurney equation [40] estimates the current resulting from this conduction process,

$$J = \frac{9 \mu_{\text{eff}} \varepsilon_0 \varepsilon_r}{8} \left( \frac{V^2}{d^3} \right) \quad (2.13)$$

Thus  $\mu_{\text{eff}}$  of the charge carrier has been obtained from the mid-voltage region of the J vs.  $V^2$  curve, where, d denotes the film thickness ( $\sim 1 \mu\text{m}$ ),  $\varepsilon_r$  represents the synthesized film's dielectric constant and  $\varepsilon_0$  indicates the free space permittivity. The value of the dielectric constant has been calculated using the capacitance vs. frequency graph (Fig. 2.11).

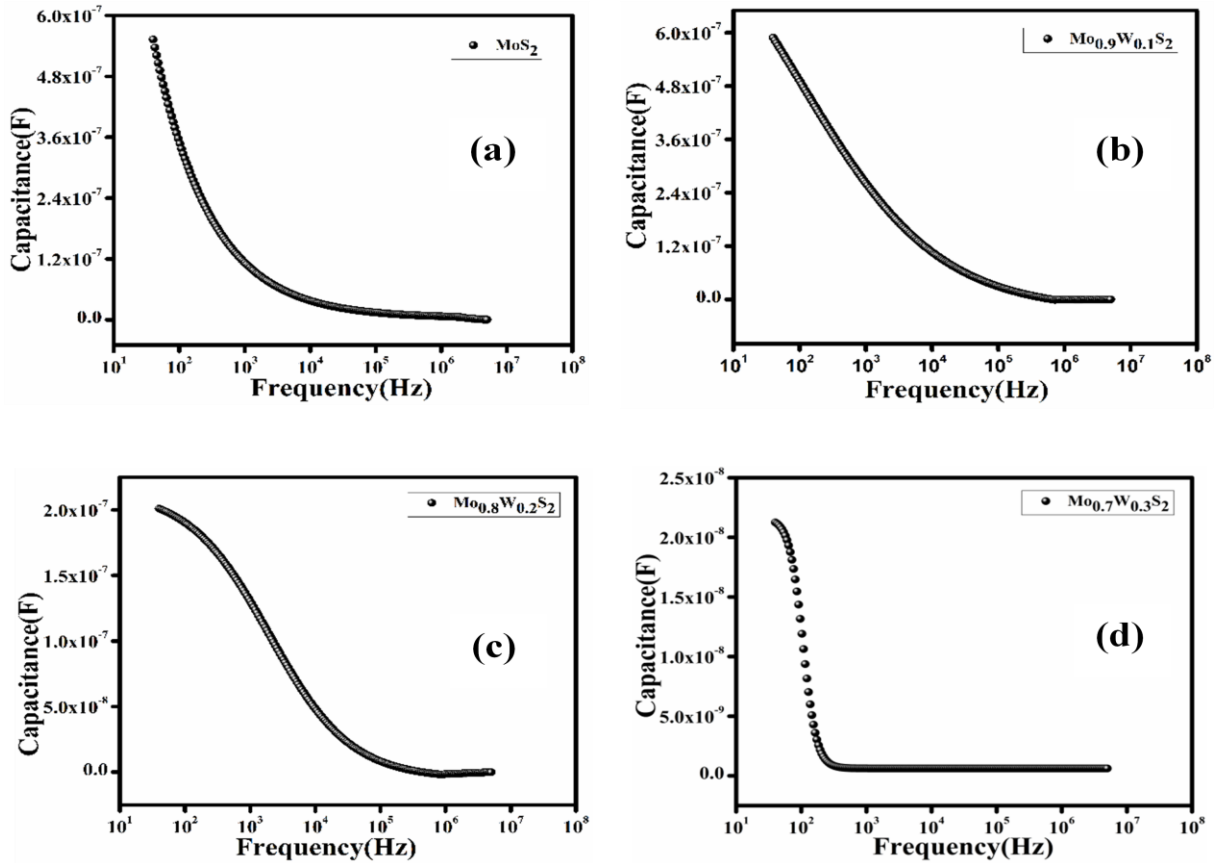


Fig. 2.11: Capacitance vs. frequency graph of  $\text{MoS}_2$ ,  $\text{Mo}_{0.9}\text{W}_{0.1}\text{S}_2$ ,  $\text{Mo}_{0.8}\text{W}_{0.2}\text{S}_2$ , and  $\text{Mo}_{0.7}\text{W}_{0.3}\text{S}_2$ .

Using the capacitance value at the saturation level, the following expression has been used to derive  $\epsilon_r$  [40]

$$\epsilon_r = \frac{1}{\epsilon_0} \frac{C_{\text{sat}} d}{A} \quad (2.14)$$

Here,  $C_{\text{sat}}$  implies the capacitance value at saturation;  $d$  denotes the film thickness, and  $A$  represents the active area.

It is observed using the capacitance vs. frequency plot that, the capacitance at saturation level for  $\text{MoS}_2$  and  $\text{MoWS}_2$  ( $x=0.1, 0.2, 0.3$ ) alloy composites are  $5.21 \times 10^{-10}$  F,  $1.46 \times 10^{-10}$  F,  $3.99 \times 10^{-11}$  F, and  $6.20 \times 10^{-10}$  F respectively. Depending on this capacitance value, the dielectric constant ( $\epsilon_r$ ) has been calculated as 8.33, 2.34, 0.64, and 9.92 respectively.

From Region II, the transit time has been evaluated depending on the current density vs. voltage curve slope which is in the following equation, [40]

$$\tau = \frac{9\epsilon_0\epsilon_r}{8d} \left( \frac{V}{J} \right) \quad (2.15)$$

The excellent mobility along with the short transit time for  $\text{Mo}_{0.8}\text{W}_{0.2}\text{S}_2$  composite indicates improved charge transit via the Schottky junction. The good crystalline structure of  $\text{Mo}_{0.8}\text{W}_{0.2}\text{S}_2$  compound with a larger particle size results in a reduced grain boundary effect improving the charge transfer phenomena. As previously explained, the applied potential causes the Fermi level to move toward the conduction band edge. This approximation gives a good concept of the defect state distribution density in the area of the band gap [40, 41]. The den Boer technique [42] is used to calculate the density of states ( $N_F$ ) around the Fermi level using the SCLC J-V properties, which is written as,

$$N_F = \frac{2\epsilon_0\epsilon_r(V_2-V_1)}{qd^2\Delta E_F} \quad (2.16)$$

In this case,  $\Delta E_F$  depicts the change in the quasi-Fermi level as, [34]

$$\Delta E_F = KT \ln \frac{J_2 V_1}{J_1 V_2} \quad (2.17)$$

Here, two distinct forward bias voltages gained are  $V_1$  and  $V_2$  from the SCLC Region-II of each of the diodes, where  $J_1$  and  $J_2$  denote the current densities that correspond to them. Thus, the lowest density of states for the Al/Mo<sub>0.8</sub>W<sub>0.2</sub>S<sub>2</sub>/ITO diode indicates the presence of the fewest traps in the forbidden gaps. I also calculated the SCLC region conductivity for each diode which is significantly improved for the Al/Mo<sub>0.8</sub>W<sub>0.2</sub>S<sub>2</sub>/ITO device.

All the parameters related to the SCLC conduction mechanism are tabulated in Table 2.4. The entire diode specifications of the Mo<sub>0.8</sub>W<sub>0.2</sub>S<sub>2</sub>-based diodes reveal significantly improved dynamic charge transfer. Therefore, this MoWS<sub>2</sub> composite with 20% alloying of tungsten has a very promising potential in the thin film MS junction device as well as the Schottky diode switching application.

Current (I) - voltage (V) is measured at room temperature at illuming condition with the same bias voltage range (-1 V to +1 V) in order to analyze its application as photodiode. The obtained J-V plots of compounds at illuming conditions is represented in Fig. 2.8 (b). Compounds display an improved rectifying property in illumination which also implies a higher conductivity. All the photo response study has been carried out under AM 1.5 radiation. I have calculated the on-off ratio of the Schottky diode based on our synthesized material as 2.96, 3.72, 4.32, and 3.91 for MoS<sub>2</sub>, Mo<sub>0.9</sub>W<sub>0.1</sub>S<sub>2</sub>, Mo<sub>0.8</sub>W<sub>0.2</sub>S<sub>2</sub> and Mo<sub>0.7</sub>W<sub>0.3</sub>S<sub>2</sub> respectively.

**Table 2.4: Charge Transport Parameter of devices**

Sample	SCLC conductivity( $\sigma$ ) S/m	Mobility ( $\mu_{\text{eff}}$ ) ( $\text{m}^2\text{V}^{-1}\text{S}^{-1}$ )	Transit Time ( $\tau$ ) (sec)	$\mu_{\text{eff}} \times \tau$	Density of States $N_F$ ( $\text{m}^{-3}$ )	Charge Carrier's Lifetime (s)
MoS <sub>2</sub>	$3.59 \times 10^{-4}$	$3.75 \times 10^{-6}$	$24.18 \times 10^{-8}$	$9.07 \times 10^{-13}$	$12.88 \times 10^{21}$	$22.44 \times 10^{-5}$
Mo <sub>0.9</sub> W <sub>0.1</sub> S <sub>2</sub>	$5.26 \times 10^{-4}$	$20.10 \times 10^{-6}$	$44.67 \times 10^{-9}$	$8.98 \times 10^{-13}$	$3.66 \times 10^{21}$	$40.35 \times 10^{-5}$
Mo <sub>0.8</sub> W <sub>0.2</sub> S <sub>2</sub>	$42.66 \times 10^{-4}$	$56.47 \times 10^{-5}$	$1.59 \times 10^{-9}$	$8.98 \times 10^{-13}$	$0.87 \times 10^{21}$	$72.56 \times 10^{-5}$
Mo <sub>0.7</sub> W <sub>0.3</sub> S <sub>2</sub>	$12.87 \times 10^{-4}$	$11.03 \times 10^{-6}$	$82.12 \times 10^{-9}$	$9.06 \times 10^{-13}$	$9.68 \times 10^{21}$	$54.11 \times 10^{-5}$

Current (I) - voltage (V) is measured at room temperature at illuming condition with the same bias voltage range (-1 V to +1 V) in order to analyze its application as photodiode. The obtained J-V plots of compounds at illuming conditions is represented in Fig. 2.8 (b). Compounds display an improved rectifying property in illumination which also implies a higher conductivity. All the photo response study has been carried out under AM 1.5 radiation. I have calculated the on-off ratio of the Schottky diode based on our synthesized material as 2.96, 3.72, 4.32, and 3.91 for  $\text{MoS}_2$ ,  $\text{Mo}_{0.9}\text{W}_{0.1}\text{S}_2$ ,  $\text{Mo}_{0.8}\text{W}_{0.2}\text{S}_2$  and  $\text{Mo}_{0.7}\text{W}_{0.3}\text{S}_2$  respectively. Different photodiode parameters like photosensitivity, photoconductivity sensitivity (S), Responsivity (R) and specific detectivity ( $D^*$ ) have also been calculated and tabulated in Table 2.5 using the following set of equations.

$$\text{Photosensitivity} = \frac{J_{\text{Light}} - J_{\text{Dark}}}{J_{\text{Dark}}} \times 100\% \quad (2.18)$$

$$\text{Photoconductivity sensitivity, } S = \frac{J_{\text{Light}} - J_{\text{Dark}}}{P \times V_{\text{max}}} \times d \quad (2.19)$$

$$\text{Responsivity, } R = \frac{J_{\text{Light}} - J_{\text{Dark}}}{P} \quad (2.20)$$

$$\text{Specific detectivity, } D^* = \frac{R}{\sqrt{2qAJ_{\text{Dark}}}} \quad (2.21)$$

Here,  $J_{\text{Dark}}$  and  $J_{\text{Light}}$  are the values of current density (J) at particular bias  $V_{\text{max}}$  i.e. 1 Volt under dark and illumination condition respectively. Total power of the incident light is symbolized as P, which is taken as 100 mW per unit area. Film thickness is defined as 'd', 'q' is the charge of electron, and 'A' is active diode area of the fabricated device.

**Table 2.5: Photodiode Parameters**

Compound	On/Off Ratio	Photosensitivity (%)	Photoconductivity Sensitivity (S) $\text{A m}^{-1}\text{W}^{-1}$	Responsivity (R) $\text{A m}^{-2}\text{W}^{-1}$	Specific Detectivity ( $D^*$ ) (Jones)
<b>MoS<sub>2</sub></b>	2.96	196.10	$12.29 \times 10^{-3}$	$12.29 \times 10^3$	$32.65 \times 10^{13}$
<b>Mo<sub>0.9</sub>W<sub>0.1</sub>S<sub>2</sub></b>	3.72	272.21	$28.63 \times 10^{-3}$	$28.63 \times 10^3$	$58.72 \times 10^{13}$
<b>Mo<sub>0.8</sub>W<sub>0.2</sub>S<sub>2</sub></b>	4.32	332.01	$15.42 \times 10^{-2}$	$15.42 \times 10^4$	$15.05 \times 10^{14}$
<b>Mo<sub>0.7</sub>W<sub>0.3</sub>S<sub>2</sub></b>	3.91	291.01	$71.75 \times 10^{-3}$	$71.75 \times 10^3$	$96.10 \times 10^{13}$

### 2.3.5. Impedance Spectroscopy analysis

Impedance spectroscopy (IS) study aside from the J-V characteristics can also provide information about the devices' charge transport features, especially at the interfaces. The IS study of Al/Mo<sub>1-x</sub>W<sub>x</sub>S<sub>2</sub> (x = 0, 0.1, 0.2, 0.3)/ITO Schottky diode was carried out using a 50 mV oscillating voltage and a frequency regime of 40 Hz to 5 MHz at zero bias voltage results in Nyquist plots with deformed semicircles displayed in Fig. 2.12 (a). The implicit variable frequency rises from the right end to the left end of the x-axis. It is noticed that the resulting impedance spectra are almost semi-semicircular and the total device impedance is indicated by the diameter of the semicircles. The Nyquist plots show that the semicircle diameter of the Mo<sub>0.8</sub>W<sub>0.2</sub>S<sub>2</sub>-based device is much lower than the semicircle diameter of other composites. In Mo<sub>0.8</sub>W<sub>0.2</sub>S<sub>2</sub>, the smaller semicircle indicates less charge recombination and lower charge transfer resistance. Hence, faster charge transfer was achieved in the Mo<sub>0.8</sub>W<sub>0.2</sub>S<sub>2</sub> thin film. An equivalent circuit parallel resistance and capacitance (R||C) network can be built for each semicircle in the Nyquist plot. As a result, a representation of an ac equivalent circuit was devised to explore the effect of impedance on the Mo<sub>1-x</sub>W<sub>x</sub>S<sub>2</sub> fabricated device. The semicircles are not accurate, implying that the diode has another R||C network. The major source of this inaccurate semicircle is the contact regions of every interface, which provide an additional capacitive component to the device. There are two interfaces which are Al/Mo<sub>1-x</sub>W<sub>x</sub>S<sub>2</sub> and Mo<sub>1-x</sub>W<sub>x</sub>S<sub>2</sub>/ITO (x = 0, 0.1, 0.2, 0.3) in our Schottky diode. Therefore the corresponding circuit (Fig. 2.13) contains two R||C networks linked serially, as well as R<sub>S</sub> and a parasitic inductance (L) connected in series. The Al-Mo<sub>1-x</sub>W<sub>x</sub>S<sub>2</sub> and Mo<sub>1-x</sub>W<sub>x</sub>S<sub>2</sub>-ITO (x = 0, 0.1, 0.2, 0.3) interfaces are associated to R<sub>1</sub>C<sub>1</sub> and R<sub>2</sub>C<sub>2</sub>, respectively.

The ac impedance is often described by

$$Z(w) = Z'(w) - jZ''(w) \quad (2.22)$$

Here, w denotes the frequency, Z' and Z'' indicate the real impedance and imaginary impedance respectively. In order to analyze the identical circuit design mathematically as depicted in Fig. 2.13, Z' and Z'' can be defined as



$$Z'(w) = \frac{R_1}{1+(wR_1C_1)^2} + \frac{R_2}{1+(wR_2C_2)^2} + R_s \quad (2.23)$$

$$Z''(w) = \frac{wR_1^2C_1}{1+(wR_1C_1)^2} + \frac{wR_2^2C_2}{1+(wR_2C_2)^2} - wL_1 \quad (2.24)$$

The simulated data is generated from equations. (23) and (24) are well matched with the experimental data, as shown in Fig. 2.12 (a). The values of  $R_s$ ,  $R_1$ ,  $R_2$ ,  $C_1$ ,  $C_2$ , and  $L_1$  for  $\text{Al/Mo}_{1-x}\text{W}_x\text{S}_2/\text{ITO}$  structure fitted with an equivalent circuit model are shown in Table 2.6.

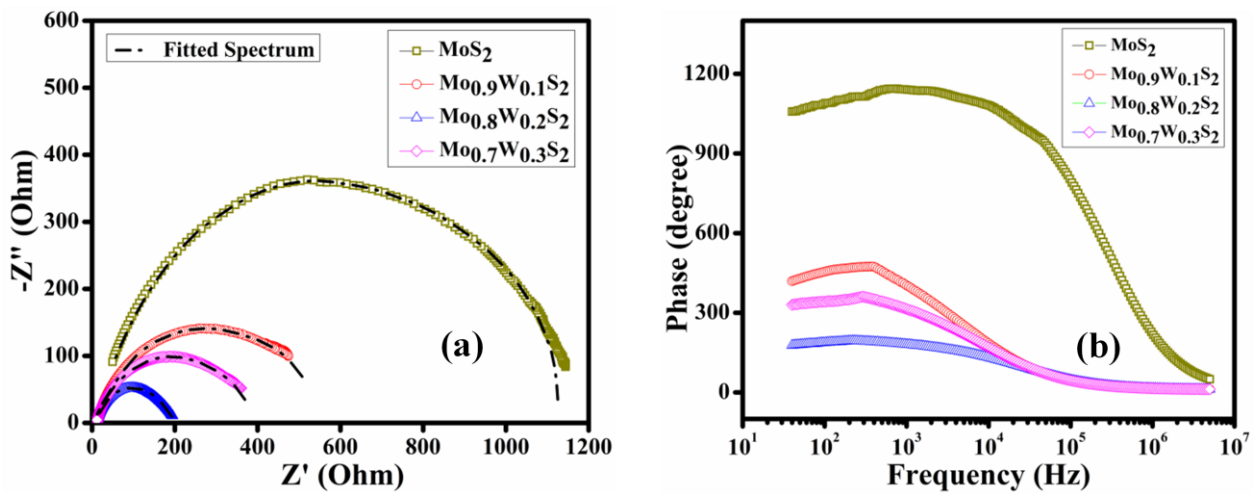
Whereas the Nyquist plot provides information about charge transport resistance, the Bode phase diagram can help us understand the charge carrier's lifetime. The related Bode phase diagram presented in Fig. 2.12 (b), reveals that the characteristic frequency peak for  $\text{Mo}_{0.8}\text{W}_{0.2}\text{S}_2$ -based SBD takes place at a lesser magnitude than its counterpart. The charge carrier's lifetime ( $\tau_L$ ) can be calculated from this frequency peak ( $f_{\text{peak}}$ ) using the following equation,

$$\tau_L = \frac{1}{2\pi f_{\text{peak}}} \quad (2.25)$$

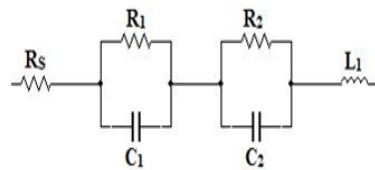
The value of charge carrier lifetime for  $\text{Mo}_{1-x}\text{W}_x\text{S}_2$  compounds (for  $x=0, 0.1, 0.2, 0.3$ ) were obtained as 0.22 ms, 0.40 ms, 0.73 ms and 0.54 ms respectively. As a result, the charge carrier lifetime of  $\text{Mo}_{0.8}\text{W}_{0.2}\text{S}_2$  was longer, which is another reason for its improved performance. Here, I wish to highlight once more that for effective charge carrier transfer to opposing electrodes, the charge carrier lifetime of the materials should be greater than their respective transit times. The lifetime of the carrier of other composites was slightly more than their carrier transit time; although in the case of  $\text{Mo}_{0.8}\text{W}_{0.2}\text{S}_2$ , the carrier lifetime was much greater than the carrier transit time, therefore ensuring its enhanced device efficiency. It can also be observed that the synthesized  $\text{MoWS}_2$  materials have high mobility. Therefore, based on the obtained results for  $\text{MoWS}_2$ -based Schottky diodes, it is obvious that the  $\text{MoWS}_2$  nanocomposites have a high potential for M-S junction thin film device applications. Finally, the quicker charge transport properties of  $\text{Mo}_{0.8}\text{W}_{0.2}\text{S}_2$  contributed to its overall superior performance.

**Table 2.6: Fitted values of  $R_s$ ,  $R_1$ ,  $R_2$ ,  $C_1$ ,  $C_2$  and  $L_1$  for Al/Mo<sub>1-x</sub>W<sub>x</sub>S<sub>2</sub>/ITO structure using equivalent circuit model**

Sample	$R_s$ ( $\Omega$ )	$R_1$ ( $\Omega$ )	$R_2$ ( $\Omega$ )	$C_1$	$C_2$	$L_1$
Al/MoS <sub>2</sub> /ITO	10.01	838.46	1106	$1.49 \times 10^{-08}$	$1.89 \times 10^{-08}$	$1.88 \times 10^{-07}$
Al/Mo <sub>0.9</sub> W <sub>0.1</sub> S <sub>2</sub> /ITO	9.62	295.69	457.17	$2.87 \times 10^{-08}$	$1.22 \times 10^{-06}$	$3.57 \times 10^{-06}$
Al/Mo <sub>0.8</sub> W <sub>0.2</sub> S <sub>2</sub> /ITO	11.15	65.76	115.73	$2.51 \times 10^{-10}$	$3.49 \times 10^{-06}$	$8.24 \times 10^{-08}$
Al/Mo <sub>0.7</sub> W <sub>0.3</sub> S <sub>2</sub> /ITO	10.65	113.45	248.76	$4.36 \times 10^{-10}$	$4.46 \times 10^{-06}$	$9.57 \times 10^{-08}$



**Fig. 2.12: (a) Nyquist Plot and (b) Bode phase plot for the Al/MoS<sub>2</sub>/ITO, Al/Mo<sub>0.9</sub>W<sub>0.1</sub>S<sub>2</sub>/ITO, Al/Mo<sub>0.8</sub>W<sub>0.2</sub>S<sub>2</sub>/ITO, and Al/Mo<sub>0.7</sub>W<sub>0.3</sub>S<sub>2</sub>/ITO Schottky barrier diodes.**



**Fig. 2.13: The RC equivalent circuit model of the Schottky diode.**

## 2.4. Conclusions

The hydrothermal method was employed to synthesize  $\text{Mo}_{1-x}\text{W}_x\text{S}_2$  nano-composites with the different molar concentrations of tungsten (i.e.  $x=0, 0.1, 0.2, 0.3$ ). The successful synthesis of the desired products was confirmed by detailed characterization. Thin-film Schottky devices were fabricated with the synthesized materials and comparative studies were carried out to evaluate their relative performance. It was found that after incorporating tungsten in  $\text{MoS}_2$  TMD, the  $\text{Mo}_{1-x}\text{W}_x\text{S}_2$  alloy nano-composite structure produced considerably better device performance compared to pristine  $\text{MoS}_2$ . Moreover, the specific  $\text{Mo}_{0.8}\text{W}_{0.2}\text{S}_2$  nano composite-based device performed better than the other counterparts. The SCLC mechanism explained the improvement in carrier transmission characteristics like mobility and transit time of charges via the metal-semiconductor junction derived from J-V data. The well-separated architecture with massive nano-petals of  $\text{Mo}_{0.8}\text{W}_{0.2}\text{S}_2$  nano-composite was confirmed to contribute to improved charge separation and transportation. The charge transport performance was investigated by impedance spectroscopy analysis. Device interfacing resistance and electron lifetime were revealed by the IS network analysis, reflecting that the  $\text{Al}/\text{Mo}_{0.8}\text{W}_{0.2}\text{S}_2/\text{ITO}$  device has improved charge transport capabilities. The study demonstrates the different molar ratio-dependent performance of  $\text{MoWS}_2$  composites in a metal-semiconductor junction Schottky barrier diode and shows that the synthesized  $\text{Mo}_{0.8}\text{W}_{0.2}\text{S}_2$  nano-composite has the best application potential for thin film switching devices. As a result of this research, the  $\text{Mo}_{1-x}\text{W}_x\text{S}_2$ -based Schottky device will be improved further, serving as an excellent starting point for building diodes, sensors, and solar cells.

## References

- [1] Y.W. Song, S.Y. Jang, W.S. Han, M.K. Bae, *Applied Physics Letters*, 96(2010)051122.
- [2] S.M. Tabatabaei, N. Honari, M.J. Farshchi-Heydari, M. Rastgoo, M. Fathipour, *Applied Surface Science*, 501(2020) 143892.
- [3] H. Ahmad, M.A. Ismail, M. Suthaskumar, Z.C. Tiu, S.W. Harun, M.Z. Zulkifli, S. Sivaraj, *Laser Physics Letters*, 13(2016)035103.
- [4] M. Buscema, D.J. Groenendijk, S.I. Blanter, G.A. Steele, H.S. Van Der Zant, A. Castellanos-Gomez, *Nano letters*, 14 (2014) 3347-3352.
- [5] D. Jariwala, V.K. Sangwan, L.J. Lauhon, T.J. Marks, M.C. Hersam, *ACS Nano*, 8 (2014) 1102-1120.
- [6] Y. Liu, W. Huang, W. Chen, X. Wang, J. Guo, H. Tian, H. Zhang, Y. Wang, B. Yu, T.L. Ren, J. Xu, *Applied Surface Science*, 481 (2019) 1127-1132.
- [7] M. Buscema, J.O. Island, D.J. Groenendijk, S.I. Blanter, G.A. Steele, H. S. Van Der Zant, A. Castellanos-Gomez, *Chemical Society Reviews*, 44(2015) 3691–3718.
- [8] K.F. Mak, J. Shan, *Nature Photonics*, 10 (2016) 216–226.
- [9] D.B. Velusamy, R.H. Kim, S. Cha, J. Huh, R. Khazaeinezhad, S.H. Kassani, G. Song, S.M. Cho, S.H. Cho, I. Hwang, J. Lee, K. Oh, H. Choi, C. Park, *Nature Communications*, 6(2015) 8063.
- [10] F. I. Alzakia, B. Tang, S. J. Pennycook, S. C. Tan, *Materials horizons*, 7(2020)3325-3338.
- [11] R. Gatensby, N. McEvoy, K. Lee, T. Hallam, N.C. Berner, E. Rezvani, S. Winters, M. O'Brien, G.S. Duesberg, *Applied Surface Science*, 297 (2014) 139–146.
- [12] S. Zhang, N. Dong, N. McEvoy, M. O'Brien, S. Winters, N.C. Berner, C. Yim, Y. Li, X. Zhang, Z. Chen, *ACS Nano*, 9 (2015) 7142–7150.
- [13] H. Li, J. Wu, Z. Yin, H. Zhang, *Accounts of chemical research*, 47 (2014) 1067–1075.
- [14] P.D. Tran, S.Y. Chiam, P.P. Boix, Y. Ren, S.S. Pramana, J. Fize, V. Artero, J. Barber, *Energy & Environmental Science*, 6 (2013) 2452–2459.
- [15] Y. Lei, S. Pakhira, K. Fujisawa, X. Wang, O.O. Iyiola, N.P. Lopez, A.L. Elías, L.P. Rajukumar, C. Zhou, B. Kabius, N. Alem, M. Endo, R. Lv, J.L. Mendoza-Cortes, M. Terrones, *ACS Nano*, 11 (2017) 5103–5112.

- [16] J. Rong, Y. Ye, J. Cao, X. Liu, H. Fan, S. Yang, M. Wei, L. Yang, J. Yang, Y. Chen, *Applied Surface Science*, 579 (2022) 152216.
- [17] H. Li, K. Yu, Z. Tang, Z. Zhu, *ACS Applied Materials & Interfaces*, 8 (2016) 29442–29451.
- [18] M.A. Lukowski, A.S. Daniel, C. R. English, F. Meng, A. Forticaux, R. J. Hamers, S. Jin, *Energy & Environmental Science*, 7 (2014) 2608–2613.
- [19] Z. Chen, H. Yan, T. Liu, S. Niu, *Composites Science and Technology*, 125 (2016) 47-54.
- [20] X. Zhao, M. Bo, Z. Huang, J. Zhou, C. Peng, L. Li, *Applied Surface Science*, 462 (2018) 508–516.
- [21] S. K. Ravi, W. Sun, D. K. Nandakumar, Y. Zhang, S. C. Tan, *Science advances*, 4(2018) eaa06050.
- [22] Q. Zhang, Q. Liang, D. K. Nandakumar, S. K. Ravi, H. Qu, L. Suresh, X. Zhang, Y. Zhang, L. Yang, A.T. Wee, S. C. Tan, *Energy & Environmental Science*, 13(2020) 2404-2413.
- [23] S. Muthukumaran, R. Gopalakrishnan, *Journal of Sol-Gel Science and Technology*, 62 (2012) 193–200.
- [24] P.P. Hankare, P.A. Chate, D.J. Sathe, P.A. Chavan, V.M. Bhuse, *Journal of Materials Science: Materials in Electronics*, 20 (2009) 374–379.
- [25] H. Liu, K.K.A. Antwi, S. Chua, D. Chi, *Nanoscale*, 6(2014) 624-629.
- [26] A.A. Al-Ghamadi, W.E. Mahmoud, S.J. Yaghmour, F.M. Al-Marzouki, *Journal of Alloys and Compounds*, 486 (2009) 9–13.
- [27] K.C. Kwon, T.H. Lee, S. Choi, K.S. Choi, S.O. Gim, S.R. Bae, J.L. Lee, H.W. Jang, S. Y. Kim, *Applied Surface Science*, 541 (2021) 148529.
- [28] G. Pradhan, A. K. Sharma, *Applied Surface Science*, 479 (2019) 1236–1245.
- [29] S. Xu, X. Gao, M. Hu, J. Sun, D. Jiang, D. Wang, F. Zhou, L. Weng, W. Liu, *Applied Surface Science*, 298 (2014) 36–43.
- [30] H. Qiu, H. Zheng, Y. Jin, M. Jia, Q. Yuan, C. Zhao, M. Jia, *Ionics*, 26 (2020) 5543-5551.
- [31] C.C. Tu, P.W. Peng, L.Y. Lin, *Applied Surface Science*, 444 (2018) 789–799.
- [32] A. Pandey, S. Dutta, A. Kumar, R. Raman, A. K. Kapoor, R. Muralidhran, *Advanced materials letters*, 7 (2016) 777-782.
- [33] P. Das, B. Pal, M. Das, S. Sil, D. Das, A. Layek, P.P. Ray, *Result in Physics*, 42 (2022) 105996.

- [34] L. Xu, J. Zhang, J. Ding, T. Liu, G. Shi, X. Li, W. Dang, Y. Cheng, R. Guo, Minerals, 10 (2020) 72.
- [35] S. Halder, B. Pal, A. Dey, S. Sil, P. Das, A. Biswas, P.P. Ray, Materials research bulletin, 118(2019)110507.
- [36] S. K. Cheung and N. W. Cheung, Applied Physics Letters, 49 (1998) 85–87.
- [37] R. Jana, A. Dey, M. Das, J. Datta, P. Das, P.P. Ray, Applied Surface Science, 452 (2018) 155-164.
- [38] H. Norde, Journal of Applied Physics, 50 (1979) 5052–5053.
- [39] S. Islam, B. Pal, S. Khan, S. Maity, S. Naaz, P. Ghosh, P. P. Ray, M. H. Mir, CrystEngComm, 22 (2020) 6720-6726
- [40] P. Das, B. Pal, J. Datta, M. Das, S. Sil, P.P. Ray, Journal of Physics and Chemistry of Solids, 148 (2021) 109706.
- [41] J. Datta, M. Das, A. Dey, S. Halder, S. Sil, P.P. Ray, Applied Surface Science, 420 (2017) 566-578.
- [42] W. den Boer, Journal de Physique Colloques, 42 (1981) C4-451-C4-454.

\*\*\*



*"Success can come to you by courageous devotion to the task lying in front of you"*

- CV Raman





# Chapter 3

---

**Investigating charge transportation and photo-responsive outcome of a Schottky diode fabricated by 2-amino terephthalic acid directed supramolecular Mn(II)-metallogel**

## Abstract

This study investigates a supramolecular metallogel formed using an ultrasonication technique and employing manganese acetate tetrahydrate as a metal salt, 2-amino terephthalic acid (ATA) as an organic gelator, and N,N'-dimethyl formamide and dimethyl sulfoxide as mixed solvents. The mechanical toughness and viscoelastic parameters of the metallogel material were well demonstrated by rheology-based experimental values of storage and loss moduli with rotational frequency, shear strain, and shear stress of the Mn(II)-metallogel (Mn-ATA). The microstructural analysis along with chemical composition were shown using field emission scanning electron microscopy and energy dispersive X-ray analysis-based elemental research. Analysis of the infrared spectrum aided in determining how Mn-ATA was formed. Electrospray ionization mass investigation of Mn-ATA demonstrated the existence of several metallogel components and their engagement in producing the metallogel structure. Different diode parameters (i.e. photosensitivity, photoconductivity sensitivity, responsivity, specific detectivity, ideality factor, barrier height, and series resistance) were measured, revealing the semiconducting property of the metallogel. The current–voltage characteristics of a Mn-ATA-based thin-film type metal–semiconductor junction device demonstrated non-linear rectifying behavior, indicating Schottky diode behavior with dominating electronic-charge transport features. The device displayed an improved rectifying property under illumination, which also implied higher conductivity. The device's measured conductivity in the low-voltage domain (equivalent to ohmic behavior) was  $1.03 \times 10^{-5}$  and  $4.12 \times 10^{-5} \text{ Sm}^{-1}$  under darkness and illumination, respectively, implying photo-responsive behavior.

### 3.1. Introduction

Molecular self-assembly [1], a fundamental theme of supramolecular chemistry, is increasingly important in the material and technological fields. Supramolecular gels [2] are the fascinating result of a molecular self-assembly process. Gelator and solvent molecules are the two main constituents for fabrication of a supramolecular gel system [3]. Several polar and non-polar solvents [4–6] including water, N,N'-dimethyl formamide (DMF), dimethyl sulfoxide (DMSO), tetrahydrofuran, toluene, dichloromethane, acetone, ethanol, methanol, acetonitrile and carbon tetrachloride are immobilized within the chemical components based on the gelator types during gel formation. In addition to the use of different polymeric gelators [7],  $\pi$ -gelators [8], and oligomeric gelators [9], low molecular-weight gelators (LMWGs) are a specific form of gelators that are widely recognized for obtaining supramolecular-type soft gel systems [3]. The LMWGs use distinct types of non-covalent interactions to generate a stable gel, and the LMWG-directed quasi-solid viscoelastic gel is usually referred to as supramolecular material [10]. Due to the wide range of applications in diverse areas, academic to industrial, research in the field of gelation technology is quickly expanding. Supramolecular gels have numerous potential applications from material science to biological fields including catalytic activity [11], electrochemical device fabrication [12], lithographic application [13], chemical sensing [14], optical and electronic devices [15], drug transporting behavior [16], cellular supportive nature [17] and tissue culture [18].

Besides supramolecular organogels and hydrogels, metallo-organogel and metallo-hydrogel systems have rapidly advanced during recent decades [19–25]. Metal ions are the key trigger for formation of metallogel, and they impart a variety of functionalities such as redox activity, conductivity, optical activity, and magnetic features. Metallogel systems can be useful for catalytic applications, actuators, cosmetics, foods, environmental remediation, nano-electronics, and nano-science [19–35].

Surprisingly, various non-covalent type interactions are major factors in the formation of stable supramolecular metallogel architecture, including electrostatic, aryl-system directed, hydrogen-bonding, van der Waals forces, hydrophilic, and hydrophobic interactions [36–38].

Because of their relatively low price and availability of the involved metal ions required, functional supramolecular soft gels are economic for practical applications. Specifically, the role of Mn(II) in many diverse effective applications has been widely discussed, including in metal–

organic frameworks, coordination complex formation, quantum dot formation, catalysis, coordination polymer synthesis, organometallic chemistry, and semiconducting devices [34,39–42]. The key advantages of using Mn(II) are economic viability, well-known semiconducting and physicochemical properties, high power density, high specific energy, promising electrode material applicable in energy or power storage devices, and reversible electrochemical redox activity. For formation of supramolecular metal–organic networks, 2-amino terephthalic acid (ATA) can bind with metal ions [43–50]. Recently, Lovitt et al. explored the Mn(II)-metallogel with N-picolyl-1,8-naphthalimides acting as the LMWG [51]. The significance of ATA is mainly explored through the formation of crystal-based non-flexible metal–organic frameworks. Additionally, Mn(II) complexes are well-recognized using several metal–ligand coordinating systems. However, the design, synthesis, and usefulness of the flexible-type network constructed using ATA and Mn(II)-salt for a soft-scaffold-based semiconducting micro-electronic material are not known. The flexibility of such semiconducting devices is an added benefit for technological advancement because diodes can be fabricated in a desired shape and positioned in any place in a device. Inspired by previous literature [52–55], I investigated metallogel generation using ATA and a Mn(II)-source in a mixed solvent of DMF and DMSO (1:1 v/v) to achieve Mn-ATA. I tested device applicability of the Mn-ATA metallogel. The use of these materials in practical semiconducting equipment is always a technological challenge. I was able to effectively deploy these gel-materials in metal–semiconductor junction-based thin-film devices to examine their electronic device applications and charge transport capabilities. My constructed devices had non-linear rectifying current (I)–voltage (V) characteristics, expressed in terms of a Schottky junction diode feature with a high on/off ratio. I investigated device performance of our Mn-ATA metallogel-based Schottky diode. The photosensitivity of the Mn-ATA-directed device was also explored. The experimental evidence clearly established better I–V characteristics in presence of a light source.

## 3.2. Experimental section

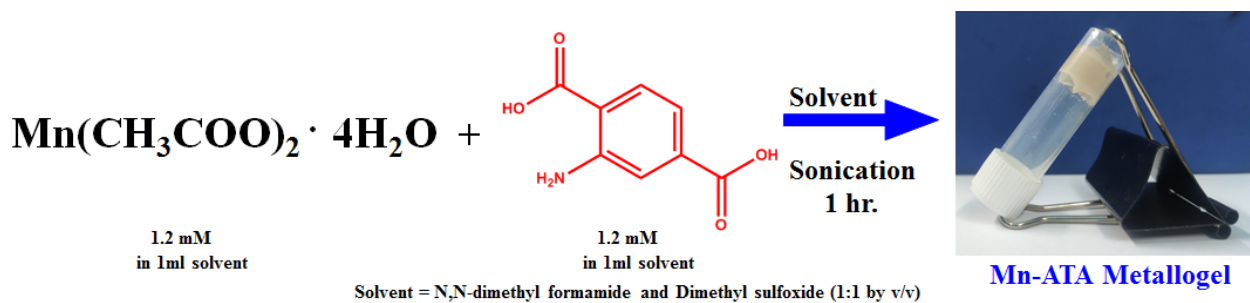
### 3.2.1. Materials

Manganese acetate tetrahydrate  $[\text{Mn}(\text{OAc})_2 \cdot 4\text{H}_2\text{O}]$ , ATA, DMSO, and DMF were obtained from Sigma-Aldrich Chemicals, and used for formation of the gel.

### 3.2.2. Characterizations

Literature reports [3–5] were used as the basis of the inversion vial test for checking the stability of the gel against gravitational force. A Biobase ultrasonic cleaner UC-20STII with AC 230V/50Hz, and operating an ultrasound frequency 80kHz was employed for metallogel synthesis. Anton–Paar equipment was used to conduct the rheological analysis. Field emission scanning electron microscopy (FESEM)–energy dispersive X-ray (EDX) spectroscopy mapping was used to examine the chemical composition of metallogels (Zeiss GeminiSEM 450 and associated EDAX). Fourier-transform infrared (FT-IR) spectrum data were obtained using the KBr pellet technique on a Perkin Elmer FT-IR spectrometer. An Agilent Q-TOF mass spectrometer was used to obtain electrospray ionization (ESI) mass patterns. Electrical conductivity was calculated by means of a computer-interfaced Keithley Source Meter 2635B to measure the I–V properties of the Mn-ATA-based thin-film device (Model no: 2635B). The capacitance–frequency measurement was done with a computer-controlled impedance analyzer (Agilent 4294A).

### 3.2.3. Synthesis of Mn-ATA



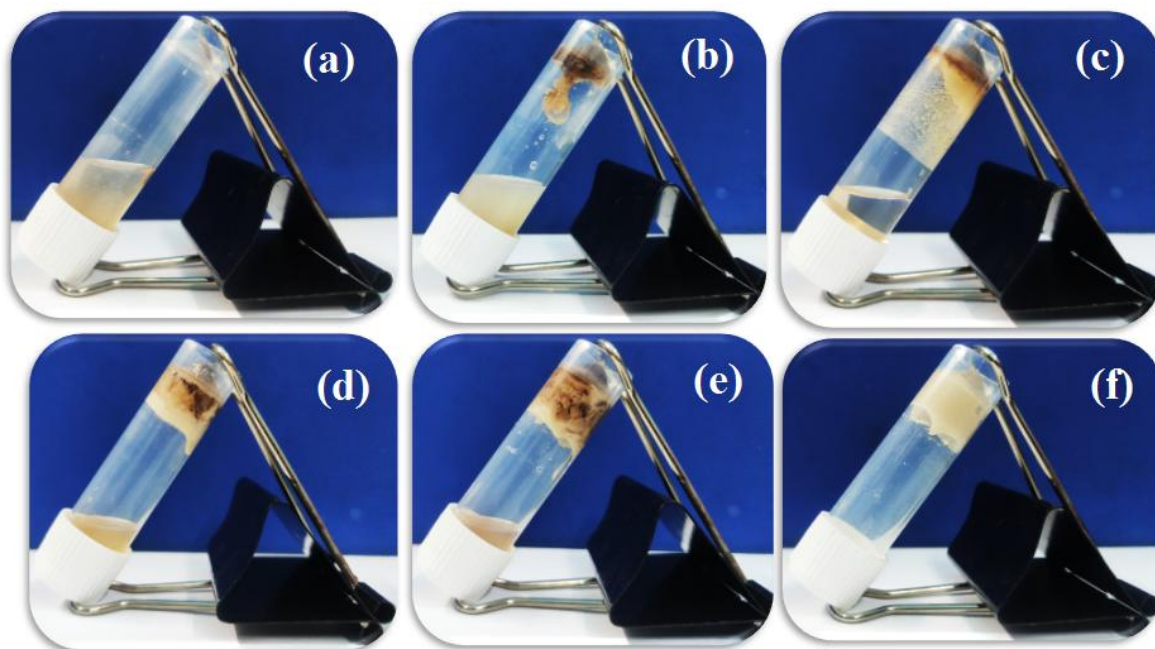
**Fig. 3.1:** Synthetic approach for ATA-established Mn-ATA metallogel in N,N'-dimethyl formamide and dimethyl sulfoxidesolvent system. Ultrasonication was used for gelation.

Manganese acetate tetrahydrate (294.11 mg, 1.2 mmol) was taken as a source of Mn(II), and ATA (217.38 mg, 1.2 mmol) as the gel-establishing organic component – each taken in 1 ml of mixed solvents of DMSO and DMF (1:1 by v/v) at ambient conditions. These two solutions, which included a pale pink Mn(II)-salt solution and a yellow-colored ATA solution, were quickly mixed in a glass vial. This produced a semi-solid off-white-colored substance and this

was then ultra-sonicated in a sophisticated ultra-sonicating bath for 60 min. The result was off-white-colored Mn-ATA in the solvent mixture (Fig. 3.1 shows construction of ATA-directed Mn-ATA metallogel in DMF–DMSO solvent system). Under exposed aerial conditions, the Mn-ATA retains its stability for a few months at normal ambient temperature with humidity range 50–55%. An inversion vial experiment was performed to determine stability, initially to confirm the gel-state of the soft-scaffold. The gel melting temperature ( $T_{\text{gel}}$ ) was measured through digital melting point apparatus, with  $T_{\text{gel}} = 238 \pm 2$  °C.

### 3.2.4. Minimum critical gelation concentration (MGC) of the synthesized Mn-ATA metallogel

The MGC of Mn-ATA was carefully determined by varying the concentration of both Mn(II)-salt and ATA. For gelation, the chemical components [i.e.  $\text{Mn}(\text{CH}_3\text{COO})_2 \cdot 4\text{H}_2\text{O}$  and ATA] were both dissolved individually in solvent mixture of DMF and DMSO (1:1 by v/v) at a 1:1 molar ratio. The most stable gel was obtained with concentrations of Mn(II)-salt and ATA of 294.11 and 217.38  $\text{mgml}^{-1}$ , respectively (Fig. 3.2 and Table 3.1).



**Fig. 3.2: Determination of Minimum Critical Gelation Concentration of the Mn-ATA metallogel with step-wise photography of Mn-ATA metallogel forming chemical constituents having varied concentrations.**

**Table 3.1: Determination of Minimum Critical Gelation Concentration of the Mn-ATA**

Serial No.	Metal Concentration 1 ml mixed solvent of N,N-dimethyl formamide and Dimethyl sulfoxide (1:1 by v/v)	Gelator concentration 1 ml mixed solvent of N,N-dimethyl formamide and Dimethyl sulfoxide (1:1 by v/v)	Phase
(a)	49.0 mg/ml	36.2 mg/ml	Sol
(b)	98.0 mg/ml	72.5 mg/ml	Sol
(c)	147.0 mg/ml	108.7 mg/ml	Sol
(d)	196.0 mg/ml	144.9 mg/ml	Viscous sol
(e)	245.0 mg/ml	181.1 mg/ml	Weak gel
(f)	294.1 mg/ml	217.4mg/ml	Gel

### 3.2.5. Testing gel-forming ability of different solvents in producing stable Mn-ATA

**Fig. 3.3: Role of versatile solvents in forming stable metallogel of Mn-ATA.**

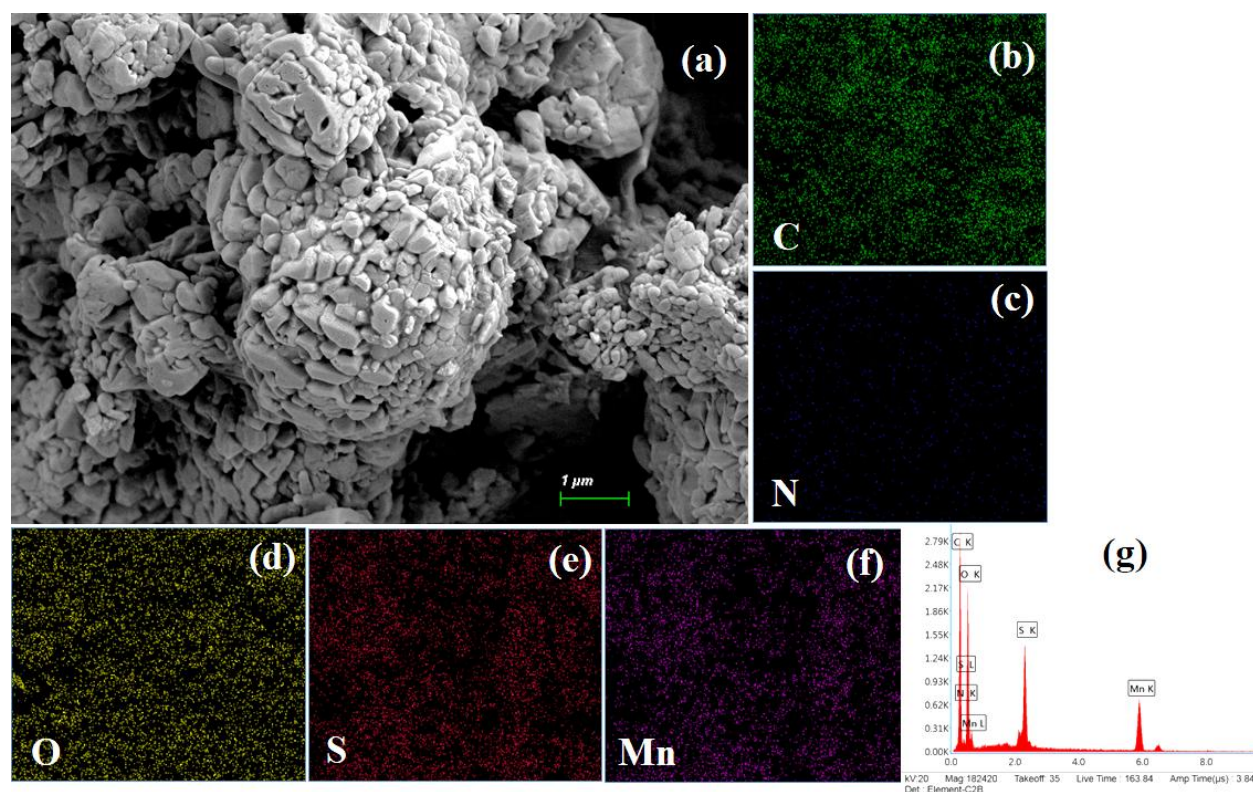


The gel-forming ability of the chemical components of Mn-ATA was examined in different solvents (non-polar to polar). This clearly showed that the 1:1 (v/v) DMF–DMSO mixture was the optimum mixed solvent to form stable Mn-ATA gel through ultrasonication for a certain time. Most specifically individual solvents of DMF or DMSO were independently unable to form the metallogel under optimum gel-forming conditions (Fig. 3.3).

### 3.3. Results and discussions:

#### 3.3.1. Morphological and elemental study

The FESEM studies of the xerogel state of Mn-ATA explored the microstructural pattern of DMF–DMSO (1:1 v/v) based Mn-ATA metallogel systems. The self-assembled network of inter-linked irregular-type block-shaped architectures was visualized using FESEM (Fig. 3.4 (a)). A hierarchal arrangement of inter-linked agglomerated stacked-type networks of the xerogel form of Mn-ATA was shown.



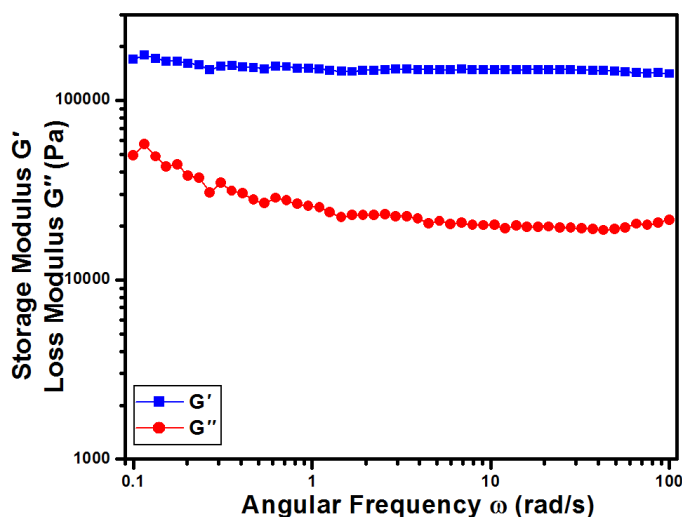
**Fig. 3.4:** (a) FESEM microstructural arrangements of Mn-ATA metallogel; (b–f) elemental mapping analyses showing the presence of elements C, N, O, S and Mn of Mn-ATA; and (g) EDX elemental spectrum of synthesized Mn-ATA.



The stacked agglomerated assembly originated via ATA, consisting of  $\pi$ -system facilitated interconnection in the synthesized metallogel framework. Presence of Mn, C, N, O, and S elements in this framework was identified by elemental mapping technique (Fig. 3.4 (b–f)) and EDX spectral data showed the role of participating elements (Fig. 3.4 (g)). Presence of element S showed the importance of DMSO solvent in the metallogel development. The active influence of Mn(II) ion accompanied by the ATA in metallogel formation was clarified by the elemental analysis.

### 3.3.2. Rheological study

Rheological investigations such as storage modulus ( $G'$ ) and loss modulus ( $G''$ ) with rotational frequency, as well as shear strain, were used to investigate the mechanical toughness and solvent encapsulation tendency of supramolecular Mn-ATA metallogel. The viscosity and elastic characteristics of the gel substance were tested. The viscous and semi-solid nature of Mn-ATA was demonstrated by the rotational frequency dependence of  $G'$  and  $G''$ .



**Fig. 3.5:** Frequency sweep of Mn-ATA from rheological experimentation.

$$G' = (\sigma_0/\gamma_0) \cos(\delta) \text{ and } G'' = (\sigma_0/\gamma_0) \sin(\delta)$$

Where  $\gamma_0$ ,  $\sigma_0$ ,  $\sigma_0/\gamma_0$ , and  $\delta$  are strain amplitude, shear stress amplitude, amplitude ratio, and phase angle respectively.

For a given metallogel system concentration (Fig. 3.5),  $G'$  of Mn-ATA was substantially larger than  $G''$ , and the plot characteristics (Fig. 3.5) were true for particular angular frequency values. Here both  $G'$  and  $G''$  ran almost parallel, i.e. imitated in the complex viscosity vs. angular frequency plot (Fig. 3.6) and ascertained the pure gel nature of the synthesized material.

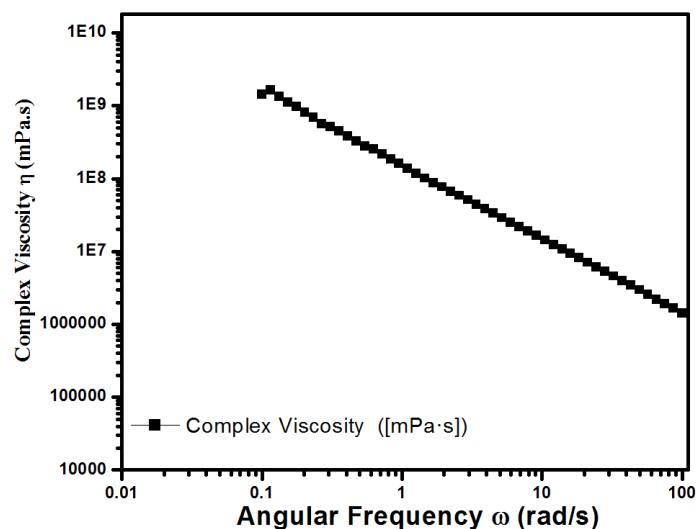


Fig. 3.6: Complex viscosity vs. angular frequency plot of Mn-ATA metallogel.

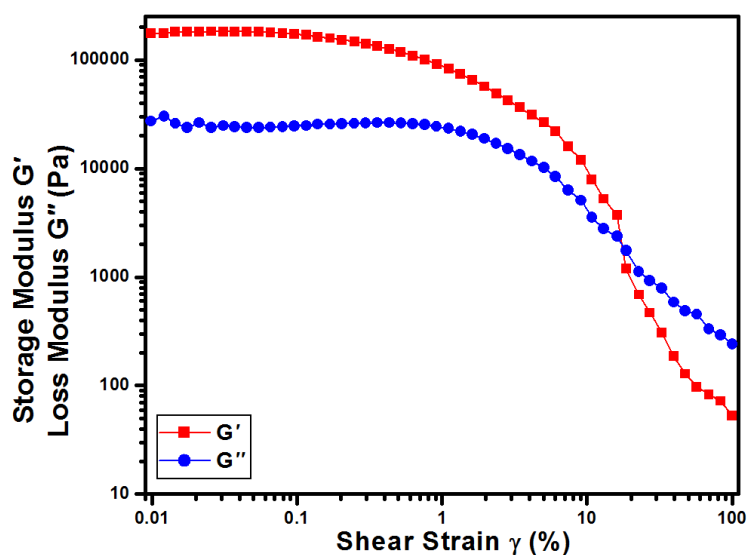


Fig. 3.7: Strain sweep of Mn-ATA metallogel from rheological experimentation.

The visco-elastic type of semi-solid outlook of the mechanically stable Mn-ATA was shown by rheological parameters based on angular frequency. The gel nature of Mn-ATA was further revealed by rheological experiments based on  $G'$  and  $G''$  vs. changing shear strain (Fig. 3.7). The Fig.  $G'$  and  $G''$  intersected at a particular degree of shear strain (i.e. 17.4%) or 2645.4 Pa of shear stress (Fig. 3.8). The critical strain is the lowest quantity of shear strain demanded for gel-breaking of the Mn-ATA metallogel network. Hence, the mechanical effectiveness of Mn-ATA was clearly established.

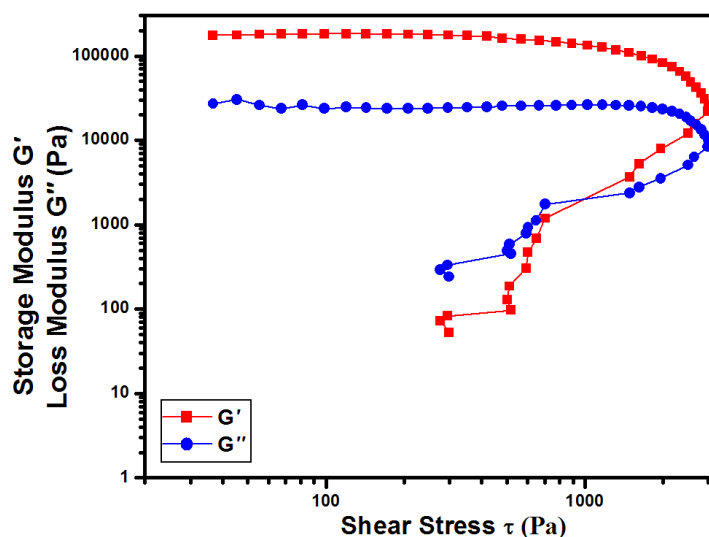
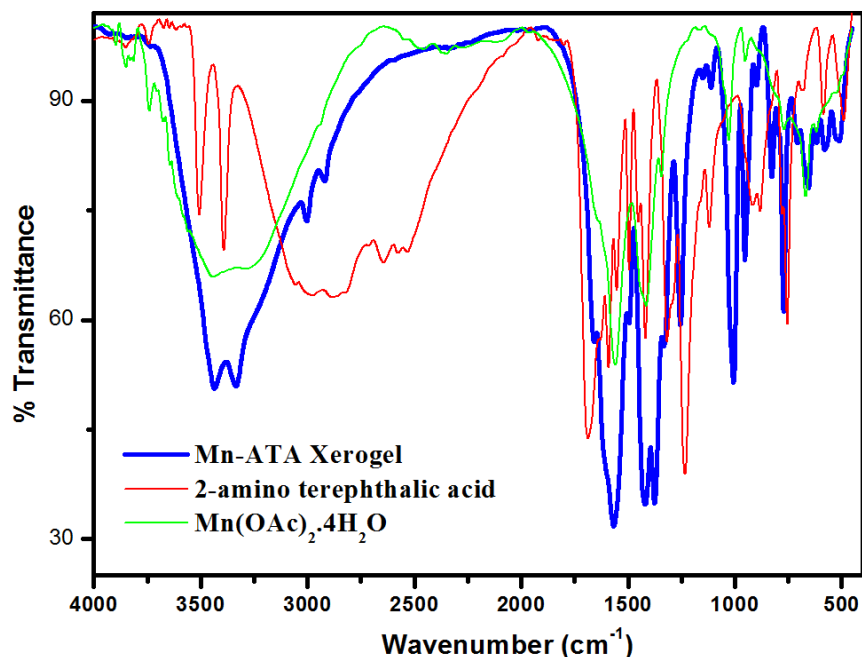


Fig. 3.8 Stress sweep of Mn-ATA metallogel.

### 3.3.3. FT-IR spectroscopic study

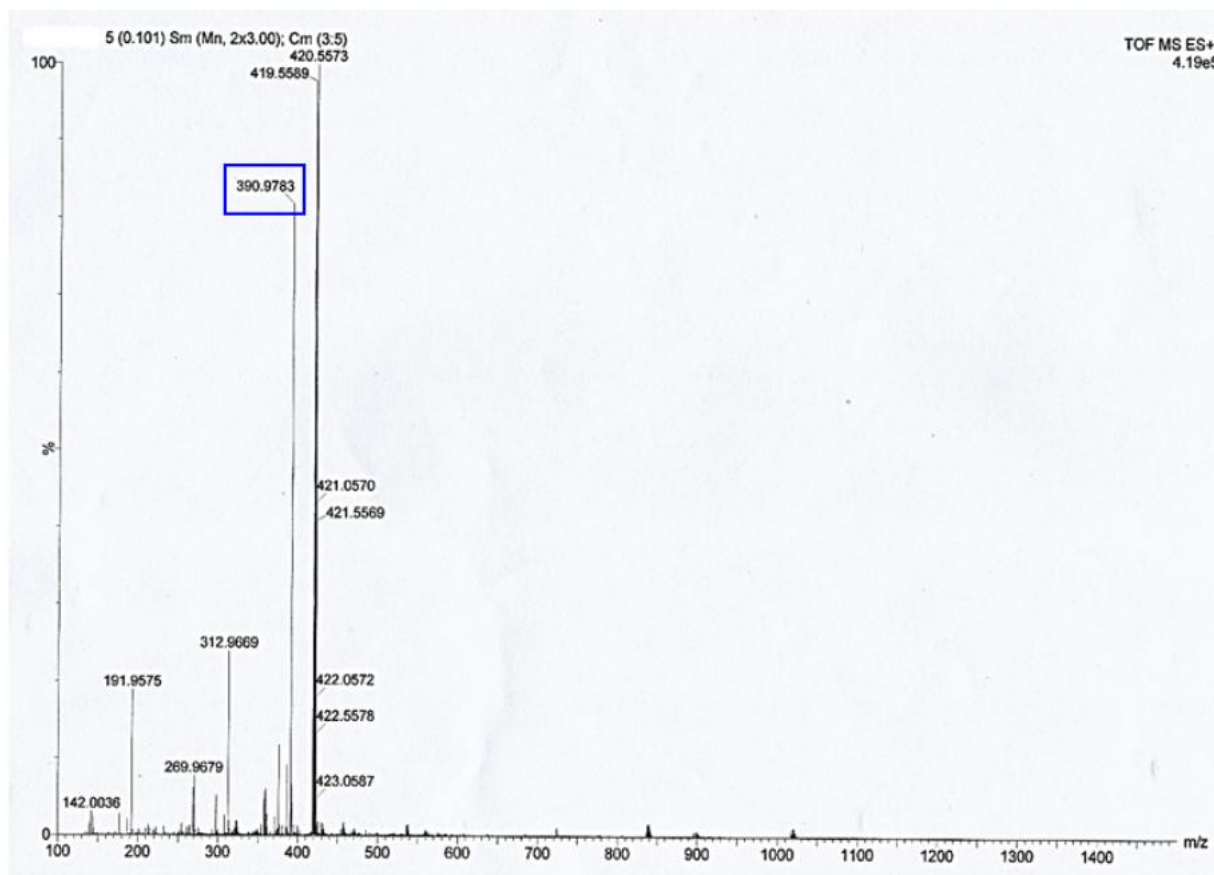
The xerogel obtained from Mn-ATA metallogel was analyzed using FT-IR spectroscopy (Fig. 3.9). The involvement of several metallogel-forming chemical substances, such as Mn-salt, organic ligands like ATA, and trapped solvents like DMF and DMSO in the formation of Mn-ATA was investigated using FT-IR. The production of a ATA-directed stable supramolecular metallogel of Mn(II) was promoted by non-covalent supramolecular factors such as the  $\pi$ -system and hydrogen-bonding patterns, according to FT-IR data.



**Fig. 3.9:** Pictorial illustration of FT-IR spectral data of Mn-ATA xerogel, 2-amino terephthalic acid, and  $\text{Mn}(\text{OAc})_2 \cdot 4\text{H}_2\text{O}$ .

### 3.3.4. ESI mass analysis

The ESI mass investigation of Mn-ATA demonstrated the existence of several metallogel-materializing components and their dynamic engagement in the production of metallogel structure. The highlighted points in the ESI mass pattern reveal the fundamental repeating chemo-construct or responsible for building the non-covalent connections of the supramolecular gel of Mn-ATA – this indicated that the continuously iterating metallogel-developing chemical units involved ATA and  $\text{Mn}(\text{OAc})_2 \cdot 4\text{H}_2\text{O}$ . This study explores the evidential role of the metal-salt-directed self-assembly feature as the key factor to obtain a stable gel-structure (Fig. 3.10).



**Fig. 3.10: ESI-MS Spectra of Mn-ATA metallogels.**

### 3.3.5. Optical study

For optical band gap measurement, I recorded the absorption spectra (Fig. 3.11 inset) of the synthesized gel in the wavelength range of 280–450 nm using a UV-visible spectrophotometer. The optical band gap was determined by analyzing the Tauc's diagram using the following equation [56]:

$$\alpha h\nu = A(h\nu - E_g)^n \quad (3.1)$$

Where,  $\alpha$  is absorption coefficient,  $h$  is Planck's constant,  $\nu$  is light frequency,  $A$  is an energy dependent constant (assumed to be 1),  $E_g$  is band gap, and  $n$  is an electron transition process dependent constant (for direct transition  $n=1/2$ ). Extrapolation of the linear part of the  $(\alpha h\nu)^2$  vs.  $h\nu$  curve (Fig. 3.11) showed that the material had a direct optical band gap of 3.34 eV.

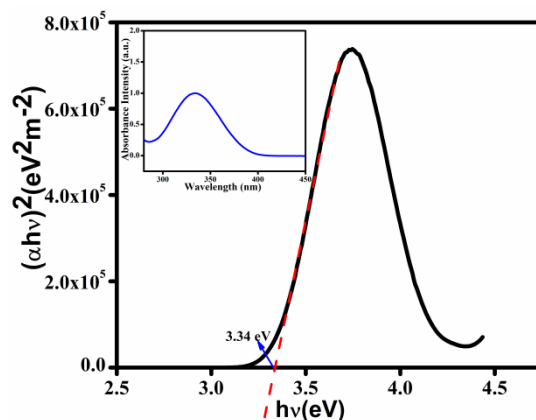


Fig. 3.11:  $(\alpha h\nu)^2$  versus  $h\nu$  curve and UV-vis absorption spectra (inset) determined using Tauc's equation

### 3.3.6. Fabrication of indium tin oxide (ITO)/gel compound/aluminum (Al)-based Schottky barrier diode

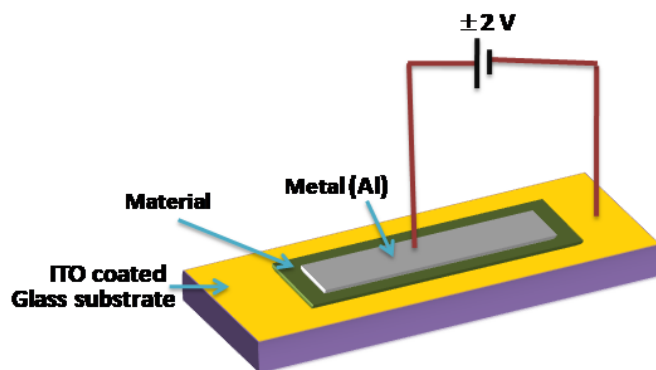


Fig. 3.12: Schematic representation of Schottky diode based on aluminum/gel/ITO structure.

Initially, an ITO-coated glass substrate was washed through a 10 min ultrasonic bath containing acetone, isopropyl alcohol, and DI water. Following the cleaning operation, a thin film (thickness  $\sim 1 \mu\text{m}$ ) of synthesized gel compound was placed on front of the ITO-coated glass. After complete drying, a Schottky diode (SD) in sandwiched patterns of ITO/gel compound/Al was

formed, with Al acting as the metal electrode (schematically represents in Fig.3.12). In the given structure, a Schottky barrier is formed at the interface between the gel compound and the Al electrode. The effective diode area was considered as  $7.065 \times 10^{-6} \text{ m}^2$ . In the sandwich structure of Al/gel compound/ITO, the +ve contact was on the Al side and the -ve contact on the ITO side. Illumination was provided from the ITO side only. In this part of experiment, the light source was AM 1.5 G radiation from a Model 10500 Solar Simulator (Abet Technologies).

### 3.3.7. Analysis of electrical characteristics

A Keithley Source Meter was employed to measure I–V at room temperature with a –2 to +2 V bias range in order to analyze the charge transmission procedure via the interface. The obtained J–V plots of the gel compound for both dark and light conditions are presented in Fig. 3.13, where J signifies the current density (current/area) and the log J vs. V graph is depicted in the inset. The SD behavior is revealed by the rectifying or non-linear nature in forward bias. Table 3.2 shows the photodiode parameters and Table 3.3 shows Schottky diode parameters like the rectification ratio, calculated using the exponential J–V plot. The compound displayed an improved rectifying property under illumination, which also implies a higher conductivity. The ratio of J in the material to the applied bias voltage that generates the current flow is used to determine how well that compound conducts electricity, i.e. its electrical conductivity. This compound-based device's measured conductivity in the low-voltage domain (equivalent to ohmic behavior) was  $1.03 \times 10^{-5}$  and  $4.12 \times 10^{-5} \text{ Sm}^{-1}$  for darkness and illumination, respectively. When light falls on the device it absorbs the photons and converts the light energy to electrical current, thus I had enhanced I–V characteristics. The photo-response study was carried out under AM 1.5 radiation. The calculated on/off ratio for the SD based on my synthesized material was 7.96.

Different diode parameters like photosensitivity, photoconductivity sensitivity(S), responsivity (R), and specific detectivity ( $D^*$ ) were also calculated (Table 3.2) using the following equations [57]:

$$\text{Photosensitivity} = \frac{J_{\text{Light}} - J_{\text{Dark}}}{J_{\text{Dark}}} \times 100\% \quad (3.2)$$

$$\text{Photoconductivity sensitivity, } S = \frac{J_{\text{Light}} - J_{\text{Dark}}}{P \times V_{\text{max}}} \times d \quad (3.3)$$

$$\text{Responsivity, } R = \frac{J_{\text{Light}} - J_{\text{Dark}}}{P} \quad (3.4)$$

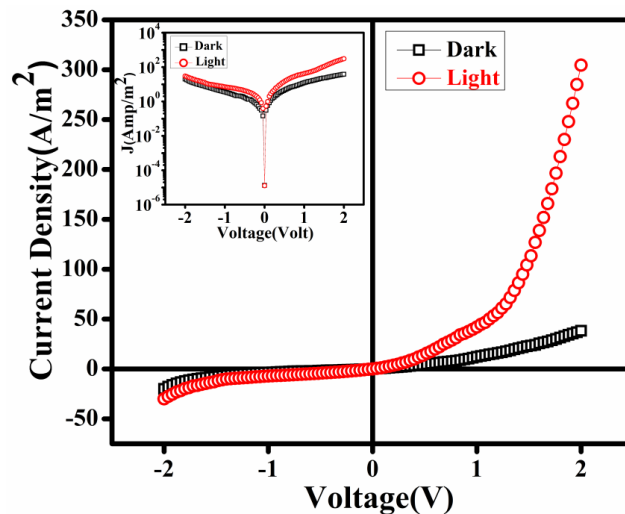
$$\text{Specific detectivity, } D^* = \frac{R}{\sqrt{2qA} J_{\text{Dark}}} \quad (3.5)$$

Where,  $J_{\text{Dark}}$  and  $J_{\text{Light}}$  are the values of  $J$  at particular bias  $V_{\text{max}}$ , i.e. 2 V under dark and illumination condition, respectively; total power of incident light is given by  $P$ , which is taken as  $100 \text{ mWcm}^{-2}$ ;  $d$  is film thickness;  $q$  is the charge of an electron; and  $A$  is active diode area of the fabricated device.

The theory of thermionic emission, was utilized to estimate additional ITO/gel compound/Al-structured SD characteristics [57]. I derived the ideality factor ( $\eta$ ), barrier height ( $\Phi_B$ ), and series resistance ( $R_s$ ) from the linear component using Cheung's equation (explained in Section 1.14) [58].

**Table3.2: Photodiode parameters.**

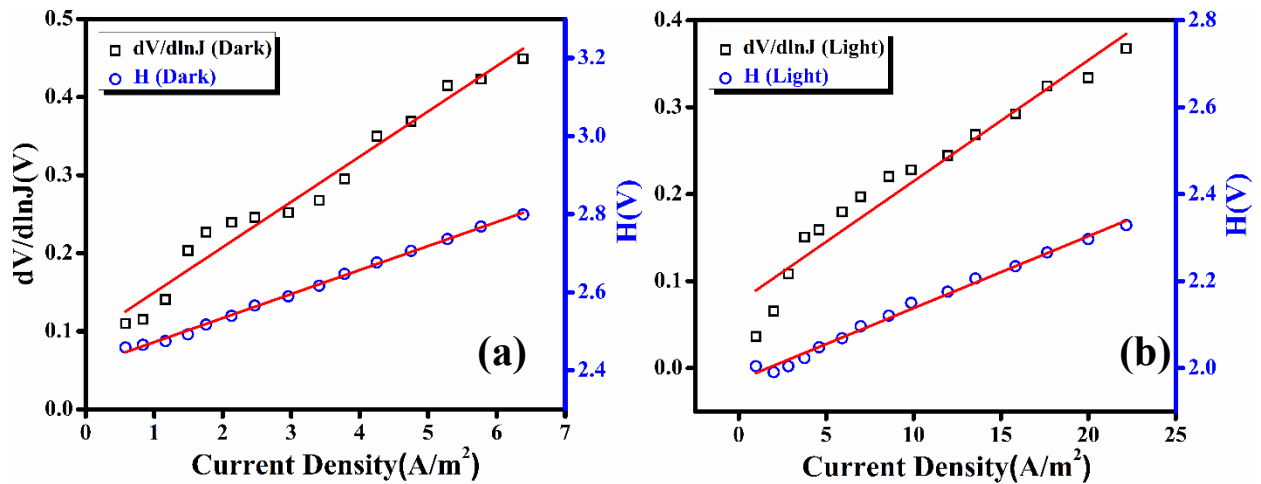
On/off ratio	Photosensitivity (%)	Photoconductivity sensitivity (S) $\text{A m}^{-1}\text{W}^{-1}$	Responsivity (R) $\text{A m}^{-2}\text{W}^{-1}$	Specific detectivity( $D^*$ ) (Jones)
7.96	695.51	$13.32 \times 10^{-4}$	$2.66 \times 10^3$	$90.51 \times 10^{12}$



**Fig. 3.13: Current density–voltage characteristics curve (J–V).**



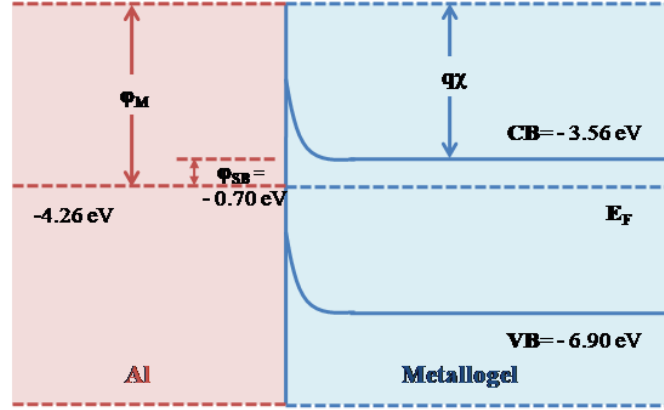
The  $\eta$  and  $R_s$  in both dark and light conditions were derived from the intercept and slope of the linearly fitted  $dV/d\ln J$  against  $J$  curve (Fig. 3.14 (a) and (b)) using Cheung's model (mentioned in Section 1.14, equation 1.11), and listed in Table 3.3. The  $\eta$  in these two cases differed, implying inhomogeneity at the metal–semiconductor junction. In the case of  $\eta$ , the SD under dark condition differed much more from the desired properties than under the illuminated condition. Furthermore, I computed  $\Phi_B$  and  $R_s$  using this model by linearly fitting the  $H(J)$  vs.  $J$  curve (Fig. 3.14 (a) and (b)) from the intercept and slope, respectively (Table 3.3) (explained in Section 1.14, equation 1.12).



**Fig. 3.14:**  $dV/d\ln J$  and  $H(J)$  versus current density ( $J$ ) curves for fabricated diode under (a) dark and (b) light conditions.

**Table 3.3:** Schottky diode parameters.

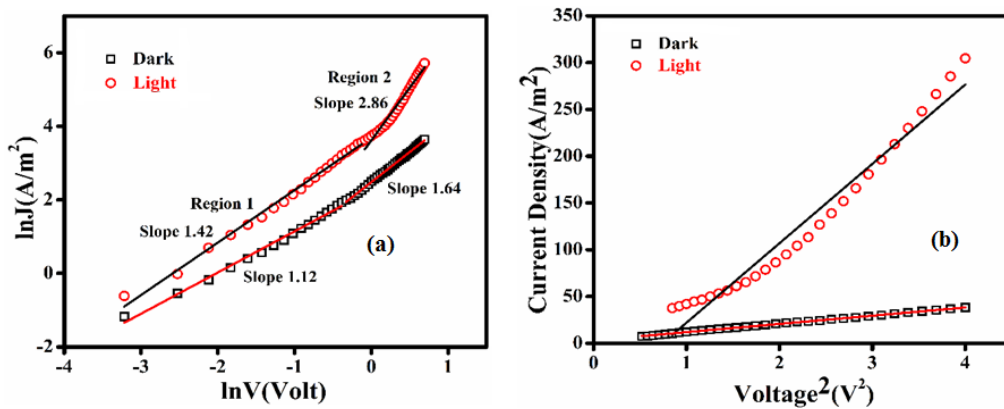
Condition	Rectification ratio	Conductivity $\sigma_{\text{ohmic}} (\text{S m}^{-1})$	$\eta$	$R_s$ from $dV/d\ln J$ vs. $J$ curve (k $\Omega$ )	$R_s$ from $H$ vs. $J$ curve (k $\Omega$ )	$\Phi_B$ from $H$ vs. $J$ curve (eV)
Dark	1.91	$1.03 \times 10^{-5}$	3.51	8.21	8.71	0.70
Light	10.18	$4.12 \times 10^{-5}$	2.89	1.97	2.34	0.68



**Fig. 3.15:** Energy-band diagram of Al/metallogel interface of the Schottky diode.

The  $R_s$  values generated from these two approaches were similar (Table 3.3). The SD under light had lower  $R_s$  with lower  $\Phi_B$ , implying comparatively enhanced behavior as a photodiode. Here the energy band diagram at gel/Al interface for the device ITO/gel/Al has been provided in Fig. 3.15.

To acquire deeper knowledge of the charge transfer process via the metal–semiconductor junction,  $\ln J$  vs.  $\ln V$  plots for the forward bias voltage region were obtained by plotting and linear fitting (Fig. 3.16 (a)). The slope value was close to 1 (in Region 1), indicating that ohmic conduction regulated the movement of carriers. However, for Region 2, slope was approximately 2, demonstrating the space-charge-limited conduction (SCLC) procedure due to the trap assisted carrier [59].



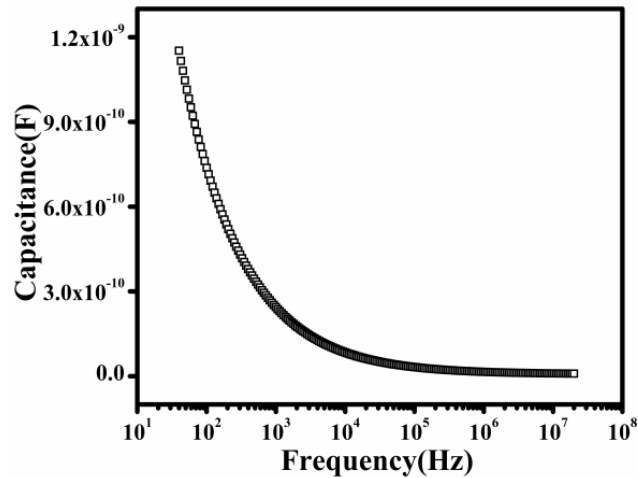
**Fig. 3.16:** (a)  $\ln J$  vs.  $\ln V$  graph and (b) current density vs.  $\text{voltage}^2$  curve showing the SCLC region used to calculate the mobility of the effective interface.

In the SCLC region (Region 2), we evaluated conductivity ( $\sigma_{\text{SCLC}}$ ) due to this conduction mechanism in darkness as  $2.42 \times 10^{-5} \text{ Sm}^{-1}$  from the slope of the  $J$  vs.  $V$  graph; after illumination,  $\sigma_{\text{SCLC}}$  rose to  $24.72 \times 10^{-5} \text{ Sm}^{-1}$ . To analyze the device in detail, I estimated charge transport metrics from this region (e.g. effective interface mobility, transit time, carrier concentration, diffusion coefficient, and diffusion length). One of the most crucial characteristics of any semiconductor material is carrier mobility, which determines whether it can be used in a wide range of electronic products. This establishes how quickly an electron or hole can move in a solid substance when bias voltage is applied. Using Mott–Gurney SCLC density and the slope of the  $J$  vs.  $V^2$  graphs (eq. 3.6) of Region 2 (Fig. 3.16), the charge carrier's effective interface mobility ( $\mu_{\text{eff}}$ ) was determined and rose with illumination.

$$J = \frac{9 \mu_{\text{eff}} \varepsilon_0 \varepsilon_r}{8} \left( \frac{V^2}{d^3} \right) \quad (3.6)$$

$\varepsilon_0$  represents the dielectric permittivity of vacuum, while  $\varepsilon_r$  denotes the dielectric constant of the synthesized film, both determined from the capacitance ( $C$ )-frequency ( $f$ ) curve displayed in Fig. 3.17. The compound's relative dielectric constant was determined to be 1.43. By analyzing the saturation level of the curve in Fig. 3.17, the semiconductor's dielectric permittivity was calculated using the provided equation.

$$\varepsilon_r = \frac{1}{\varepsilon_0} \frac{C_{\text{sat}} d}{A} \quad (3.7)$$



**Fig. 3.17: Capacitance versus frequency plot.**

Where  $d$  is the film thickness and  $A$  is the area of the diode. The time needed to go from the anode to the cathode is known the carrier's transit time, or time of flight ( $\tau$ ). High mobility with short  $\tau$  under illumination shows superior charge transport at the Schottky interface. I determined  $\tau$  from the slope of the J–V graph in Region 2 using the Mott–Gurney equation [59].

$$\tau = \frac{9\epsilon_0\epsilon_r}{8d} \left( \frac{V}{J} \right) \quad (3.8)$$

This equation was also utilized for estimating the charge carrier concentration ( $N$ ) near the Fermi level, which moves to the edge of the conduction band due to the applied potential.

$$N = \frac{\sigma_{\text{SCLC}}}{q \mu_{\text{eff}}} \quad (3.9)$$

Where,  $\sigma_{\text{SCLC}}$  is the SCLC region conductivity.

$$L_D = \sqrt{2D\tau} \quad (3.10)$$

Here,  $D$  is the diffusion co-efficient. Recognizing the diffusion length of charge carriers is essential for understanding their effective transmission from one electrode to the opposing electrode over the thin film. The diffusion length value may be utilized to determine the synthesized material's suitability for device application. The Einstein–Smoluchowski expression was also used to compute the diffusion coefficient [57].

$$\mu_{\text{eff}} = \frac{qD}{KT} \quad (3.11)$$

This approximation gives a fairly accurate idea of the density of defect states distribution in the band gap region [60]. The denBoer technique [61] was used to calculate the density of states ( $N_F$ ) around the Fermi level using the SCLC J–V properties; the lower density of states under illumination indicates the presence of fewest traps in the forbidden gaps.

$$N_F = \frac{2\epsilon_0\epsilon_r(V_2-V_1)}{qd^2\Delta E_F} \quad (3.12)$$

Here,  $\Delta E_F$  represents the change in quasi-Fermi level, defined as follows:

$$\Delta E_F = KT \ln \frac{J_2 V_1}{J_1 V_2} \quad (3.13)$$

Here,  $V_1$  and  $V_2$  represent two different forward bias voltages obtained from the SCLC Region-II of each diode, with  $J_1$  and  $J_2$  representing the corresponding current densities. Therefore, under illumination, density of the injected photo-generated charge carrier increases and the photo-induced electrons contribute to the forward current. Interestingly,  $\eta$  and the barrier potential improved with light soaking. This may be due to the enrichment of the metallogel's vibration states, which also increases mobility and is also aided by a lower  $\tau$  under illumination. The effective improvement in mobility after light soaking is consistent with the light-induced current mentioned above. The barrier potential height that occurs in the metal–semiconductor interface layer probably depends on the diffusivity and charge-carrying capacity of the metal–semiconductor junction. The potential barrier was reduced to 0.68 eV as the light-induced electron mobility increased. Thus, the forward current was increased due to light soaking. When the light is turned off, the number of free electrons decreases and the diode current decreases accordingly [62].

Table 3.4 lists all parameters related to SCLC conduction mechanism, i.e. the values of  $\sigma_{\text{SCLC}}$ ,  $\mu_{\text{eff}}$ ,  $\tau$ ,  $N$ ,  $N_F$ , and diffusion length. All the diode parameters of the gel-based diode revealed significantly improved charge transfer kinetics under illumination. The better conduction mechanism is indicated by reduced  $\tau$ , higher  $\mu_{\text{eff}}$ , lower density of states, and higher conductivity of compound-fabricated SD [63]. Higher diffusion length under light indicates greater potential applications. The study demonstrates that the gel compound is a Schottky-type photodiode and shows that it has possible applications in other optoelectronic devices.

**Table 3.4: Charge transport parameters of device.**

<b>Condi- on</b>	<b>SCLC conductivity <math>\sigma_{\text{SCLC}}</math> (<math>\text{Sm}^{-1}</math>)</b>	<b>Mobility <math>\mu_{\text{eff}}</math> (<math>\text{m}^2\text{V}^{-1}\text{S}^{-1}</math>)</b>	<b>Carrier concentration <math>N</math> (<math>\text{m}^{-3}</math>)</b>	<b>Transit time <math>\tau</math> (s)</b>	<b>Density of states <math>N_F</math> (<math>\text{eV}^{-1}\text{m}^{-3}</math>)</b>	<b>Diffusion length (<math>\mu\text{m}</math>)</b>
<b>Dark</b>	$2.42 \times 10^{-5}$	$6.17 \times 10^{-7}$	$2.44 \times 10^{20}$	$594 \times 10^{-9}$	$7.66 \times 10^{40}$	1.38
<b>Light</b>	$24.72 \times 10^{-5}$	$59.57 \times 10^{-7}$	$2.60 \times 10^{20}$	$59 \times 10^{-9}$	$3.11 \times 10^{40}$	1.45

### 3.4. Conclusions

A stable supramolecular metallogel of Mn(II) and ATA was explored, including mechanical toughness and viscoelastic parameters. The morphological textures of the metallogel system were investigated using FESEM. A hierarchical-type association of the self-assembled network found in the metallogel system was scrutinized using FESEM imaging. The EDX analysis associated with FESEM instruments established the role of Mn(II)-source, organic aromatic acid, and the DMF–DMSO mixed solvent in forming the metallogel structure. The mechanistic idea regarding the metallogel formation was substantiated using FT-IR spectral data and ESI-MS analysis. The metallogel was successfully used to fabricate a metal–semiconductor junction based thin-film device to study semiconducting properties. Different measured charge transport parameters of the fabricated device clearly demonstrated the semiconducting SD feature. The photosensitivity of the semiconducting diode was also shown. My results may start a new dimension in the research of mechanically flexible networks for fabricating functional optoelectronic devices, generated through the use of small molecules via judicial utilization of non-covalent supramolecular interactions. This may lead to flexible smart electronic diodes with light sensitivity and technologically advanced functionality.

## References

- [1] D. Pochan, O. Scherman, *Chemical reviews*, 121 (2021) 13699–13700.
- [2] J.W. Steed, *Chemical Communications*, 47 (2011) 1379–1383.
- [3] P. Dastidar, *Chemical Society Reviews*, 37 (2008) 2699–2715.
- [4] S. Majumdar, M. Ghosh, S. Mukherjee, B. Satpati, B. Dey, *Journal of molecular liquids*, 342 (2021) 117482.
- [5] S. Dhibar, A. Dey, D. Ghosh, S. Majumdar, A. Dey, P. Mukherjee, A. Mandal, P.P. Ray, B. Dey, *ChemistrySelect* 4 (2019) 1535–1541.
- [6] X. Ma, S. Liu, Z. Zhang, Y. Niu, J. Wu, *Soft Matter*, 13 (2017) 8882–8885.
- [7] X. Qi, L. Lin, L. Shen, Z. Li, T. Qin, Y. Qian, X. Wu, X. Wei, Q. Gong, J. Shen, *Chemical Engineer*, 7 (2019) 11014–11023.
- [8] S.S. Babu, V.K. Praveen, A. Ajayaghosh, *Chemical reviews*, 114 (2014) 1973–2129.
- [9] P.L. Kuo, C.H. Tsao, C.H. Hsu, S.T. Chen, H.M. Hsu, *Journal of Membrane Science*, 499 (2016) 462–469.
- [10] P. Terech, R.G. Weiss, *Chemical reviews*, 97 (1997) 3133–3159.
- [11] D. Diaz Diaz, D. Kuhbeck, R.J. Koopmans, *Chemical Society Reviews*, 40 (2011) 427–448.
- [12] K.N. Hosbein, A.H. England, C.A. Price, T.L. Clare, *Electroanalysis*, 29 (2017) 1377–1387.
- [13] S.M. Mehta, T. Jin, I. Stanciulescu, K.J. Grande-Allen, *Acta Biomater.* 75 (2018) 52–62.
- [14] Q. Lin, T.-T. Lu, X. Zhu, B. Sun, Q.-P. Yang, T.-B. Wei, Y.-M. Zhang, *Chemical Communications*, 51 (2015) 1635–1638.
- [15] J. Gierschner, J. Cornil, H.J. Egelhaaf, *Advanced materials*, 19 (2007) 173–191.
- [16] S.J. Buwalda, T. Vermonden, W.E. Hennink, *Biomacromolecules*, 18 (2017) 316–330.
- [17] L.J. Smith, S.M. Taimoory, R.Y. Tam, A.E.G. Baker, N.B. Mohammad, J.F. Trant, M.S. Shoichet, *Biomacromolecules*, 19 (2018) 926–935.
- [18] Y. Zhao, S. Song, X. Ren, J. Zhang, Q. Lin, Y. Zhao, *Chemical reviews*, 122 (2022) 5604–5640.
- [19] S. Saha, E.-M. Schon, C. Cativiela, D. Diaz, R. Banerjee, *Chemistry – A European Journal*, 19 (2013) 9562–9568.
- [20] H.B. Aiyappa, S. Saha, P. Wadge, R. Banerjee, S. Kurungot, *Chemical Science*, 6 (2015) 603–607.

- [21] S. Dhibar, A. Dey, S. Majumdar, D. Ghosh, A. Mandal, P.P. Ray, B. Dey, Dalton Transactions, 47 (2018) 17412–17420.
- [22] V. Kumar, R.K. Upadhyay, D. Bano, S. Chandra, D. Kumar, S. Jit, S.H. Hasan, New Journal of Chemistry, 45 (2021) 6273–6280.
- [23] P.K. Yadav, R.K. Upadhyay, D. Kumar, D. Bano, S. Chandra, S. Jit, S.H. Hasan, New Journal of Chemistry, 45 (2021) 12549–12556.
- [24] S. Majumdar, A. Dey, R. Sahu, S. Dhibar, P.P. Ray, B. Dey, ACS Applied Nano Materials, 3 (2020) 11025–11036.
- [25] S. Majumdar, P.P. Ray, R. Sahu, A. Dey, B. Dey, International Journal of Biological Macromolecules, 195 (2022) 287–293.
- [26] P. Grondin, O. Roubeau, M. Castro, H. Saadaoui, A. Colin, R. Clerac, Langmuir, 26 (2010) 5184–5195.
- [27] A.R. Hirst, B. Escuder, J.F. Miravet, D.K. Smith, Angewandte Chemie International Edition, 47 (2008) 8002–8018.
- [28] S. Majumdar, T. Singha, S. Dhibar, A. Mandal, P.K. Datta, B. Dey, ACS Applied Electronic Materials, 2 (2020) 3678–3685.
- [29] G. Lepcha, T. Singha, S. Majumdar, A.K. Pradhan, K.S. Das, P.K. Datta, B. Dey, Dalton Transactions, 51 (2022) 13435–13443.
- [30] S. Majumdar, B. Pal, R. Sahu, K.S. Das, P.P. Ray, B. Dey, Dalton Transactions. 51 (2022) 9007–9016.
- [31] A. Dey, S. Sil, S. Majumdar, R. Sahu, M. Ghosh, G. Lepcha, P.P. Ray, B. Dey, Journal of Physics and Chemistry of Solids, 160 (2022) 110300.
- [32] S. Chandra, V.K. Singh, P.K. Yadav, D. Bano, V. Kumar, V.K. Pandey, M. Talat, S.H. Hasan, Analytica Chimica Acta, 1054 (2019) 145–156.
- [33] S. Dhibar, A. Dey, D. Ghosh, S. Majumdar, A. Dey, P.P. Ray, B. Dey, ACS Omega, 5 (2020) 2680–2689.
- [34] S. Majumdar, S. Sil, R. Sahu, M. Ghosh, G. Lepcha, A. Dey, S. Mandal, P.P. Ray, B. Dey, Journal of Molecular Liquids, 338 (2021) 116769.
- [35] J.L. Drury, D.J. Mooney, Biomaterials, 24 (2003) 4337–4351.
- [36] A. Harada, R. Kobayashi, Y. Takashima, A. Hashidzume, H. Yamaguchi, Nature Chemistry, 3 (2011) 34–37.



- [37] T. Park, S.C. Zimmerman, *Journal of the American Chemical Society*, 128 (2006) 11582–11590.
- [38] J.R. Moffat, G.J. Seeley, J.T. Carter, A. Burgess, D.K. Smith, *Chemical Communications*, 38 (2008) 4601–4603.
- [39] D. Magana, S.C. Perera, A.G. Harter, N.S. Dalal, G.F. Strouse, *Journal of the American Chemical Society*, 128 (2006) 2931–2939.
- [40] P. Dastidar, S. Ganguly, K. Sarkar, *Chemistry—An Asian Journal*, 11 (2016) 2484–2498.
- [41] L. Xu, Y.-U. Kwon, B. d. Castro, L. Cunha-Silva, *Crystal Growth & Design*, 13 (2013) 1260–1266.
- [42] E.N. Cook, C.W. Machan, *Chemical Communications*, 58 (2022) 11746–11761.
- [43] Z. Liu, F. Cao, M. Wang, M. Wang, L. Li, *Angewandte Chemie International Edition*, 59 (2020) 4161–4167.
- [44] C.-I. Shih, Y.-C. Chou, H.-Y. Chen, K.-H. Chen, I.-H. Wang, Y.-C. Yeh, *ACS Applied Bio Materials*, 3 (2020) 2516–2521.
- [45] S.N. Tambat, P.K. Sane, S. Suresh, N. Varadan O, A.B. Pandit, S.M. Sontakke, *Advanced Powder Technology*, 29 (2018) 2626–2632.
- [46] R. Lv, J. Wang, Y. Zhang, H. Li, L. Yang, S. Liao, W. Gu, X. Liu, *Journal of Materials Chemistry A*, 4 (2016) 15494–15500.
- [47] W. Bai, G. Qin, J. Wang, L. Li, Y. Ni, *Dyes and Pigments*, 193 (2021) 109473.
- [48] X. Meng, H.-F. Wang, H. Chen, Z.-Y. Zhou, H.-N. Wang, *Functional Materials Letters*, 11 (2018) 1850027.
- [49] T. Ladrak, S. Smulders, O. Roubeau, S.J. Teat, P. Gamez, J. Reedijk, *European Journal of Inorganic Chemistry*, 2010 (2010) 3804–3812.
- [50] T.K. Vo, V.N. Le, V.C. Nguyen, M. Song, D. Kim, K.S. Yoo, B.J. Park, J. Kim, *Journal of Industrial and Engineering Chemistry*, 86 (2020) 178–185.
- [51] J.I. Lovitt, C.S. Hawes, A.D. Lynes, B. Haffner, M.E. Möbius, T. Gunnlaugsson, *Inorganic Chemistry Frontiers*, 4 (2017) 296–308.
- [52] S. Dhibar, A. Dey, A. Dey, S. Majumdar, D. Ghosh, P.P. Ray, B. Dey, *ACS Applied Electronic Materials*, 9 (2019) 1899–1908.
- [53] S. Dhibar, A. Dey, S. Majumdar, P.P. Ray, B. Dey, *International Journal of Energy Research*, 45 (2021) 5486–5499.

- [54] S. Majumdar, G. Lepcha, R. Sahu, B. Dey, *Journal of Physics and Chemistry of Solids*, 170 (2022) 110903.
- [55] S. Majumdar, A. Dey, R. Sahu, G. Lepcha, A. Dey, P.P. Ray, B. Dey, *Materials Research Bulletin*, 157 (2023) 112003.
- [56] B. Pal, P. Das, J. Datta, U. Gangopadhyay, P.P. Ray, *Materials Science in Semiconductor Processing*, 162 (2023) 107535.
- [57] S. Halder, B. Pal, A. Dey, S. Sil, P. Das, A. Biswas, P.P. Ray, *Materials Research Bulletin*, 118 (2019) 110507.
- [58] S. Cheung, N. Cheung, *Applied Physics Letters*, 49 (1986) 85–87.
- [59] R. Jana, J. Datta, S. Sil, A. Dey, B. Pal, A. Biswas, P.P. Ray, *Materials Research Express*, 6 (2019) 1050d1.
- [60] M. Şahin, H. Durmuş, R. Kaplan, *Applications of Surface Science*, 252 (2006) 6269–6274.
- [61] W. den Boer, *Journal de Physique, Colloque*, 42 (1981) C4-451–C4-454.
- [62] F. Yakuphanoglu, W.A. Farooq, *Materials Science in Semiconductor Processing*, 14 (2011) 207–211.
- [63] P. Das, B. Pal, J. Datta, M. Das, S. Sil, P.P. Ray, *Journal of Physics and Chemistry of Solids*, 148 (2021) 109706.

\*\*\*



*"Nothing in life is to be feared, it is only to be understood. Now is the time to understand more, so that we may fear less."*

- Marie Curie



# Chapter 4

---

**Comparative outcomes of the voltage-dependent current density, charge transportation and rectification ratio of electronic devices fabricated using mechanically flexible supramolecular networks**

## Abstract

In this study, I report the synthetic method of two distinct supramolecular metallogels, namely Mn-BDA and Cd-BDA, using Mn(II) acetate tetrahydrate, Cd(II) acetate dihydrate and butane-1,4-dicarboxylic acid (BDA). DMF, a polar aprotic solvent, was immobilized in both metallogel-networks for their synthesis. The metallogelation of Mn-BDA was successfully attained through the instant mixing of a Mn(II)-source and BDA in DMF solvent media. By applying ultrasonication, a Cd-BDA metallogel was prepared. The stoichiometry of gel-forming components concerning metal salts and the LMWG are accountable to obtain respective stable metallogels. Rheological parameters such as storage modulus ( $G'$ ) and loss modulus ( $G''$ ) explored the mechanical flexibility of the synthesized metallogels through amplitude and angular frequency sweep experiments. Both the metallogels possess significant mechanical stability, which was determined by monitoring diverse gel-to-sol transition shear strain values ( $\gamma\%$ ). Distinctive morphological visualizations of both of these metallogels (i.e., Mn-BDA and Cd-BDA) were made via field emission scanning electron microscopic (FESEM) studies, demonstrating a fibrous inter-connected network with a hierarchical self-assembled arrangement for Mn(II)-based metallogels and a typical stacked-flake-like association with hierarchical motifs for Cd(II)-based metallogels. EDAX elemental mapping substantiated the presence of metallogel-forming agents such as individual metal acetate salts, BDA acting as a low-molecular weight gelator, and gel-immobilized solvents such as DMF. Furthermore, Fourier transform infrared spectroscopy and ESI-mass spectroscopy were performed for both these supramolecular metallogels. FT-IR spectroscopic and ESI-mass spectroscopic results clearly substantiate the possible non-covalent supramolecular interactions among basic molecular repeating moieties, i.e., butane-1,4-dicarboxylic acid (the low-molecular weight gelator), individual metal salts and gel-immobilized polar aprotic solvent DMF for the construction of distinct stable supramolecular metallogel-systems. The semiconducting property of the fabricated metallogels was investigated. Two Schottky diodes (SDs) composed of ITO/Cd-BDA/Al and ITO/Mn-BDA/Al in a sandwich pattern with Al serving as the metal electrode were fabricated. Both these metallogel-based devices effectively offer significant semiconducting diode features with nonlinear J–V characteristics. The non-ohmic conduction protocol of the fabricated metallogel-based devices was explored. Mn-BDA and Cd-BDA metallogel-based fabricated devices have rectification

ratios of 6.67 and 23.50, respectively. The gel-based diode performances were examined by observing the voltage-dependent current density, charge transportation and rectification ratio.

## 4.1. Introduction

Natural gels are highly valued in science and technology [1]. Gel is the gift of serendipity acquired through chemical interactions [2, 3]. Gels can be primarily identified using the inversion vial test of soft-scaffolds, in which the inversion stabilities of semi-solid materials against gravity are being established [4]. According to the International Union of Pure and Applied Chemistry, gel is defined as a nonfluid colloidal/polymer network with the ability to expand [5]. Rheologically, it has been found that gels can display the properties of both solids and liquids and are also termed visco-elastic materials [6]. It is evident from the research arena focusing on gel-scaffolds that these are principally made of gelators with low amounts of gelling materials and gel-immobilized suitable pure or mixed solvent-media. The gel-forming solvent is typically a large amount of trapped liquid responsible for the formation of a mechanically flexible 3D soft-network [6]. If a gel network is constructed through non-covalent interactions, then physical gels or supramolecular gels are formed [6]. Gels can be further classified into hydrogels and organogels on the basis of gelling solvents, including polar to non-polar and protic to aprotic features. If the gelling media is water or an aqueous solvent environment, then the corresponding gel is considered a hydrogel. Furthermore, for organogels, the gelling solvent falls under the organic category. However, if the gelator undergoes gelation with both aqueous and organic solvents, then such gelators are called ambidextrous gelators [7]. Non-covalent interaction-directed supramolecular gels are manifested through implementing versatile interactions including van der Waals, hydrogen bonding, dipole–dipole, ion–dipole, ion–ion,  $\pi$ – $\pi$ , cation– $\pi$ , and anion– $\pi$  [8].

Gels having vast applications over a miscellaneous region of materials science are effective for catalysis, magnetic materials, optical activity, conductivity, optoelectronic devices, energy storage, charge transportation, photo physics, lithography, actuators, nano electronics and nano science, tissue engineering, drug delivery, medical diagnostics, cosmetics, foods, bio mineralization environment, etc. [9–13]. One of the prominent classes of exploring supramolecular gels is the metallogelation protocol. The first reported attempt of metallogelation was a lithium urate-derived hydrogel formation strategy [14]. In metallogels, the 3D flexible-network, entrapping appropriate solvents, is made by the non-covalent interactions mainly hydrogen bonding as well as metal–ligand coordination between metal ions/salts and gelators



[15]. The presence of metal ions in the metallogel influences a wide range of functionalities, e.g. catalytic activity [16], semiconducting opto-electronic diode fabrication [17,18], non-linear optical device [19], magnetism [20], antipathogenic effect [21,22], proton-conduction [23], tissue engineering [24,25], and transportation of drug [26–29]. The role of low-molecular weight gelators, particularly involved in the origination of supramolecular metallogel systems, is really fascinating to get functionally intriguing metallogels using organic gelators such as aliphatic type (monoethanolamine, suberic acid, sebacic acid, adipic acid, itaconic acid, citraconic acid, etc.) [13, 30–32] and aromatic type (nitroterephthalic acid, aminoterephthalic acid, bipyridine, terephthalic acid, etc.) [33–35].

The use of particular mechanical behaviours such as toughness, flexibility, elasticity, thermo reversibility, and notably thixotropic features of synthesized supramolecular gels in diverse applications for offering advanced technology has not been systematically explored till date [1–4, 6, 36]. The proper implementation of self-repairing supramolecular gel and metallogel materials in the domain of fabricating sophisticated technical devices is extremely urgent in contemporary period [22, 32]. The auto-restoration of performances of self-healing gel-based devices after mechanical damage may play a significant role in preparing classy functional entities including photo-responsive diodes [34, 37], higher order NLO devices [30, 38], and ion conducting materials [39, 40]. Even the approach of research in self-healing gel-based bio-active systems might be tremendously effective toward bio-technological outlook [38, 41]. The prospect of having a transistor application  $\pi$ -ion gel as the supramolecular material is reported to perform as the active layer and gate capacitor, exhibiting large transconductance [42]. Influenced by this up-to-date research, I am trying to obtain more spaces in the literature for acquiring the metallogel-based devices applicable for scientific and technological uses to have advanced functional materials with utmost flexibility. In this context, the fabrication of semiconducting devices with self-restoring capacity is really a challenging attempt for next generation. Usually, silicon-based materials are highly esteemed in fabricating diodes with versatile applicability [43–47]. The role of germanium-based diodes is also noteworthy in material research [44, 45, 47, 48]. Besides, the importance of metal oxide-based diodes is reported in the literature [49, 50]. Uniquely, achieving proficient diode performances with mechanically flexible semiconducting materials is really exciting in the field of science and technology. I am highly engaged to offer

such flexible material-based device fabrication [22, 32, 51]. In this content, the significance of mechanically flexible supramolecular gel-based devices earns special interest.

Through my current endeavour I have tried to accomplish butane-1,4-dicarboxylic acid-directed formation of supramolecular Mn(II) and Cd(II)-metallogels and to unveil several metallogel-related features such as rheological, morphological and mechanistic strategies, using spectroscopic outcomes. Regarding the exploration of metallogel-based functional devices, I attempted to study the voltage-dependent current density, charge transportation, and rectification ratio of metallogel-based fabricated diodes. The non-ohmic conduction mechanism of supramolecular metallogel-directed devices has been exhaustively studied through the attempt. Hoping to achieve suitable materialistic applications, I feel that the study will be beneficial toward the advancement of mechanically flexible-type material-based device fabrication for technological appliances.

## **4.2. Experimental Section:**

### **4.2.1. Materials**

Cadmium(II) acetate dihydrate, manganese(II) acetate tetrahydrate metal salts and butane-1,4-dicarboxylic acid (BDA) were purchased from Sigma-Aldrich chemicals and utilized in experiments. *N, N'*-Dimethylformamide (DMF), acetone, chloroform, ethyl acetate, benzene, ethanol, tetrahydrofuran (THF), methanol, acetic acid, acetonitrile, petroleum ether, and dichloromethane (DCM) were also taken from Sigma-Aldrich chemicals and consumed as solvents during experiments.

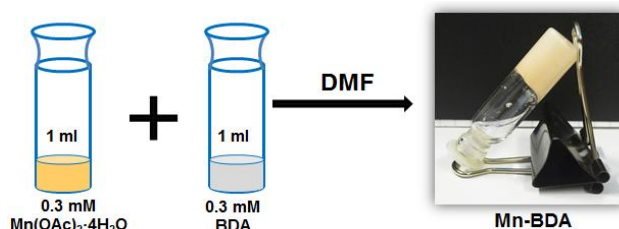
### **4.2.2. Characterizations**

Preliminarily metallogels were characterized through the inversion of vial visualizations. Microstructural images and elemental mapping were investigated using a ZEISS GeminiSEM 450 (Gemini 2) and EDAX instrument. A Malvern, KINEXUS Pro+ rheometer with an 8 mm parallel plate was used for the rheological study of metallogel systems. The FT-IR experimental data collection was accomplished using a PerkinElmer Fourier transform infrared spectrometer. ESI mass spectral analyses were performed using an Agilent Q-TOF mass spectrometer. The current–voltage measurements of the Schottky device made-up with metallogel were carried out using a Keithley 2635B source meter.

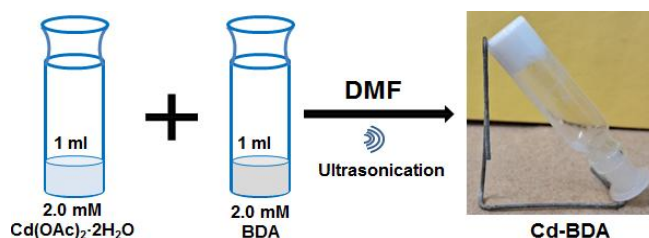
### 4.2.3. Synthesis method of Mn-BDA and Cd-BDA metallogels

Butane-1,4-dicarboxylic acid (BDA)-based Mn-BDA and Cd-BDA metallogels were synthesized through the direct mixing of DMF solutions of individual metal acetate salts and butane-1,4-dicarboxylic acid used as the low-molecular weight gelating agent. The metallogel-forming chemical constituents with suitable stoichiometric ratios (*i.e.*, Mn(II) acetate tetrahydrate (0.3 mM, 73.6 mg) and BDA (0.3 mM, 43.9 mg)) were independently dissolved in 1 ml DMF solutions. Instant formation of Mn-BDA metallogels was established through the direct mixing of the solutions of Mn(II) acetate tetrahydrate and BDA in a glass-vial.

Similarly, for Cd-BDA metallogels, 1 ml DMF solutions of Cd(II) acetate dihydrate (2.0 mM, 533.1 mg) and BDA (2.0 mM, 292.3 mg) were separately prepared in a glass vial. Off-white coloured Cd-BDA metallogels were obtained *via* ultra-sonication of the mixture having Cd(II) acetate dihydrate and BDA in a DMF solvent medium for ~1 hour. These two metallogels remained stable for few months under ordinary atmospheric conditions. The inversion-vial test for individual cases was executed for the preliminary investigation of the gel-like behaviour of Mn-BDA and Cd-BDA metallogels (see Schemes 4.1 and 4.2 for the synthetic protocol of Mn-BDA and Cd-BDA metallogels, respectively).



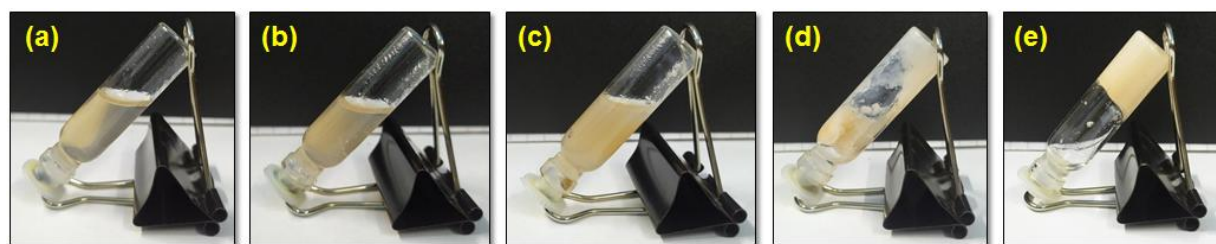
**Scheme 4.1: Synthetic scheme of the Mn-BDA metallogel in a DMF solvent medium.**



**Scheme 4.2: Synthetic approach of the Cd-BDA metallogel in a DMF solvent medium.**

#### 4.2.4. Minimum critical gelation (MCG) concentration of Mn-BDA and Cd-BDA metallogels

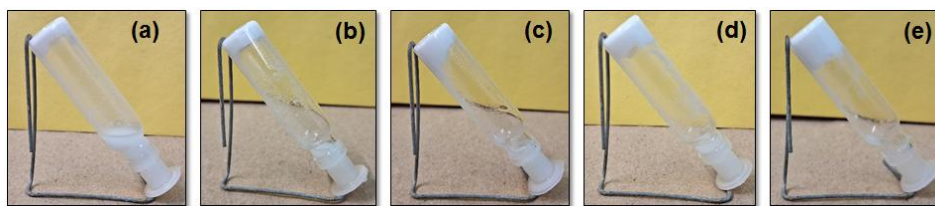
Minimum critical gelation (MCG) concentration for a gel-material is the minimum concentration at which the finest quality gel-scaffold is formed. This experiment was executed for both fabricated Mn-BDA, and Cd-BDA metallogels. The concentrations of the individual metal acetate salts and BDA were varied in static amount of DMF solvent with fixed stoichiometry. Experimental outcomes establish that the premium quality Mn-BDA metallogel was obtained when the concentrations of Mn(II) acetate salt and BDA were maintained as  $73.6 \text{ mg ml}^{-1}$  (0.3 mM) and  $43.9 \text{ mg ml}^{-1}$  (0.3 mM), respectively in a DMF medium. It was initially confirmed through the inversion of vial test (Fig. 4.1 and Table 4.1). Following the identical optimized environment, the minimum critical gelation (MCG) concentration for the Cd-BDA metallogel was achieved at the requisite concentration level of Cd(II) acetate-salt (*i.e.*, [Cd(II) acetate dihydrate] =  $533.1 \text{ mg ml}^{-1}$ , and [butane-1,4-dicarboxylic acid] =  $292.3 \text{ mg ml}^{-1}$ ) (Fig. 4.2 and Table 4.2).



**Fig. 4.1: Determination of Minimum Critical Gelation Concentration (MCG) of the Mn-BDA metallogel with step-wise photography (a-e) of Mn-BDA metallogel-forming chemical constituents having varied concentrations.**

**Table 4.1: Determination of Minimum Critical Gelation Concentration of the Mn-BDA.**

Serial No.	[Mn(OAc) <sub>2</sub> ·4H <sub>2</sub> O] (in 1 ml DMF)	[BDA] (in 1 ml DMF)	Phase
1	12.3 mg/ml	7.3 mg/ml	Sol
2	19.6 mg/ml	11.7 mg/ml	Sol
3	24.5 mg/ml	14.6 mg/ml	Viscous sol
4	49.1 mg/ml	29.3 mg/ml	Weak gel
5	73.6 mg/ml	43.9 mg/ml	Gel

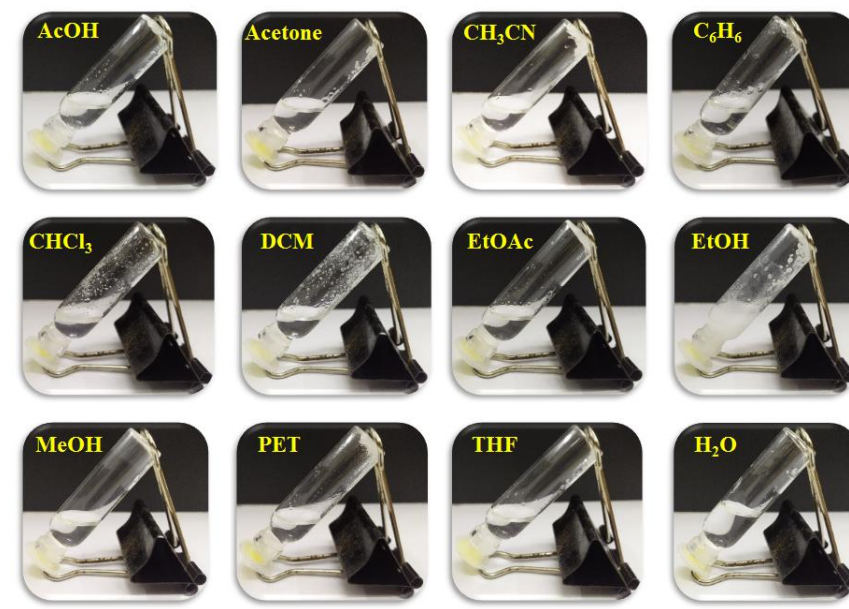


**Fig. 4.2:** Determination of Minimum Critical Gelation Concentration of the Cd-BDA metallogel with step-wise photography of Cd-BDA metallogel-forming chemical constituents having varied concentrations.

**Table 4.2:** Determination of Minimum Critical Gelation Concentration of the Cd-BDA.

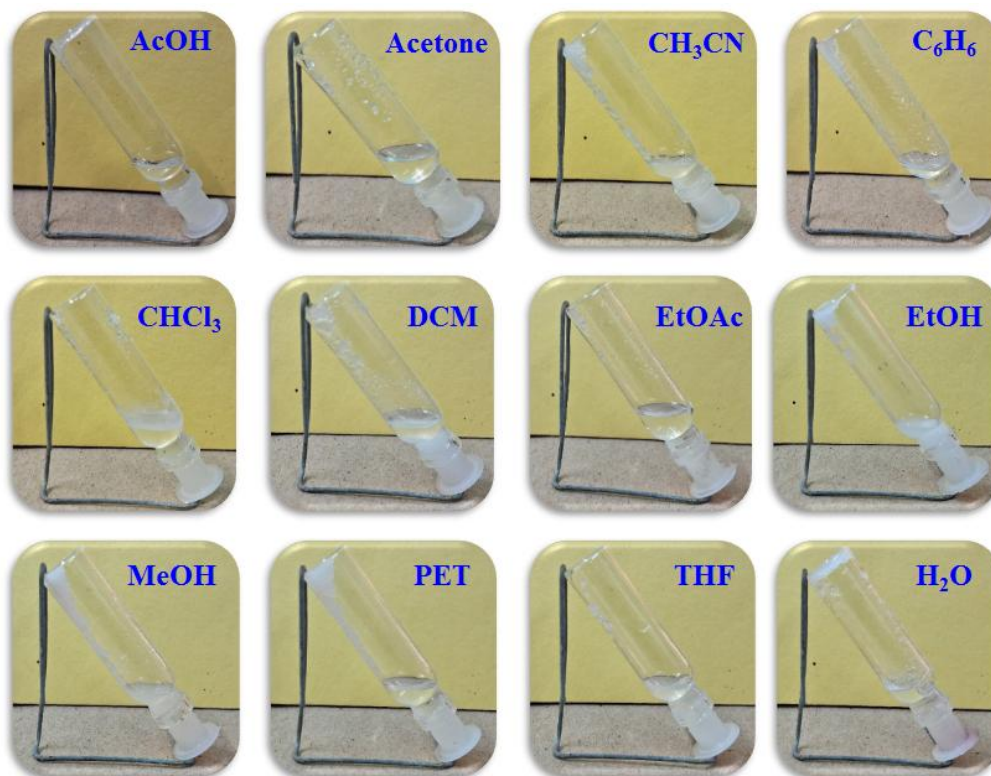
Serial No.	[Cd(OAc) <sub>2</sub> ·2H <sub>2</sub> O] (in 1 ml DMF)	[Gelator] (in 1 ml DMF)	Phase
1	266.5 mg/ml	146.2 mg/ml	Sol
2	319.8 mg/ml	175.4 mg/ml	Viscous Sol
3	399.8 mg/ml	219.2 mg/ml	Viscous sol
4	453.1 mg/ml	248.5 mg/ml	More viscous sol
5	533.1 mg/ml	292.3 mg/ml	Gel

#### 4.2.5. Inspecting the trend of Mn-BDA, and Cd-BDA metallogel formation in diverse solvent media



**Fig. 4.3:** Role of versatile solvents in forming stable metallogel of Mn-BDA.

Metallogelation capability of metallogel-forming ingredients was experimentally investigated in a wide range of solvent media ranging from polar to non-polar type. The study revealed that the polar aprotic-type solvent DMF is the most favourable solvent and gets indigenously entrapped in a stable network of metallogel soft-scaffolds, contributed by the distinct metal acetate salt and the gelator molecule of BDA. The trend of Mn-BDA and Cd-BDA metallogel formation in diverse solvent media was also critically investigated through these studies involving several solvent systems (Fig. 4.3 and 4.4). Non-covalent supramolecular interactions acting within the LMWG [13,30–32] (i.e., butane-1,4-dicarboxylic acid) and particular metal acetate sources become exclusively effective through the contribution of polar aprotic-type solvents such as DMF as the metallogel-constituting optimum solvent medium to have a stable gel-network of Mn-BDA and Cd-BDA. The polar aprotic solvent DMF is a vital agent for synthesizing LMWG-directed individual metallogels using non-covalent supramolecular interactions[18,19,30–32], resulting in built inter-linked three-dimensional metallogel systems as experimentally tested through rheological, spectroscopic, and morphological investigations.

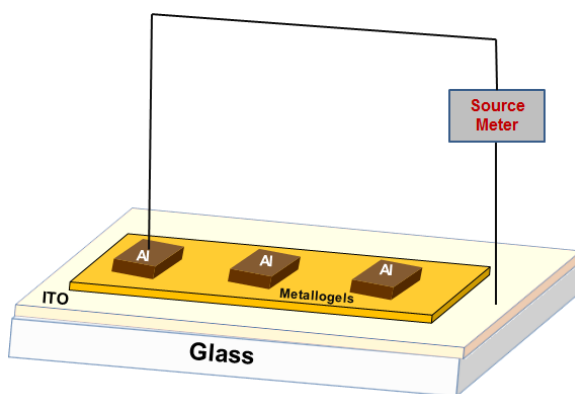


**Fig. 4.4:** Role of versatile solvents in forming stable metallogel of Cd-BDA.



#### 4.2.6. Device Fabrication and Characterization

Two ITO (indium tin oxide)-coated glass materials were washed in an ultrasonic bath for 10 minutes each using acetone, isopropyl alcohol (IPA) and DI water. Following the cleaning procedure, thin films of synthetic gel compounds (film thickness  $\sim 1\ \mu\text{m}$ ) were applied to the front surfaces of two ITO-coated glasses. Finally, two Schottky diodes (SDs) comprising ITO/Cd-BDA/Al and ITO/Mn-BDA/Al in a sandwich pattern with Al serving as the metal electrode were synthesized using the synthesized samples (Scheme 4.3). The Al electrodes' surface area was kept constant at  $7.065 \times 10^{-6}\ \text{m}^2$ . A Keithley 2635B source metre interfaced with a PC was used to measure the current–voltage of the constructed devices using Cd-BDA and Mn-BDA, while they were in the darkness and operating in the range from  $-1\ \text{V}$  to  $+1\ \text{V}$  at room temperature.



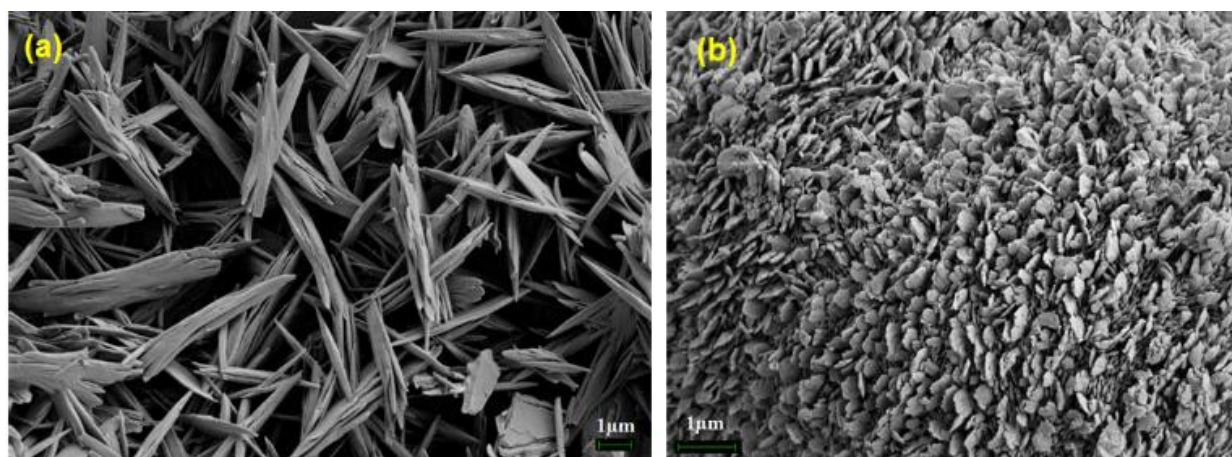
**Scheme 4.3: Semiconducting diode fabrication (ITO/metallogels (i.e., Mn-BDA, and Cd-BDA)/Al sandwich pattern).**

### 4.3. Results and discussion

#### 4.3.1. FESEM Microstructural and EDAX Elemental Studies

The morphological organization of the xerogel sample of Mn-BDA was uncovered by the use of FESEM images. FESEM microstructural vision (Fig. 4.5a) depicts the inter-linked fibrous network with self-assembled structural patterns in the metallogel systems. The self-assembled relatively elongated fibers with the average length of few micrometers within the xerogel-

network were experientially visualized. The active participation of metal acetate salts with conjugated organic counter anions and BDA-based association with a suitable solvent medium (*i.e.*, DMF) lead to the formation of LMWG-dominated supramolecular 3D soft-scaffolds, where the dicarboxylic acid parts of BDA with appropriate metal source in DMF prevailed to achieve the gel-structure having utmost mechanical flexibility. A critical insight of hierarchical type fibrous morphology was gained through FESEM images (Fig. 4.5a). The effectiveness of metallogel-forming chemical constituents was examined by EDS elemental analyses (Fig. 4.6), confirming the presence of diverse gel-forming elements such as C, N, O, and Mn in the Mn-BDA metallogel. The direct impact of the metallogel-forming gel constituents on the formation of Mn-BDA metallogels was systematically explored..



**Fig. 4.5: FESEM morphological patterns of (a) Mn-BDA, and (b) Cd-BDA.**

The highly systematic hierarchical morphology with regular-type stacked-flake arrangement was visualized through the FESEM analysis of the xerogel state of Cd-BDA metallogels. The self-assembled and highly compact microstructural patterns with inter-connected flakes having the extension of almost sub-micrometer range are critically accountable for offering the stable metallogel structure of Cd-BDA (Fig. 4.5b). The dicarboxylic acid moieties of BDA provides a critical insight into the non-covalent supramolecular interactions with the metal acetate salt of Cd(II) in DMF solvent media and, in a combined way, these are directed to achieve the self-assembled metallogel structure of Cd-BDA. The use of metallogel-forming chemical sources was inspected by EDS elemental analyses (Fig. 4.7), confirming the presence of diverse gel-forming



elements such as C, N, O, and Cd of Cd-BDA metallogels. The straight control of the metallogel-forming ingredients to build Cd-BDA metallogels was systematically revealed. Through EDS elemental analyses (Fig. 4.6 and 4.7 for Mn-BDA and Cd-BDA, respectively), it was found that the presence of ‘N’ elements in both of these metallogels (*i.e.*, Mn-BDA and Cd-BDA) implies the role of the DMF polar aprotic solvents in the formation of stable metallogel structures for Mn-BDA and Cd-BDA.

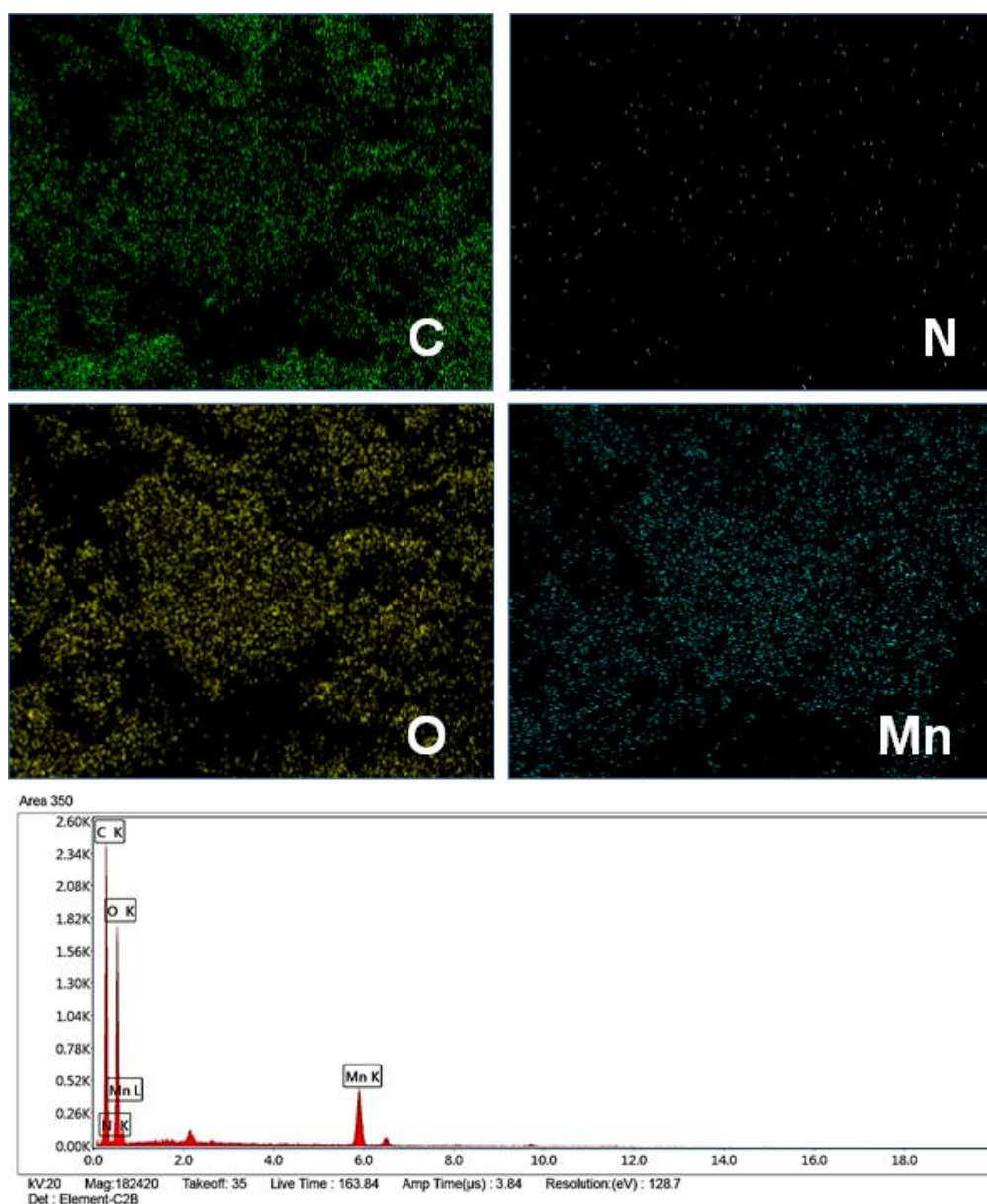
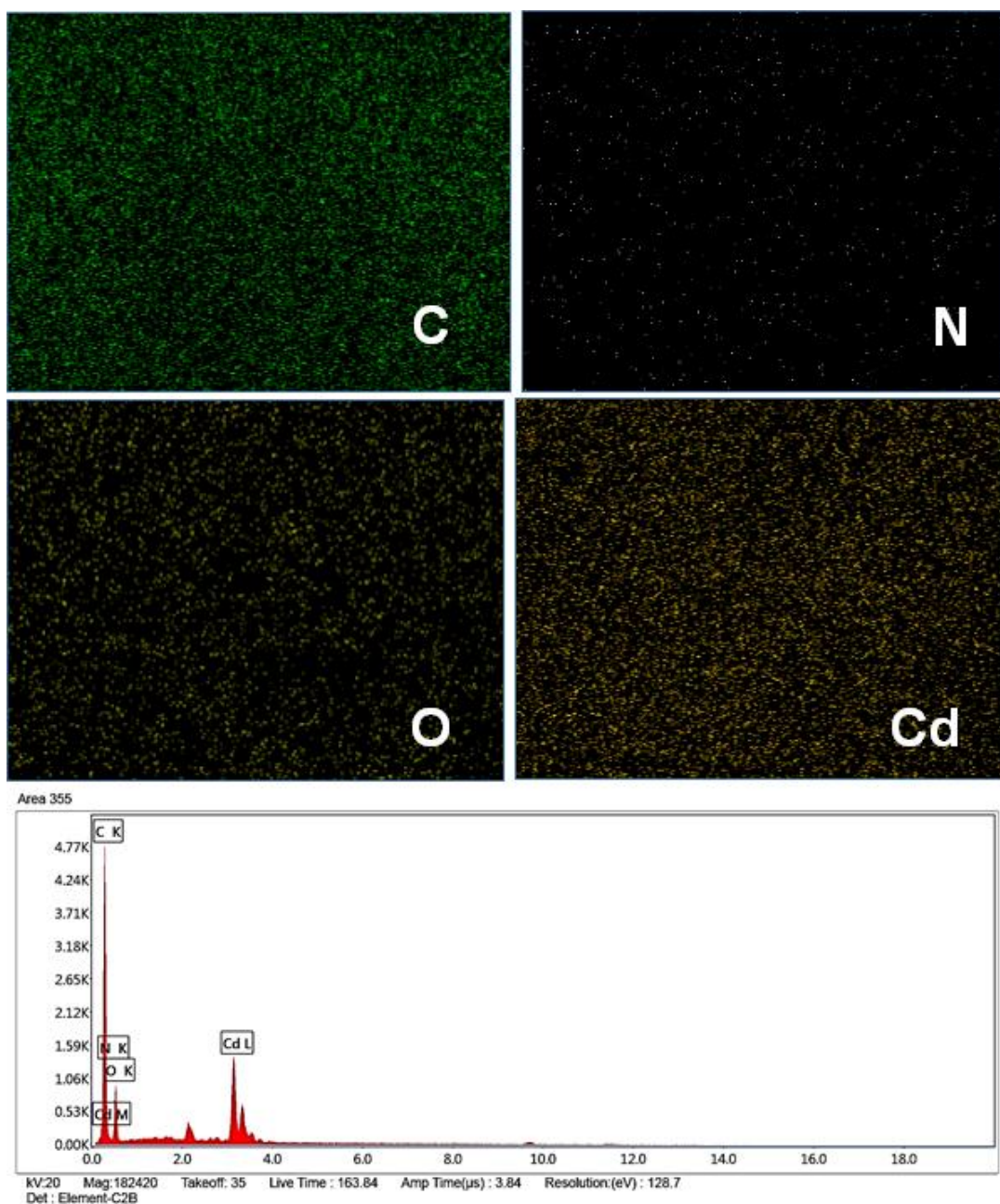


Fig. 4.6: EDAX elemental mapping with spectrum of Mn-BDA metallogel.

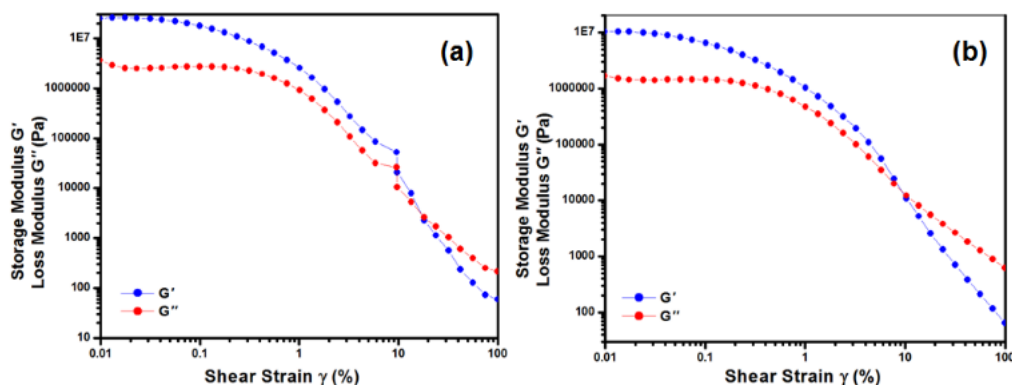


**Fig. 4.7.** EDAX elemental mapping with spectrum of Cd-BDA metallogel.

### 4.3.2. Rheological characterizations of Mn-BDA, and Cd-BDA metallogels

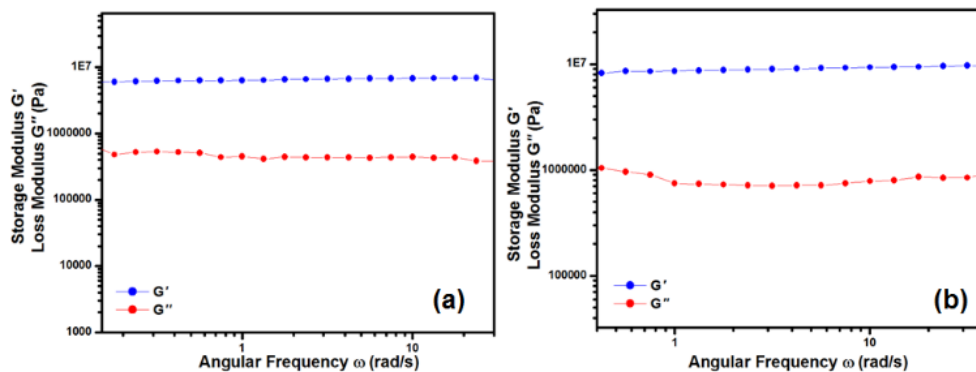
Stability against the mechanical distress of flexible semi-solid supramolecular soft-scaffolds was extensively investigated using a Malvern, KINEXUS Pro+ rheometer. The experiment was

carried out for both Mn-BDA and Cd-BDA metallogels through the gradual increment of the shear strain ( $\gamma\%$ ) from 0.01% to 100% at a fixed angular frequency ( $\omega$ ) of  $10 \text{ rad s}^{-1}$ . At the beginning of the experiment, the storage modulus ( $G'$ ) predominates over the loss modulus ( $G''$ ), and this is a signature of best quality gel. With the progression of experiments, the storage modulus ( $G'$ ) progressively decreases until it crossed over by the loss modulus ( $G''$ ), causing the larger  $G''$  value than  $G'$  (*i.e.*,  $G'' > G'$ ), which indicates the gel-to-sol transition phenomena [18, 19]. This crossover point was observed at 16.84% of the shear strain ( $\gamma\%$ ) for Mn-BDA and 9.29% of the shear strain ( $\gamma\%$ ) in case of Cd-BDA metallogels (Fig. 4.8a and b). These data verify that, in terms of rheological aspects, the Mn-BDA metallogel is rheologically superior.



**Fig. 4.8. Strain sweep rheological test of (a) Mn-BDA, and (b) Cd-BDA metallogels.**

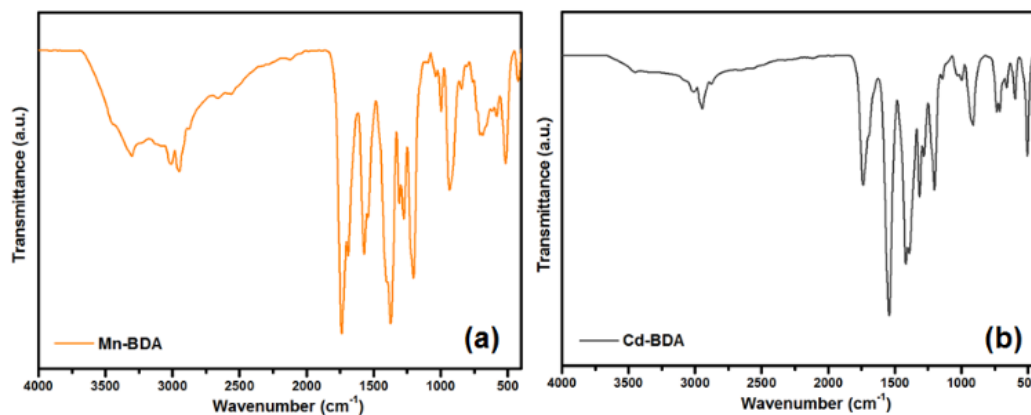
Moreover, the frequency sweep experiment was accomplished to visualize the viscoelastic nature of both metallogel samples. Experimentation was done within an angular frequency ( $\omega$ ) array of  $100 \text{ rad s}^{-1}$  to  $0.1 \text{ rad s}^{-1}$  with the application of constant 0.01% shear strain ( $\gamma\%$ ). No entanglement effect was observed within this experimental angular frequency range (Fig. 4.9a and b), *i.e.*, the storage modulus ( $G'$ ) and loss modulus ( $G''$ ) run parallel to each other, which signifies the dominant viscoelastic nature of the synthesized Mn-BDA and Cd-BDA metallogels within the applied angular frequency range (*i.e.*,  $100 \text{ rad s}^{-1}$  to  $0.1 \text{ rad s}^{-1}$ ) [22, 30, 51-55].



**Fig. 4.9:** Angular frequency sweep rheological measurement of (a) Mn-BDA, and (b) Cd-BDA metallogels.

### 4.3.3. FT-IR spectroscopic study of the synthesized Mn-BDA, and Cd-BDA metallogels

The strategy of metallogel construction of Mn-BDA and Cd-BDA *via* versatile non-covalent supramolecular interactions, interplaying within distinct metal(II) acetate salts and BDA ligands in DMF as the polar aprotic solvent medium under ordinary environmental condition, was comprehensively studied by FT-IR spectroscopy. The experimental outcomes evidentially approve the active participation of the non-covalent-type supramolecular interactions throughout the soft-scaffolds of individual metallogels. The comparison of significant FT-IR stretching frequencies of the xerogel form of Mn-BDA and Cd-BDA metallogel samples is tabulated in Table 4.3 and Fig. 4.10a (for Mn-BDA) and Fig. 4.10b (for Cd-BDA).



**Fig. 4.10:** FT-IR spectra of xerogel samples: (a) Mn-BDA, and (b) Cd-BDA metallogels.

**Table 4.3: FT-IR stretching frequency of the xerogel samples of Mn-BDA, and Cd-BDA metallogels.**

<b>Mn-BDA</b>		<b>Cd-BDA</b>	
<b>Modes of Vibration</b>	<b>Wavenumber (in cm<sup>-1</sup>)</b>	<b>Modes of Vibration</b>	<b>Wavenumber (in cm<sup>-1</sup>)</b>
$\nu(\text{OH})$	3305	$\nu(\text{OH})$	3451
$\nu(\text{alkyl C-H})$	2950	$\nu(\text{alkyl C-H})$	2947
$\nu(\text{CO})$	1739	$\nu(\text{CO})$	1739
$\nu_a(\text{COO})$	1572	$\nu_a(\text{COO})$	1543
$\nu_s(\text{COO})$	1374	$\nu_s(\text{COO})$	1419
$\nu(\text{acyl C-O})$	1276	$\nu(\text{acyl C-O})$	1203
$\nu(\text{CN})$	935	$\nu(\text{CN})$	913
$\nu(\text{OCN})$	687	$\nu(\text{OCN})$	713
$\nu(\text{Mn-O})$	517	$\nu(\text{Cd-O})$	505

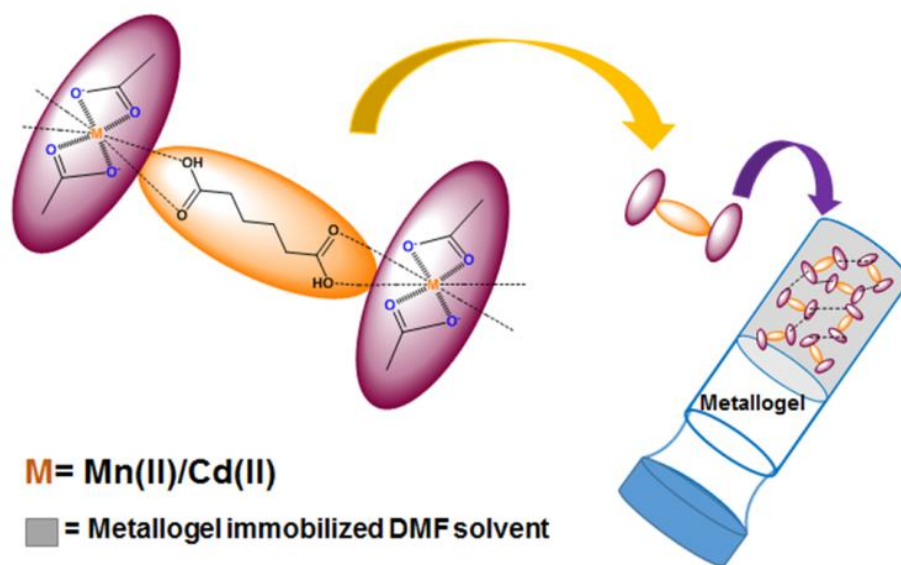
For Mn-BDA, different IR-stretching frequencies including  $\nu(\text{OH})$ ,  $\nu(\text{alkyl C-H})$ ,  $\nu(\text{CO})$ ,  $\nu_a(\text{COO})$ ,  $\nu_s(\text{COO})$ ,  $\nu(\text{acyl C-O})$ ,  $\nu(\text{CN})$ ,  $\nu(\text{OCN})$ , and  $\nu(\text{Mn-O})$  are shifted to lower values with respect to the pure gel-forming constituents such as  $\text{Mn}(\text{OAc})_2 \cdot 4\text{H}_2\text{O}$  as metal sources and butane-1,4-dicarboxylic acid as the LMWG [30, 33]. Similarly, the values of IR-stretching frequencies such as  $\nu(\text{OH})$ ,  $\nu(\text{alkyl C-H})$ ,  $\nu(\text{CO})$ ,  $\nu_a(\text{COO})$ ,  $\nu_s(\text{COO})$ ,  $\nu(\text{acyl C-O})$ ,  $\nu(\text{CN})$ ,  $\nu(\text{OCN})$ , and  $\nu(\text{Cd-O})$  for Cd-BDA are shifted to lower values than the pure Cd(II) metallogel-forming constituents such as  $\text{Cd}(\text{OAc})_2 \cdot 2\text{H}_2\text{O}$  and the LMWG (*i.e.*, butane-1,4-dicarboxylic acid) [22, 30]. The experimental results revealed that for both of these metallogels, the perceptible shifts of FT-IR stretching frequencies compared to the metallogel-forming constituents are obtained [22, 30, 33]. The results designate the manifestation of several possible non-covalent supramolecular interactions among the gel-forming ingredients including metal acetate salts, and in particular BDA as the gel-immobilized solvent medium. This ultimately contributes to the formation of stable metallogel structures of Mn-BDA and Cd-BDA.

#### 4.3.4. ESI Mass Analyses

The ESI-mass spectroscopic results obtained from Fig. 4.11 and 4.12 for the metallogels of Mn-BDA and Cd-BDA, respectively, are accounted to get the essence of a metallogel-forming strategy at the molecular level. The investigated data of ESI-mass spectral study expose the



persistence of the metallogel-forming chemical ingredients. The marked  $m/z$  peaks in the ESI-mass result (Fig. 4.11 and 4.12) dictate to catch the most plausible vision to find the repeating units, responsible to construct each of the metallogels. For both the metallogel networks (*i.e.*, Mn-BDA and Cd-BDA), the individual metal acetate salts with butane-1,4-dicarboxylic acid, source of dicarboxylic acids and acting as the LMWG in both metallogel systems, are assembled through involving non-covalent supramolecular interactions and this is counted as the pivotal repeating parts of constructing the soft metallogel-scaffold. This ESI-mass based exploration is a signature of metal acetate-directed supramolecular self-assembly phenomena, which is principally executed by the influence of low-molecular weight gelators of butane-1,4-dicarboxylic acid capable of interacting with metal sources of individual metallogels. Both of the acid moieties of butane-1,4-dicarboxylic acid are extremely effective to independently coordinate with the metal centres of individual metal salts including Mn(II) acetate tetrahydrate (for Mn-BDA) and Cd(II) acetate dihydrate (for Cd-BDA), and this might be critically accountable to form the metallogel-constructing networks, which are able to immobilize the polar aprotic solvent DMF *via* versatile non-covalent supramolecular interactions for offering the stable metallogel structure of Mn-BDA and Cd-BDA. The possible repeating constituent for both metallogels (*i.e.*, Mn-BDA and Cd-BDA) is exposed through Scheme 4.4.



**Scheme 4.4: Schematic of the possible metallogel-forming network of Mn-BDA and Cd-BDA metallogels in DMF solvent media**

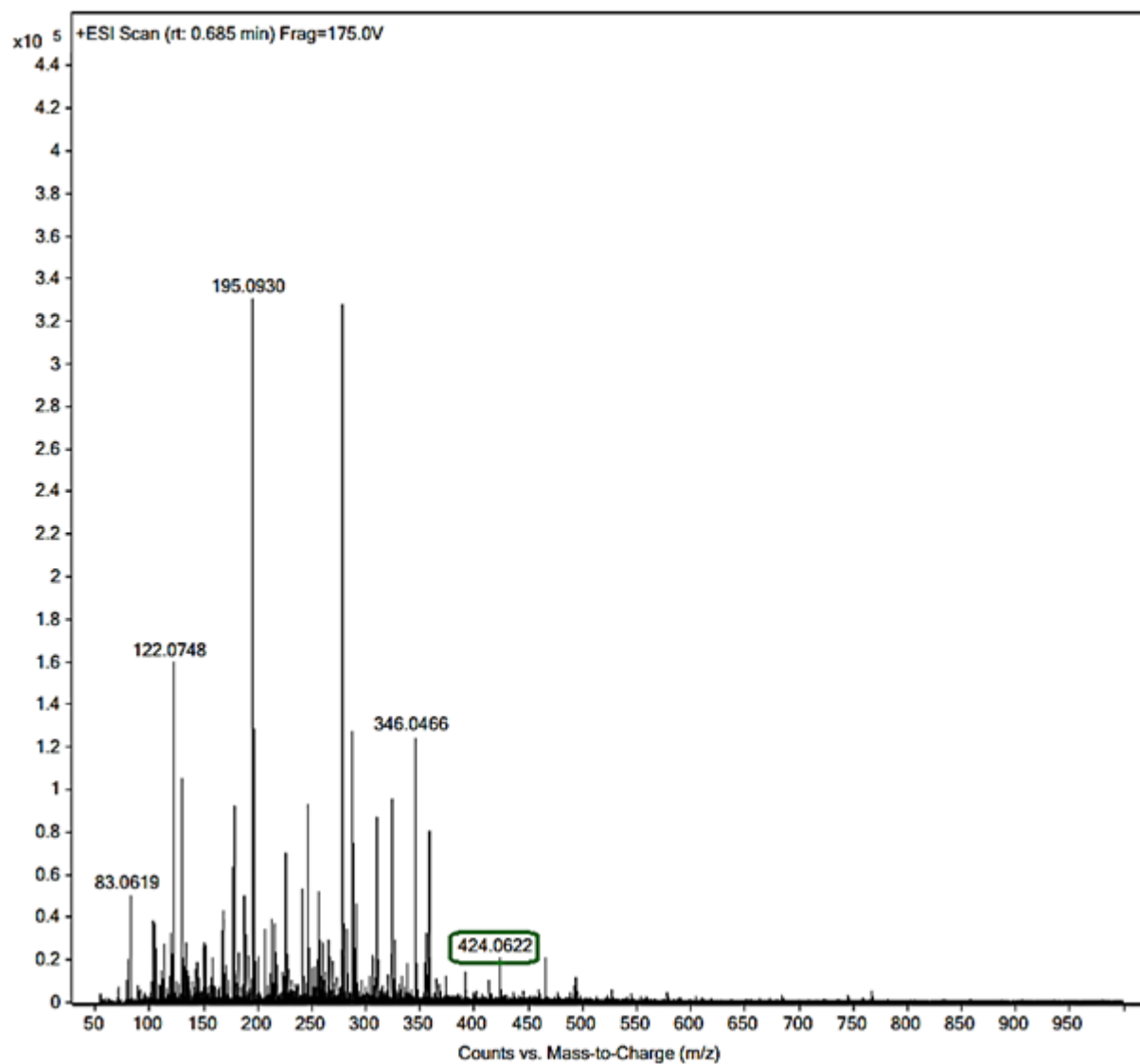


Fig. 4.11: ESI-Mass Spectra of Mn-BDAmetallogel

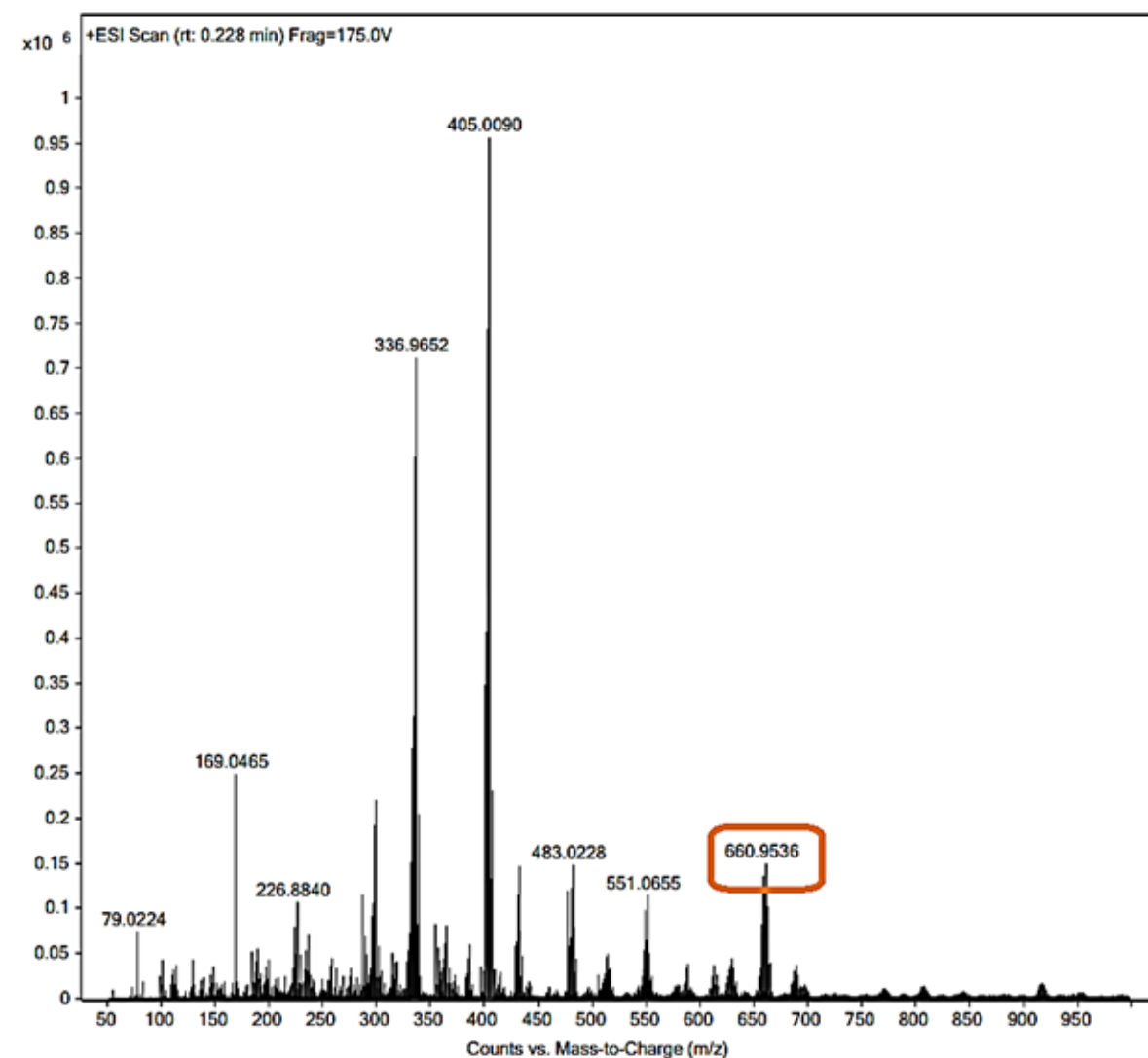


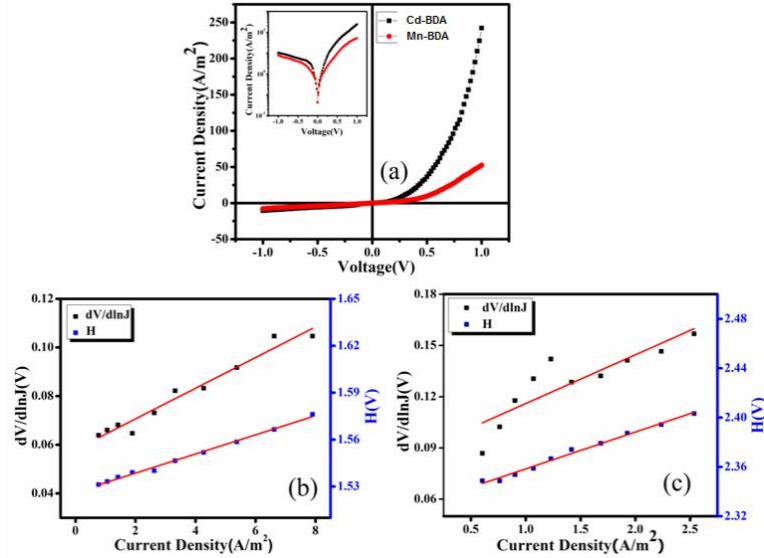
Fig. 4.12: ESI-Mass Spectra of Cd-BDA metallogel

### 4.3.5. Electrical characterization

The manufactured devices' current–voltage properties were measured at room temperature in a certain bias voltage range (*i.e.*,  $\pm 1$  V) under dark conditions. The two samples' observed J–V curves in complete darkness are shown in Fig. 4.13a, where J represents the current density (current/area). The inset of Fig. 4.13a displays the logarithmic representation of current density considering a function of voltage. The device based on Cd-BDA has a better rectifying property that implies good Schottky nature. The higher current recorded for the Cd-BDA device suggests



a higher conductivity, as shown in Table 4.4, which shows the rectification ratio computed from the exponential  $J$ – $V$  curve. The ohmic conductivity of the Cd-BDA based device was determined to be  $3.24 \times 10^{-5} \text{ S m}^{-1}$  at room temperature, whereas the conductivity of the Mn-BDA-based device was  $1.02 \times 10^{-5} \text{ S m}^{-1}$ .



**Fig. 4.13: (a) Current density-voltage (J-V) characteristics curve;  $dV/d\ln J$  and  $H(J)$  versus current density curves for (b) Cd-BDA and (c) Mn-BDA based diodes.**

**Table 4.4: Schottky Diode Parameters**

Sample	Rectification Ratio	$\sigma_{\text{ohmic}}$ S/m	$\eta$	$R_s$ from		$\Phi_B$ from H vs J curve (eV)
				$dV/d\ln J$ vs J curve ( $\text{K}\Omega$ )	H vs J curve ( $\text{K}\Omega$ )	
<b>Cd-BDA</b>	23.50	$3.24 \times 10^{-5}$	2.22	0.89	0.87	0.69
<b>Mn-BDA</b>	6.67	$1.02 \times 10^{-5}$	3.34	4.03	4.22	0.70

The charge transport method in the devices has been better understood using thermionic emission (TE) theory [56]. In terms of TE theory, the current density of diodes is represented as follows [57]:

$$J = J_0 \left[ \exp \left( \frac{qV}{\eta k T} \right) - 1 \right] \quad (1)$$

$$\text{Where, } J_0 = A^* T^2 \exp \left( - \frac{q\Phi_B}{kT} \right) \quad (2)$$

$q$  is the electronic charge,  $J_0$  is the representing saturation current density,  $V$  is given as the forward bias voltage,  $k$  is the Boltzmann constant,  $\eta$  is the ideality factor,  $T$  stands for the temperature in Kelvin,  $\Phi_B$  is the effective barrier height at zero bias,  $A$  is used for diode area ( $7.065 \times 10^{-6} \text{ m}^2$ ), and  $A^*$  is the effective Richardson constant ( $1.2 \times 10^6 \text{ A m}^{-2} \text{ K}^{-2}$ ). Some significant diode parameters were obtained using Cheung's technique [58]. According to Cheung's method, the forward bias  $J$ - $V$  characteristics with regard to series resistance are represented as follows [58]:

$$J = J_0 \left[ \exp \left( \frac{q(V - I R_S)}{\eta k T} \right) \right] \quad (3)$$

where the voltage drop through a device's series resistance is referred to as the  $IR_S$  term.

By entering the value of the saturation current density into the specified equation (i.e., eqn (3)) and differentiating considering  $\ln J$ , the amount of series resistance can now be calculated from the functions given as follows [33]:

$$\frac{dV}{d \ln J} = A J R_S + \frac{\eta k T}{q} \quad (4)$$

$$H(J) = V - \frac{\eta k T}{q} \ln \left( \frac{J}{A^* T^2} \right) = A J R_S \quad (5)$$

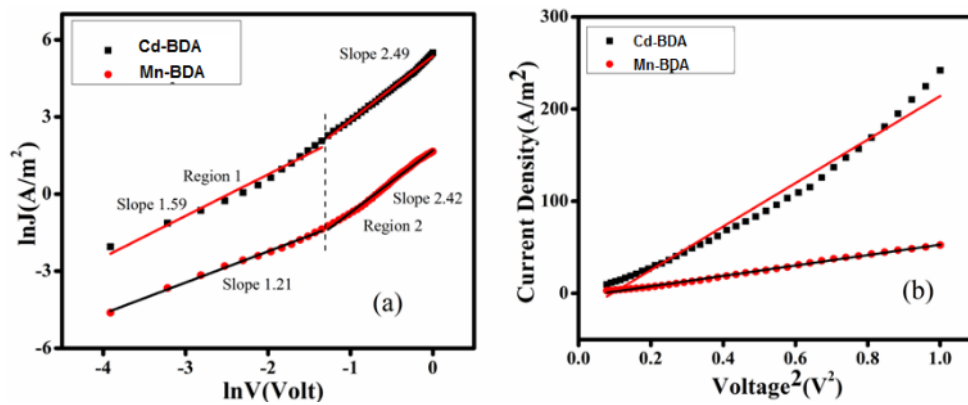
The slope and intercept of the  $dV/d \ln(J)$  vs.  $J$  plot (Fig. 4.13b and c) were used to calculate the series resistance ( $R_S$ ) and ideality factor ( $\eta$ ) for both devices. The y-axis intercept of the  $H(J)$  vs.  $J$  curve was used to estimate the barrier height ( $\Phi_B$ ) for devices (Fig. 4.13b and c). Another estimation of the series resistance is given by the slope of this plot. The resulting ideality factor ( $\eta$ ), barrier height ( $\Phi_B$ ), and series resistance ( $R_S$ ) values are listed in Table 4. 4.

The values of ideality factor ( $\eta$ ) for both devices deviate from ideal behaviours, due to the presence of inhomogeneities of the Schottky barrier height and existence of interface states, and series resistance [33] indicating an inhomogeneous metal–semiconductor contact. When compared to SD based on Cd-BDA, SD based on Mn-BDA in this case strayed further from the

ideal behaviour, but there was no obvious relation between the active materials and the ideality factor.

Table 4.4 shows how close is the  $R_s$  value estimated using two distinct techniques. The lower barrier height and lower series resistance of Cd-BDA's SD compared to the other, signal improved performance. It is seen that the device performance of Cd-BDA improved for all the cases, compared to Mn-BDA. Therefore, the synthesized Cd-BDA is expected to be a better candidate than Mn-BDA for fast switching device application.

According to the power law,  $J \propto V^m$  [59], where  $m$  stands for the slope of  $J$  vs.  $V$  plot, is stated to regulate the current conduction process in Schottky diodes. The  $J$  vs.  $V$  curves for each device based on the samples are shown on a logarithmic scale under the forward bias as shown in Fig. 4.14a, which depicts two separate areas with different slopes. The  $J$ – $V$  curves were further analyzed by evaluating mobility, transit time and carrier concentration of the carriers and provide a deeper conception of charge transport mechanisms in devices. The standard SCLC theory was employed for this purpose. Both samples exhibit ohmic behaviour at a low bias voltage (region I), where the current is directly proportional to the implemented bias voltage ( $m \sim 1$ ). The region II exhibits the current variation with the square of forward bias voltage ( $m \sim 2$ ) and correlates in terms of higher-ordered magnitude of slope. In this area, the conduction process is controlled via SCLC mechanism [60].



**Fig. 4.14: (a)  $\ln J$  vs.  $\ln V$  plot; (b) Effective interface mobility measured using the Current density vs. voltage<sup>2</sup> plot of the SCLC region.**

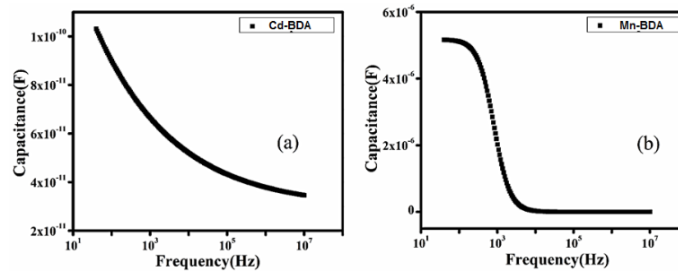
If the injected carriers are more than the background carriers, they disperse and create a space charge field. Under these conditions, the currents are mostly governed by this field and are known as SCLC [61]. As determined by the slope of the J–V curve, the conductivity of the device based on Mn-BDA in the SCLC zone (region-II) is  $6.88 \times 10^{-5} \text{ S m}^{-1}$ , whereas the conductivity of the device based on Cd-BDA increases to  $3.23 \times 10^{-4} \text{ S m}^{-1}$ . The carriers' mobility and transit times ( $\tau$ ) have a big influence on how well the device works. Therefore, using the Mott–Gurney space-charge-limited-current (SCLC) equation [62], the effective carrier mobility was determined from the J versus  $V^2$  plot (Fig. 4.14b) in region II as follows:

$$J = \frac{9 \mu_{\text{eff}} \epsilon_0 \epsilon_r}{8} \left( \frac{V^2}{d^3} \right) \quad (6)$$

where  $\epsilon_0$  shows the dielectric permittivity of free space,  $\mu_{\text{eff}}$  is the effective interface mobility of electrons,  $d$  is the film thickness and  $\epsilon_r$  stands for the dielectric constant of the synthesized material.

The value of material's dielectric constant was calculated from the saturation point of the curve in the capacitance vs. frequency data plot (C–f) (Fig. 4.15) using the following equation [63]:

$$\epsilon_r = \frac{1}{\epsilon_0} \frac{C_{\text{sat}} d}{A} \quad (7)$$



**Fig. 4.15: Capacitance versus frequency plot for Cd-BDA, and Mn-BDA.**

According to calculations, Cd-BDA's relative dielectric constant ( $\epsilon_r$ ) is 0.553, whereas Mn-BDA's is 0.395. The amount of time a carrier takes to go from an anode to a cathode is known as the transit time ( $\tau$ ). It can be represented as the summation of average total time spent by each electron as a free carrier plus total amount of time spent in the trap [64]. The following equation can be used to estimate the transit time ( $\tau$ ) of the charge carrier from the  $\ln J$  vs.  $\ln V$  graph:

$$\tau = \frac{9\varepsilon_0\varepsilon_r}{8d} \left( \frac{V}{J} \right) \quad (8)$$

The charge carrier concentration ( $N$ ) near the junction of the devices was estimated using the following formula:

$$N = \frac{\sigma_{\text{SCLC}}}{q \mu_{\text{eff}}} \quad (9)$$

Where,  $\sigma_{\text{SCLC}}$  is the SCLC region conductivity. It can be seen that the effective carrier mobility is higher for Cd-BDA with a carrier mobility of  $4.28 \times 10^{-5} \text{ m}^2 \text{ V}^{-1} \text{ s}^{-1}$ , which is a 3-fold increase compared to the Mn-BDA. Not only that, the carrier concentration also increased by as much as 58%. In Mn-BDA, longer transit times result in increased trapping probabilities [65].

Table 4.5 lists the effective carrier mobility and transit time data for Mn-BDA and Cd-BDA. Therefore, it can be seen from the table that there is an improvement in charge transport kinetics for Cd-BDA. The improvement is attributed to the excellent conductivity and high carrier mobility of Cd-BDA. The enhanced effective interface mobility, conductivity, and shorter transit time of the SD generated by Cd-BDA point to a superior conduction mechanism [66]. The morphological compactness of Cd-BDA is more prominent, as evident from the FESEM microstructures of Mn-BDA and Cd-BDA, and this might be regarded for the better semiconducting diode performances of Cd-BDA-based metal–semiconductor junction-type devices. Moreover, the size factor of the metal centres of the corresponding metal acetate salts including  $\text{Mn}(\text{OAc})_2 \cdot 4\text{H}_2\text{O}$  and  $\text{Cd}(\text{OAc})_2 \cdot 2\text{H}_2\text{O}$  of individual metallogel systems is also considered for the variation in the diverse parameters of metallogel-based metal–semiconductor junction-type Schottky diodes [51].

**Table 4.5: SCLC/Charge Transport Parameters.**

Sample	SCLC conductivity $\sigma_{\text{SCLC}} (\text{Sm}^{-1})$	Mobility $\mu_{\text{eff}} (\text{m}^2 \text{V}^{-1} \text{S}^{-1})$	Transit time $\tau (\text{s})$	Carrier concentration $N (\text{m}^{-3})$
<b>Cd-BDA</b>	$3.23 \times 10^{-4}$	$4.28 \times 10^{-5}$	$2.33 \times 10^{-8}$	$4.71 \times 10^{19}$
<b>Mn-BDA</b>	$6.88 \times 10^{-5}$	$1.44 \times 10^{-5}$	$6.97 \times 10^{-8}$	$2.99 \times 10^{19}$

## 4.4. Conclusions

The effective attainment of a protocol for the formation of a mechanically flexible supramolecular metallogel using metal acetate salts of Mn(II) and Cd(II) with butane-1,4-dicarboxylic acid as a low-molecular weight gelator in a gel-immobilized appropriate polar aprotic-type solvent medium (*i.e.*, DMF) has been explored. The comparative idea of individual gel-synthesis procedure dictates that the diversity of stoichiometries of gel-forming constituents involving distinct metal salts and LMWG is accountable to get respective stable metallogels. Particularly, the ultrasonication-based reaction condition is critically liable toward the formation of Cd(II)-based stable metallogels. The synthesized metallogels are exhaustively characterized through a considerable number of experimental performances such as rheological and FESEM microstructural scrutiny, EDX elemental testing, FT-IR spectroscopy studies and ESI-mass results. The values of FT-IR stretching frequencies of individual xerogel samples validate the contributing role of non-covalent supramolecular interactions in metallogel construction. Even, ESI-mass results depict the possible basic repeating sector of metal acetate salts and butane-1,4-dicarboxylic acid capable of constructing specific metallogel systems. Using synthesized metallogels, the semiconducting devices on metal–semiconductor junctions have been developed. Comparative studies in diode parameters were explained by evaluating the carrier transport mechanism through the metal–semiconductor junction and this revealed the supremacy of the Cd-BDA-based SBD for all the cases. Markedly, the experimental data of  $J$ – $V$  curves reveal a distinct non-linear nature for both Mn-BDA and Cd-BDA metallogels, and these demonstrate rectification ratios of 6.67, and 23.50, respectively. This non-ohmic conduction behaviour gets categorized. Heightened voltage-dependent current density, charge transportation across the MS interface, mobility and carrier concentration, and the diode performances of the fabricated devices have been monitored by SCLC theory, which reflected the superior transport properties of the Cd-BDA Schottky device. In light of these results, I infer that Cd-BDA is a promising alternative to Mn-BDA for better rectification and fast switching device application. Predominant microstructural compactness of Cd-BDA as found through FESEM images might be responsible to have better semiconducting diode performances of Cd-BDA-based devices. Moreover, the size factor of Cd(II) centres in the  $\text{Cd}(\text{OAc})_2 \cdot 2\text{H}_2\text{O}$ -directed Cd-BDA metallogel system might be effective to substantiate the improved diode performances of the Cd-BDA-

based semiconducting device. Thus, this work provides an effective way of fabricating flexible semiconducting devices using versatile metallogel systems for offering electrical materials, suggesting their considerable involvement in advanced technology.

## References

- [1] K. Almdal, J. Dyre, S. Hvidt and O. Krame, *Polymer Gels and Networks*, 1 (1993) 5–17.
- [2] S. Y. Chan, S. S. Goh, Q. Dou, B. Q. Y. Chan, W. S. Choo, D. J. Young and X. Loh, *Chemistry-An Asian Journal*, 13 (2018) 1797– 1804.
- [3] P. Dastidar, *Chemical Society Reviews*, 37 (2008) 2699–2715.
- [4] P. Chakraborty and P. Dastidar, *Chemistry—An Asian Journal*, 13 (2018) 1366–1378.
- [5] J. V. Alemán, A. V. Chadwick, J. He, M. Hess, K. Horie, R. G. Jones, P. Kratochvíl, I. Meisel, I. Mita, G. Moad, S. Penczek and R. F. T. Stepto, *Pure and Applied Chemistry*, 79 (2007) 1801–1829.
- [6] P. Dastidar, S. Ganguly and K. Sarkar, *Chemistry—An Asian Journal*, 11 (2016) 2484–2498.
- [7] P. K. Vemula, U. Aslam, V. Ajay Mallia and G. John, *Chemistry of Materials*, 19 (2007) 138–140.
- [8] M. D. Ward, *Chemical Society Reviews*, 26 (1997) 365–375.
- [9] T. Zhao, S. Chen, K. Kang, J. Ren and X. Yu, *Langmuir*, 38 (2022) 1398–1405.
- [10] A. Y.-Y. Tam and V. W.-W. Yam, *Chemical Society Reviews*, 42 (2013) 1540–1567.
- [11] P. Terech and R. G. Weiss, *Chemical Reviews*, 97 (1997) 3133–3159.
- [12] H. Guo, Q. Feng, K. Xu, J. Xu, J. Zhu, C. Zhang and T. Liu, *Advanced Functional Materials*, 29 (2019) 1903660.
- [13] S. Dhibar, A. Dey, A. Dey, S. Majumdar, A. Mandal, P. P. Ray and B. Dey, *New Journal of Chemistry*, 43 (2019) 15691–15699.
- [14] A. V. Lipowitz, *Justus Liebig's Annalen der Chemie*, 38 (1841) 348–355.
- [15] S. Majumdar, S. Sil, R. Sahu, M. Ghosh, G. Lepcha, A. Dey, S. Mandal, P. P. Ray and B. Dey, *Journal of Molecular Liquids*, 338 (2021) 116769.
- [16] D. DíazDíaz, D. Kühbeck and R. J. Koopmans, *Chemical Society Reviews*, 40 (2011) 427–448.
- [17] S. Dhibar, A. Dey, D. Ghosh, S. Majumdar, A. Dey, P. Mukherjee, A. Mandal, P. P. Ray and B. Dey, *ChemistrySelect*, 4 (2019) 1535–1541.
- [18] S. Dhibar, A. Dey, A. Dey, S. Majumdar, D. Ghosh, P. P. Ray and B. Dey, *ACS Applied Electronic Materials*, 9 (2019) 1899–1908.



- [19] S. Majumdar, T. Singha, S. Dhibar, A. Mandal, P. K. Datta and B. Dey, *ACS Applied Electronic Materials*, 2 (2020) 3678–3685.
- [20] P. Grondin, O. Roubeau, M. Castro, H. Saadaoui, A. Colin and R. Clerac, *Langmuir*, 26 (2010) 5184–5195.
- [21] S. Majumdar, G. Lepcha, K. T. Ahmed, I. Pal, S. R. Biswas and B. Dey, *Journal of Molecular Liquids*, 368 (2022) 120619.
- [22] G. Lepcha, S. Majumdar, B. Pal, K. T. Ahmed, I. Pal, B. Satpati, S. R. Biswas, P. P. Ray and B. Dey, *Langmuir*, 39 (2023) 7469–7483.
- [23] S. Saha, E.-M. Schön, C. Cativiela, D. Díaz-Díaz and R. Banerjee, *Chemistry – A European Journal*, 19 (2013) 9562–9568.
- [24] N. Zhang, J. Lock, A. Sallee and H. Liu, *ACS Applied Materials & Interfaces*, 7 (2015) 20987–20998.
- [25] Y. Zhao, S. Song, X. Ren, J. Zhang, Q. Lin and Y. Zhao, *Chemical Reviews*, 122 (2022) 5604–5640.
- [26] W. Zhao, K. Odelius, U. Edlund, C. Zhao and A.-C. Albertsson, *Biomacromolecules*, 16 (2015) 2522–2528.
- [27] P. Biswas, H. K. Datta and P. Dastidar, *Chemical Communications*, 58 (2022) 969–972.
- [28] M. Tao, K. Xu, S. He, H. Li, L. Zhang, X. Luo and W. Zhong, *Chemical Communications*, 54 (2018) 4673–4676.
- [29] P. Biswas, A. Dutta and P. Dastidar, *Crystal Growth & Design*, 23 (2023) 342–353.
- [30] G. Lepcha, T. Singha, S. Majumdar, A. K. Pradhan, K. S. Das, P. K. Datta and B. Dey, *Dalton Transactions*, 51 (2022) 13435–13443.
- [31] S. Majumdar, D. Mukherjee, G. Lepcha, K. K. Saha, K. S. Das, I. Pal, N. C. Mondal and B. Dey, *New Journal of Chemistry*, 47 (2023) 9643–9653.
- [32] G. Lepcha, B. Pal, S. Majumdar, K. T. Ahmed, I. Pal, P. P. Ray, S. R. Biswas and B. Dey, *Materials Advances*, 4 (2023) 2595–2603.
- [33] B. Pal, S. Majumdar, K. S. Das, G. Lepcha, I. Pal, P. P. Ray and B. Dey, *Journal of Physics and Chemistry of Solids*, 182 (2023) 111612.
- [34] P. Das, S. Majumdar, A. Dey, S. Mandal, A. Mondal, S. Chakrabarty, P. P. Ray and B. Dey, *New Journal of Chemistry*, 45 (2021) 15920–15927.

- [35] S. Majumdar, G. Lepcha, R. Sahu and B. Dey, *Journal of Physics and Chemistry of Solids*, 170 (2022) 110903.
- [36] J. H. Lee, J. Park, J.-W. Park, H.-J. Ahn, J. Jaworski and J. H. Jung, *Nature Communications*, 6 (2015) 6650.
- [37] B. C. Roy and T. S. Mahapatra, *Soft Matter*, 19 (2023) 1854–1872.
- [38] R. Abazari, E. Yazdani, M. Nadafan, A. M. Kirillov, J. Gao, A. M. Z. Slawin and C. L. Carpenter-Warren, *Inorganic Chemistry*, 60 (2021) 9700–9708.
- [39] Y. Kumar, C. Mahendar, A. Kalam and M. Dubey, *Sustainable Energy Fuels*, 5 (2021) 1708–1713.
- [40] I. Pal, S. Majumdar, G. Lepcha, K. T. Ahmed, S. K. Yatirajula, S. Bhattacharya, R. Chakravarti, B. Bhattacharya, S. R. Biswas and B. Dey, *ACS Applied Bio Materials*, 6 (2023) 5442–5457.
- [41] D. Bairagi, P. Ghosh, P. Roy and A. Banerjee, *ACS Applied Nano Materials*, 6 (2023) 2299–2309.
- [42] S. Kushida, E. Smarsly, K. Yoshinaga, I. Wacker, Y. Yamamoto, R. R. Schröder and U. H. F. Bunz, *Advanced Materials*, 33 (2021) 2006061.
- [43] Y. Huang, Y. Cui, H. Deng, J. Wang, R. Hong, S. Hu, H. Hou, Y. Dong, H. Wang, J. Chen, L. Li, Y. Xie, P. Sun, X. Fu, L. Yin, W. Xiong, S.-H. Shi, M. Luo, S. Wang, X. Li and X. Sheng, *Nature Biomedical Engineering*, 7 (2023) 486–498.
- [44] E. T. Simola, V. Kiyek, A. Ballabio, V. Schlykow, J. Frigerio, C. Zucchetti, A. D. Iacovo, L. Colace, Y. Yamamoto, G. Capellini, D. Grützmacher, D. Buca and G. Isella, *ACS Photonics*, 8 (2021) 2166–2173.
- [45] W. Du, Y. Zhou, S. A. Ghetmiri, A. Mosleh, B. R. Conley, A. Nazzal, R. A. Soref, G. Sun, J. Tolle, J. Margetis, H. A. Naseem and S.-Q. Yu, *Applied Physics Letters*, 104 (2014) 241110.
- [46] L. B. Taşyürek, A. Sarılmaz, A. Rüßen, E. Yiğit, F. Özel and İ. Orak, *Materials Science and Engineering: B*, 287 (2023) 116139.
- [47] N. S. Boltovets, V. V. Kholevchuk, R. V. Konakova, V. F. Mitin and E. F. Venger, *Sensors and Actuators A*, 92 (2001) 191–196.

- [48] S. Lischke, A. Peczek, J. S. Morgan, K. Sun, D. Steckler, Y. Yamamoto, F. Korndörfer, C. Mai, S. Marschmeyer, M. Fraschke, A. Krüger, A. Beling and L. Zimmermann, *Nature Photonics*, 15 (2021) 925–931.
- [49] J. Zhang, P. Dong, K. Dang, Y. Zhang, Q. Yan, H. Xiang, J. Su, Z. Liu, M. Si, J. Gao, M. Kong, H. Zhou and Y. Hao, *Nature. Communications*, 13 (2022) 3900.
- [50] N. A. Al-Ahmadi, *Materials Research Express*, 7 (2020) 032001.
- [51] I. Pal, A. Biswas, S. Majumdar, G. Lepcha, B. Pal, P. P. Ray and B. Dey, *ACS Applied Engineering Materials*, 1 (2023) 3005–3015.
- [52] I. Pal, N. K. Pathak, S. Majumdar, G. Lepcha, A. Dey, S. K. Yatirajula, U. Tripathy and B. Dey, *Langmuir*, 39 (2023) 16584–16595.
- [53] D. Zhang, N. Jiang, X. Chen and B. He, *Journal of Applied Polymer Science*, 137 (2020) 48421.
- [54] H. Ramli, N. Fatahah, A. Zainal, M. Hess and C. H. Chan, *Chemistry Teacher International*, 4 (2022) 307–326.
- [55] M. E. De Rosa and H. H. Winter, *RheologicaActa*, 33 (1994) 220–237.
- [56] E. H. Rhoderick and R. H. Williams, *Current Transport Mechanism in Metal–semiconductor contacts*, Clarendon Press, Oxford, 2nd edn, 1988, pp. 89–107.
- [57] S. M. Sze, *Physics of Semiconductor Devices*, Wiley, New York, 2nd edn, 1981, pp. 134–158.
- [58] S. K. Cheung and N. W. Cheung, *Applied Physics Letters*, 49 (1986) 85–87.
- [59] P. Das, B. Pal, J. Datta, M. Das, S. Sil and P. P. Ray, *Journal of Physics and Chemistry of Solids*, 148 (2021) 109706.
- [60] A. Jain, P. Kumar, S. C. Jain, V. Kumar, R. Kaur and R. M. Mehra, *Journal of Applied Physics*, 102 (2007) 94505–94509.
- [61] W. Hwang and K. Kao, *Electrical transport in solids with particular reference to organic semiconductors*, Pergamon Press, Oxford/New York, 1981, pp. 663.
- [62] B. Pal, P. Das, J. Datta, U. Gangopadhyay and P. P. Ray, *Materials Science in Semiconductor Processing*, 162 (2023) 107535.
- [63] S. Halder, B. Pal, A. Dey, S. Sil, P. Das, A. Biswas and P. P. Ray, *Materials Research Bulletin*, 118 (2019) 110507.

- [64] P. W. M. Blom, M. J. M. de Jong and M. G. van Munster, Physical Review B: Condensed Matter and Materials Physics, 55 (1997) R656– R659.
- [65] B. Pal, S. Dhibar, R. Mukherjee, S. Bhattacharya, P. P. Ray and B. Saha, Materials Advances, 4 (2023) 3628–3635.
- [66] R. Jana, J. Datta, S. Sil, A. Dey, B. Pal, A. Biswas and P. P. Ray, Materials Research Express, 6 (2019) 1050d1.

\*\*\*



*"A physicist is just an atom's way of looking at itself."*

- Niels Bohr



# Chapter 5

---

**A Semiconducting Supramolecular novel Ni(II)-Metallogel derived from 5-aminoisophthalic acid low molecular weight gelator: An Efficient Schottky Barrier Diode Application**

## Abstract

An outstanding approach for the development of supramolecular metallogel with nickel(II) ion and 5-aminoisophthalic acid as a gelator (LMWG) in DMF medium had been accomplished at room temperature. The rheological studies of supramolecular Ni(II)-metallogel established the mechanical compactness of the gel material. The FESEM microstructural study and EDX elemental mapping showed the flake-like morphological patterns and major chemical constituents of Ni(II)-metallogel. The possible metallogel formation approach has been examined using FT-IR spectroscopic study. Moreover, supramolecular Ni(II)-metallogel assemblies show electrical conductivity in metal-semiconductor (MS) junction electronic devices. The metallogel based thin film device shows electrical conductivity as  $1.53 \times 10^{-5} \text{ S.m}^{-1}$ . Semiconductor properties such as Schottky barrier diode nature of the synthesized Ni(II)-metallogel based devices were explored.



## 5.1. Introduction

Gels are often thought to consist of an elastic cross-linked network and the trapped liquid [1]. Gels are ubiquitous in daily life; notable examples are hair gels, toothpaste, and soft contact lenses. The field of material science and its associated industrial applications are constantly being reinforced by molecular self-assembly, one of the main branches of supramolecular chemistry [2]. The spontaneous self-assembly of molecules produces three-dimensional frameworks known as supramolecular gels [3]. The gelators and solvent molecules, which are immobilised by the gelator molecules in the 3D soft gel scaffolds, are the two principal elements making up the supramolecular gel [4]. The inversion vial test, which demonstrates that a vial of gel remains stabilized against gravity, provides the most direct primary evidence of gel formation [5]. The organic and/or inorganic gelators trap various solvents, such as water ( $\text{H}_2\text{O}$ ) [6], acetonitrile ( $\text{H}_3\text{C}-\text{C}\equiv\text{N}$ ) [7], ethanol ( $\text{CH}_3\text{CH}_2\text{OH}$ ) [8], methanol ( $\text{CH}_3\text{OH}$ ) [9], dichloromethane ( $\text{CH}_2\text{Cl}_2$ ) [10], deuterated dichloromethane ( $\text{CD}_2\text{Cl}_2$ ) [11], 1,2-dichlorobenzene ( $\text{C}_6\text{H}_4\text{Cl}_2$ ) [12], acetone ( $\text{CH}_3\text{COCH}_3$ ) [13], carbon tetrachloride ( $\text{CCl}_4$ ) [14], DMF ( $(\text{CH}_3)_2\text{NC}(\text{O})\text{H}$ ) [15], tetrahydrofuran ( $(\text{CH}_2)_4\text{O}$ ) [16], dimethyl sulfoxide ( $\text{C}_2\text{H}_6\text{OS}$ ) [17], and toluene ( $\text{C}_6\text{H}_5\text{CH}_3$ ) [18], etc. to create three-dimensional gel structures [19]. Polymers such as polyester, poly(ethylene glycol), polyolefins, polycaprolactones, and polycarbonates often serve as gelators to produce a variety of stable gel compositions [20]. However, low molecular weight gelators (LMWGs), which have molecular weights under 3000, have a strong capacity in supramolecular gel formation through immobilization of solvent molecules [21, 22]. Literature is full with various low molecular weight gelators such as alkenes [23], amides [24], modified amino acids [25], urea [26], peptides [27], sugars [28], dendrimers [29], etc. which have wonderful gelation property in presence of different solvent molecules. Supramolecular gel formation is the output of intriguing non-covalent interactions including hydrogen bonds [30], electrostatic interactions [31], hydrophobic [32], and hydrophilic forces [33], van der Waals forces [30], aryl-system-based interactions [34], etc. Supramolecular gels have become vital area in material science due to its numerous applications in both the academic and industrial arena like catalysis [6a, 6b, 35], lithography [36], opto-electronic devices [37], electrochemical devices [38], chemo-sensors [39], cell culture [40], drug delivery [41], tissue engineering [42], semiconductors [15], etc.

Metallogels are significant class of supramolecular gels which are formed by the incorporation of metal ions with the appropriate LMWG to create a 3D supramolecular soft gel structure that may exhibit intriguing and unusual features [5]. In metallogels, metal ions impart a number of significant functionalities into the metallogel scaffolds, including redox activity [43], magnetic behaviour [44], conductivity [45], actuators [46], catalytic activity [47], optical activity [48], etc. As smart functional materials, supramolecular metallogel systems based on transition metals have recently received interest because of their affordability and availability. Researchers have recognized several useful metallogels of transition metal ions like Co(II) [49-51], Ni(II) [51, 52], Cu(II) [15d, 15e, 15g], Cd(II) [15a], Fe(II/III) [53-55], Zn(II) [15h, 15i], Mn(II) [5], with their strong applications in science [56]. However, metallogels with Ni(II)-ion have important applications in fluorescence switching [57], electrocatalysis [58], non-linear property [59], self-healing property [60], semiconducting device [52], catalysis [61], magnetic [62] etc. In recent times, Dhibar et al. continuously reported different metallogel mediated metal-semiconductor (MS) junction device for Schottky barrier diode application. Metallogel-based Schottky diodes are highly significant in various applications for several reasons. First, metallogels offer tunable electronic properties that can be customized by selecting specific metals and ligands during synthesis. This tunability allows for precise control over the energy band structure and electronic behavior of the Schottky diode, enabling the creation of tailored device characteristics. Second, metallogels exhibit excellent stability, ensuring the long-term performance and reliability of Schottky diodes. Their robust structure and resistance to degradation make them suitable for deployment in diverse environments and applications. Third, metallogels can be fabricated using a range of techniques, including solution processing, self-assembly, and templating methods. This versatility in fabrication enables compatibility with various substrates and facilitates scalable production, facilitating the integration of metallogel-based Schottky diodes into different electronic devices. Furthermore, metallogels can be easily integrated with other electronic components, such as transistors and sensors, due to their compatibility with different materials and fabrication techniques. This seamless integration allows for the development of multifunctional devices and systems with enhanced performance and expanded

functionality. Overall, metallogel-based Schottky diodes offer a unique combination of tunable electronic properties, stability, versatile fabrication methods, tailored surface properties, and compatibility with other electronic components. These characteristics make them indispensable for a wide range of electronic applications, where precise control over device properties and reliable performance are paramount. Following the trend, here I have demonstrated the synthetic procedure of a room temperature stable metallogel of Nickel(II)-ion and 5-aminoisophthalic acid as a LMWG in DMF medium (Fig. 5.1) for tunable, stable electronic device fabrication. The inversion vial test of Ni(II)-metallogel (i.e. Ni@5AIA) shows the stability of Ni@5AIA gel against the gravitational force (Fig. 5.1). The mechanical property and morphological patterns had been established. Targeting to achieve the capability of the metallogel based metal-semiconductor (MS) junction device, I have succeeded to fabricate a Schottky barrier diode (SD).

## 5.2. Experimental

### 5.2.1. Materials

Nickel(II) acetate tetrahydrate (98%), 5-aminoisophthalic acid (94%) were purchased from Sigma-Aldrich chemical company and used as received. Dry solvents (i.e. N, N-dimethyl formamide (DMF) was used for entire work.

### 5.2.2. Apparatus and measurements

A SHIMADZU made UV-3101PC spectrophotometer to collect UV-vis absorption spectral data.

Rheology experiment of the gel was done by an Anton Paar 100 rheometer with a cone and plate geometry (CP 25-2). All the mechanical measurements were done fixing the gap distance between the cone and the plate at 0.05 mm. The gels were scooped on the plate of the rheometer. An oscillatory strain amplitude sweep experiment was performed at a constant oscillation frequency of 1 Hz for the applied strain range 0.001-10 % at 20 °C.

Microstructural feature was analysed using a Carl Zeiss SUPRA 55VP FESEM FESEM instrument. The ZEISS, EVO 18 apparatus was used to perform EDX elemental mapping studies.

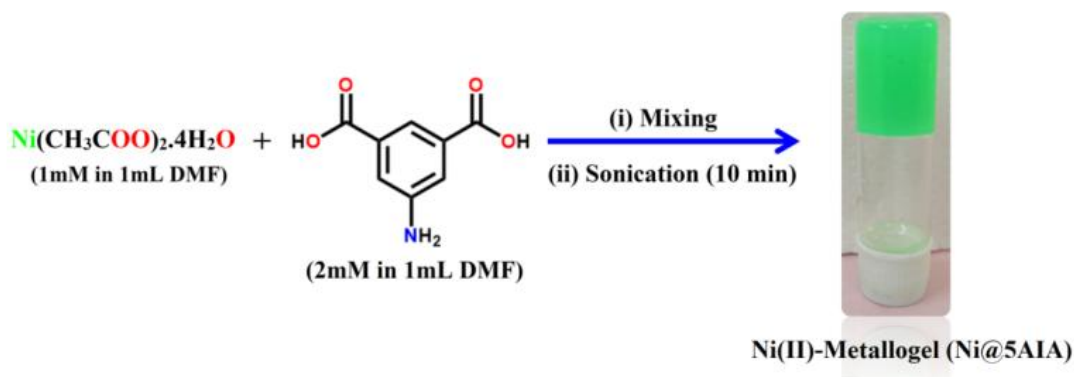
A Shimadzu FTIR-8400S made FTIR spectrometer was used for IR study.

A digital gel melting point measurement apparatus (Aplab MPA-01) was used to the  $T_{gel}$  of the Ni@5AIA metallogel.

Keithley 2401 sourcemeter interfaced with computer was used to perform the current-voltage (I-V) characteristics of our synthesized metallogel material based thin film device.

### 5.2.3. Synthetic Procedure of Ni(II)-metallogel (Ni@5AIA)

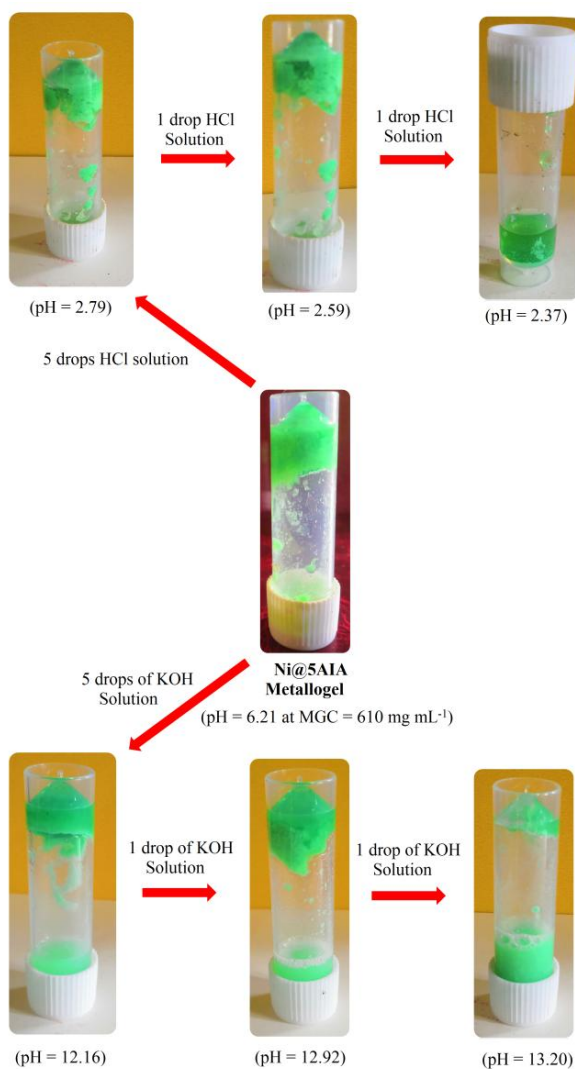
Greenish-yellow colour stable Ni(II)-metallogel (Ni@5AIA) was synthesized by one shot mixing of 1ml DMF solution of Nickel(II) acetate tetrahydrate (0.248 g, 1 mmol) and 1ml DMF solution of 5-aminoisophthalic acid (0.362 g, 2 mmol) followed by the continuous sonicated of the mixture for 10 minutes at room temperature (Fig. 5.1). The inversion vial of Ni@5AIA metallogel proves its stability against the gravitational force (Fig. 5.1). The minimum critical gelation concentration (MGC) of Ni@5AIA metallogel was recorded at  $\sim 610 \text{ mg mL}^{-1}$ . The concentrations of  $\text{Ni}(\text{CH}_3\text{COO})_2 \cdot 4\text{H}_2\text{O}$  and 5-aminoisophthalic acid were varied in a certain range (i.e.  $30\text{--}610 \text{ mg mL}^{-1}$ ) to evaluate the MGC of Ni@5AIA metallogel. Here, the ratio of the Ni@5AIA metallogel forming components was maintained as  $[\text{Ni}(\text{CH}_3\text{COO})_2 \cdot 4\text{H}_2\text{O}]:[5\text{-aminoisophthalic acid}] = 1:2$ , (w/w). The Greenish-yellow colour stable Ni@5AIA metallogel was obtained at  $610 \text{ mg mL}^{-1}$  concentration of Ni(II)-acetate salt and 5-aminoisophthalic acid in DMF solvent. The gel melting temperature ( $T_{gel}$ ) of Ni@5AIA metallogel was recorded as  $120^\circ\text{C} \pm 2^\circ\text{C}$  via a digital melting-point measuring apparatus.



**Fig. 5.1:** Synthetic procedure of gelation and photographic image of Ni(II)-metallogel (Ni@5AIA).

#### 5.2.4. Stability of the Ni@5AIA metallogel in different pH media:

I conducted experiments to assess the stability of Ni@5AIA metallogel under varying pH conditions, including acidic conditions using hydrochloric acid (HCl) solution and alkaline conditions using potassium hydroxide (KOH) solution. In the acidic environment experiments, I adjusted the gel's pH by adding HCl solution in the range of 6.21 to 2.37. Through these trials, I noted a deterioration in the stability of the Ni@5AIA metallogel at a pH of 2.37. Similarly, in the alkaline environment experiments, I tested the gel's stability with KOH solution at pH levels from 6.21 to 13.20. My observations indicated a loss of stability in the gel at a pH of 13.20.

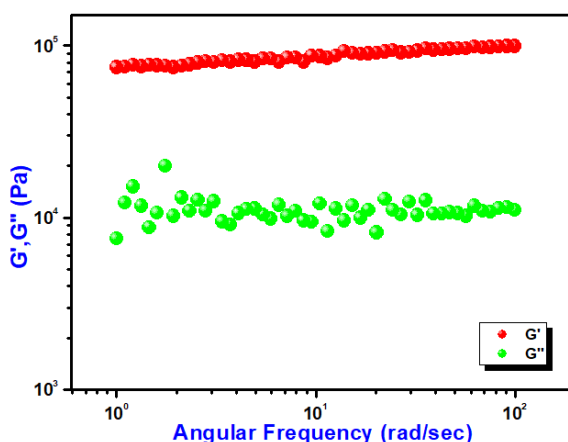


**Fig. 5.2: Stability studies of the Ni@5AIA metallogel in different pH media.**

## 5.3. Results and discussions

### 5.3.1. Rheological Analysis

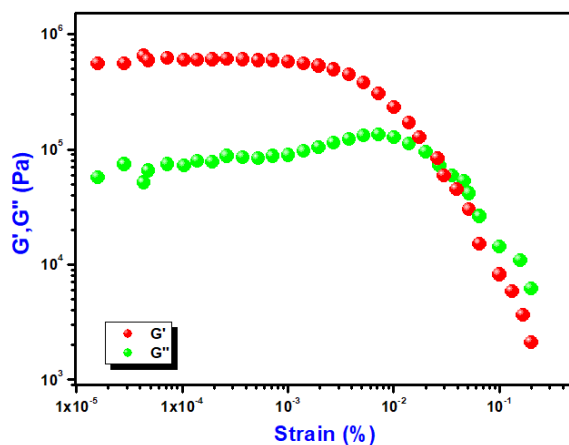
The mechanical properties of the Ni@5AIA metallogel were characterized through a rheometer instrument of angular frequency and strain-sweep measurement. The higher values of storage modulus ( $G'$ ) than loss modulus ( $G''$ ) approve the sample as gel material. Rheological investigation proved that  $G'$  of Ni@5AIA metallogel is noticeably higher than that of  $G''$  maintaining at the definite concentration of  $\text{Ni}(\text{CH}_3\text{COO})_2 \cdot 4\text{H}_2\text{O}$  and 5-aminoisophthalic acid (i.e. MGC = 610 mg/mL) (Fig.5.3).



**Fig. 5.3: Angular frequency measurements vs  $G'$  and  $G''$  of Ni@5AIA metallogel.**

The rheological data of Ni@5AIA shows that  $G' > G''$  which establishes the gel nature with semi-solid like performance. The average storage modulus of Ni@5AIA metallogel (i.e.  $G' > 10^4$  Pa) was detected to be significantly higher than the loss modulus ( $G''$ ) in favour of the considerable endurance limit of Ni@5AIA metallogel (Fig. 5.3).

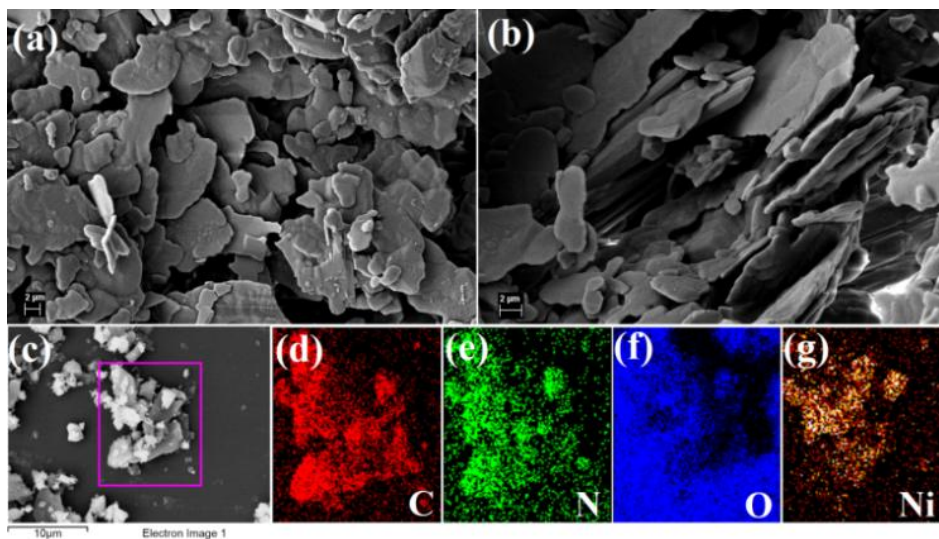
Fig. 5.4 depicts a strain-sweep experiment on Ni@5AIA metallogel material at a constant frequency of 6.283 rad/sec. Results from the strain-sweep experiment show that the critical strain, the lowest strain for gel breakdown of Ni@5AIA metallogel, occurs at a strain of 0.45%, when  $G'$  mixes with  $G''$  (Fig. 5.4).



**Fig. 5.4:** Strain-sweep measurements of Ni@5AIA metallogel performed at a constant frequency of 6.283 rad/sec.

### 5.3.2. Microstructural Study

The FESEM microstructural pattern of the Ni@5AIA reveal with flake like hierarchical network (Fig. 5.5 (a,b)).

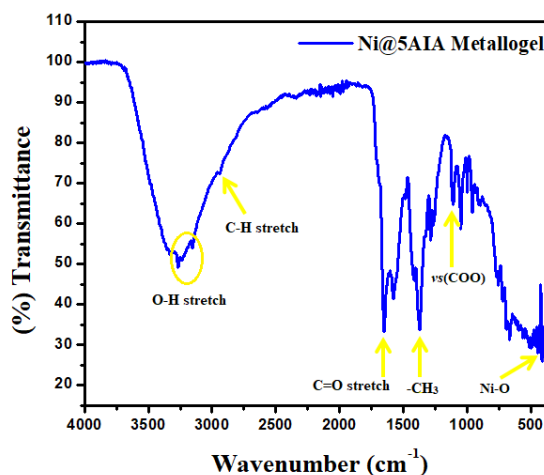


**Fig. 5.5:** (a, b) The FESEM microstructural pattern of Ni@5AIA metallogel, Chemical compositions by EDS are shown in (c-g).

The FESEM structural arrangements of the Ni@5AIA metallogel were formed due to the combination of  $\text{Ni}(\text{OAc})_2 \cdot 4\text{H}_2\text{O}$  and 5-aminoisophthalic acid in DMF medium over continuous sonication. EDX elemental mapping confirms the presence of C, N, O and Ni elements of  $\text{Ni}(\text{OAc})_2 \cdot 4\text{H}_2\text{O}$ , 5-aminoisophthalic acid and DMF molecules, accountable for the Ni@5AIA metallogel networks formation (Fig. 5.5 (c-g)).

### 5.3.3. FT-IR analysis of Ni@5AIA metallogel

The FT-IR spectral data of Ni@5AIA metallogel in xerogel form unveils the key peaks are located at 3320-3150, 2940, 1650, 1370, 1108  $\text{cm}^{-1}$ , for OH stretching,  $-\text{CH}$  stretching,  $\text{C}=\text{O}$  (carboxylic) stretching,  $-\text{CH}_3$ ,  $\nu_s(\text{COO})$ , and additional peaks centered at 402  $\text{cm}^{-1}$  attributed to Ni-O stretching vibrations (Fig. 5.6). FT-IR spectral data displays the supramolecular interactions in Ni@5AIA metallogel among the metallogel forming chemical components.

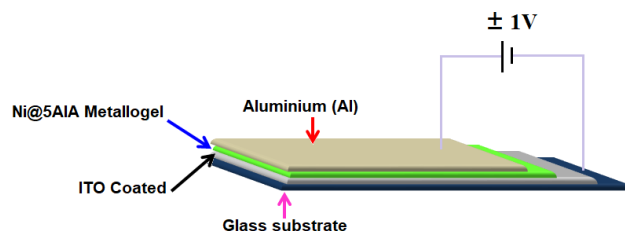


**Fig. 5.6: FT-IR spectra of the xerogel form of Ni@5AIA metallogel.**

### 5.3.4. Fabrication of thin film Device

The Schottky device for the gel was made in a sandwich configuration with ITO/Ni@5AIA metallogel/Al structure. Prior to device manufacturing, Soap Solution, Acetone, Ethanol, and Distilled Water were used sequentially in an ultrasonic bath to clean and dry Indium Tin Oxide (ITO) coated glass substrates (Fig. 5.7).



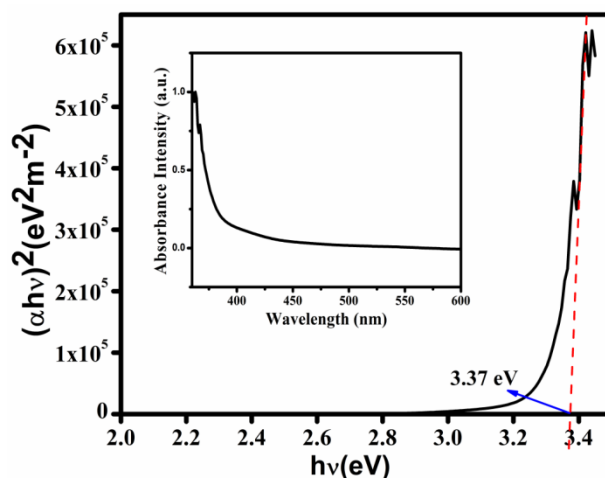


**Fig. 5.7:** Schematic diagram of MS junction device based on Ni@5AIA metallogel.

### 5.3.5. Optical characterization

To measure the optical band gap I recorded the absorption spectra of this synthesized gel in the wavelength region of 360 to 600 nm using a UV-Vis spectrophotometer and the recorded spectra are shown in Fig. 5.8 (inset). The optical band gap was determined from the analysis of the Tauc's plot using the equation

$$\alpha h\nu = A(h\nu - E_g)^n \quad (5.1)$$



**Fig. 5.8:**  $(\alpha h\nu)^2$  versus  $h\nu$  curves of Ni@5AIA, UV-vis absorption spectra (inset) were determined with the help of Tauc's equation.

Where,  $\alpha$  = Absorption coefficient,  $h$  = Planck's constant,  $\nu$  = Frequency of light,  $A$  = Energy dependent constant (which is taken as 1),  $E_g$  = Band gap,  $n$  = electron transition process dependent

const (for direct transition  $n=1/2$ ).  $(\alpha h\nu)^2$  vs  $h\nu$  plot had been shown in Fig. 5.8 where, by extrapolation of the linear part of the curve I can conclude that the material has a direct optical band gap of 3.37 eV.

### 5.3.6. Electrical Characterization of Device

I investigated the electrical properties of my synthetic gel. To explore the charge transport properties, I fabricated my synthesized gel-based thin film MS junction devices and measured current density–voltage (J–V) data within a bias range of  $\pm 1$  V. The J–V characteristics of the gel-based metal-semiconductor junction device are shown in Fig. 5.9. My synthetic gel-based device has an approximate conductivity of  $1.53 \times 10^{-5} \text{ S}\cdot\text{m}^{-1}$ , similar to that of a semiconductor. The measured J–V curve of the gel-based device shows that it has good rectifying properties, establishing Schottky diode (SD) behavior. The rectification ratio ( $J_{\text{on}}/J_{\text{off}}$ ) of the gel-based SD was determined as 34.77 based on the JV characteristic at  $\pm 1$  V.

To examine the J–V characteristics obtained in this case, I used the thermionic emission theory and applied the technique proposed by Cheung to extract some key diode parameters [63]. The following general equations are used to initiate the analysis of the J–V curve [63, 64]:

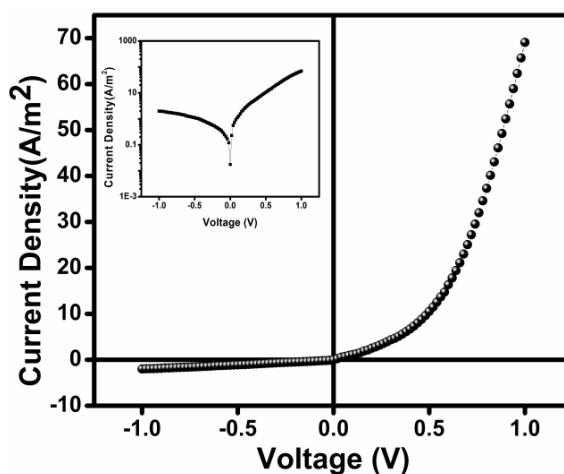
$$J = J_0 \left[ \exp\left(\frac{qV}{\eta kT}\right) - 1 \right] \quad (5.2)$$

$$J_0 = \text{Saturation Current Density} = A^* T^2 \exp\left(-\frac{q\Phi_B}{kT}\right) \quad (5.3)$$

Each parameter has its conventional interpretation [mentioned in section 1.14]. I also calculated the series resistance, ideality factor and potential barrier height using equations 5.4 and 5.5 [64, 65],

$$\frac{dV}{d \ln J} = A J R_S + \frac{\eta k T}{q} \quad (5.4)$$

$$H(J) = V - \frac{\eta k T}{q} \ln\left(\frac{J}{A^* T^2}\right) = A J R_S + \eta \Phi_B \quad (5.5)$$



**Fig. 5.9: Current Density-Voltage (J-V) graph of artificial gel under dark condition. The insets show respective J vs. V plots (in log scale).**

For complex-based devices, the ideality factor ( $\eta$ ) was calculated from the intercept of the  $dV/d(\ln J)$  vs.  $J$  plot, while the barrier height was calculated from the intercept of the  $H$  vs.  $J$  plot (Fig. 5.10). The calculated ideality factor value shows that the MS junction is not behaving ideally. This departure from the ideal value may be primarily due to barrier height, presence of series resistance and inhomogeneity of MS junction interface conditions [66]. The series resistance ( $R_s$ ) has been determined using the slope of the  $H$  vs.  $J$  and the  $dV/d(\ln J)$  vs.  $J$  plots (Fig. 5.10). Table 5.1 provides an overview of the estimated barrier potential height ( $\phi_B$ ), series resistance ( $R_s$ ), and ideality factor ( $\eta$ ) for the synthesised complex-based SD. The results shown in the table make it clear that both approaches (eqs 5.4 and 5.5) employing Cheung's functions produce results that are very similar. The synthesized complex can play an important role in the development of metallogel-based semiconductor devices, according to all measured parameters.

I have compared the parameters of my fabricated semiconductor device with other reported various semiconductor devices and presented in Table 5.2. From the Table 5.2 it is clear that my synthesized Ni(II)-Metallogel has greater electrical conductivity than other materials reported.

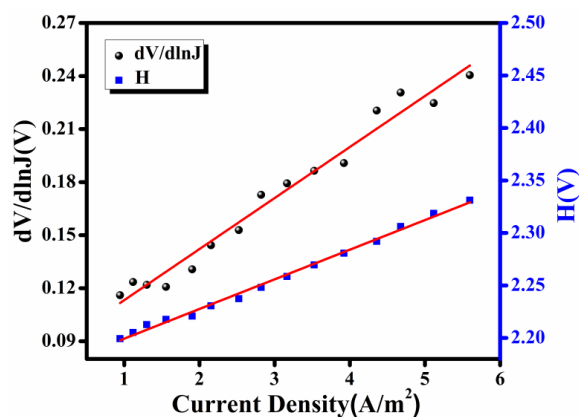


Fig. 5.10: Under dark conditions,  $dV/d\ln J$  vs.  $J$  and  $H(J)$  vs.  $J$  curves in double y axis.

Table 5.1: Electrical parameters of Gel based SD.

Rectification Ratio	Conductivity (S/m)	Series Resistance ( $\Omega$ ) from		Ideality factor ( $\eta$ )	Barrier Height $\phi_B$ (eV)
		$dV/d\ln J$ vs. $J$ curve	$H$ vs. $J$ curve		
34.77	$1.53 \times 10^{-5}$	4.17 K	3.99 K	3.18	0.68

Table 5.2: Comparison table of electrical parameters of Ni(II)-Metallogel based device with other reported results

Device Based on	Rectification Ratio	Conductivity ( $\text{Sm}^{-1}$ )	Ideality Factor ( $\eta$ )	Barrier Height ( $\phi_b$ ) (eV)	Series Resistance $R_s$ (Ohm)		Ref
					$dV/d\ln J$ vs. $J$	$H(J)$ vs. $J$	
Ni(II)-Metallogel	34.77	$1.53 \times 10^{-5}$	3.18	0.68	4170	3990	This work
Cd-CADS	19.51	$1.49 \times 10^{-5}$	0.61	0.62	2372	2220	67
Cd-N <sub>2</sub> H <sub>4</sub>	23.53	$2.04 \times 10^{-6}$	3.01	0.47	6730	6640	67
C <sub>40</sub> H <sub>34</sub> Cu <sub>2</sub> N <sub>6</sub> O <sub>18</sub>	8.46	$2.02 \times 10^{-6}$	2.78	0.47	81.7	84.3	68
C <sub>20</sub> H <sub>18</sub> CuN <sub>2</sub> O <sub>10</sub>	8.49	$2.34 \times 10^{-6}$	2.08	0.44	50150	53170	68

<b>Zn@TA</b>	37.06	$7.77 \times 10^{-6}$	3.78	0.47	3751.26	3587.73	69
<b>Ni-SA</b>	21.54	$11.16 \times 10^{-6}$	1.79	0.66	1700	1880	70
<b>Zn-SA</b>	20.83	$6.72 \times 10^{-6}$	2.53	0.70	2890	3000	70
<b>Cd-SA</b>	20.11	$4.02 \times 10^{-6}$	2.61	0.73	4110	4170	70
<b>Ni-SB</b>	1.64	$2.62 \times 10^{-6}$	3.00	0.74	18900	18830	71
<b>Zn-SB</b>	14.63	$1.18 \times 10^{-6}$	3.93	0.75	37340	3930	71
<b>Fe-metallogel</b>	42.19	$4.53 \times 10^{-6}$	2.92	0.78	14080	13420	72
<b>[(NiLB)<sub>2</sub>(SCN)<sub>2</sub>Mn]</b>	-	$5.29 \times 10^{-6}$	1.22	0.70	4025	3016	73

## 5.4. Conclusions

Briefly, a novel supramolecular Ni(II)-metallogel based on 5-aminoisophthalic acid gelator was prepared by immediate mixing of nickel acetate and 5-aminoisophthalic acid in DMF followed by sonication at room temperature. Various non-covalent interactions contribute to the formation of stable Ni@5AIA metallogels at room temperature. FESEM microstructural analyzes of the Ni@5AIA metallogel explored the flake like hierarchical architecture of the hydrogel. The mechanical stability of the Ni@5AIA metallogel material was verified by rheological tests. Optical band-gap measurements of our synthesized Ni@5AIA metallogel suggest the semiconducting nature of the metallogel. In addition, I fabricated a metal-semiconductor junction thin film device using Au metal and semiconducting Ni@5AIA metallogel. The nonlinear charge transport of the device obtained from the I-V characteristic graph confirmed the fabrication of a Schottky diode. Thus, the present study of sandwich-like configuration of ITO/Ni@5AIA metallogel/Au suggests the future possibility of achieving supramolecular Ni<sup>2+</sup> metallogel based electronic devices for advanced technology. Indeed, the work on Ni@5AIA metallogel based on 5-aminoisophthalic acid and nickel(II) source indicates a pioneering method and metallogel for the fabrication of semiconducting devices.

## References

- [1] R. Kuosmanen, K. Rissanen and Elina Sievänen, *Chemical Society Reviews*, 49 (2020) 1977-1998.
- [2] G. M. Whitesides, J. P. Mathias, C. T. Seto, *Science*, 254 (1991) 1312-1319.
- [3] J. W. Steed, *Chemical Communications*, 47 (2011) 1379-1383.
- [4] P. Dastidar, *Chemical Society Reviews*, 37 (2008) 2699-2715.
- [5] S. Dhibar, A. Dey, S. Majumdar, D. Ghosh, P. P. Ray, B. Dey, *ACS Applied Electronic Materials*, 1 (2019) 1899-1908.
- [6] (a) S. Dhibar, D. Ghosh, S. Majumdar, B. Dey, *ACS Omega*, 5 (2020) 2680-2689; (b) S. Dhibar, A. Dey, R. Jana, A. Chatterjee, G. K. Das, P. P. Ray, B. Dey, *Dalton Transactions*, 48 (2019) 17388-17394; (c) S. Dhibar, R. Jana, P. P. Ray, B. Dey, *Journal of Molecular Liquids*, 289 (2019) 111-126; (d) S. Dhibar, A. Dey, D. Ghosh, A. Mandal, B. Dey, *Journal of Molecular Liquids*, 276 (2019) 184-193; (e) S. Dhibar, A. Dey, A. Dey, S. Majumdar, A. Mandal, P. P. Ray, B. Dey, *New Journal of Chemistry*, 43 (2019) 15691-15699; (f) D. Ghosh, S. Dhibar, A. Dey, S. Mukherjee, N. Joardar, SP SinhaBabu, B. Dey, *Journal of Molecular Liquids*, 280 (2019) 1-12; (g) S. Majumdar, T. Singha, S. Dhibar, A. Mandal, P. K. Datta, B. Dey, *ACS Applied Electronic Materials*, 2 (2020) 3678-3685; (h) S. Majumdar, A. Dey, R. Sahu, S. Dhibar, P. P. Ray, B. Dey, *ACS Applied Nano Materials*, 3 (2020) 11025-11036.
- [7] (a) C. Po, Z. Ke, A. Y. Y. Tam, H. F. Chow, V. W. W. Yam, *Chemistry: A European Journal*, 19 (2013) 15735-15744; (b) S. Ganta, D. K. Chand, *Inorganic Chemistry*, 57 (2018) 3634-3645; (c) P. Chen, Q. Li, S. Grindy, N. Holten-Andersen, *Journal of American Chemical Society*, 137 (2015) 11590-11593.
- [8] (a) Q. Lin, Q. P. Yang, B. Sun, Y. P. Fu, X. Zhu, T. B. Wei, Y. M. Zhang, *Soft Matter*, 10 (2014) 8427-8432; (b) A. M. Amacher, J. Puigmartí-Luis, Y. Geng, V. Lebedev, V. Laukhin, K. Kramer, J. Hauser, D. B. Amabilino, S. Decurtins, S. X. Decurtins, *Chemical Communications*, 51 (2015) 15063-15066; (c) S. Sarkar, S. Dutta, P. Bairi, T. Pal, *Langmuir*, 30 (2014) 7833-7841.
- [9] (a) C. K. Karan, M. Bhattacharjee, *ACS Applied Materials Interfaces*, 8 (2016) 5526-5535; (b) S. Dey, D. Datta, K. Chakraborty, S. Nandi, A. Anoop, T. Pathak, *RSC Advances*, 3 (2013) 9163-9166; (c) M. O. M. Piepenbrock, N. Clarke, J. W. Steed, *Soft*

- Matter, 6 (2010) 3541-3547; (d) M. O. M. Piepenbrock, N. Clarke, J. W. Steed, Langmuir, 25 (2009) 8451-8456.
- [10] (a) Z. Yao, Z. Wang, Y. Yu, C. Zeng and K. Cao, Polymer, 119 (2017) 98-106; (b) P. Rajamalli, P. Malakar, S. Atta, E. Prasad, Chemical Communications, 50 (2014) 11023-11025.
- [11] K. Mitsumoto, J. M. Cameron, R. J. Wei, H. Nishikawa, T. Shiga, M. Nihei, G. N. Newton, H. Oshio, Chemistry: A European Journal, 23 (2017) 1502-1506.
- [12] X. Q. Wang, W. Wang, G. Q. Yin, Y. X. Wang, C. W. Zhang, J. M. Shi, Y. Yu, H. B. Yang, Chemical Communications, 51 (2015) 16813-16816.
- [13] B. Jiang, L. J. Chen, G. Q. Yin, Y. X. Wang, W. Zheng, L. Xu, H. B. Yang, Chemical Communications, 53 (2017) 172-175.
- [14] (a) F. Gou, J. Cheng, X. Zhang, G. Shen, X. Zhou, H. Xiang, European Journal of Inorganic Chemistry, 30 (2016) 4862-4866; (b) N. Kelly, K. Gloe, T. Doert, F. Hennersdorf, A. Heine, J. Marz, U. Schwarzenbolz, J. J. Weigand, K. J. Gloe, Journal of Organometallic Chemistry, 821 (2016) 182-191.
- [15] (a) S. Dhibar, A. Dey, S. Majumdar, D. Ghosh, A. Mandal, P. P. Ray, B. Dey, Dalton Transactions, 47 (2018) 17412-17420; (b) S. Dhibar, A. Dey, D. Ghosh, S. Majumdar, A. Dey, P. Mukherjee, A. Mandal, P. P. Ray, B. Dey, Chemistry Select, 4 (2019) 1535-1541; (c) S. Dhibar, A. Dey, S. Majumdar, A. Dey, P. P. Ray, B. Dey, Industrial & Engineering Chemistry Research, 59 (2020) 5466-5473; (d) S. Dhibar, A. Dey, S. Majumdar, P. P. Ray, B. Dey, International Journal of Energy Research, 45 (2021) 5486-5499; (e) S. Dhibar, S. K. Ojha, A. Mohan, S. P. C. Prabhakaran, S. Bhattacharjee, K. Karmakar, P. Karmakar, P. Predeep, A. K. Ojha, B. Saha, New Journal of Chemistry, 46 (2022) 17189-17200; (f) S. Dhibar, H. Dahiya, K. Karmakar, S. Kundu, S. Bhattacharjee, G. C. Nayak, P. Karmakar, G. D Sharma, B. Saha, Journal of Molecular Liquids, 370 (2023) 121020; (g) S. Dhibar, A. Dey, A. Dalal, S. Bhattacharjee, R. Sahu, R. Sahoo, A. Mondal, S. M. Rahaman, S. Kundu, B. Saha, Journal of Molecular Liquids, 370 (2023) 121021; (h) S. Dhibar, S. Babu, A. Mohan, G. K. Chandra, S. Bhattacharjee, K. Karmakar, P. Karmakar, S. M. Rahaman, P. Predeep, B. Saha, Journal of Molecular Liquids, 375 (2023) 121348; (i) K. Karmakar, A. Dey, S. Dhibar, R. Sahu, S. Bhattacharjee, P. Karmakar, P. Chatterjee, A. Mondal, B. Saha, RSC Advances, 13

- (2023) 2561-2569; (j) S. Dhibar, B. Pal, K. Karmakar, S. Kundu, S. Bhattacharjee, R. Sahoo, S. M. Rahaman, D. Dey, P. P. Ray, B. Saha, *Chemistry Select*, 8 (2023) e202204214.
- [16] (a) Z. Yao, Z. Wang, Y. Yu, C. Zeng & K. Cao, *Polymer*, 119 (2017) 98-106; (b) P. Rajamalli, P. Malakar, S. Atta, E. Prasad, *Chemical Communications*, 50 (2014) 11023-11025.
- [17] (a) S. Ganta, D. K. Chand, *Dalton Transactions*, 44 (2015) 15181-15188; (b) L. Yang, L. Luo, S. Zhang, X. Su, J. Lan, C. T. Chen, J. You, *Chemical Communication*. 46 (2010) 3938-3940; (c) B. Xing, M.-F. Choi, Z. Zhou, B. Xu, *Langmuir*, 18 (2002) 9654-9658; (d) X. Ma, S. Liu, Z. Zhang, Y. Niu, J. Wu, *Soft Matter*, 13 (2017) 8882-8885.
- [18] C. A. Offiler, C. D. Jones, J. W. Steed, *Chemical Communications*. 53 (2017) 2024-2027.
- [19] X. Yu, Z. Wang, Y. Li, L. Geng, J. Ren, G. Feng, *Inorganic Chemistry*, 56 (2017) 7512-7518.
- [20] M. Suzuki, K. Hanabusa, *Chemical Society Reviews*, 39 (2010) 455-463.
- [21] P. Terech, R. G. Weiss, *Chemical Reviews*, 97 (1997) 3133-3159
- [22] J. Raeburn, D. J. Adams, *Chemical Communications*, 51 (2015) 5170-5180.
- [23] S. J. Wezenberg, C. M. Croisetu, M. C. A. Stuartab, B. L. Feringa, *Chemical Science*, 27 (2016) 4341-4346.
- [24] N. Shi, G. Yin, H. Li, M. Hana, Z. Xu, *New Journal of Chemistry*, 32 (2008) 2011-2015.
- [25] K. Hanabusa, K. Hiratsuka, Kimura, M. H. Shirai, *Chemistry of Materials*, 11 (1999) 649-655.
- [26] J. W. Steed, *Chemical Society Reviews*, 39 (2010) 3686-3699.
- [27] C. Tomasini, N. Castellucci, *Chemical Society Reviews*, 42 (2013) 156-172.
- [28] A. Prathap, K. M. Sureshan, *Langmuir*, 35 (2019) 6005-6014.
- [29] D. K. Smith, *Advanced Materials*, 18 (2006) 2773-2778.
- [30] R. G. Weiss, P. Terech, Springer: Dordrecht, 2005.
- [31] (a) T-A. Asoh, A. Kikuchi, *Chemistry Communications*, 48 (2012) 10019-10021; (b) X Wang, F. Liu, X. Zheng, J. Sun, *Angewandte Chemie International Edition*, 50 (2011) 11378-11381; (c) H. Wang, M. B. Hansen, D. W. P. M. Löwik, J. C. M. van Hest, Y. Li, J. A. Jansen, S. C. G. Leeuwenburgh, *Advanced Materials*, 23 (2011) H119-H124.



- [32] (a) A. Y-Y. Tam, V. W-W. Yam, *Chemical Society Reviews*, 42 (2013) 1540-1567; (b) C. Tomasini, N. Castellucci, *Chemical Society Reviews*, 42 (2013) 156-172; (c) L. Meazza, J. A. Foster, K. Fucke, P. Metrangolo, G. Resnati, J. W. Steed, *Nature Chemistry*, 5 (2013) 42-47.
- [33] (a) M. Shirakawa, N. Fujita, S. Shinkai, *Journal of the American Chemical Society*, 125 (2003) 9902-9903; (b) J. R. Moffat, G. J. Seeley, J. T. Carter, A. Burgess, D. K. Smith, *Chemistry Communications*, 0 (2008) 4601-4603.
- [34] (a) Y. Xu, Q. Wu, Y. Sun, H. Bai, G. Shi, *ACS Nano*, 4 (2010) 7358-7362; (b) S. Burattini, B. W. Greenland, D. H. Merino, W. Weng, J. Seppala, H. M. Colquhoun, W. Hayes, M. E. Mackay, I. W. HamLey, S. J. Rowan, *Journal of the American Chemical Society*, 132 (2010) 12051-12058.
- [35] W. Fang, Y. Zhang, J. Wu, C. Liu, H. Zhu, T. Tu, *Chemistry : An Asian Journal*, 13 (2018) 712-729.
- [36] J. Kim, J. A. Hanna, M. Byun, C. D. Santangelo, R. C. Hayward, *Science*, 335 (2012) 1201-1205.
- [37] A. R. Hirst, B. Escuder, J. F. Miravet, D. K. Smith, *Angewandte Chemie International Edition* 47 (2008) 8002-8018.
- [38] X. Cheng, J. Pan, Y. Zhao, M. Liao, H. Peng, *Advanced Energy Materials*, 8 (2018) 1702184.
- [39] (a) S. Sarkar, S. Dutta, S. Chakrabarti, P. Bairi, T. Pal, *ACS Applied Materials Interfaces*, 6 (2014) 6308-6316; (b) Q. Lin, T. T. Lu, X. Zhu, B. Sun, Q. P. Yang, T. B. Wei, Y. M. Zhang, *Chemistry Communications*, 51 (2015) 1635-1638.
- [40] W. Wang, H. Wang, C. Ren, J. Wang, M. Tan, J. Shen, Z. Yang, P. G. Wang, L. Wang, *Carbohydrate Research*, 346 (2011) 1013-1017.
- [41] Md. R. Saboktakin, R. M. Tabatabaei, *International Journal of Biological Macromolecules*, 75 (2015) 426-436.
- [42] Y. Zhao, S. Song, X. Ren, J. Zhang, Q. Lin, Y. Zhao, *Chemistry Review*, 122 (2022) 5604-5640.
- [43] W. L. Guan, K. M. Adam, M. Qiu, Y. M. Zhang, H. Yao, T. B. Wei, Q. Lin, *Supramolecular Chemistry*, 32 (2020) 578-596.

- [44] W. H. Binder, L. Petraru, T. Roth, P. W. Groh, V. Pálfi, S. Keki, B. Ivan, *Advanced Functional Materials*, 17 (2007) 1317-1326.
- [45] A. Khan, R. R. Kisannagar, C. Gouda, D. Gupta, H. C. Lin, *Journal of Materials Chemistry A*, 8 (2020) 19954-19964.
- [46] B. Xue, M. Qin, T. Wang, J. Wu, D. Luo, Q. Jiang, Y. Li, Y. Cao, W. Wang, *Advanced Functional Materials*, 26 (2016) 9053-9062.
- [47] B. Zhang, J. N. H. Reek, *Chemistry: An Asian Journal*, 16 (2021) 3851-3863.
- [48] S. Biswas, U. Chatterjee, S. Sarkar, F. Khan, D. Bera, M. Mukhopadhyay, S. Goswami, S. Chakrabarti, S. Das, *Colloids & Surfaces B*, 188 (2020) 110803.
- [49] N. Kelly, K. Gloe, T. Doert, F. Hennersdorf, A. Heine, J. Maerz, U. Schwarzenbolz, J. J. Weigand, K. Gloe, *Journal of Organometallic Chemistry*, 821 (2016) 182-191.
- [50] L. Yan, C. Liu, L. Shen, J. Li, X. Liu, M. Lv, C. Su, Z. Ye, *Chemistry Letters*, 47 (2018) 640-642.
- [51] J. H. Lee, Y. E. Baek, K. Y. Kim, H. Choi, J. H. Jung, *Supramolecular Chemistry*, 28 (2016) 870-873.
- [52] S. Dhibar, S. K. Ojha, K. Karmakar, P. Karmakar, S. Bhattacharjee, P. Chatterjee, A. K. Ojha, B. Saha, *Chemistry Africa*, 6 (2023) 3217-3228.
- [53] J. Chen, T. Wang, M. Liu, *Inorganic Chemistry Frontiers*, 3 (2016) 1559-1565.
- [54] J. L. Zhong, X. J. Jia, H. J. Liu, X. Z. Luo, S. G. Hong, N. Zhang, J. B. Huang, *Soft matter*, 12 (2016) 191-199.
- [55] L. Arnedo-Sánchez, Nonappa, S. Bhowmik, S. Hietala, R. Puttreddy, M. Lahtinen, L. D. Cola, K. Rissanen, *Dalton Transactions*, 46 (2017) 7309-7316.
- [56] X. Li, J. Shi, Y. Gao, H. C. Lin, B. Xu, *Journal of American Chemical Society*, 133 (2011) 17513-17518.
- [57] V. Singh, S. Kala, T. Rom, A. K. Paul, R. Pandey, *Dalton Transactions*, 52 (2023) 7088-7103.
- [58] H. Guo, Q. Feng, K. Xu, J. Xu, J. Zhu, C. Zhang, T. Liu, *Advanced Functional Materials*, 29 (2019) 1903660.
- [59] G. Lepcha, T. Singha, S. Majumdar, A. K. Pradhan, K. S. Das, P. K. Datta, B. Dey, *Dalton Transactions*, 51 (2022) 13435-13443.

- [60] P. Terech, M. Yan, M. Maréchal, G. Royal, J. Galveza, S. K. P. Velu, *Physical Chemistry Chemical Physics*, 15 (2013) 7338-7344.
- [61] N. Malviya, C. Sonkar, B. K. Kundu, S. Mukhopadhyay, *Langmuir*, 34 (2018) 11575-11585.
- [62] (a) E. M. M. Ibrahim, L. H. Abdel-Rahman, A. M. Abu-Dief, A. Elshafaie, S. K. Hamdan, A. M. Ahmed, *Materials Research Bulletin*, 107 (2018) 492-497; (b) A. Elshafaie, L. H. Abdel-Rahman, A. M. Abu-Dief, S. K. Hamdan, A. M. Ahmed, E. M. M. Ibrahim, *Nano*, 13 (2018) 1850074; (c) L. H. Abdel Rahman, A. M. Abu-Dief, R. M. El-Khatib, S. M. Abdel-Fatah, A. M. Adam, E. M. M. Ibrahim, *Applied Organometallic Chemistry*, 32 (2018) e4174.
- [63] R. Jana, S. Sil, A. Dey, J. Datta and P. P. Ray, *AIP Advances*, 2018, 8, 125104.
- [64] J. Datta, A. Dey, S. K. Neogi, M. Das, S. Middya, R. Jana, S. Bandopadhyay, A. Layek, P. P. Ray, *IEEE Transactions on Electron Devices*, 64 (2017) 4724-4730.
- [65] S. K. Cheung, N. W. Cheung, *Applied Physics Letters*, 49 (1986) 85-87.
- [66] J. Datta, M. Das, S. Sil, S. Kumar, A. Dey, R. Jana, S. Bandyopadhyay, P. P. Ray, *Material Science in Semiconductor Processing*, 91 (2019) 133-145.
- [67] S. Majumdar, B. Pal, R. Sahu, K. S. Das, P. P. Ray, B. Dey, *Dalton Transactions*, 51 (2022) 9007-9016.
- [68] A. Hossain, A. Dey, S. K. Seth, P. P. Ray, P. Ballester, R. G. Pritchard, J. Ortega-Castro, A Frontera, S. Mukhopadhyay, *ACS Omega*, 3 (2018) 9160-9171.
- [69] S. Majumdar, A. Dey, R. Sahu, G. Lepcha, A. Dey, P. P. Ray, B. Dey, *Materials Research Bulletin*, 157 (2023) 112003.
- [70] G. Lepcha, S. Majumdar, B. Pal, K. T. Ahmed, I. Pal, B. Satpati, S. R. Biswas, P. P. Ray, B. Dey, *Langmuir*, 39 (2023) 7469-7483.
- [71] G. Lepcha, B. Pal, S. Majumdar, K. T. Ahmed, I. Pal, S. R. Biswas, P. P. Ray, B. Dey, *Materials Advances*, 4 (2023) 2595-2603.
- [72] S. Saha, B. Pal, K. S. Das, P. K. Ghosh, A. Ghosh, A. De, A. K. Das, P. P. Ray, R. Mondal, *ChemistrySelect*, 7 (2022) e202203307.
- [73] M. Das, M. Das, S. Ray, U. K. Das, S. Laha, P. P. Ray, B. C. Samanta, T. Maity, *New Journal of Chemistry*, 46 (2022) 21103-21114.

\*\*\*





*"Our greatest weakness lies in giving up. The most certain way to succeed is always to try just one more time."*

- Thomas A. Edison



# Chapter 6

---

## **Introduction to Crystalline Silicon selective emitter solar cell**

## 6.1. Introduction

The growing need for electricity prompts the exploration of cost-effective renewable energy sources. Solar photovoltaic technology emerges as a crucial renewable resource due to its abundance, cost-effectiveness, and higher efficiency. Although various solar cell technologies are globally adopted, many are not feasible for large-scale production due to budget constraints. This thesis aims to develop cost-effective solar cells with industrial potential.

A selective emitter refers to an emitter selectively doped rather than uniformly doped. Selective emitter solar cells are introduced to simultaneously address surface recombination velocity and contact resistance, aiming to minimize both. The lightly doped emitter region, where light-generated carriers are collected, reduces recombination velocity, thus increasing both  $V_{oc}$  &  $I_{sc}$ . Meanwhile, the heavily doped emitter region beneath the metal contact reduces contact resistance, improving the fill factor. Selective emitter structures are widely employed due to their high optical absorption, enhancing overall solar cell efficiency. While conventional techniques for forming selective emitters exist, this thesis elaborates on newly adopted methods. The significance of selective emitters in solar cell technologies is discussed in detail.

## 6.2. Energy Scenario

The global demand for energy is steadily increasing each year. Projections suggest that total energy consumption on Earth will rise by 0.7% to 1.4% annually from 2008 to 2035, contingent upon the selected energy projection [1]. This surge is primarily driven by the rapid growth of the world population and economic conditions, necessitating the production of sustainable energy sources. Till now, fossil fuels such as oil (40%), coal (33%), and natural gas (27%) have been the main sources of energy production [2]. However, due to resource limitations and environmental concerns, this reliance on fossil fuels is unsustainable in the long run [3]. This situation has spurred efforts to explore alternative energy sources.

Renewable energy sources, including nuclear, wind, geothermal, and solar power, offer low-carbon alternatives with unlimited and pollution-free resources. Solar energy, in particular, stands out as a highly promising solution to our energy needs due to its abundance, cost-effectiveness, and higher efficiency [4]. Unlike wind power, which relies on specific wind



conditions, solar power is universally accessible, making it a viable option for energy generation worldwide [5].

### 6.3. Utilization of Solar Energy

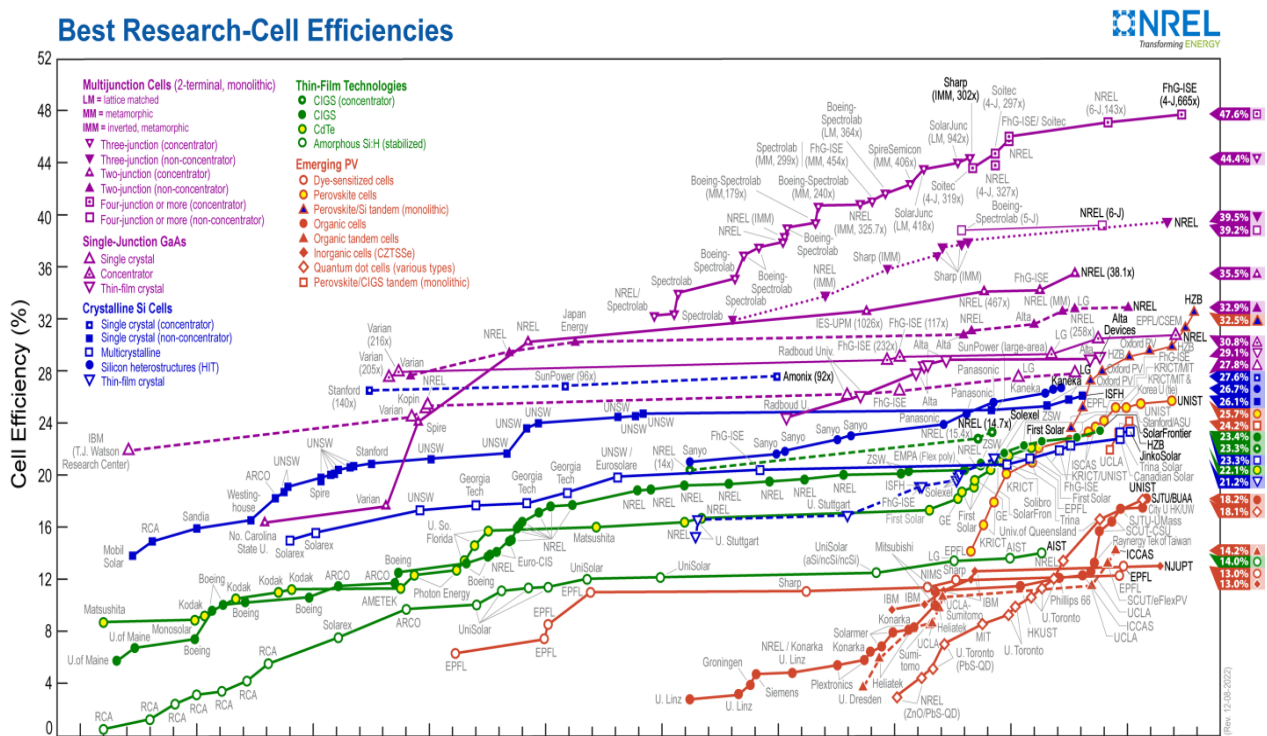
Solar energy conversion is broadly categorized into two technologies: solar thermal and photovoltaic (PV). In solar thermal systems, sunlight is utilized to generate heat for household purposes or to be converted into electricity within extensive concentrated solar power facilities. On the other hand, PV technology directly converts sunlight into DC electricity. This concept was initially observed by French physicist Edmond Becquerel in 1839 [6]. The absorption of photons and subsequent generation of charge carriers within the semiconductor material depend on the energy of the incident photons and the material's band gap. Typically, semiconductors possess band gap values within the visible or near-infrared range of the solar spectrum [7], making them ideal for solar energy conversion [8]. In the presence of an electric field, typically created by a p-n junction formed through doping of semiconductor materials, photo-generated charge carriers are separated and extracted from the device, resulting in the conversion of sunlight into DC electricity. PV devices have gained popularity due to their versatility, scalability, independence from large infrastructure, and decentralized nature, making them suitable for various applications and off-grid locations. Consequently, the global market share of PV in the energy sector has experienced significant growth in recent years.

### 6.4. A Brief History of Solar Cell

His experiment involved submerging platinum or silver electrodes covered with a light-responsive material such as AgCl or AgBr into an acidic solution, then subjecting them to different types of light (sunlight, blue, or ultraviolet). This setup allowed for the demonstration of electricity generation through the photovoltaic effect. Forty years later, William Adams and Richard Day improved upon this work by discovering that selenium, when brought into contact with heated platinum contacts, could produce an electric current [9]. In 1894, Charles Fritts produced the first large-area solar cell, consisting of a layer of selenium sandwiched between gold and another metal, a design that now bears his name [10]. In 1914, Goldman and Brodsky proposed the existence of a potential barrier to current flow at the interface of the semiconductor metal, which is now known as a rectifying action [11]. Throughout the 1930s, Walter Schottky

and others developed the theory of metal semiconductor barrier layers, now known as Schottky barriers. The modern era of photovoltaic began in 1948 with Teal and Little adapting the Czochralski process [12, 13] to obtain crystalline wafers of germanium or silicon [14].

In 1954, Chapin, Fuller, and Pearson of Bell Laboratories produced the first p-n homojunction silicon-based solar cell, boasting an efficiency of 6%, a significant improvement over previous attempts [15]. That same year, Reynolds and colleagues introduced the initial heterojunction photovoltaic device utilizing cadmium sulfide (CdS) [16], also achieving 6% efficiency. Despite this, silicon remained the primary material for photovoltaic devices.



**Fig. 6.1: Improvements in the efficiency of different categories of solar cells over time.**  
(Adapted from Ref. 21)

Efforts to improve solar cell efficiency continued, with Shockley and Queisser reporting a theoretical efficiency of 30% for a solar cell with a band gap of 1.1 eV in 1961 [17]. In 1970, Zhores Ivanovich Alferov and his team developed the first highly effective heterostructure solar

cell made of GaAs for space applications [18], a significant milestone in solar cell technology. Solar cells have since found extensive use in power satellites and telecommunication systems. Alferov received the Nobel Prize in Physics in 2000 for his contributions to this area [19]. In 1985, the Green team at the University of New South Wales (UNSW) reported a breakthrough in solar cell efficiency, achieving over 20% conversion efficiency on a silicon wafer [20]. The efficiency of various types of PV cells has continued to increase over the years (Fig. 6.1).

By the 2000s, solar cell technologies had greatly improved, with many becoming commercially available, leading to a cumulative worldwide installation capacity of 40 GW by 2010 [22]. Despite global economic challenges, research and industrial efforts have persisted in enhancing solar cell performance while reducing costs.

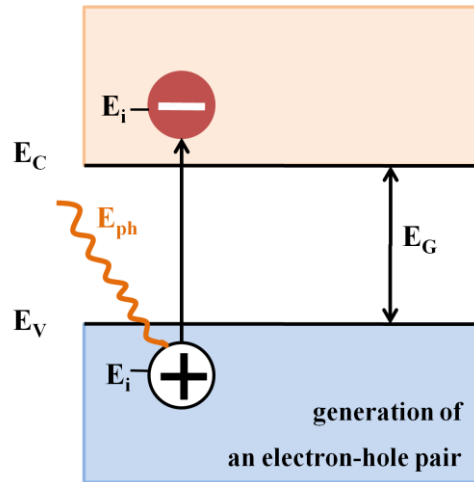
## 6.5. Solar Cell: Basics

Solar cells operate on the concept of the phenomenon of photovoltaic, which involves the creation of an electric potential where two distinct materials meet upon exposure to electromagnetic radiation. This phenomenon is intricately linked to the photoelectric phenomenon, where electrons are discharged from a substance upon capturing photon energy surpassing a specific threshold frequency inherent to the material. Albert Einstein comprehended in 1905 that this occurrence could be elucidated by considering light as composed of discrete energy packets known as photons. The photovoltaic effect encompasses three fundamental stages:

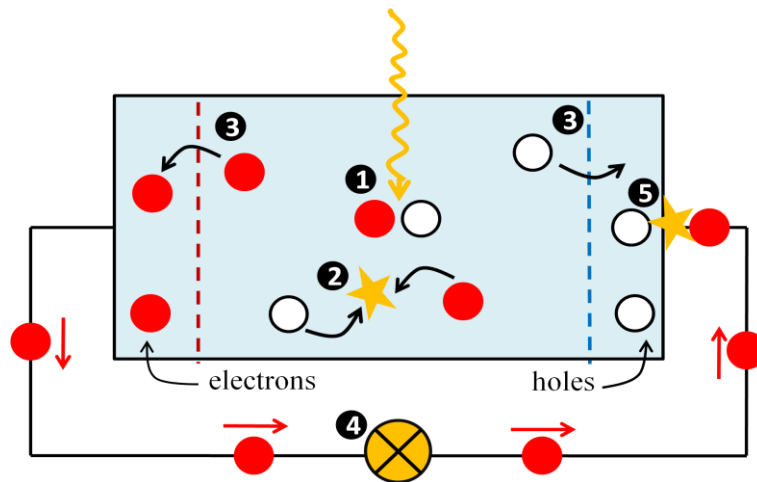
### 6.5.1 Creation of Charge Carriers through Photon Absorption in Junction-Forming Materials

When a photon is absorbed within a material, its energy is utilized to elevate an electron to a higher energy level ( $E_f$ ) from its initial energy level ( $E_i$ ) (as depicted in Fig. 6.2). The absorption of photons occurs only when the energy levels of the electron ( $E_i$  and  $E_f$ ) match the energy of the photon, described by the equation  $h\nu = E_f - E_i$ . In a perfect semiconductor, electrons have the potential to occupy energy levels situated beneath the valence band edge ( $E_v$ ) and beyond the conduction band edge ( $E_c$ ). The region between these bands doesn't contain permissible energy states for electron occupancy, defining what's known as the band gap ( $E_g = E_c - E_v$ ). If a photon

carrying an energy level lower than  $E_g$  interacts with an ideal semiconductor, it will pass through without being absorbed.



**Fig. 6.2:** illustrates the absorption of a photon by a semiconductor with a band gap  $E_g$ . When the photon, with energy  $E_{ph} = h\nu$ , interacts with the semiconductor, it prompts the electron's transition from the initial energy state ( $E_i$ ) to the final energy state ( $E_f$ ), creating a hole at the initial energy state ( $E_i$ ).



**Fig. 6.3:** A basic solar cell model: (1) When a photon is absorbed, it produces an electron-hole pair. (2) Typically, these electrons and holes recombine. (3) However, with semi-permeable membranes, the electrons and holes can be isolated. (4) The isolated electrons can power an electric circuit. (5) Once the electrons complete the circuit, they recombine with holes.

When an electron transitions from  $E_i$  to  $E_f$ , an empty space is formed at  $E_i$ , known as a hole, which behaves as a particle carrying a positive elementary charge. Photon absorption results in the formation of an electron-hole pair within the semiconductor material, converting the photon's radiative energy into the chemical energy of the pair, as depicted in Fig. 6.3(1). The highest possible efficiency of converting radiant energy into chemical energy is constrained by the laws of thermodynamics, ranging from 67% for non-concentrated sunlight to 86% for fully concentrated sunlight [23].

### **6.5.2. Sequential Segregation of the Photo-Induced Charge Carriers within the Junction**

Typically, the pair of electrons and holes tends to recombine, where the electron returns to its starting energy level,  $E_i$ , depicted in Fig. 6.3(2). Subsequently, the energy is discharged either as a light particle through transferring its energy to other electrons or radiative recombination, holes, or lattice vibrations through nonradiative processes.

To harness the energy contained within the electron-hole pair for external work in a circuit, semi-permeable or selective-permeable membranes are necessary on both sides of the absorber. These membranes ensure that electrons can only exit across one side and holes through the other, as shown in Fig. 6.3(3), typically composed of n- and p-type materials in solar cells.

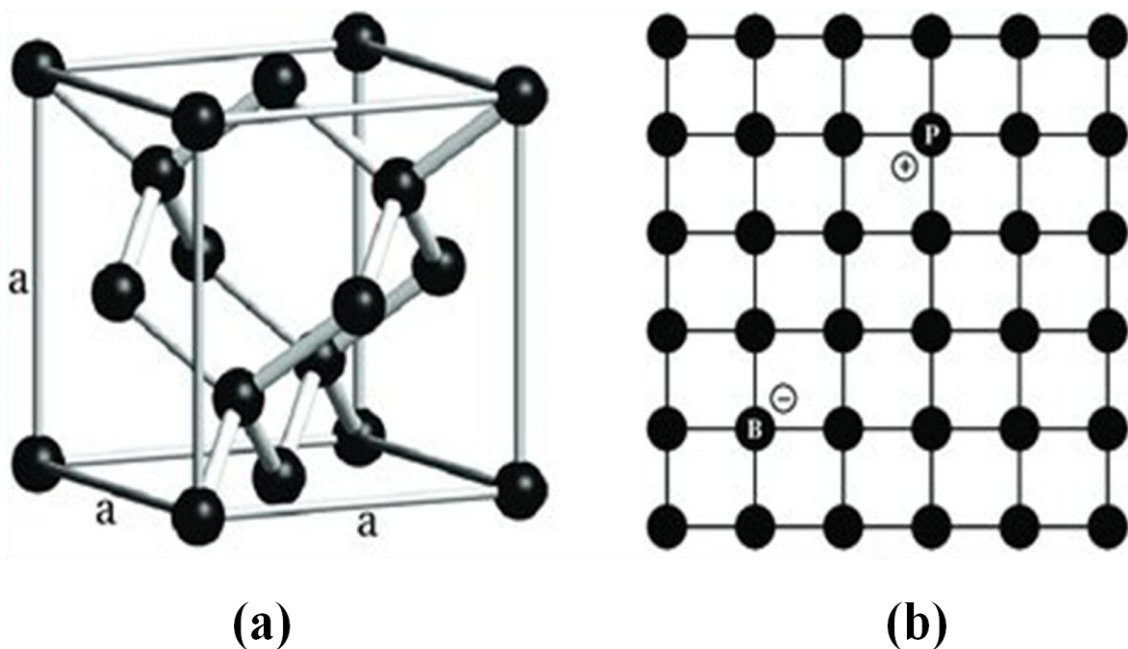
The design of a solar cell must facilitate the timely arrival of electrons and holes at the membranes before they undergo recombination, entails that the period for charge carriers to reach the membranes needs to be briefer than their lifespan. This necessity imposes a limitation on the absorber's thickness.

### **6.5.3. Gathering the Photo-generated Charge Carriers at the Terminals of the Junction**

In the end, electrical contacts are utilized to draw out the charge carriers from the solar cells, enabling them to perform work in an external circuit, as depicted in Fig. 6.3(4). The chemical energy stored in the pairs of electron & hole is then transformed into electrical energy. Subsequently, once the electrons traverse across the circuit, they reunite with holes at the interface of a metal absorber, as shown in Figure 6.3(4).

## 6.6. Crystalline Silicon Solar Cell: PV market overview

Approximately 95% of the photovoltaic (PV) market remains dominated by crystalline silicon (c-Si) solar cells [24]. This prevalence can be attributed to several factors: its widespread availability, resistance to high temperatures, extended lifetime for minority carriers with significant diffusion lengths, resistance to aging, cost-effectiveness, and lack of toxicity [25]. The crystallographic unit cell of c-Si, depicted in Fig. 6.4(A), exhibits a diamond cubic structure, wherein each silicon atom forms four bonds with others. C-Si functions as an indirect semiconductor possessing a band gap of 1.12 eV. Crystalline silicon-based PV systems command such a substantial market share due to the fusion of advanced production methods, achieving module efficiencies exceeding 15%, utilization of readily available manufacturing equipment, and processing with minimal capital investment. The origins of c-Si solar cells trace back to 1954 when Bell Laboratories unveiled the first iteration with 6% conversion efficiency [26]. Subsequent research endeavors have focused on enhancing efficiency, culminating in contemporary c-Si solar cells achieving efficiencies of up to 25.0% [27].

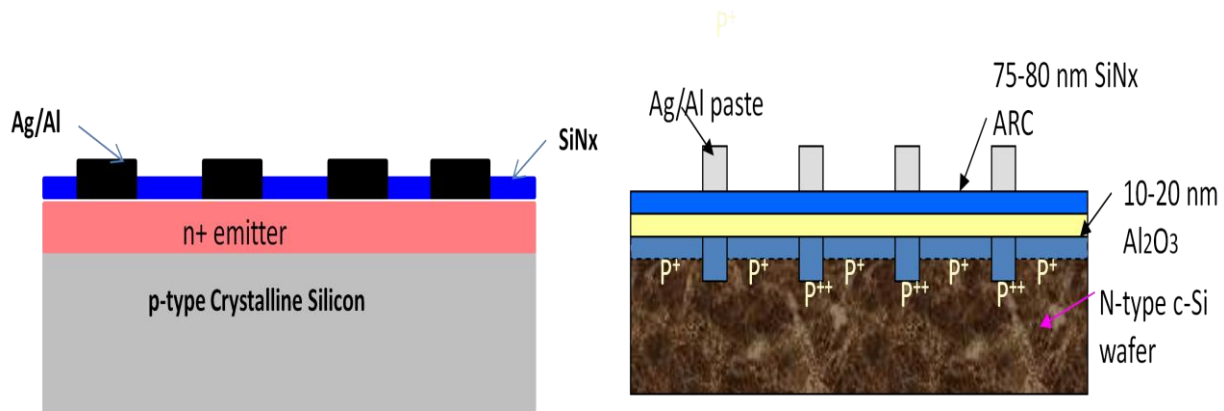


**Fig. 6.4: The three-dimensional arrangement of crystalline silicon (a) and its two-dimensional depiction (b) with boron and phosphorus doping substituted at lattice sites (Adapted from Ref. 11)**

## 6.7. Selective Emitter Solar cell: efficient Solar cell design

The quality of the front contact, particularly with a selective emitter, is notably better compared to cells featuring uniformly doped emitters. The sheet resistance is a critical factor affecting the efficiency of crystalline silicon (C-Si) solar cells as it influences surface recombination velocity. While a uniform doping method can lower the contact resistance at the metal-semiconductor interface, it tends to increase surface recombination velocity, thereby reducing cell performance. Employing a lightly doped emitter results in higher sheet resistance and lower surface recombination rate, leading to improved internal quantum efficiency, especially in the short wavelength range. Conversely, heavily doped emitters offer lower contact resistance but decrease carrier lifetime due to heightened Auger recombination and Shockley-Read-Hall recombination. To address the challenge of balancing recombination and contact resistance, selective emitter solar cells have been developed. These cells feature a lightly doped emitter in the region where light-generated carriers are collected to reduce recombination velocity, while the region below the contact is heavily doped to minimize contact resistance.

Efficient crystalline silicon solar cells necessitate an effective emitter design that minimizes both contact resistance and surface recombination velocity. This entails designing an emitter capable of efficiently gathering light-generated carriers while minimizing surface recombination and establishing good metal contacts with low resistance. Achieving these dual objectives is unattainable with a uniformly doped i.e. homogeneous emitter (Fig. 6.5(a)). Hence, the adoption of a selective emitter (Fig. 6.5(b)) structure becomes crucial due to its superior blue response in the short wavelength spectrum, leading to enhanced conversion of light into electricity in that range. This structure resolves the inherent trade-off between surface recombination velocity and contact resistance. The illuminated emitter surface, where light is absorbed and carriers are generated, features light doping to reduce surface recombination velocity, thereby boosting both short circuit current density ( $J_{sc}$ ) and open circuit voltage ( $V_{oc}$ ). Conversely, the non-illuminated emitter surface beneath the metal finger contact is heavily doped to mitigate contact resistance, thereby enhancing the fill factor [28].



**Fig. 6.5: Schematic diagram of (a) Homogeneous emitter, (b) Selective emitter**

In the selective emitter formation process, I opted for n-type silicon wafer due to several reasons:

- N-type silicon offers a higher minority carrier lifetime compared to p-type silicon [29].
- N-type silicon does not experience light-induced degradation (LID) because it lacks Boron [29, 30].
- Both theoretical and experimental findings suggest that n-type silicon has fewer recombination-active defects [31].
- N-type silicon exhibits greater tolerance to high-temperature processing compared to p-type silicon [29].
- N-type silicon is less sensitive to transition metal impurities like iron (Fe), resulting in a higher tolerance for variations in the feedstock [30, 32].

## 6.8. Fabrication of selective emitter using different techniques

A notable advancement in research on selective emitters provides a compelling rationale to undertake a review and explore the evolution of the growth mechanism over time and its practical application in solar cells. In 1997, U. Besu-Vetrella et al. produced solar cells made of silicon with selective emitters and a large surface area. They initially created a lightly doped uniform emitter through rapid thermal diffusion originating from a Phosphorous-doped Spin-On Glass (SOG) film. Laser over-doping was then performed utilizing a Q-switched, Frequency doubled Nd-YAG laser to achieve the selective emitter [33]. In the same year, J. Horzel et al. introduced a technique to create selective emitters in a single diffusion process without the need



for masking or etching. They selectively applied a phosphorous-containing doping source to the front side of a p-type crystalline Si substrate in paste form, which was then processed in a conveyor belt furnace. This resulted in two simultaneous diffusion processes at different rates, leading to deeply diffused regions under the printed doping source and adjacent regions with shallower doping due to indirect diffusion of phosphorous atoms through the gas ambient [34].

In 2003, A. Mouhoub et al. presented two primary methods for realizing multicrystalline silicon selective emitters: homogeneous diffusion of a heavily doped emitter followed by chemical etching, and deposition of a doping source via screen printing followed by annealing in a belt furnace. The doping paste was selectively applied to the front side of the wafer, resulting in deeply diffused regions under the printed doping source and diffusion of doping atoms into adjacent regions via the gas atmosphere [35].

In 2008, A. Dastgheib-Shirazi et al. proposed a wet chemical approach for fabrication of selective emitters on monocrystalline and multicrystalline silicon solar cells using a single-side diffusion process. Initially, emitter diffusion was performed using  $\text{POCl}_3$ , followed by homogenous etching-back in an acidic etch bath and deposition of a silicon nitride anti-reflection layer on the front side using Plasma-Enhanced Chemical Vapor Deposition (PECVD). Contacts were then screen printed, sintered, and edge isolated [36].

In 2010, T. C. Röder et al. suggested add-on laser tailored selective emitter solar cells, where an n-type phosphorus-doped emitter and phosphosilicate glass (PSG) layer were created on the wafer surface through conventional furnace diffusion using  $\text{POCl}_3$ . Subsequently, laser pulses were used to locally melt the wafer surface, allowing for re-crystallization and epitaxial formation of a highly phosphorus-doped n-type selective emitter without the inclusion of dislocations or grain boundaries. Subsequently, the PSG layer is removed using HF, and a  $\text{SiN}_x$  ARC is deposited on the top of the cell utilizing PECVD. Screen printing, firing of both front and rear contacts, and laser edge isolation are then carried out to complete the fabrication of the solar cell [37]. In the same year, Homer Antoniadis and colleagues introduced a novel approach to silicon nanoparticle ink selective emitter solar cells. Their method involved a sequence of steps: initial screen-printing to apply silicon ink for forming heavily doped regions, followed by a drying phase to eliminate organic solvents and enhance the density of the silicon ink film.

Subsequently, n-type diffusion was conducted, followed by the removal of PSG. The process concluded with contact co-firing and laser edge isolation [38].

In 2012, Ulrich Jäger and co-authors demonstrated the advantages of selective emitters produced through laser doping from PSG for p-type silicon solar cells with passivated surfaces. Following an alkaline texturization step, a diffusion barrier was applied to the rear side of the cell using PECVD. The wafers underwent thermal tube furnace diffusion in a  $\text{POCl}_3$  atmosphere, with a thin thermal oxide passivating both front and rear surfaces. A silicon nitride  $\text{SiN}_x$  anti-reflective coating was applied to the front side, while a dielectric layer deposited by PECVD capped the rear passivation layer to enhance passivation quality and internal reflectivity. Metallization was achieved through screen printing, and localized contacts at the back surface were established using the laser-fired contacts (LFC) method [39].

In 2013, Yen-Po Chen and collaborators proposed a different approach involving single-crystalline silicon selective emitter solar cells, created through a chemical etching method. This technique began with the formation of shallow trenches, corresponding to the metal contact areas, achieved through screen printing of a mask and chemical etching. Heavy doping was then applied across the entire front surface of the silicon wafer in a high-temperature diffusion furnace. An acid-resistant polymer mask was screen-printed and aligned to cover the shallow trenches, followed by an etch-back process utilizing acid etching to create a selective emitter structure. Notably, this method required two screen printing steps for achieving the selective emitter structure and differed from other etch-back methods in two key aspects: firstly, the creation of shallow trenches followed by heavy doping, as opposed to doping preceding the etch-back in alternative methods; secondly, the presence of shallow grooves with a depth of several micrometers or greater for metal contacts within this selective emitter design, contrasting with methods not involving trench formation [40].

In 2014, Prabir Kanti Basu and colleagues introduced a method for creating selective emitters in p-type monocrystalline silicon wafer solar cells using a non-acidic etch-back process. The procedure included inline phosphorus diffusion (resulting in a sheet resistance of approximately  $40\Omega/\text{sq}$ ), removal of the rear junction using  $\text{HF-HNO}_3\text{-H}_2\text{SO}_4$ , and KOH solutions, application of

an etch mask on the emitter side via screen printing, PSG removal, etch back to achieve a sheet resistance of around  $100\Omega/\text{sq}$ , and subsequent removal of the etch mask. This process combined emitter etch-back and etch-mask dissolution into a single procedure, diminishing the total count of processing stages in contrast to etch-back-dependent selective emitter methods [41]. A method called "laser-assisted doping" was utilized by A. Djelloul et. al. in the same year to create a selective emitter on multicrystalline silicon (mc-Si). They formed homogeneous and lightly doped  $\text{POCl}_3$  emitters through thermal diffusion, removing the PSG layer immediately with an HF dip. Silicon nitride ( $\text{SiN}_x$ ) ARC was then deposited via PECVD. During the laser doping process, the highly doped  $n^{++}$  regions of the selective emitter were aligned based on the grid of front-side metallization. The naturally formed phosphorus-rich dead layer, resulting from the diffusion process, served as the phosphorus source for the  $n^{++}$  region. Front and back contacts were screen-printed and subjected to co-firing in a belt furnace, after which laser edge isolation was performed [42].

In 2015, a double textured selective emitter (DTSE) solar cell was fabricated by C. Kim et al. using a silicon wafer. The  $40 \times 40 \text{ mm}^2$  silicon substrates underwent texturing to create a surface with pyramid-shaped features, while nanowires were generated through a metal-assisted chemical etching process utilizing silver nanoparticles. All surface modifications involving micro and nanostructures were carried out using wet-based methods. The heavily doped and shallow emitters required for selective emitter solar cells were created via  $\text{POCl}_3$  diffusion and a subsequent chemical etch-back process. Front and rear electrodes were prepared using a conventional screen printing technique [43].

In 2016, R. S. Davidsen et al. describe the production of nanostructured silicon solar cells with a laser-doped selective emitter (LDSE). These nanostructured cells were achieved using a one-step, mask-free, scalable reactive ion etch (RIE) process to texture the surface. The selective emitter was created by laser doping using a continuous wave (CW) laser, followed by contact formation through light-induced plating of nickel and copper [44].

In 2017, Y. Tao presented the creation of a selective boron emitter ( $p^+/p^{++}$ ) using a process involving screen-printed resist masking and wet chemical etching. Initially, a porous silicon layer was grown and then removed using this method. Different wet-chemical solutions for producing the porous silicon layer were explored. Following the etch-back procedure, the boron emitter

underwent thermal oxidation to reduce the surface concentration and the emitter saturation current density  $J_{0e}$ . Various etched-back emitters were assessed by measuring  $J_{0e}$  on symmetric test structures with passivation by atomic layer deposited aluminum oxide ( $\text{Al}_2\text{O}_3$ ) [45]. In that year, S. Wang proposed a novel approach to laser doping combined with grooving, creating narrow grooves with heavily doped walls in a single step, followed by the formation of self-aligned metal contacts through plating. This method combines the advantages of both buried contact solar cells (BCSC) and laser-doped selective emitter cells [46].

In the year 2018, W. Wu stated that implementing a laser-doped selective emitter can enhance the balance between recombination in the emitter and the specific contact resistance of Ag-Si. Additionally, Wu noted that incorporating a double-screen-printed rear aluminum grid can reduce the series resistance in industrial bifacial passivated emitter and rear cells (PERC) [47]. In that same year, S. Simayi introduced the advancement of an n-type bifacial solar cell featuring a boron selective emitter ( $p^+/p^{++}$ ). The cells were crafted through a standard fabrication process involving tube-furnace thermal diffusion utilizing liquid sources:  $\text{BBr}_3$  for the front-side boron emitter and  $\text{POCl}_3$  for the rear-side phosphorus back-surface field (BSF). The  $p^+/p^{++}$  configuration was achieved via screen-printed resist masking and wet chemical etching technology. Both the front and rear electrodes were created using screen-printed contacts featuring H-patterns. While the cell efficiency with the selective boron emitter closely matched that with the homogeneous emitter, the selective emitter solar cell exhibited a 4.4 mV higher  $V_{oc}$  compared to the homogeneous emitter solar cell. Finally, a recombination analysis of the completed cell was conducted [48].

## References

- [1] U.S. Energy Information Administration, International Energy Outlook 2010 (2010).
- [2] BP Statistical Review of World Energy 2010 (2010).
- [3] International Energy Agency, World Energy Outlook 2010 (2010).
- [4] German Advisory Council on Global Change (WBGU), World in Transition – Towards Sustainable Energy Systems (2004).
- [5] Global Energy Review 2020, Flagship report — April 2020.
- [6] A. E. Becquerel, Comptes Rendus – Academia des sciences, 9 (1839) 145.
- [7] R. S. Muller & T. I. Kamins, Device Electronics for Integrated Circuits, John Wiley and Sons, New York, NY, Third Edition (2003).
- [8] A. Goetzberger, W. Shockley, Journal of Applied Physics, 31 (1960) 1821.
- [9] W. G. Adams, R. E. Day, Proceedings of the Royal Society of London, A25 (1877) 113.
- [10] C. E. Fritts, American Journal of Science, 26 (1883) 465.
- [11] J. Nelson, The Physics of Solar Cells. Imperial College Press, First Edition (2003).
- [12] J. Czochralski, Zeitschrift fur Physikalische Chemie 92 (1917) 219.
- [13] W. Zulehner, Journal of Crystal Growth, 65 (1983) 189
- [14] D. C. Brock, Useless No More: Gordon K. Teal, Germanium, and Single-Crystal Transistors, Chemical Heritage Newsmagazine (Chemical Heritage Foundation) 24, 1, Spring 2006.
- [15] D. M. Chapin, C. S. Fuller, G. L. Pearson, Journal of Applied Physics, 25 (1954) 676.
- [16] D. C. Reynolds, G. Leies, L. L. Antes, R. E. Marburger, Physical Review Journals, 96 (1954) 533.
- [17] W. Shockley, H. J. Queisser, Journal of Applied Physics, 32 (1961) 510.
- [18] Z. I. Alferov, V. M. Andreev, M. B. Kagan, I. I. Protasov, V. G. Trofim, Soviet Physics Semiconductors, 4 (1971) 2047.
- [19] [http://www.nobelprize.org/nobel\\_prizes/physics/laureates/2000/alferov-lecture.pdf](http://www.nobelprize.org/nobel_prizes/physics/laureates/2000/alferov-lecture.pdf).
- [20] A. W. Blakers, M. A. Green, Applied Physics Letters 48 (1986) 215.
- [21] [https://en.wikipedia.org/wiki/Solar\\_cell\\_efficiency#/media/File:PVeff\(rev171030\)](https://en.wikipedia.org/wiki/Solar_cell_efficiency#/media/File:PVeff(rev171030)).
- [22] Renewables Global Status Report 2011  
([http://www.ren21.net/Portals/97/documents/GSR/GSR2011\\_Master18.pdf](http://www.ren21.net/Portals/97/documents/GSR/GSR2011_Master18.pdf)).

- [23] R. Brendel, J. H. Werner, H. J. Queisser, *Solar Energy Materials and Solar Cells*. 41-42 (1996) 419.
- [24] S. Metha, *PV News*, 30-5 (2011) 3.
- [25] Rajendra Singh, —Why silicon is and will remain the dominant photovoltaic materiall, *Journal of Nanophotonics*, 3 (2009) 032503-1-11.
- [26] D. M. Chapin, C. S. Fuller, G. L. Pearson, *Journal of Applied Physics*, 25 (1954) 676.
- [27] J. Zhao, A. Wang, M.A. Green, *Progress in Photovoltaics: Research and Applications*, 7 (1999) 471.
- [28] Y. P. Chen, C. T. Li & L. Wang, *International Journal of Photo Energy*, 2013 (2013) 510242.
- [29] G. Romij et al, ECN Solar Energy, Yingli Solar, Tempres System BV, “Solar Con/CPTIC China, 2012, Shanghai, China”.
- [30] V. D. Mihailetschi et al, ECN Solar Energy, 16th Crystalline silicon workshop, 2006, Colorado, USA.
- [31] D. MacDonald et al, “*Applied Physics Letters*, 85 (2004) 4061.
- [32] D. MacDonald, The Australian National University, “The emergence of n-type silicon for solar cell manufacture”.
- [33] U. Besu-Vetrella, L. Pirozzi, E. Salza, G. Ginocchietti, F. Ferrazza, L. Ventura, ... & J. C. Muller,. In *Conference Record of the 26th IEEE Photovoltaic Specialists Conference (PVSC)*, IEEE, 1997, 135-138.
- [34] J. Horzel, J. Szlufcik, J. Nijs, R. Mertens., *A simple processing sequence for selective emitters*, 1997
- [35] A. Mouhoub, B. Benyahia, B. Mahmoudi & A. Mougas, *Selective Emitters for Screen Printed Multicrystalline Silicon Solar Cells*, *Rev. Energ. Ren.: ICPWE*, 2003, 83-86.
- [36] B. Dastgheib-Shirazi, H. Haverkamp, B. Raabe, F. Book, G. Hahn, 2008
- [37] T. C. Ro“ der, S. J. Eisele, P. Grabitz, C. Wagner, G. Kulushic, J. R. Ko“ hler & J. H. Werner, *Progress in Photovoltaics: Research and Applications*, 18 (2010) 505-510.
- [38] H. Antoniadis, F. Jiang, W. Shan and Y. Liu, in *35th IEEE Photovoltaic Specialists Conference (PVSC)*, IEEE, 2010, pp. 001193-001196.
- [39] U. Jäger, S. Mack, C. Wufka, A. Wolf, D. Biro, R. Preu, *IEEE Journal of Photovoltaics*, 3 (2012) 621-627.

- [40] Y. P. Chen, C. T. Li, & L. Wang, Single-crystalline silicon solar cell with selective emitter formed by screen printing and chemical etching method: a feasibility study, *International Journal of Photoenergy*, 2013.
- [41] P. K. Basu, J. Cunnusamy, D. Sarangi, M. B. Boreland, *Renewable energy*, 66 (2014) 69-77.
- [42] A. Djelloul, A. Moussi, S. Meziani, M. Mebarki, L. Mahiou, A. Noukaz and K. Bourai, *Rev. des Energies Renouvelable SHENR-14 Ghardaiu*, 2014, 129-144.
- [43] A. Kim, J. Lee, S. Lim, C. Jeong, *Solar Energy*, 116 (2015) 265-271.
- [44] R. S. Davidsen, H. Li, A. To, X. Wang, A. Han, J. An, J. Colwell, C. Chan, A. Wenham, M. S. Schmidt, A. Boisen, O. Hansen, S. Wenham, A. Barnett, *Solar Energy Materials and Solar Cells*, 144 (2016) 740-747,
- [45] Y. Tao, K. Madani, E. Cho, B. Rounsaville, V. Upadhyaya & A. Rohatgi, *Applied Physics Letters*, 110 (2017).
- [46] S. Wang, L. Mai, A. Wenham, Z. Hameiri, D. Payne, C. Chan, ... & S. Wenham, *Solar Energy Materials and Solar Cells*, 169 (2017) 151-158.
- [47] W. Wu, Z. Zhang, F. Zheng, W. Lin, Z. Liang & H. Shen, *Progress in photovoltaics: research and applications*, 26 (2018) 752-760.
- [48] S. Simayi, Y. Kida, S. Utsunomiya, K. Shirasawa & H. Takato, *Japanese Journal of Applied Physics*, 57 (2018) 08RB09.

\*\*\*







*"Lectures which really teach will never be popular; lectures which are popular will never really"*

- Michael Faraday



# Chapter 7

---

## **Novel Technique for Fabrication of n-type Crystalline Silicon Selective Emitter for Solar Cell Processing**

## Abstract

A new way of realizing crystalline silicon selective emitter by simultaneous formation of front side selective emitter as well as rear back surface field (BSF) layer in rear side diffusion step has been presented in this work. In this chapter, I have demonstrated a novel technique to achieve a selective emitter having a highly diffused region with lower sheet resistance around 30-32  $\Omega/\text{sq}$  along with peak doping concentration  $7.34 \times 10^{19} \text{ atoms/cm}^3$ , junction depth around 0.97  $\mu\text{m}$  and lightly diffused region with higher sheet resistance around 78-80  $\Omega/\text{sq}$  along with peak doping concentration  $4.57 \times 10^{19} \text{ atoms/cm}^3$ , junction depth around 0.64  $\mu\text{m}$ . These results show that selective emitter has been formed in single diffusion process without any extra heat treatment and chemical etching process, thus this process becomes cost effective.

## 7.1. Introduction

**H**igh efficiency crystalline silicon solar cells require a good emitter design where contact resistance and surface recombination velocity both will be minimum i.e. emitter design should be able to collect all light generated carriers with less surface recombination and good metal contacts with low contact resistance. Fulfilling these two requirements at the same time is not possible in homogeneous doping emitter.

Selective emitter structure is of great importance because of its better blue response in short wavelength region and thus enhanced light-to electricity conversion in that region. It solves the problem of trade-off between surface recombination velocity and contact resistance. The illuminated emitter surface where light falls and carriers generated are collected is lightly doped to reduce the surface recombination velocity which leads to increase in both open circuit voltage ( $V_{oc}$ ) & short circuit current density ( $J_{sc}$ ), and the non-illuminated emitter surface beneath the metal finger contact is highly doped to decrease the contact resistance, which improves the fill factor [1].

Many selective emitter solar cell fabrication processes involve double diffusion steps; however the major difficulty associated with this process is the alignment-accuracy of the front side metal grid with the highly doped emitter surface at the time of contact formation. The double diffusion technique with photolithography is used to form high efficiency solar cells but this is very costly method [2, 3].

Industrial selective emitter solar cell can be formed by the coating of phosphorus containing metal paste by screen printing in the selected portion of the emitter of a p-type crystalline silicon substrate. This process is well-matched with common mass production technique where silver paste is used to form the front contact by screen printing. This phosphorus contained metal paste worked as a source of direct diffusion by which the coated layer covered region becomes heavily doped, and gas-phase out diffusion by which other region becomes lightly doped into the substrate. This forms the highly doped area and the lightly doped area at the same time. But to obtain target doping, concentration management is necessary for uniform diffusion [4-6].

Innovalight had formed selective emitter using doped silicon ink and it had proved its viability in mass production [7].

Another industrial approach to form selective emitter is light diffusion of phosphorus in the full front surface of a p-type substrate followed by anti-reflection coating (ARC) and then screen printing of phosphorus contained silver paste to form the front contacts. At the time of firing, phosphorus diffuses into the front surface and form heavily doped region below the contact. But in the presence of phosphorus silver would diffuse faster into the substrate which produces an adverse effect on leakage current [8, 9].

There are another process to form selective emitter in laboratory is etch back method. Advantage of this process is it needs one diffusion process but difficulty of this process is uncontrolled etching process. At first the total front area of the p-type textured wafer will be heavily doped [10-14] followed by masking of selective region (where to form highly doped region i.e. below the metal contact) while the rest of the front surface is etched to form lightly doped region.

One more process to form selective emitter in single diffusion process is to cover the front surface of a substrate before diffusion with a selectively patterned masking layer of silicon dioxide ( $\text{SiO}_2$ )/silicon nitride ( $\text{SiN}_x$ ) through Plasma Enhanced Chemical Vapour Deposition (PECVD) [15-18] followed by a high temperature diffusion process for the formation of highly doped area and lightly doped area simultaneously. Heavily doped region is formed by direct diffusion whereas lightly doped region is formed by gaseous out-diffusion. The disadvantage of this method is the requirement of costly equipment PECVD to form the coating used as mask.

In laser doped selective emitter (LDSE) technique metal contact is formed via a self aligned mechanism for plating and that plated metal contacts require a separate interconnection method, which is not conventionally used in the commercial purpose [19-23]. There are another new selective emitter formation process by laser over-doping treatment. After diffusion the surface is treated by laser where the grid structure will be formed and then the metal contacts will be deposited [24].

Because of enhanced  $n^+$  contacting pastes for  $n^+$  emitter of p-type solar cells, selective emitter formation and research on tooling of its different parameter has become obsolete. On the other hand, for n-type solar cells this is still a challenge [25-27].

In this study, it has been shown that it is possible to form a crystalline silicon selective emitter with n-type silicon wafer as base material by a patterned selective masking of the homogenously

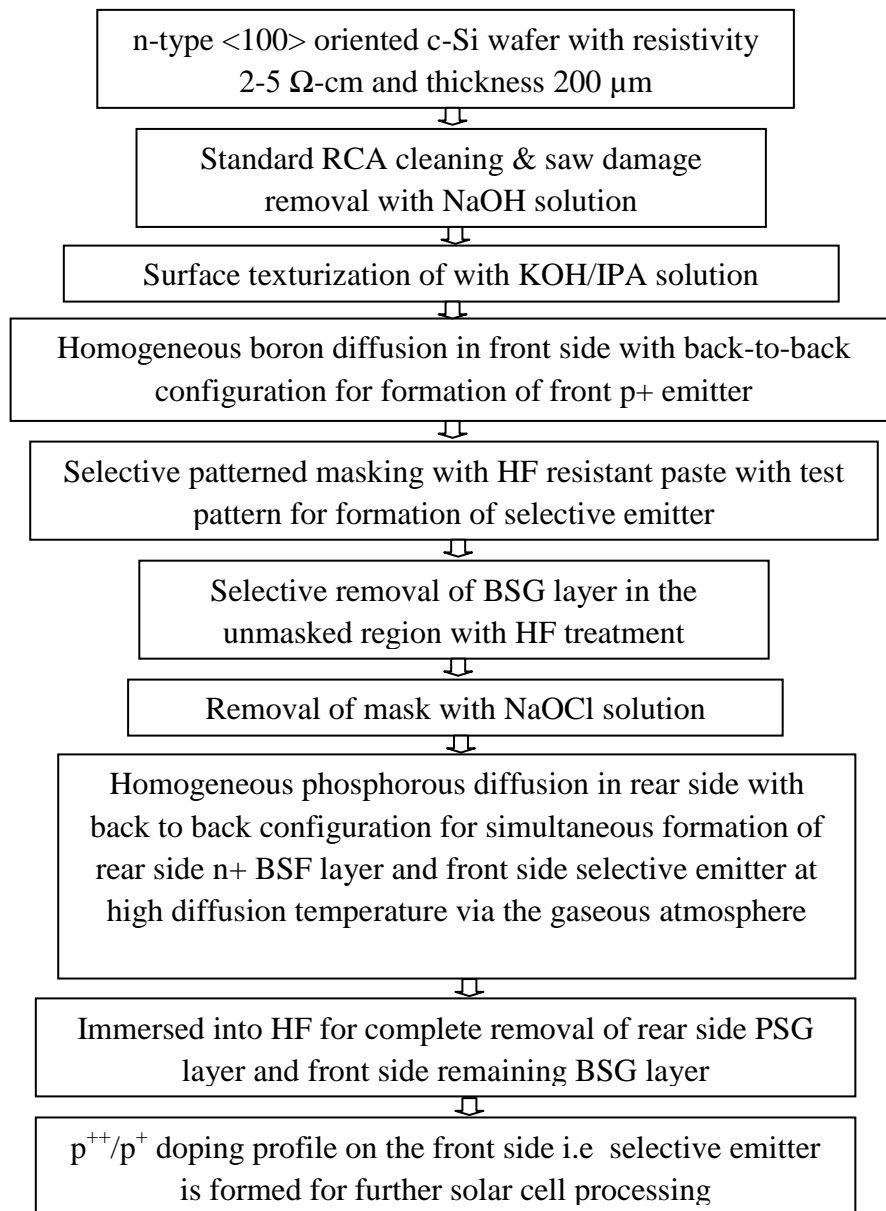
doped  $p^+$  emitter with a screen printable resist before the removal of boro silicate glass (BSG) layer. Then after the complete removal of the selectively open BSG layer and the deposited patterned mask, rear side  $n^+$  diffusion is done to form the rear side BSF as well as front side selective emitter in which highly doped regions (HDR) and lightly doped regions (LDR) has been formed simultaneously by the heat treatment at the time of high temperature diffusion. No additional heat treatment is required, this provides a cost reduction. For further fabrication of n-type crystalline silicon selective emitter solar cell highly boron doped regions must be as narrow as possible because it delivers high surface recombination losses, which should be located below metal contact. So the print of acid resistant ink paste used as mask for formation of selective emitter and print of metallic contact finger should be performed with same patterned screen with proper alignment of screen printing equipment. Also between the metallic fingers where light will be illuminated and generated carriers will be collected, lightly doped emitter is required which should be passivated properly with some thin oxide layer to keep the surface recombination losses as low as possible and to obtain a high open circuit voltage ( $V_{oc}$ ).

The process is applicable for both n-type and p-type crystalline silicon selective emitter solar cell. But here I choose n-type silicon material because of high minority carrier lifetime and no light induced degradation due to absence of boron [28]. This chapter focuses on the utilization of diamond wire saw (DWS) c-Si wafers, which are readily available on an industrial production scale. These wafers have garnered significant interest from the solar cell technology sector because of their minimal kerf loss, efficient throughput, and cost-effectiveness compared to SWS technology.

Another key issue for Photo-Voltaic world is “COST”. The major bottleneck is to form a high efficiency crystalline silicon solar cell within a low cost. This process in our work needs single diffusion and no additional heat treatment process is required, so it is cost effective also.

## 7.2. Experimental details

For selective emitter formation n-type diamond cut crystalline silicon  $\langle 100 \rangle$  oriented  $76 \times 76 \text{ mm}^2$  wafer with resistivity of 2-5  $\Omega\text{-cm}$  were used as substrate. This wafer had thickness of approximately 200  $\mu\text{m}$ . The main steps for fabricating the selective emitter for solar cell processing in my presented method is depicted by means of a flow chart in Fig. 7.1.



**Fig. 7.1: Processing step for fabricating the n-type c-Si selective emitter**

At first the samples were cleaned by standard RCA cleaning process and then immersed in 10% NaOH solution at 80°C for 3 minutes to remove the saw damage. After that to decrease the optical losses texturisation process of the surface of the wafer was performed. In my work, a 2% KOH-6.5% IPA-0.033% NaOCl solution at 85°C was used for texturing the c-Si substrates. It takes 45 minutes to texturise the surface of the wafer. Then homogeneous boron diffusion was



performed in front side of the wafer by back-to-back configuration to form moderately doped  $p^+$  emitter.

This thermal diffusion is formed in open tube diffusion furnace using liquid Boron tribromide ( $BBr_3$ ) source kept at  $20^\circ\text{C}$ . The diffusion is carried out at temperature  $940^\circ\text{C}$  for 50 min pre-deposition followed by 40 min drive-in and finally low temperature oxidation for 10 min. This was followed by selective patterned masking of the emitter applying a screen printable HF resistant paste before the removal of BSG layer. In the subsequent HF (10%) treatment the BSG layer can be selectively removed. The mask covered area was protected against the HF, while the remaining area was BSG layer free. After the selective removal of BSG layer the acid resistant mask was removed by dipping the wafer in sodium hypochlorite ( $NaOCl$ ) solution. After the complete removal of mask phosphorus diffusion is performed in rear side with back-to-back configuration in batch process for formation of rear  $n^+$  BSF layer. This rear side diffusion is performed by liquid Phosphorus oxychloride ( $POCl_3$ ) source (also kept at  $20^\circ\text{C}$ ) again in open tube diffusion furnace at temperature  $950^\circ\text{C}$  for 20 min pre-deposition followed by 10 min drive-in and finally low temperature oxidation for 7 min. During this process front side selective emitter is also formed at high diffusion temperature via the gaseous atmosphere. In that high temperature process deeply diffused regions  $p^{++}$  (which was under the deposited mask, and where the BSG was not removed) was formed having a lower sheet resistance and in the adjacent regions a lightly doped region were formed having higher sheet resistance. Thus no additional heat treatment is required for formation of selective emitter. Next the complete removal of rear side Phosphosilicate glass (PSG) and front side remaining BSG layer was performed by subsequent HF (10%) treatment.

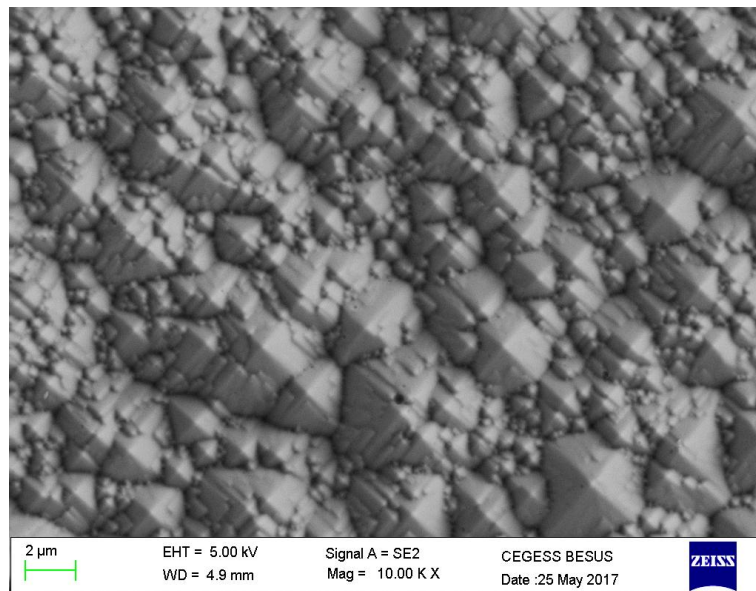
Here I have followed a test pattern for masking the wafer with acid resistant paste but for further solar cell processing the masks will be on those regions where the metal finger contacts will be formed, so the printed masking and printed metallic finger should be performed by same patterning screen with screen printing equipment.

## 7.3. Results and Discussions

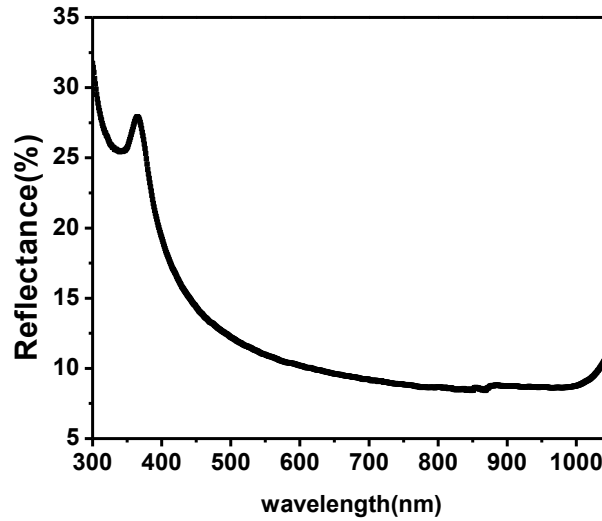
### 7.3.1. Texturization and spectral response

In solar cell reflectance should be minimum, to minimize the amount of reflection texturization is done. When light is illuminated on the solar cell, light get reflected from the top surface of the cell. This loss of light reduces the number of generated electron hole pair as well as reduces the current.

Texturization of diamond cut mono n-type wafers of size 76 mm×76 mm is done in a batch process consisting of 10 wafers at a time. Texturization is done using KOH-IPA-NaOCl (Pottasium Hydroxide-Isopropyl Alcohol-Sodium Hypochlorite) solution at temperature 82-85°C for 45 minutes. After texturization characterization like FESEM (QUANTA FEG 25) images, Reflection property by UV-VIS-NIR Spectrophotometer (SolidSpec-3700, SHIMADZU) is examined. FESEM images in Fig. 7.2 shows uniform pyramid through all over the surface. Because of this pyramid like structure reflection from the front surface was reduced as compared to as-cut silicon wafer whose reflectance is ~ 40%. The spectral reflectance of textured c-Si wafer in the wavelength range 300-1050 nm is also shown in Fig. 7.3 and SWAR (Solar Weighted Average Reflectance) is 10.4%.



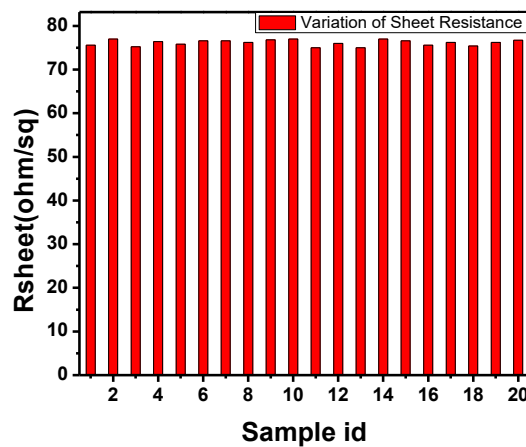
**Fig. 7.2: FESEM image of n-type diamond cut c-Si substrate after KOH-IPA-NaOCl texturization.**



**Fig. 7.3: Spectral response of n-type diamond cut c-Si substrate after KOH-IPA-NaOCl texturization using UV-VIS-NIR spectrophotometer**

### 7.3.2. Formation of homogeneously doped emitter & sheet resistance measurement

The homogeneous diffusion process by  $\text{BBr}_3$  (Boron Tribromide) liquid source kept at  $20^\circ\text{C}$  for  $76\text{mm} \times 76\text{mm}$  wafers using open tube diffusion furnace is optimized and  $\text{p}^+$  surface on n type wafer is formed.



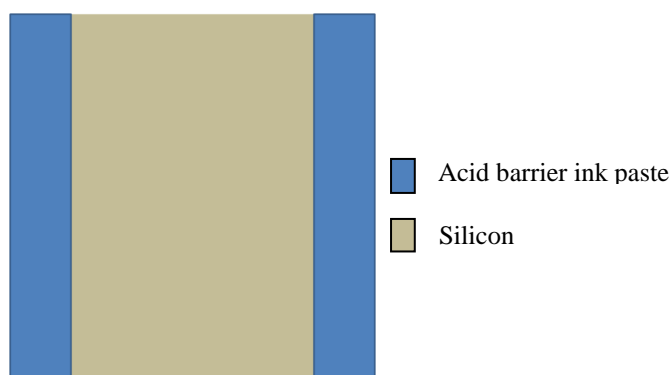
**Fig. 7.4: Mean value of sheet resistance after homogeneous born diffusion**

Diffusion process is carried out in a batch sequence with 20 back to back configured wafers at a time. The diffusion is carried out at temperature  $940^{\circ}\text{C}$  for 50 min pre-deposition followed by 40 min drive-in and finally low temp oxidation for 10 min. Then the sheet resistance is measured by four-probe method.

Measurement shows uniform sheet resistance and the average sheet resistance is approx  $75\text{-}77\ \Omega/\text{sq}$ . Fig. 7.4 shows the uniformity of the sheet resistance as well as diffusion of different samples in same batch.

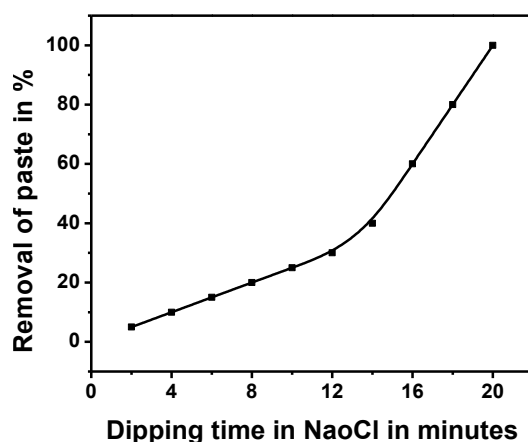
### 7.3.3. Stability of paste in HF solution & stripping of paste

In this work, I have used an acid resistant dielectric ink paste DH001, DONGHUA, CHAINA (Batch no: 17011203, Viscosity:  $175\pm 25$  PS). The stability of acid resistant ink paste in HF solution, the stripping of the paste and also the screen cleaning liquid has been identified for that paste. I have been able to remove the paste successfully from the wafer and from the screen by NaOCl (sodium hypochlorite) solution. At first, I have taken textured diffused n-type mono c-Si wafer before the removal of BSG layer. Then the acid barrier screen printable ink paste is coated on the wafer in two side of the wafer leaving the space in between two paste coated region blank (Fig. 7.5).



**Fig. 7.5: Acid barrier ink paste coated wafer**

In this test pattern, the width of the empty region (without paste region) much wider than the width of the paste coated region to prevent the effect of lateral diffusion as much as possible.



**Fig. 7.6: Removal of paste in 4% NaOCl solution**

Afterwards the wafers are dried in sunlight till the paste is dried properly. In the next step, I baked the wafers in hot air oven at  $70^{\circ}\text{C}$  temperature for 30 min. After baking the wafers they are dipped into 10% HF solution for 20 mins. Then the wafers are rinsed into the DI water to taste whether the paste remains in same condition or not. After that the wafers are dipped in NaOCl solution at room temp for some time till the full paste is removed. It takes approx 20 min for complete removal of paste. The corresponding graph is given in Fig. 7.6.

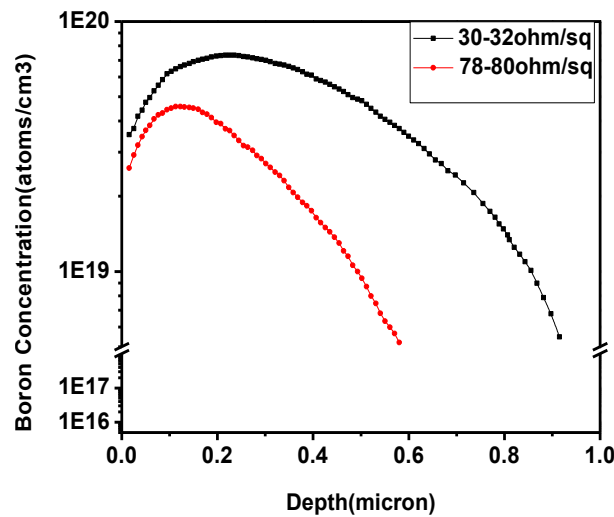
As an alternative of this paste I may use any type of dielectric ink paste which is acid (mainly HF) resistant and screen printable. For further solar cell processing I have identified another acid resistant screen printable dielectric ink paste (118-12A as Solvent Resistant Dielectric Ink, B119-44 as Catalyst and 113-12 as Thinner) from Creative materials, USA.

#### **7.3.4. Formation of rear side diffusion as well as front side selective emitter & sheet resistance measurement**

After the removal of acid resistant ink paste phosphorus diffusion is performed in rear side with back-to-back configuration in batch process for formation of rear  $n^{+}$  BSF layer. This rear side diffusion is performed by liquid  $\text{POCl}_3$  source (also kept at  $20^{\circ}\text{C}$ ) in open tube diffusion furnace at temperature  $950^{\circ}\text{C}$  for 20 min pre-deposition followed by 10 min drive-in and finally low temperature oxidation for 7 min. Sheet resistance of the diffused rear side is measured by four probe method and it is around  $18\text{-}20\ \Omega/\text{sq}$ . During this process front side selective emitter is also

formed at high diffusion temperature ( $950^{\circ}\text{C}$ ) via the gaseous atmosphere. In that high temperature process deeply diffused regions  $p^{++}$  (which was under the deposited mask, and where the BSG was not removed) was formed having a lower sheet resistance and in the adjacent regions a lightly doped region were formed having higher sheet resistance. For the high temperature diffusion on the back side I have been benefitted from two sides - one is that I have got a lower sheet resistant BSF and the other is that highly doped region in the front side have been formed from the boron rich layer (BRL) by this high temperature treatment.

Sheet resistance of the front emitter has been also measured by four probe method. At highly doped region it was constant source diffusion and the sheet resistance is 30-32 ohm/sq, besides that in the lightly doped region it was limited source diffusion and the sheet resistance is 78-80 ohm/sq. Sheet resistance of the emitter can be changed further by changing the diffusion parameters, i.e. by changing the time and temperature of the pre-deposition and drive-in step in diffusion process.



**Fig. 7.7: Emitter profiles of electrically active boron of two different doping regions as measured by ECV after diffusion.**

Emitter profiling and its diffusion depth is investigated by electrochemical-capacitance voltage (ECV) curve. Highest boron concentration at the peak point of the highly doped region is  $7.34 \times 10^{19} \text{ atoms/cm}^3$  with junction depth around  $0.97 \mu\text{m}$  corresponding to the sheet resistance

30-32  $\Omega/\text{sq}$  and at the peak point of the lightly doped region is  $4.57 \times 10^{19} \text{ atoms/cm}^3$  with junction depth around  $0.64 \mu\text{m}$  corresponding to the sheet resistance 78-80  $\Omega/\text{sq}$  (Fig. 7.7).

In the lightly doped region sheet resistance and the peak doping concentration has been measured in the middle of the total width of that region to ignore the effect of lateral diffusion. Here in the lightly doped region sheet resistance increases 3.8%-4%, because in that region there was no source for diffusion and only heat treatment applied. In this heat treatment surface atoms reached deeper to the junction and thus the concentration of the atoms in the surface decreases and sheet resistance increases.

## 7.4. Conclusions

I have presented a novel fabrication method for the formation of selective emitter for further solar cell processing. FESEM results show uniform pyramid through all over the surface and UV-VIS-NIR spectroscopy shows 10.4% SWAR in the wavelength range 300-1050 nm. From the results of four probe method it is clear that uniform diffusion has been done and two different doping regions i.e. highly doped region with sheet resistance 30-32  $\Omega/\text{sq}$  and lightly doped region with sheet resistance 78-80  $\Omega/\text{sq}$  have been formed in the same emitter and ECV curve validates the results with two different peak doping concentration of  $7.34 \times 10^{19} \text{ atoms/cm}^3$  &  $4.57 \times 10^{19} \text{ atoms/cm}^3$  respectively. The junction depths of the two different doping regions are about  $0.97 \mu\text{m}$  and  $0.64 \mu\text{m}$  respectively. The present technique can be considered as a different approach compared to the current selective emitter formation techniques. The novelty of this method is that front side selective emitter had been formed at the time of rear side diffusion process i.e. at the time of formation of Back Surface Field (BSF) and no double diffusion or etching process is required. I believe that my work is novel compared to the existing methods for this type of work. This new technique can be adopted by industry also, as this technique needs only diffusion and screen printing facilities. This process has been given more consistent, uniform and controllable contact resistance than Reactive Ion Etching (RIE) and Etch Back process, and hence this process can be useful for mass production in industry level. Thus by using this process low cost n-type crystalline silicon selective emitter can be made and there are many scopes to implement this method in the industry level for the formation of selective emitter solar cell because of its batch process viability, less no. of processing steps, ease of operation and maintenance and cost effectiveness.

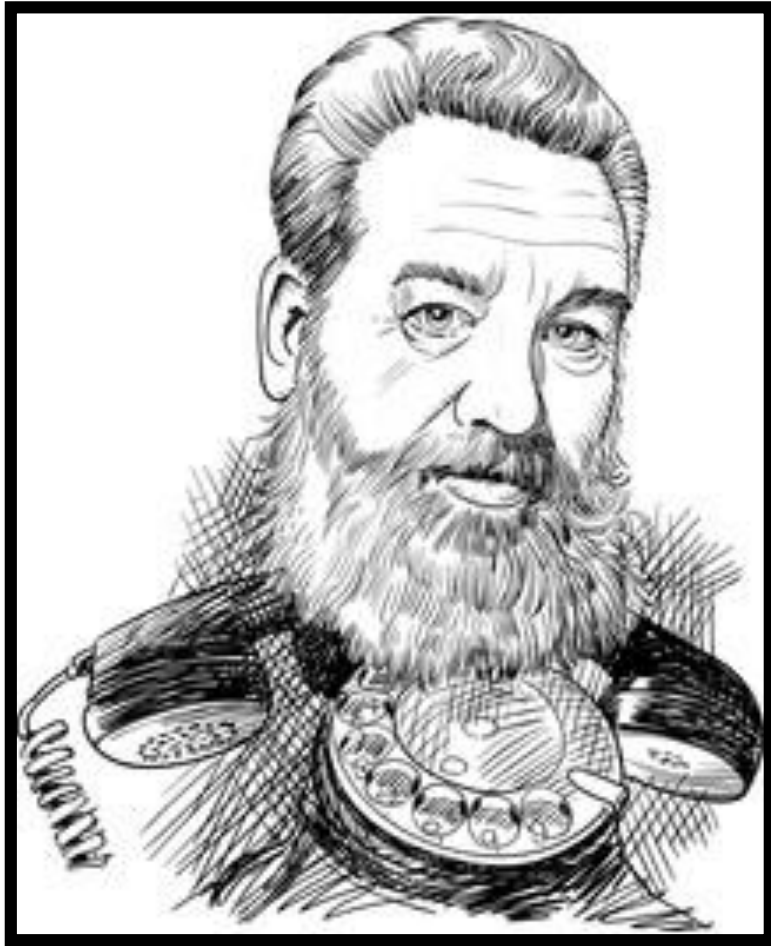
## References

- [1] Y. P. Chen, C. T. Li & L. Wang, International Journal of Photo Energy, 2013 (2013) 510242.
- [2] A. W. Blakers, A. Wang, A. M. Milne, J. Zhao & M. A. Green, Applied Physics Letters, 55 (1989) 1363–65.
- [3] J. Zhao, A. Wang & M. A. Green, Applied Physics Letters, 73 (1998) 1991–93.
- [4] J. Horzel, J. szlufcik, J. Nijs, & R. Mertens, in Proceedings of the IEEE 26<sup>th</sup> PVSC, 1997, PP. 139-142.
- [5] L. Debarge, M. Schott, J. C. Muller & R. Monna, Solar Energy Materials & Solar Cells, 74 (2002) 71–75.
- [6] A. Mouhoub, B. Benyahia, B. Mahmoudi & A. Mougas, Rev. Energ. Ren., ICPWE (2003) 83-86.
- [7] H. Antoniadis, F. Jiang, W. Shan & Y. Liu, in Proceedings of the 35<sup>th</sup> IEEE PVSC, 2010, pp. 1193-1196.
- [8] A. Rohatgi, M. M. Hilali, D. L. Meier, A. Ebong, C. B. Honsberg, A. F. Carroll & P. Hacke, in Proceedings of the EUPVSEC, 2001, PP. 1307-1310.
- [9] L. M. Porter, A. Teicher, & D. L. Meier, Solar Energy Materials & Solar Cells, 73 (2002) 209-219,2002.
- [10] M. Gauthier, M. Grau, O. Nichiporuk, F. Madon, N. Le Quang, A. Zerga, A. Slaoui, D. Blanc Pelissier, A. Kaminski & M. Lemiti, in Proceedings of the 24<sup>th</sup> EUPVSEC, Hambourg, Germany, 2009, Proc. pp. 1875-1878.
- [11] [https://www.pvtech.org/news/schmids\\_selective\\_emitter\\_technology\\_supports\\_sunrise\\_global\\_solars\\_record](https://www.pvtech.org/news/schmids_selective_emitter_technology_supports_sunrise_global_solars_record)
- [12] D. Rudolph, K. Peter, A. Meijer, O. Doll, I. Kohler, in Proceedings of the 26<sup>th</sup> European Photovoltaic Solar Energy Conference (EU PVSEC), 2011, pp.1349-1352.
- [13] T. Wong, Y. A. Chen, C. Y. Chen, C. W. Kuo, T. M. Kuan, C. Y. Yu, I. C. Chen, IEEE 7<sup>th</sup> World Conference on Photovoltaic Energy Conversion (WCPEC), (a joint conference of 45<sup>th</sup> IEEE PVSC, 28<sup>th</sup> PVSEC & 34<sup>th</sup> EU PVSEC), 2018.
- [14] F. Ye, W. Deng, W. Guo, R. Liu, D. Chen, Y. Chen, Y. Yang, N. Yuan, J. Ding, Z. Feng, P. P. Altermatt & P. J. Verlinden, IEEE 43<sup>rd</sup> Photovoltaic Specialists Conference (PVSC), 2016.
- [15] J. M. Serra, R. Gamboa & A. M. Vallera, in proceedings of the 13<sup>th</sup> European Photovoltaic Solar Energy Conference (EUPVSEC), 1995, pp. 1422-1425, 1995.



- [16] J. H. Bultman, R. Kinderman, J. Hoornstra & M. Koppes, in Proceedings of the 16<sup>th</sup> European Photovoltaic Solar Energy Conference (EUPVSEC), 2000, pp. 1424-1426.
- [17] J. H. Bultman, A. R. Burgers, J. Hoornstra, R. Kinderman, M. Koppes, W. J. Soppe, A. W. Weeber, 17<sup>th</sup> EPVSEC, Munich, 2001.
- [18] Y. H. Wu, L. L. Chen, J. R. Wu, & M. L. Wu, Semiconductor Science and Technology, 25 (2010) 015001.
- [19] B. Hallam, S. Wenham, A. Sugianto, L. Mai, C. Chong, M. Edwards, D. Jordan, P. Fath, IEEE journal of Photovoltaics, 1 (2011) 43-48.
- [20] G. Poulain, D. Blanc, A. Focsa, International Journal of Photoenergy, 2012 (2011) 413863.
- [21] W. Wu, Z. Zhang, F. Zheng, W. Lin, Z. Liang & H. Shen, Progress in Photovoltaics: Research & Application, 26 (2018) 752-760.
- [22] R. S. Davidsen, H. Li, A. To, X. Wang, A. Han, J. An, J. Colwell, C. Chan, A. Wenham, M. S. Schmidt, A. Boisen, O. Hansen, S. Wenham & A. Barnett, Solar Energy Materials & Solar Cells, 144 (2016) 740-747.
- [23] C. W. Kuo, T. M. Kuan, W. L. Chueh, L. G. Wu, C. C. Huang, & C. Y. Yu, 7<sup>th</sup> World Conference on Photovoltaic Energy Conversion (WCPEC), (a joint conference of 45<sup>th</sup> IEEE PVSC, 28<sup>th</sup> PVSEC & 34<sup>th</sup> EU PVSEC), 2018.
- [24] A. Djelloul, A. Moussi, L. Mahiou, M. Mebarki, S. Meziani, A. Guenda, K. Bourai and A. Noukaz, 3<sup>rd</sup> International Congress on Energy Efficiency and Energy Related Materials (ENEFM), Springer Proceedings in Energy, 2015.
- [25] G. J. M. Janssen, M. Koppes, Y. Komatsu, J. Anker, J. Liu, A. Gutjahr, A. A. Mewe, C. J. J. Tool, I. G. Romijn, O. Siarheyeva, M. Ernst, B. van de Loo, W. M. M. Kessels, 29<sup>th</sup> EUPVSEC, Amsterdam, The Netherlands, 2014, pp: 812-815.
- [26] G. J. M. Janssen, A. Gutjahr, A. R. Burgers, D. S. Saynova, I. Cesar & I. G. Romijn, 28<sup>th</sup> EUPVSEC, Paris, France, pp: 1548-53.
- [27] I. G. Romijn, B. B. Van Aken, J. Anker, P. Barton, A. Gutjahr, Y. Komatsu, M. Koppes, E. J. Kossen, M. W. P. E. Lamers, D. S. Saynova, K. C. J. J. Tool, Y. Zhang, P. R. Venema, A. H. G. Vlooswijk, C. Schmitt, H. Kühnlein, N. Bay, M. König & A. Stassen, 28<sup>th</sup> EUPVSEC, Paris, France, 2013, pp: 736-740.
- [28] <https://pdfs.semanticscholar.org/eb9f/41611ca37cefd0622f0876fb4756b40994ad.pdf>





*"The achievement of one goal should be the starting point of another."*

- Alexander Graham Bell



# Chapter 8

---

**Optimizing front contact Selective Emitter doping in n-substrate Solar Cells: simulation modeling and experimental application**

## Abstract

The design of the emitter surface plays a crucial role in enhancing silicon solar cell efficiency. This chapter explores the impact of different dielectric layers on the emitter surface and investigates how varying the depth of emitter etching affects the performance of selective emitter solar cells through simulation method. The efficiency of the cells varied accordingly. Additionally, a combination passivation layer was identified to yield the best solar cell performance. Simulation insights were then applied in experimental methods. A straightforward fabrication process for selective emitter solar cells on n-type textured diffused cells was examined, utilizing shallow boron emitters obtained through thermal diffusion and by adjusting the parameters of the emitter doping process. Laser over-doping from passivating layers was tested on these profiles to locally enhance emitter conductivity and improve contact properties, thereby enabling localized control over emitter sheet resistance and doping profile.

## 8.1. Introduction

Crystalline silicon (C-Si) solar cells maintain their position as a frontrunner among various solar cell technologies, owing to factors such as a stable silicon supply, well-established manufacturing processes, and the consistently high and improving conversion efficiencies achievable. Typical commercial solar cells exhibit a sheet resistance of approximately 40-50  $\Omega/\text{sq}$ , achieved through uniformly doping the emitter region. While this doping technique reduces contact resistance at the metal-semiconductor interface, it also diminishes carrier lifetime due to increased Auger recombination and Shockley-Read-Hall recombination [1], leading to suboptimal passivation on the front side and reduced cell performance [2], often resulting in weak short wavelength responses [3]. Employing a lightly doped emitter offers a higher sheet resistance and lower surface recombination rate, thereby enhancing internal quantum efficiency in the short wavelength region.

To address the challenge of balancing recombination and contact resistance, selective emitter (SE) solar cells have been introduced. In these cells, the emitter region, where light-generated carriers are produced, is lightly doped to decrease recombination velocity, thus enhancing passivation for increased photocurrent and open-circuit voltage. Conversely, the emitter region beneath the front contact is heavily doped to reduce contact resistance [4]. As a result, SE silicon solar cells demonstrate improved open-circuit voltage ( $V_{oc}$ ), higher short-circuit current density ( $J_{sc}$ ), and enhanced conversion efficiency ( $\eta$ ).

Various techniques have been proposed for fabricating SE crystalline silicon solar cells, including expensive methods such as photolithographic or screen-printed alignment techniques, as well as multiple high-temperature diffusion steps [5]. Other approaches include etch-back emitter [6-8], doped silicon ink [9-11], laser doping [12-17], ion implantation [18], and processes involving oxide, a-Si, and porous silicon masks [19-22], among others. However, the use of reactive ion etching (RIE) has been found to potentially damage the surface [23].

Generally, numerous considerations arise when implementing selective emitter (SE) technology in mass production of silicon solar cells. It's essential that any additional process steps are minimal and that the fabrication process remains largely aligned with conventional methods to ensure cost-effectiveness and ease of integration [24].

This chapter details the fabrication of a selective emitter solar cell using laser over-doping, while the modeling and design of selective emitter doping for the front contact is conducted via simulation software. The chapter aims to present the effects of different etching depths on various solar cell parameters for selective emitter formation. This involves heavily doping the entire front surface of an n-type wafer, followed by masking selective regions to prevent subsequent etching, resulting in a lightly doped surface.

The objective is to simulate the impact of alternative low doping region (LDOP) and high doping region (HDOP) profiles on the performance of C-Si SE solar cells. The analysis, facilitated by device simulating software such as Devedit, Athena, and Atlas operating in two dimensions, examines the variation of different solar cell parameters while maintaining the same HDOP profile and etching out the LDOP profile. This comparison extends to SE and homogeneous emitter (HE) solar cells, including metrics such as short-circuit current density ( $J_{sc}$ ), open-circuit voltage ( $V_{oc}$ ), fill factor (FF), and efficiency ( $\eta$ ).

## 8.2. Modeling and Design of Selective Emitter

### 8.2.1. Device Structure

Because of the regular structure of selective emitter (SE) solar cells, an elementary cell is employed as a foundation for comprehending the functioning of this cell type, as depicted in fig. 8.1. In this elementary structure, the widths of the high doping (HDOP) region and low doping (LDOP) region are identical.

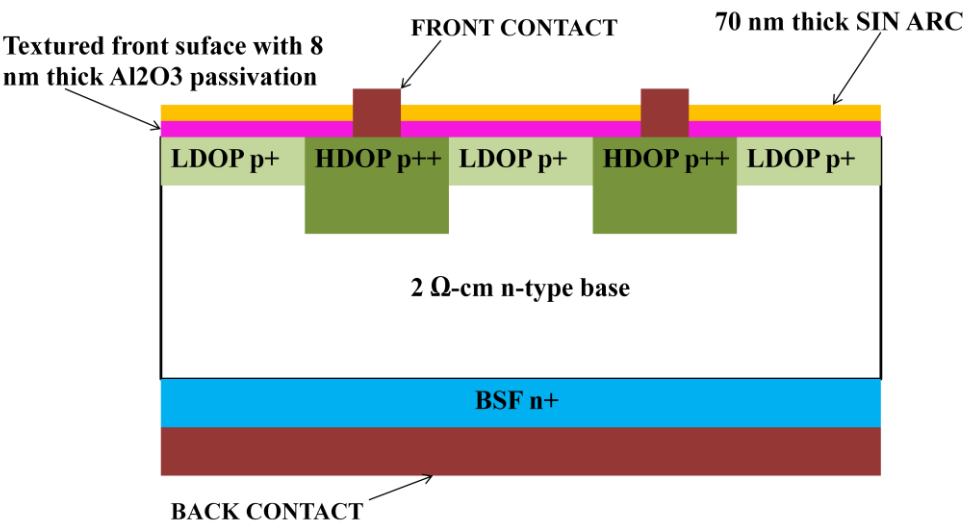


Fig. 8.1: Two dimensional cross section of the SE solar cell



### 8.2.2. Device simulation

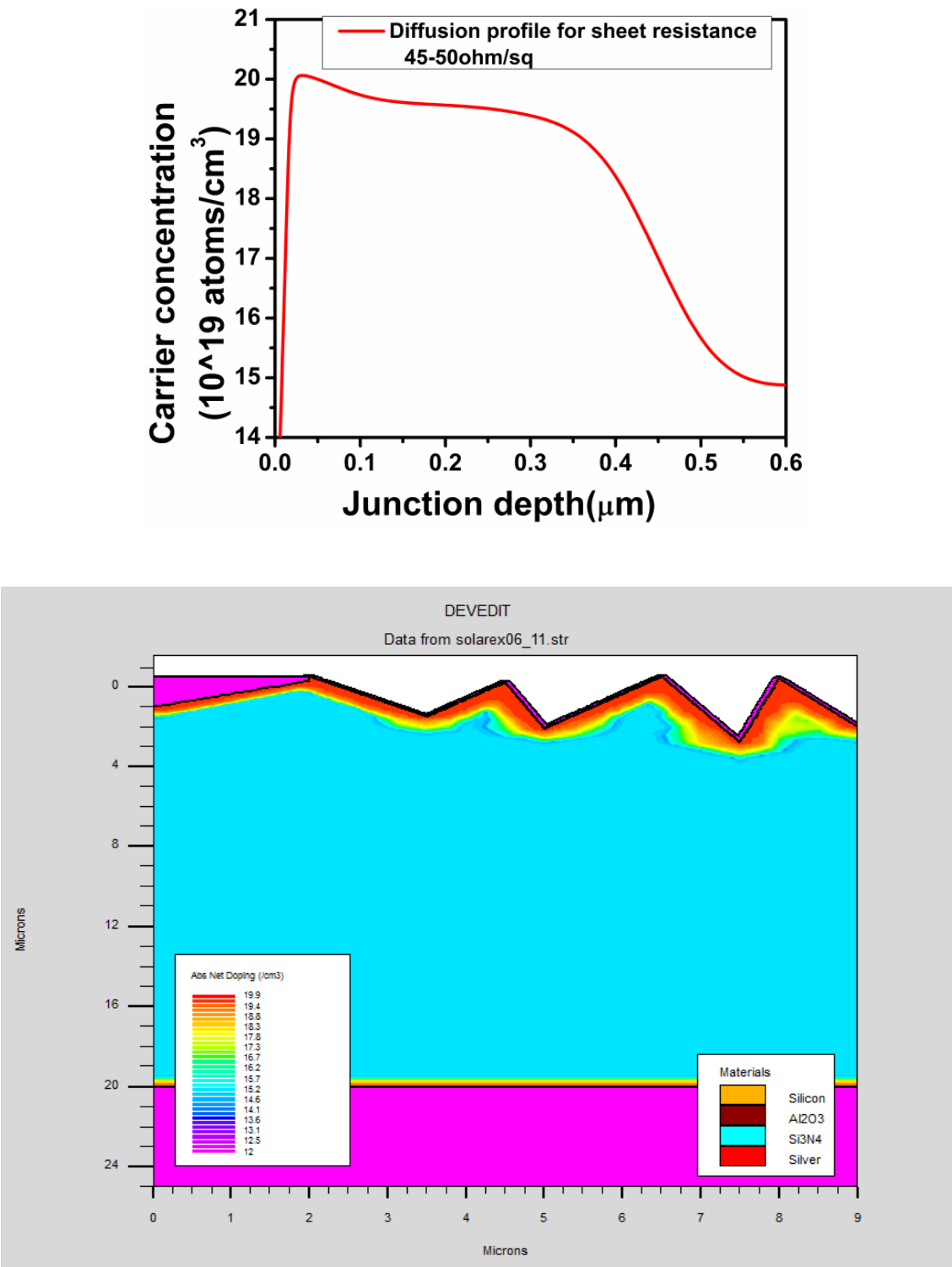
Before creating the selective emitter, I attempted to model the n-type passivated baseline crystalline silicon solar cell. To perform the electrical analysis, the device structure was simulated using SILVACO TCAD simulation software, comprising three main components: structure definition, diffusion, and numerical resolution [25]. The substrate chosen for modeling was 200  $\mu\text{m}$  thick and 9  $\mu\text{m}$  wide, consisting of 2  $\Omega\text{-cm}$  n-type ( $N_{\text{base}}=10^{15} \text{ cm}^{-3}$ ) mono crystalline silicon material. n-type base was selected due to its high minority carrier lifetime and absence of boron-induced light degradation.

### 8.2.3. Simulation Result

On the front side, a high boron diffusion with a sheet resistance of 36.62  $\Omega/\text{sq}$  (boron implant dose= $3 \times 10^{19} \text{ atoms/cm}^3$ , Energy=10, diffusion time=60 min, temperature=940  $^{\circ}\text{C}$ ) was initially performed. Subsequently, while maintaining the high doping (HDOP) region constant, the low doping (LDOP) region was etched for various durations to control the etching depth, ranging from 0.1  $\mu\text{m}$  to 0.4  $\mu\text{m}$ . On the rear side, a phosphorus diffusion with a sheet resistance of 37.03  $\Omega/\text{sq}$  (phosphorus implant dose= $1 \times 10^{19} \text{ atoms/cm}^3$ , Energy=50, diffusion time=20 min, temperature=900  $^{\circ}\text{C}$ ) was used as an n-type back surface field (BSF).

Different passivation schemes were studied on the solar cell surface, and the performance of the n-type solar cell was simulated using SILVACO software (as shown in Table 8.1). Various dielectric films such  $\text{Al}_2\text{O}_3$  (10 nm),  $\text{HfO}_2$  (10 nm),  $\text{TiO}_2$  (10 nm) and  $\text{SiN}_x$  (80 nm) were deposited on the emitter of diffused textured n-type c-Si wafer solar cells as passivating layers. Simulation analysis was conducted to understand the passivation mechanism, revealing that  $\text{Al}_2\text{O}_3$  yielded superior results compared to  $\text{TiO}_2$  and  $\text{SiN}_x$ . The short-circuit current for  $\text{Al}_2\text{O}_3$  passivated surfaces surpassed other passivation results, with the best efficiency of 17.77% achieved using a 10 nm thick  $\text{Al}_2\text{O}_3$  passivation layer and a 70 nm thick  $\text{SiN}_x$  antireflection coating (ARC). Notably, during SILVACO simulation, using Hafnium Oxide ( $\text{HfO}_2$ ) as a passivating agent on the rear n+ side of the n-type solar cell (i.e.,  $p^+nn^+$  diffused sample) resulted in an efficiency of 19.5%. The highest efficiency was achieved with  $\text{Al}_2\text{O}_3$  front passivation,  $\text{HfO}_2$  rear passivation, and  $\text{SiN}_x$  ARC, leading to increased  $V_{\text{oc}}$  and  $J_{\text{sc}}$  values of 659 mV and 35.18  $\text{mA/cm}^2$ , respectively.  $\text{Al}_2\text{O}_3$  film grown by atomic layer deposition (ALD) exhibited a negative fixed oxide charge density, reducing electron concentration near the surface of the p-type silicon substrate through a built-in electric field. This  $\text{Al}_2\text{O}_3$  film mitigated electrical loss by providing both chemical and field-effect

passivation in p-type silicon wafers, while  $\text{HfO}_2$ ,  $\text{TiO}_2$ , and  $\text{SiN}_x$  were less suitable for p-type silicon passivation due to their induction of fixed positive charges at the interface [26]. The front surface was illuminated.



**Fig. 8.1: (a) Diffusion profile of the wafer with sheet resistance 45-50 Ω/sq (b) SILVACO schematic diagram of Solar cell with sheet resistance 45-50 Ω/sq**

This chapter examines the trends in cell electrical parameters such as  $J_{sc}$ ,  $V_{oc}$ , FF, and  $\eta$  in response to variations in etching depth. The SILVACO program utilized in this study was written in ATLAS mode [27], a physically-based 2-D & 3-D device simulator that forecasts the electrical behavior of semiconductor devices under specified bias conditions. The input structures simulated with Athena were employed by Atlas, enabling the determination of how process parameters affect device characteristics. Upon defining the structure, the diffusion profile was imported, and optical data profiles were externally integrated into the beam structure. The contact structure was defined using cathode metal. Fig. 8.1 (a) & (b) illustrate the simulated doping profile and schematic of the simulated textured diffused n-type baseline solar cell.

**Table 8.1: Solar cell performance result for different front surface passivation obtained theoretically with sheet resistance 45-50  $\Omega/sq$**

Passivation (Front/Rear) & ARC	$J_{sc}$ (mA/cm <sup>2</sup> ) (Theo)	$V_{oc}$ (mV) (Theo)	FF (Theo)	$\eta$ (%) (Theo)
Front TiO <sub>2</sub> passivation (10 nm) + ARC SiN <sub>x</sub> (70 nm)	23.23	0.651	0.84	12.7
Front Al <sub>2</sub> O <sub>3</sub> passivation (10 nm) + ARC SiNx (70 nm)	31.90	0.658	0.85	17.77
ARC + passivation SiNx (80 nm)	29.83	0.653	0.84	16.39
Front Al <sub>2</sub> O <sub>3</sub> passivation (10 nm) + ARC SiNx (70 nm) Rear HfO <sub>2</sub> passivation (10nm)	35.18	0.659	0.84	19.48

In photovoltaic silicon technology, efficiency is a crucial parameter for overall cost reduction. Simulation of the SE solar cell was conducted, and fig. 8.2 presents a comparative analysis of the current density-voltage (J-V) curves between the front Al<sub>2</sub>O<sub>3</sub> passivated, SiNx ARC coated with no rear passivation, and rear HfO<sub>2</sub> passivation solar cell under the same front and rear side diffusion conditions. For the selective emitter and PERT (Passivated Emitter and Rear Totally Diffused) structure, etching of the selected area is imperative to achieve the required sheet resistance.

Following the selective emitter process, the wafer underwent initial diffusion with high doping concentration to achieve low sheet resistance. However, apart from the metal-covered

area, other surfaces were etched to attain higher sheet resistance. This approach was adopted to balance the trade-off between highly diffused emitter areas leading to low short-circuit current due to increased junction depth, and lowly diffused emitters resulting in resistive losses beneath metal coverage. Utilizing this combination aimed to enhance solar cell performance. In the SILVACO TCAD program, a similar principle was applied, where only the region under the metal contact was heavily diffused, while other areas were etched to achieve high sheet resistance.

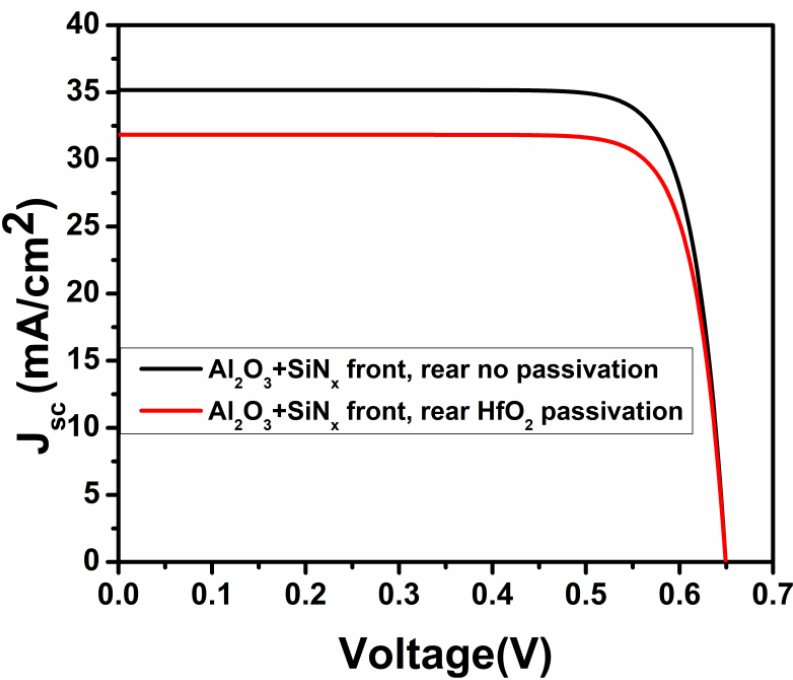


Fig. 8.2: J-V Characteristics curve of simulated baseline n-type solar cell by SILVACO simulation

Table 8.2: SILVACO simulation data of selective emitter PERT Solar cell with variation of emitter etching depth.

Etching depth (μm)	R <sub>sh</sub> (Ω/sq)	X <sub>j</sub>	N <sub>s</sub> (/cm <sup>3</sup> )
Without etch	33.4189	0.852959	8.5149e19
0.1	43.8478	0.752959	7.75276e19
0.2	62.0017	0.652959	7.08684e19
0.3	97.6776	0.552959	6.04087e19
0.4	184.519	0.452959	4.68324e19

Initially, a flat silicon surface was utilized instead of a textured surface. Following etching, changes in sheet resistance with carrier concentration were documented in Table 8.2. The rear side of the cell was configured as a PERT structure. Table 8.3 demonstrates the impact of varying etching depths, allowing a comparison between HE and SE cells to gauge the electrical performance of SE silicon solar cells. Tabular data from the J-V curves illustrates that successive etching initially enhances cell performance, followed by a decline due to very high sheet resistance. The SE cell featuring a 36.62  $\Omega/\text{sq}$  HDOP profile and LDOP profile with an etching depth of 0.3  $\mu\text{m}$  achieved maximum efficiency 23.38%, while the HE cell exhibited an efficiency of 22.54%.

**Table 8.3: Comparison between the simulated HE cells, and SE cells (36.62  $\Omega/\text{sq}$  HDOP and LDOP with varied etching depth from 0.1  $\mu\text{m}$ -0.4  $\mu\text{m}$ .**

Etching depth( $\mu\text{m}$ )	$J_{sc}$ (mA/cm <sup>2</sup> )	$V_{oc}$ (V)	FF	Eff%
Without etch	35.9	0.736	0.85	22.54
0.1	36.27	0.755	0.85	23.2
0.2	36.38	0.7558	0.85	23.35
0.3	36.39	0.756	0.85	23.38
0.4	36.29	0.756	0.85	23.32

The SE cell with maximum efficiency demonstrates an improvement in  $J_{sc}$  and  $V_{oc}$  by 0.489 mA/cm<sup>2</sup> and 0.02 mV, respectively, resulting in an efficiency gain of 0.84%. The diffusion profile with and without etching is depicted in Figure 8.3, while the SILVACO schematic structure of the selective emitter PERT n-type solar cell is illustrated in fig. 8.4.

Simulation of the Selective Emitter PERT structure on textured silicon was also conducted. A maximum efficiency of 27.80% was attained with an etching depth of 0.3  $\mu\text{m}$ , as depicted in fig. 8.6. The schematic diagram of the textured selective emitter PERT structure is presented in fig. 8.5.

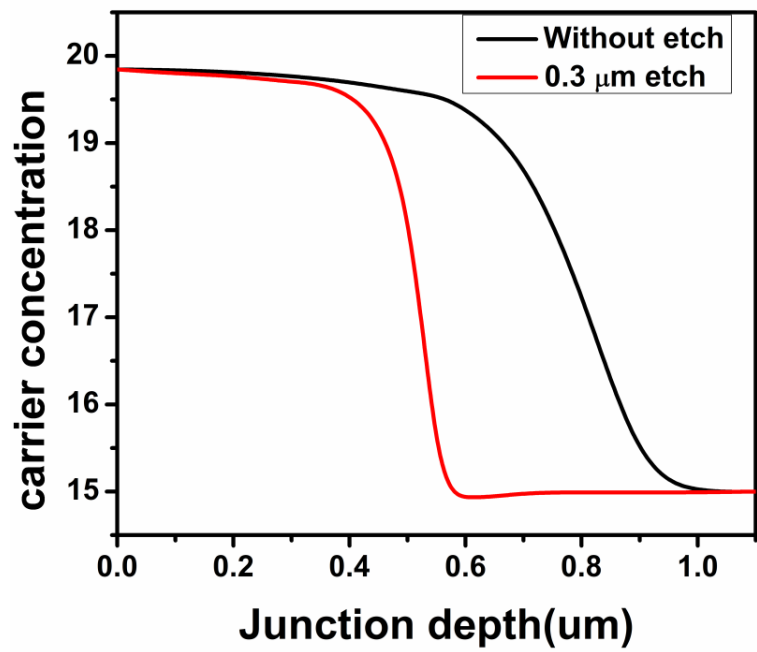


Fig. 8.3: Diffusion profile of the wafer without etches and 0.3 μm etch.

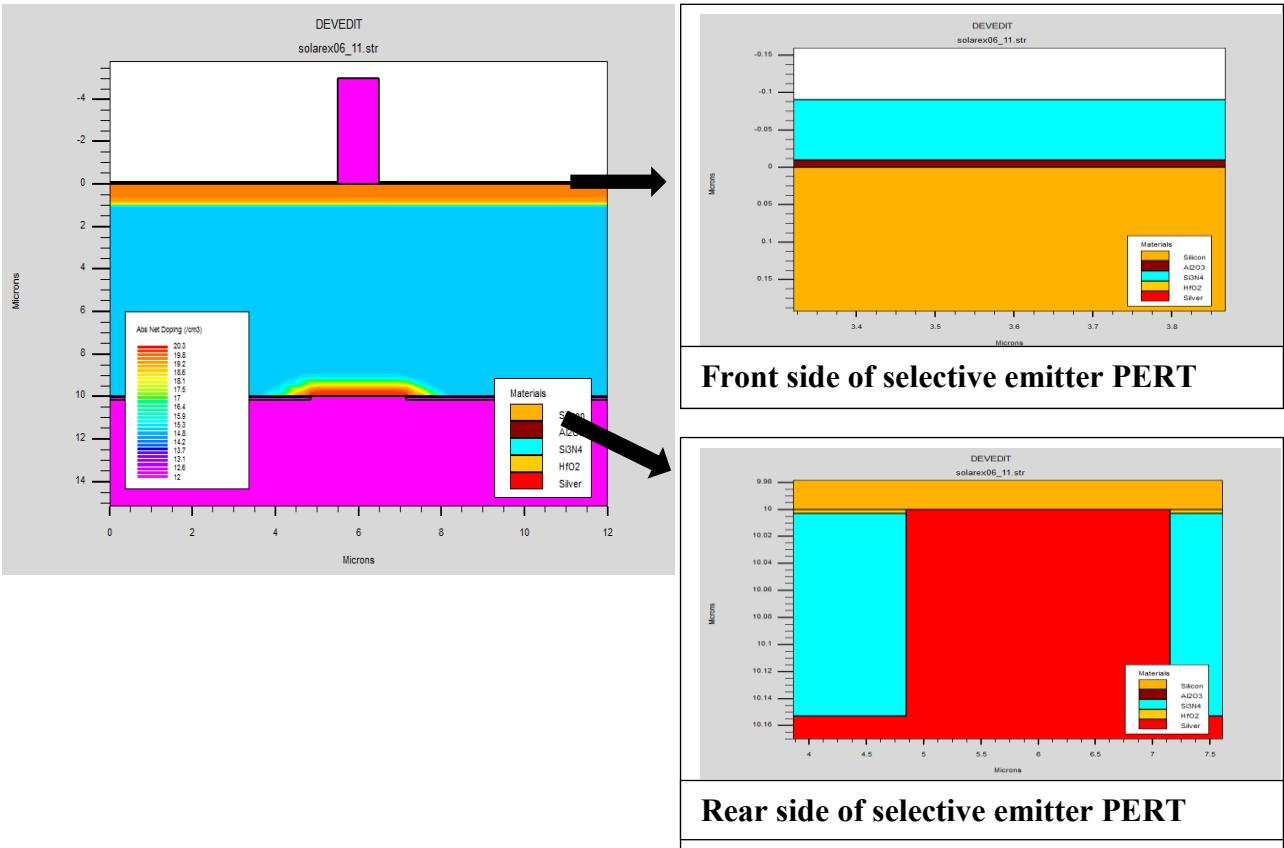


Fig. 8.4: selective emitter PERT structure SILVACO

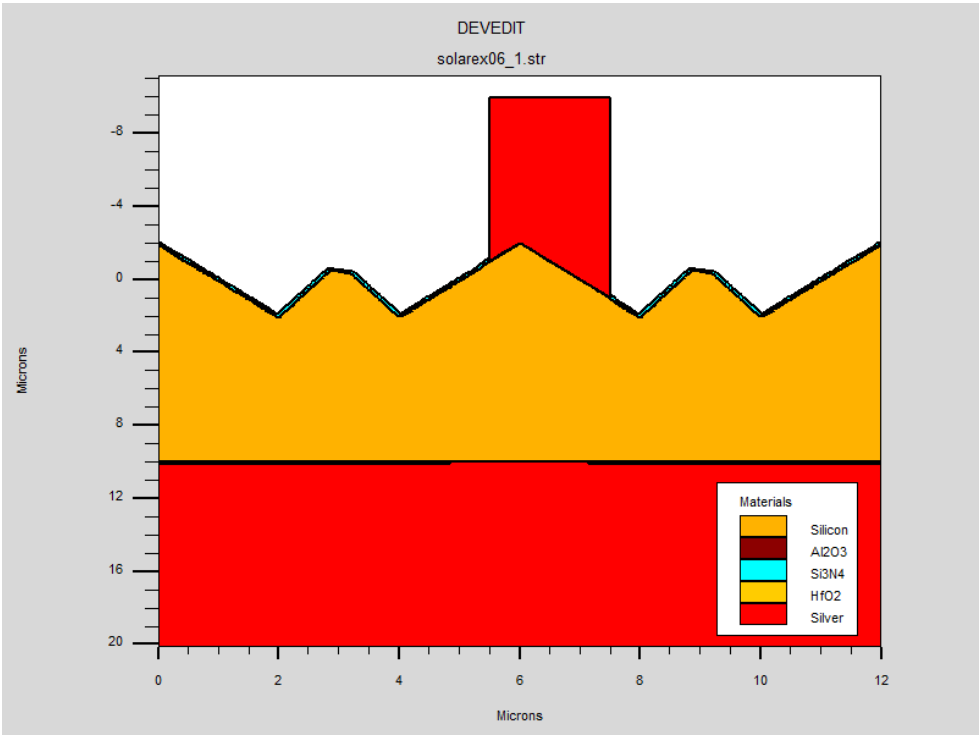


Fig. 8.5: Schematic diagram of selective emitter PERT structure in SILVACO

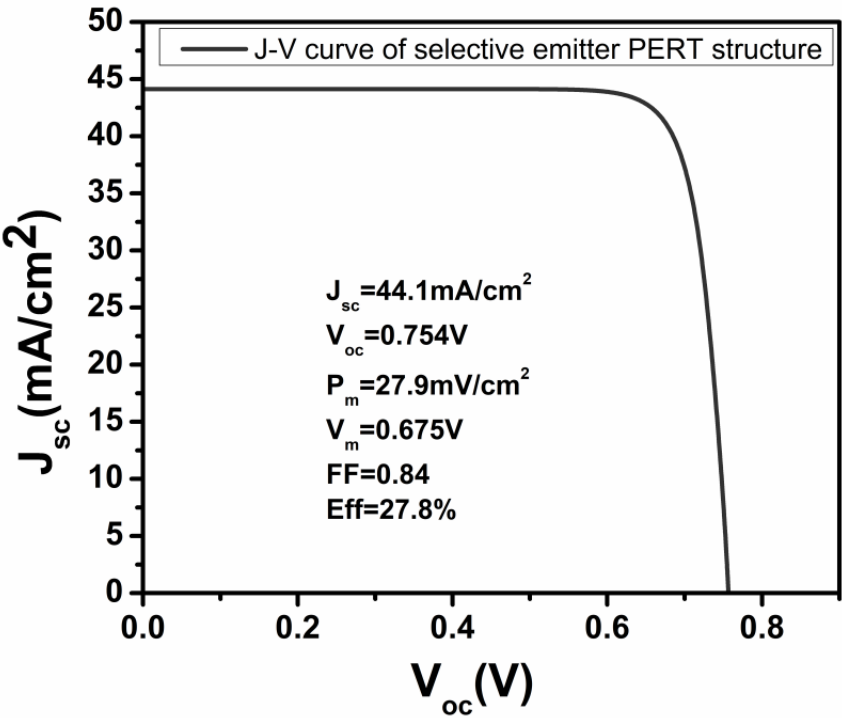


Fig. 8.6: J-V plot of wafer of selective emitter PERT structure in SILVACO

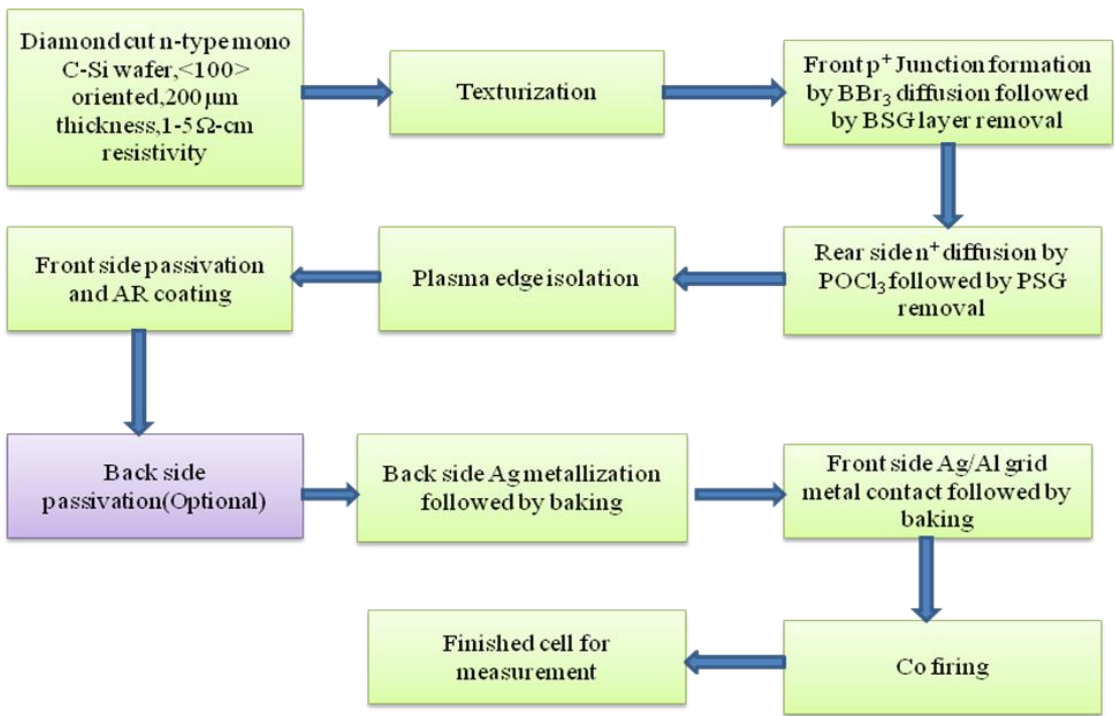
8.3. Solar cell fabrication with simulated result

8.3.1. Experimental methods

To achieve the objective of fabricating a high-efficiency Al<sub>2</sub>O<sub>3</sub> passivated, n-type crystalline silicon selective emitter solar cell, the initial step involved establishing the baseline of an n-type crystalline silicon solar cell, as outlined in the process flow chart (Scheme 1). Solar cells were experimentally fabricated on n-type CZ crystalline silicon wafers measuring 78 mm × 78 mm, with a thickness of approximately 200 μm and a surface resistivity (ρ) of ~1-5Ω-cm, as illustrated in Fig. 8.7 (a) & (b).

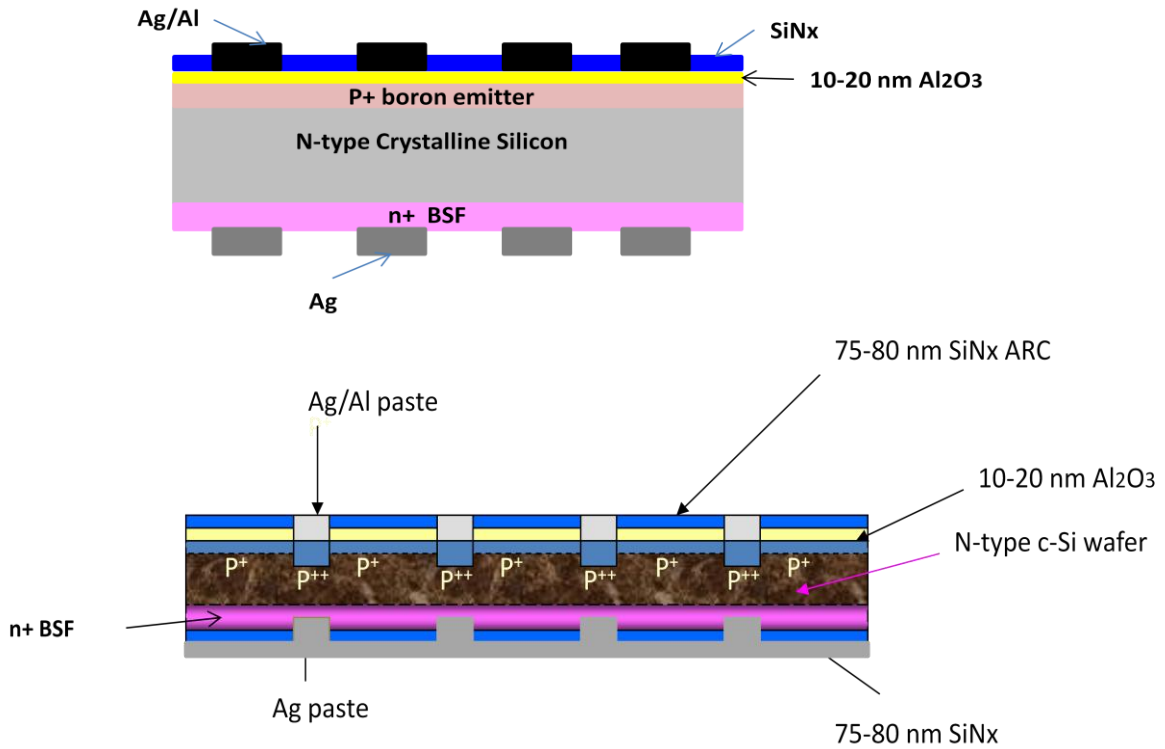
8.3.1.1. Cleaning and Texturization

Prior to texturization, the diamond wire cut silicon (DW-Si) wafers underwent an initial cleaning step using a (1:1 H<sub>2</sub>SO<sub>4</sub>:H<sub>2</sub>O<sub>2</sub>) solution, followed by immersion in a 5% HF solution. The texturization process for n-type C-Si involved standard anisotropic alkali etching using a solution comprising 2% KOH, 6.5% IPA aqueous solution, and 0.33% NaOCl, conducted for 45 minutes at 80°C. Subsequently, the samples were immersed once more in a 5% HF solution and rinsed thoroughly with deionized water multiple times.



Scheme 8.1: Base line process of n-type mono-crystalline silicon solar cell





**Fig. 8.7: Schematic diagram for n type (a) baseline solar cell (b) selective emitter solar cell**

### 8.3.2. Experimental results

#### 8.3.2.1. Front emitter and rear surface diffusion

Surface diffusion was carried out on the textured wafers in a batch process. Front side diffusion was performed to create a p<sup>+</sup> emitter using a liquid boron tri-bromide (BBr<sub>3</sub>) source maintained at 20°C in an open tube diffusion furnace. The diffusion process was executed in four sets at temperatures ranging from 925-955°C for pre-deposition durations of 15-25 minutes, followed by drive-in durations of 15-20 minutes, and concluding with a low-temperature oxidation step for 10 minutes. The resulting sheet resistance varied with different diffusion profiles: the first set achieved a sheet resistance of 45-50 Ω/sq, the second set around 50-60 Ω/sq, the third set approximately 60-70 Ω/sq, and the fourth set exhibited the highest sheet resistance, reaching 70-80 Ω/sq. After diffusion, the wafers were immersed in a 5% HF solution to completely remove the borosilicate glass (BSG) layer.

On the other hand, back side diffusion was conducted to form a rear n<sup>+</sup> back surface field (BSF) using a liquid phosphorus oxy-chloride (POCl<sub>3</sub>) source, also kept at 20°C in an open

tube diffusion furnace at a temperature of 900°C, in a back-to-back configuration in a batch process with pre-deposition and drive-in durations of 15 minutes and 10 minutes, respectively.

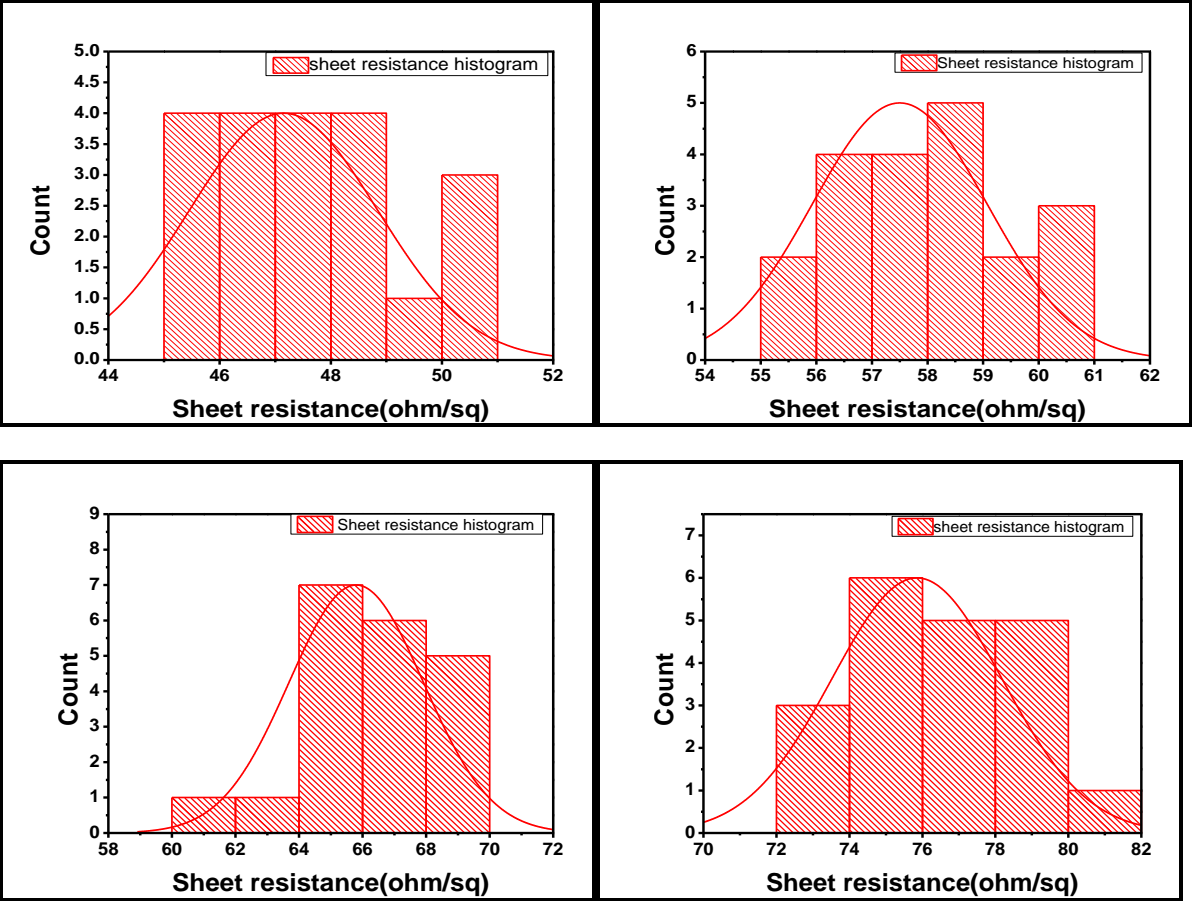


Fig. 8.8: Histogram data of four sets of diffusion (a) $R_{sh}=45-50\text{ohm/sq}$  (b)  $R_{sh}=50-60\text{ohm/sq}$  (c) $R_{sh}=60-70\text{ohm/sq}$  (d) $R_{sh}=70-80\text{ohm/sq}$

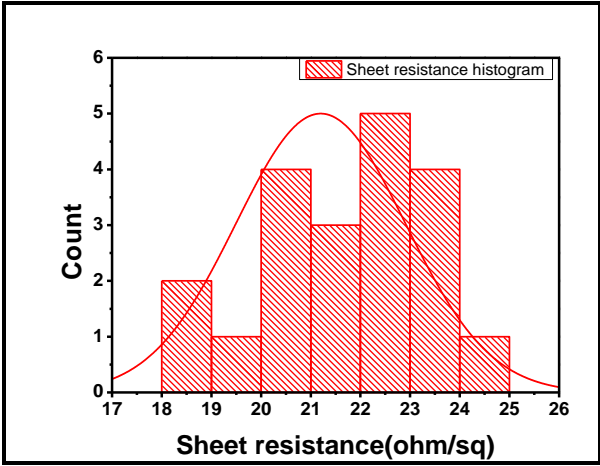
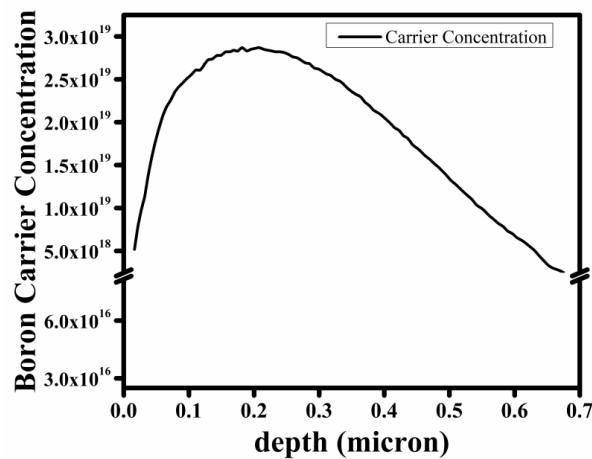


Fig. 8.9: 20-22 ohm/sq sheet resistance on rear side of n type c-Si sample

The sheet resistance on the rear surface was maintained at around 20-22  $\Omega/\text{sq}$ . Emitter sheet resistance ( $R_{\text{sheet}}$ ) was measured using a four-probe unit. Histograms depicting the different diffusion profiles of the front and rear surfaces are shown in Fig. 8.8 and 8.9, respectively.

The electro-capacitance voltage (ECV) curve for boron diffusion corresponding to the 45-50  $\Omega/\text{sq}$  profile is depicted in Fig. 8.10.



**Fig. 8.10: Emitter profiles of electrically active phosphorus as measured by ECV after diffusion.**

### 8.3.2.2. Dielectric film deposition

The optimization of dielectric layer deposition was succinctly illustrated through simulation modeling. These analyses indicated that employing  $\text{Al}_2\text{O}_3$  on the front surface and  $\text{HfO}_2$  on the rear surface led to the most significant enhancement in cell efficiency. Consequently, in the experimental fabrication of solar cells, this passivation layer combination was utilized. These optimized passivation layers also yielded the highest efficiency in this model. Following the successful Plasma Edge isolation of all diffused wafers, a conformal 10 nm thick aluminum oxide ( $\text{Al}_2\text{O}_3$ ) layer was deposited on the samples using a Thermal ALD (T-ALD) system (Gemstar, USA) for passivation purposes. Trimethylaluminum precursor (TMA) from Sigma Aldrich (stored at room temperature) and DI water served as source oxidants for the  $\text{Al}_2\text{O}_3$  layer deposition. The entire deposition process was conducted in an inert  $\text{N}_2$  ambient with a flow rate of 10 sccm. The chamber pressure was maintained below 30 mTorr by gas pumping after sample loading. The process temperature was set at  $175^\circ\text{C}$ , and 84 cycle depositions were utilized to grow a 10 nm thick  $\text{Al}_2\text{O}_3$  film. On the rear surface, a 10

nm thick layer of hafnium oxide ( $\text{HfO}_2$ ) was deposited using T-ALD. The source material, Tetrakis dimethylamino hafnium (TDMAH) from Sigma Aldrich, was kept at 60 °C. The processing temperature for the  $\text{HfO}_2$  film was 225 °C, and 110 process cycles were performed to deposit the 10 nm film. Degassing was necessary before each deposition in T-ALD to prevent impurities.

8.3.2.3. Lifetime measurement

Surface analysis of the front  $\text{Al}_2\text{O}_3$  and rear  $\text{HfO}_2$  passivation layers was conducted by measuring the minority carrier lifetime using a semilab lifetime tester. The enhancement of lifetime with annealing temperature confirms the passivation effect, with the maximum lifetime achieved at 500°C, reaching up to 170  $\mu\text{s}$ . The lifetime data before and after annealing are presented in Table 8.4.

Table 8.4: Lifetime data of samples after oxide deposition

Passivating Agent	Size of cell	Cell surface	Lifetime ( $\mu\text{s}$ ) of as-deposited	Lifetime ( $\mu\text{s}$ ) of annealed
$\text{Al}_2\text{O}_3$	78 mm $\times$ 78 mm	Front	24.5	170
$\text{HfO}_2$	78 mm $\times$ 78 mm	Rear	20	70

8.3.2.4. Deposition of anti-reflection coating

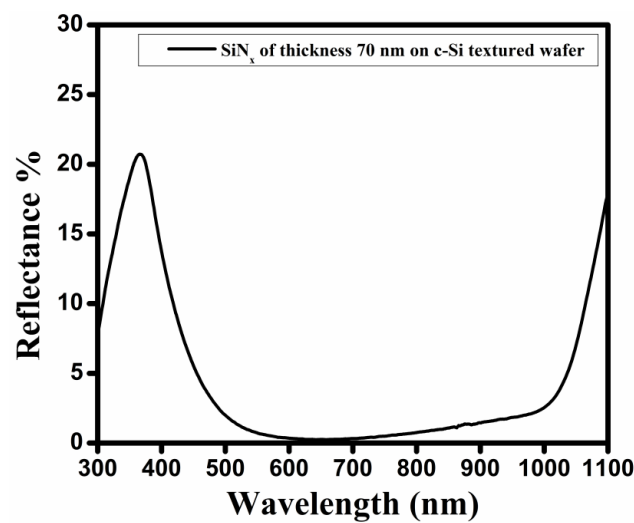


Fig. 8.11 Reflectance curve of n-type crystalline silicon substrate after silicon nitride deposition using UV-VIS-NIR spectrophotometer

Subsequently, the wafers underwent coating with a 70 nm thick SiN<sub>x</sub> layer for antireflection coating via standard PECVD technique (Hindhivac, India). Following the ARC coating, reflection data were calibrated using a UV-VIS-NIR Spectrophotometer (Shimadzu 3700), revealing approximately 5% reflectance, as depicted in fig. 8.11.

8.3.2.5. Metallization and Co-firing

Later, the wafers were screen printed for conventional metallization on the rear side with Ag paste, followed by baking at 300°C in a belt furnace. Subsequent front side metallization was conducted using Ag-Al paste, followed by baking at 300°C and co-firing at 800-850°C in a belt furnace. The high-temperature firing process facilitated metal silicon bonding as the metals punched through the ALD deposited oxides to silicon [28]. Following this, the cells were calibrated for the I-V characteristics using a Solar Simulator tester (SINTON). For a 78 mm × 78 mm solar cell, an efficiency of 16.7% was achieved for a 45-55 ohm/sq emitter surface doping. The J-V curve for the solar cell is depicted in fig. 8.12. This suggests that further optimization of the firing techniques during the metallization process may lead to an increased fill factor. Additionally, improved front and rear surface passivation could enhance efficiency.

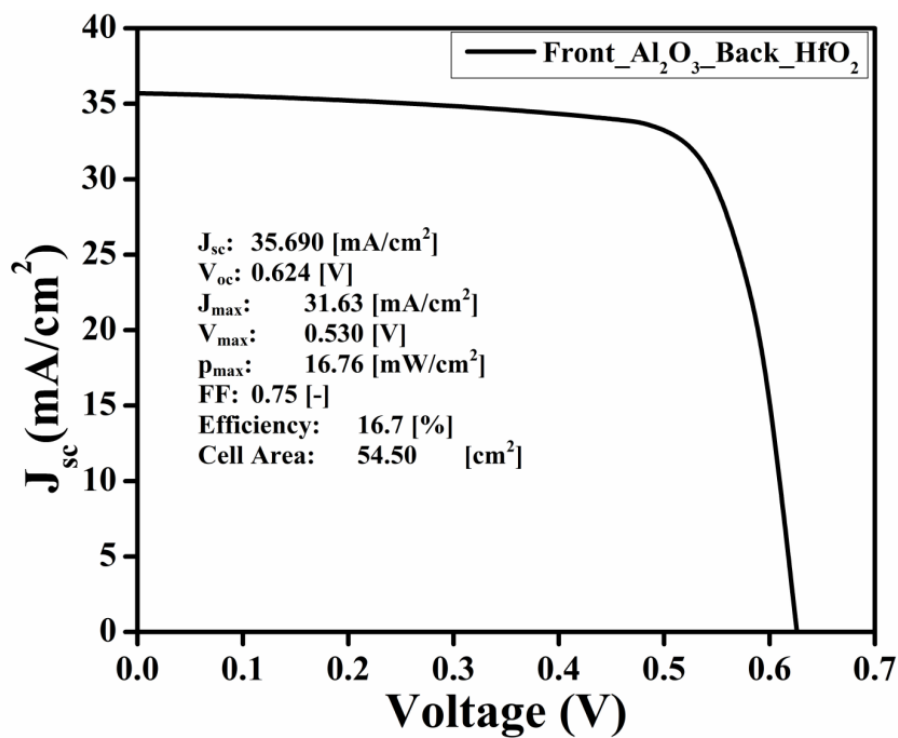
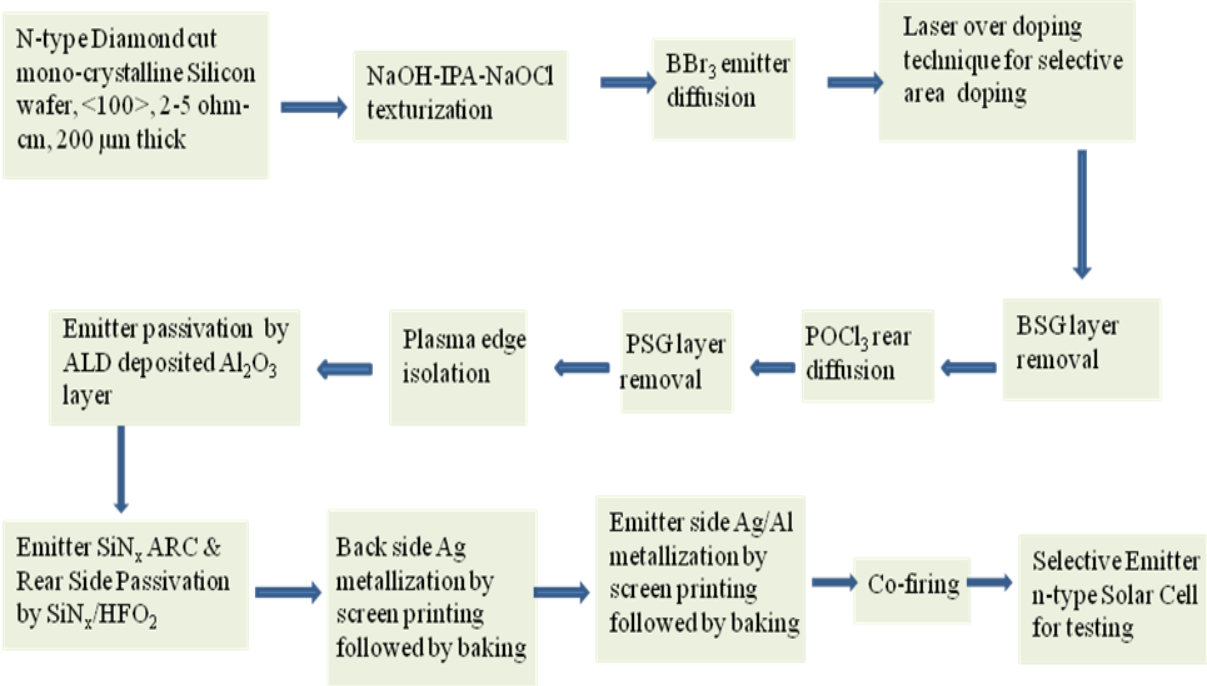


Fig. 8.12: J-V characteristics of 45-55 ohm/sq, 78 mm × 78 mm solar cell.

8.3.2.6. Fabrication of Selective emitter solar cell

Following the simulation results, I proceeded to fabricate an n-type crystalline silicon  $\text{Al}_2\text{O}_3$  passivated selective emitter solar cell with laser over-doping process, as depicted in detail in scheme 8.2.



**Scheme 8.2: Flow chart for fabrication of n-type selective emitter solar cell by laser over-doping process**

After diffusion and an HF dip, the surface underwent treatment with a green laser in a patterned style to create the grid structure. T-ALD was utilized to deposit 10 nm thick  $\text{Al}_2\text{O}_3$  layers on the front side and 10 nm thick  $\text{HfO}_2$  layer on the rear side of the wafer. Subsequently, 70 nm thick undoped hydrogenated silicon nitride ( $\text{SiN}_x\text{:H}$ ) layers were deposited by PECVD on the front side. Metal contacts were then deposited following the same pattern, and the samples underwent a firing step in an IR belt furnace at 800-850°C using a typical screen printing process.

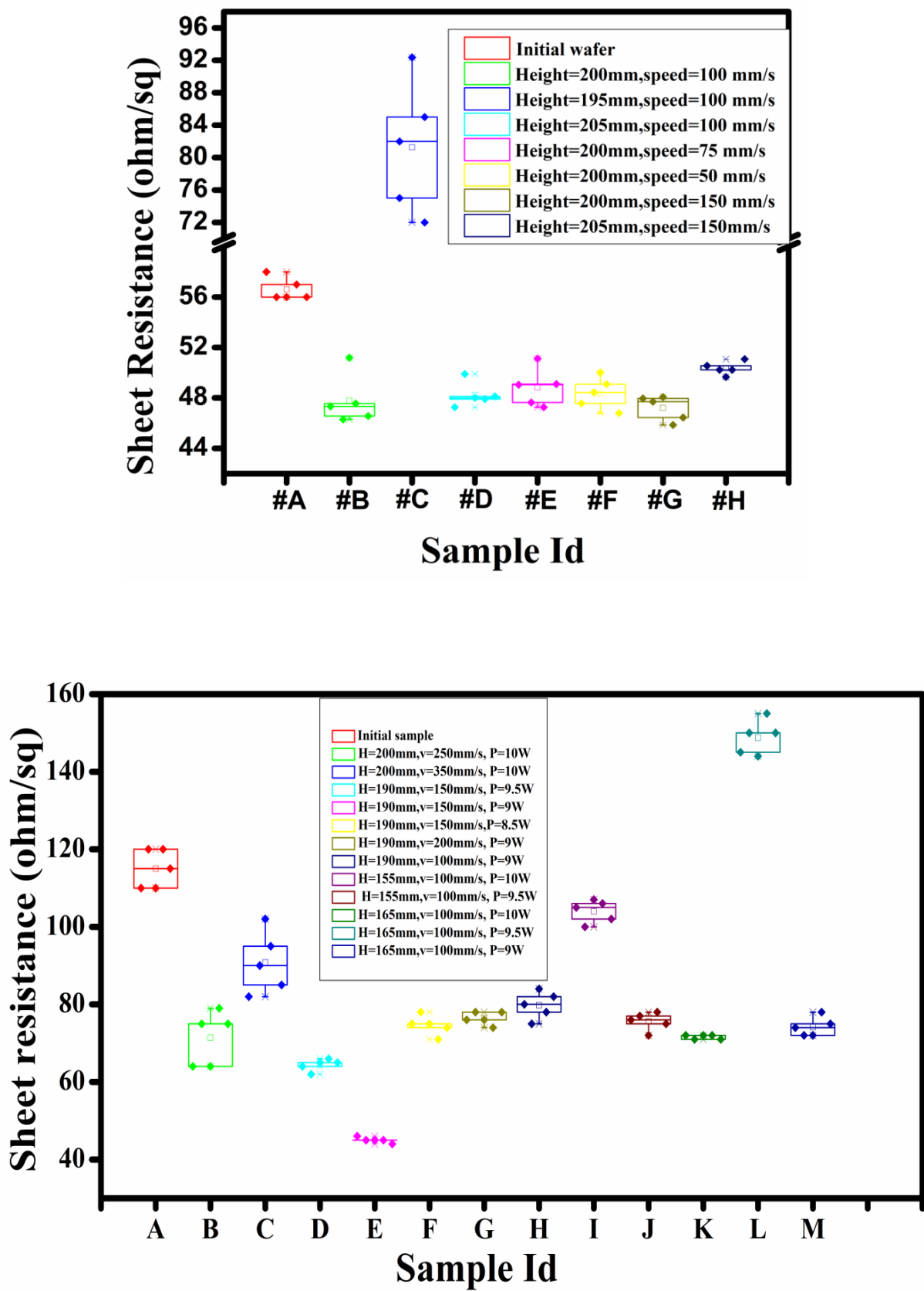


Fig. 8.13: Box chart of variation of sheet resistance (a) with the changes of height and speed of laser beam; (b) with the changes of power of laser beam for laser over-doping selective emitter

By varying the height, speed, and power of the laser, etching was performed at specific regions of the wafer beneath the metal contact, resulting in changes in sheet resistance. The remaining portion of the wafer surface was initially covered by an acid-resistant polymer TP-2019 (an in-house developed polymer). Two types of box charts were generated to illustrate the differences in sheet resistance with various samples: one depicting changes in height and speed of the laser beam (fig. 8.13a), and the other showing variations in the power of the laser beam (fig. 8.13b). Through the laser over-doping treatment, an efficiency of 17.2% was achieved for a 78 mm × 78 mm solar cell, as demonstrated by the J-V curve depicted in fig. 8.14.

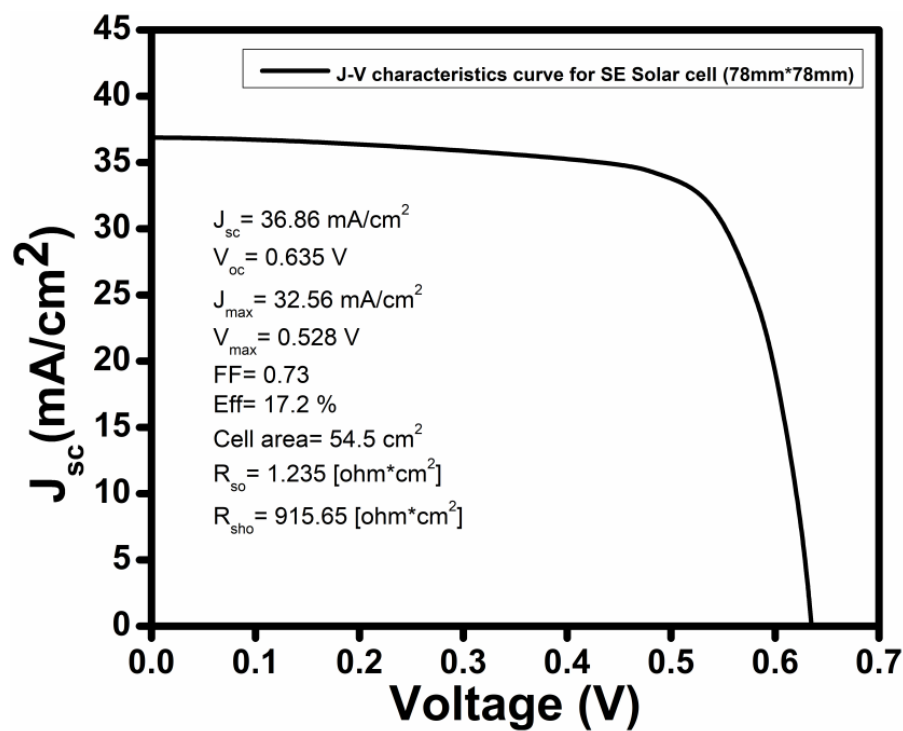


Fig. 8.14: J-V curve of 78mm×78mm laser over-doped selective emitter solar cell

8.4. Conclusions

The current focus in solar cell technology revolves around enhancing efficiency and streamlining fabrication techniques. The emerging trend in the solar photovoltaic field is the selective emitter structure, valued for its heightened efficiency and simplified fabrication process. This study explores two fabrication approaches for solar cells. The first involves modeling n-type selective emitter solar cells using simulation software, while the second



employs conventional diffusion with ALD passivation, followed by laser over-doping to produce n-type selective emitter solar cells. Initially, a uniform lightly doped emitter is created through a diffusion process using  $\text{POCl}_3$  as the source. Subsequently, laser overdoping is applied to the contact regions to establish the selective emitter structure, achieved by employing a laser beam to inscribe the grid pattern. Finally, screen-printing is employed to fabricate the contacts. I have produced multiple batches of  $78 \text{ mm} \times 78 \text{ mm}$  area solar cells, utilizing these procedures individually, to investigate the effects of key laser and dopant parameters on solar cell performance. The development of large-area devices is underway.

Both methodologies yielded promising results. The selective emitter (SE) silicon solar cell demonstrates superior performance metrics, including higher open circuit voltage ( $V_{oc}$ ), improved short circuit current density ( $J_{sc}$ ), and enhanced conversion efficiency ( $\eta$ ). This is attributed to the lightly doped emitter region, which mitigates recombination velocity, and the heavily doped emitter region beneath the front contact, which reduces contact resistance. Optimal passivation is crucial for minimizing losses. Dual passivation utilizing  $\text{Al}_2\text{O}_3$  and  $\text{HfO}_2$  proves effective in enhancing the efficiency of selective emitter silicon solar cells. Further optimization is necessary to potentially enhance solar cell efficiency even further.

## References

- [1] A. Rohatgi, M. Hilali, D. L. Meier, A. Ebong, C. Honsberg, A.F. Carrol, P. Hacke, 17<sup>th</sup> European Photovoltaic Solar Energy Conference and Exhibition (PVSEC), Munich, Germany, Atlanta: Georgia Institute of Technology, 2001.
- [2] M. J. Kerr, J. Schmidt, H. Cuevas, *Journal of Applied Physics*, 89 (2001) 3821-3826.
- [3] N. Stem, M. Cid, *Solid State Electron*, 48 (2004) 197-205.
- [4] M. Inyong, K. Kyunghae, M. Thamilselvan, K. Youngkuk, H. Kyumin, K. Doheon, K. Taeyoung, A. Dao Vinh, L. Jeongchul, J. Minkyu, L. Kyungsoo, Y. Junsin, *Sol Energy Mater Sol Cells*, 93 (2009) 846-850.
- [5] A. Dastgheib-Shirazi, H. Helge, R. Bernd, B. Felix, H. Giso: in: *Proceedings of the 23<sup>rd</sup> European Photovoltaic Solar Energy Conference and Exhibition (PVSEC)*, Valencia, Spain, Munich: WIP-Renewable Energies, 2008, pp. 1197-1199.
- [6] A. K. Volk, U. Jaeger, J. Rentsch, R. Preu, in: *Proceedings of the 26<sup>th</sup> European PVSEC*, 2011, PP-884-889.
- [7] D. Rudolph, K. Peter, A. Meijer, O. Doll, I. Kohler, in: *Proceedings of the 26<sup>th</sup> European PVSEC*, 2011, PP-1349-1352.
- [8] K. Song, B. Kim, H. Lee, Y. J. Lee, C. Park, N. Balaji, M. Ju, J. Choi, J. Yi, *Nanoscale Research Letters*, 7 (2012) 410-1-410-8.
- [9] H. Antoniadis, in: *Proceedings of the 34<sup>th</sup> IEEE Photovoltaic Specialists Conference (PVSC)*, 2009, pp. 650-654.
- [10] D. Poplavsky, G. Scardera, M. Abbott, F. Lemmi, in: *Proceedings of the 35<sup>th</sup> IEEE Photovoltaic Specialists Conference (PVSC)*, 2010, pp. 3565-3569.
- [11] G. Scardera, D. Poplavsky, M. Abbott, F. Lemmi, in: *Proceedings of the 37<sup>th</sup> IEEE Photovoltaic Specialists conference (PVSC)*, 2011, pp. 2202-2205.
- [12] Z. Hameiri, L. Mai, A. Sproul, S. R. Wenham, *Applied Physics letters*, 97 (2010) 222111-1-222111-3.
- [13] Z. Hameiri, T. Puzzer, L. Mai, A. B Sproul, S. R Wenham, *Progress in Photovoltaics*, 19 (2011) 391-405.
- [14] E. Lee, H. Lee, J. Choi, D. Oh, J. Shim, K. Cho, J. Kim, S. Lee, B. Hallam, S. R. Wenham, *Solar Energy Materials and Solar Cells*, 95 (2011) 3592-3595.
- [15] H. Nishimura, K. Hirata, M. hasegawa, T. Katagiri, T. Fuyuki, *Japanese Journal of Applied Physics*, 51 (2012) 10NA15-1-10NA15-4.

- [16] S. Wang, A. Lennon, B. Tjahjono, L. Mai, B. Vogl, S. Wenham, Solar Energy materials and Solar cells, 99 (2012) 226-234.
- [17] L. Q. Zhu, J. Gong, J. Huang, P. She, M. L. Zeng, L. Li, M. Z. Dai, Q. Wan, Solar Energy materials and Solar Cells, 95 (2011) 3347-3351.
- [18] C. E. Dube, B. Tsefreakas, D. Buzby, R. Tavares, W. M. Zhang, A. Gupta, R. J. Low, W. Skinner, J. Mullin, Energy Procedia, 8 (2011) 706-711.
- [19] D. M. Chen, Z. C. Liang, L. Zhuang, Y. F. Lin, H. Shen, Applied energy, 92(2012) 315-321.
- [20] Z. Liang, F. Zeng, H. Shen, Solar energy Materials and Solar cells, 109(2013) 26-32.
- [21] C. H. Lin, S. P. Hsu, J. J. Liou, C. P. Chuang, W. H. Lu, W. L. Chang, Solar Energy materials and Solar cells, 109(2013) 26-32.
- [22] I. Moon, K. Kim, M. Thamilselvan, Y. Kim, K. Han, D. Kyeong, T. Kwon, D. Vinh Ai, J. Lee, M. Ju, Solar Energy materials and Solar Cells, 93(2009) 846-850.
- [23] U. Jager, S. Mack, A. Kimmerle, A. Wolf, R. Preu, 35<sup>th</sup> IEEE Photovoltaic Specialists conference (PVSC), Honolulu. Piscataway: IEEE Xplore Digital Library, 2010, pp.3185-3189.
- [24] M. Z. Rahman, optics and photonics journal 02 (2012) 129-134.
- [25] D. Pysch, J. Ziegler, J. P. Becker, D. Suwito, S. Janz, S. W. Glunz, and M. Hermie, 34<sup>th</sup> IEEE Photovoltaic Specialists Conference (PVSC), IEEE, 2009, pp.000794-000799.
- [26] S. K. Oh, H. S. Shin, K. S. Jeong, M. Li, H. Lee, K. Han, Y. Lee, G. W. Lee and H. D. Lee, Journal of Semiconductor Technology and Science , 13 (2013) 6.
- [27] S. Choi, K. H. Min, M. S. Jeong, J. I. Lee, M. G. Kang, H. E. Song, Y. Kang, H. S. Lee, D. Kim & K. H. Kim, Scientific Reports, 7 (2017) 12853.
- [28] M. Pawlika, J. P. Vilcota , M. Halbwaxa , D. Aureauc , A. Etcheberryc , A. Slaouid , T. SchutzKuchlyd & R. Cabale, Energy Procedia, 60 ( 2014 ) 85 – 89.

\*\*\*





*"The most important of my discoveries have been suggested to me by failures."*

- Humphry Davy



# Chapter 9

---

**Conclusion, Novelty and Scope of future work**

## 9.1. Conclusion

Since its discovery, Transition Metal Dichalcogenides (TMDs) have garnered considerable attention from researchers eager to explore their potential in semiconductor technology. The advancements in research and their impact on our daily lives underscore the significance of metal-semiconductor interfaces in electronic devices. Besides pure TMDs, the composites i.e. alloys comprising various TMDs have gained significant traction, especially in the realm of photosensing devices. Schottky barrier diodes serve as fundamental components for metal-semiconductor interfaces in these devices, thus endorsing thorough investigation.

This study focuses on synthesizing and characterizing both pure MoS<sub>2</sub> and its alloy with tungsten, followed by the fabrication of Schottky diodes to assess the impact of W doping. Additionally, novel materials including 2-amino terephthalic acid-directed supramolecular Mn(II)-metallogel, butane-1,4-dicarboxylic acid-directed supramolecular Mn(II), Cd(II)-metallogels, and 5-aminoisophthalic acid-directed Supramolecular Ni(II)-Metallogel are synthesized and characterized to explore their potential applications in Schottky Barrier Diodes (SBDs).

By employing sodium molybdate di-hydrate and thiourea as precursors, coupled with Oxalic Acid and Hydroxylamine hydrochloride as catalysts, pure MoS<sub>2</sub> is synthesized via a hydrothermal approach. Subsequently, its alloy compounds of Tungsten with varying molar ratios are prepared by substituting sodium molybdate di-hydrate with sodium tungstate di-hydrate. These processes are followed by structural and optical characterization. Thin film Schottky Diodes fabricated using these materials are evaluated under both dark and illuminated conditions to assess their relative performance. The compounds exhibit enhanced rectifying properties under illumination, demonstrating increased current values and heightened photosensitivity of Mo<sub>1-x</sub>W<sub>x</sub>S<sub>2</sub> alloy nano-composite structure compared to pristine MoS<sub>2</sub>. To probe the charge transport properties across the metal-semiconductor (MS) junction, Space Charge Limited Current (SCLC) theory is employed, focusing on the SCLC region. Understanding the charge transport kinetics within any material necessitates insight into its microstructure. On this matter, Impedance Spectroscopy analysis is conducted to comprehend



the electric and dielectric properties of MoS<sub>2</sub> and MoWS<sub>2</sub> composites. The Nyquist plot representing the impedance at the MS interface is analyzed using an equivalent circuit model. Overall, the diode parameter values indicate that the specific Mo<sub>0.8</sub>W<sub>0.2</sub>S<sub>2</sub> nano-composite-based device outperforms its counterparts for photosensitive applications.

Furthermore, we synthesized several other metallogels, including 2-amino terephthalic acid-directed Mn(II)-metallogel, butane-1,4-dicarboxylic acid-based Mn(II) and Cd(II)-metallogels, and Ni(II)-Metallogel based on 5-aminoisophthalic acid. Our aim is to expand the literature on metallogel-based scientific and technological advancements, aiming to develop highly functional devices with exceptional flexibility. The production of ATA-directed stable supramolecular metallogel of Mn(II) was facilitated by non-covalent supramolecular factors such as the  $\pi$ -system and hydrogen bonding patterns, as indicated by FT-IR data. Its band gap value of 3.34 eV denotes its semiconducting property and entitles further investigation for diodes. The values obtained under dark and light conditions clearly underscore its significance in photosensitive devices. Our findings may open up new dimensions in the research of mechanically flexible networks for creating functional optoelectronic devices, achieved through the utilization of small molecules via strategic utilization of non-covalent supramolecular interactions. This could potentially lead to flexible smart electronic diodes with light sensitivity and advanced functionality.

Additionally, with BDA-directed Mn(II) and Cd(II)-metallogels, we aimed to elucidate various metallogel-related features such as rheological, morphological, and mechanistic strategies, using spectroscopic outcomes. The FT-IR stretching frequencies of individual xerogel samples validate the significant role of non-covalent supramolecular interactions in individual metallogel construction. In our exploration of metallogel-based functional devices, we endeavored to study the voltage-dependent current density, charge transportation, and rectification ratio of metallogel-based fabricated diodes. We anticipate that this study will contribute to the advancement of mechanically flexible type material-based device fabrication for technological applications.

To a greater extent, the novel supramolecular Ni@5AIA metallogel illustrates various non-covalent interactions that contribute to the formation of a stable metallogel at room temperature. The mechanical stability of this metallogel was confirmed through rheological tests. With a band

gap of 3.37 eV, highlighting its semiconducting nature, this metallogel is investigated for its optoelectronic behavior. The results suggest that this material holds promise for supramolecular Ni<sup>2+</sup> metallogel-based electronic devices for advanced technology.

The demand for photovoltaic technology necessitates cost-effective and highly efficient solar cell structures. Balancing surface recombination velocity and contact resistance is crucial in the utilization of selective emitters in solar cell research. In summary, three significant challenges have emerged: firstly, many fabrication processes for selective emitter solar cells involve double diffusion steps, which are prohibitively expensive; secondly, difficulties arise in aligning the front side metal grid accurately with the highly doped emitter surface during contact formation; and thirdly, the etch-back method results in an uncontrolled etching process. My research focuses on addressing these challenges, yielding promising results. In this study, a new method was utilized to create a selective emitter. I have endeavored to simultaneously form the front side selective emitter and the rear back surface field (BSF) layer during the rear side diffusion step. The consecutive advancement of solar cell development is detailed in my work. This method stands out for its omission of double diffusion or etching steps, this represents a milestone in my research. I consider my approach to be innovative in comparison to existing methods in this field. It offers more consistent, uniform, and controllable contact resistance than Reactive Ion Etching (RIE) and Etch Back processes. Moreover, this technique only requires diffusion and screen printing equipment, making it suitable for mass production in industrial settings. Consequently, this process enables the cost-effective production of low-cost n-type crystalline silicon selective emitters. I have conducted theoretical simulations to model and design selective emitter solar cells, with the optimized parameters then applied in fabricating such cells using the laser over-doping technique. Initially, Diamond Wire Saw (DWS) wafers were chosen for their widespread availability and industrial-scale production. DWS technology has garnered interest in solar cell industries due to its minimal kerf loss, high throughput, and cost-effectiveness compared to SWS technology. This research highlights the significant potential for achieving high-efficiency solar cells. Its batch processing viability, reduced number of steps, ease of operation and maintenance, and cost-effectiveness suggest numerous opportunities for its implementation at an industrial scale in the formation of selective emitter solar cells.

So, the thesis highlights the distinctive characteristics of TMD alloy, positioning it as a promising option for electronic devices. Through the investigation, insights are gained into enhancing device performance by varying the molar ratios of Tungsten in  $\text{MoS}_2$ . Additionally, a detailed examination of the MS junction and the kinetics of total charge transfer offers fundamental insights into microstructure. These findings hold significance for the development of photodetectors, transistors, solar cells, and other technologies. Furthermore, the synthesis of new semiconducting supramolecular metallogel materials from low molecular weight gelators demonstrates their potential in the opto-electronic industry. I have introduced an innovative approach to fabricate selective emitters. Our findings demonstrate the successful formation of the selective emitter in a single diffusion process, eliminating the need for additional heat treatment or chemical etching. Consequently, this method proves to be cost-effective.

## 9.2. Novelty

- While extensive research has explored  $\text{WS}_2/\text{MoS}_2$ -based composites, there remains a gap in the literature regarding the application of semiconducting  $\text{Mo}_{1-x}\text{W}_x\text{S}_2$  composite in metal-semiconductor junctions for Schottky Barrier Diode (SBD) purposes. This material holds significant promise for future studies in the metal-semiconductor junction research field.
- The adaptability of diodes provides an extra advantage for technological progress, as these semiconductor devices can be shaped as desired and located anywhere within a device. Integrating supramolecular metallogels into practical semiconductor equipment poses a consistent technological hurdle. I successfully implemented these gel-based materials in thin-film devices based on metal–semiconductor junctions to assess their potential in electronic devices and charge transport. I believe this research will contribute to advancing the fabrication of mechanically flexible material-based devices for technological applications.
- I developed a unique method to create a selective emitter, distinct from current techniques, enabling simultaneous formation of front side selective emitter and rear back surface field (BSF) layer during rear side diffusion, thereby reducing costs by eliminating the need for

double diffusion or etching processes. Due to the unavailability of  $p^+$  contacting pastes for the  $p^+$  emitter of n-type solar cells, research into selective emitter formation and its various parameters remains a challenge. I believe my approach is innovative compared to existing methods and can be adopted by the industry, requiring only diffusion and screen printing facilities. This method offers more consistent, uniform, and controllable contact resistance than Reactive Ion Etching (RIE) and Etch Back processes, making it suitable for mass production due to its batch process feasibility, fewer processing steps, ease of operation and maintenance, and cost-effectiveness.

### 9.3. Scope of future work

- The author intends to enhance the  $\text{Mo}_{1-x}\text{W}_x\text{S}_2$ -based Schottky device further and explore the application of  $\text{MoWS}_2$  in various semiconductor devices such as sensors and solar cells in the future.
- The author has initiated research on "Energy quenching and fluorescence resonance energy transfer (FRET) of excitons from Poly (3-hexylthiophene) (P3HT) to  $\text{MoWS}_2$ " and has made intriguing observations.  $\text{MoWS}_2$  demonstrates significant promise as an acceptor of excitons originating from the P3HT organic polymer. The absorption and emission characteristics strongly suggest the potential for resonance energy transfer within P3HT: $\text{MoWS}_2$ , facilitated by the energy quenching technique.
- The author aims to utilize flexible metallogels in smart electronic devices to contribute to advanced technology.
- Further optimization is required for surface passivation and metallization, particularly in refining firing techniques to potentially enhance the fill factor. Improved front and rear surface passivation could also lead to increased efficiency. The author intends to explore applying the selective emitter structure to interdigitated back contact (IBC) solar cells.

## List of Publications

### ➤ Journals Publications

- [1] Improvement of charge kinetics of MoS<sub>2</sub> nano-petal based Schottky device by incorporation of W: A comparative study of structural, optical, and electrical properties.  
**Baishakhi Pal**, Pubali Das, Joydeep Datta, Utpal Gangopadhyay, Partha Pratim Ray, Materials Science in Semiconductor Processing, 162 (2023) 107535.
  
- [2] Investigating charge transportation and photo-responsive outcome of a Schottky diode fabricated by 2-amino terephthalic acid directed supramolecular Mn (II)-metallogel.  
**Baishakhi Pal**, Santanu Majumdar, Krishna Sundar Das, Gerald Lepcha, Indrajit Pal, Partha Pratim Ray, Biswajit Dey, Journal of Physics and Chemistry of Solids, 182 (2023) 111612.
  
- [3] Comparative outcomes of voltage-dependent current density, charge transportation and rectification ratio of fabricated electronic devices by mechanically flexible supramolecular network.  
**Baishakhi Pal**, Santanu Majumdar, Indrajit Pal, Gerald Lepcha, Amiya Dey, Partha Pratim Ray, Biswajit Dey, Dalton Transactions, (2024).
  
- [4] A semiconducting supramolecular novel Ni (ii)-metallogel derived from 5-aminoisophthalic acid low molecular weight gelator: an efficient Schottky barrier diode application.  
**Baishakhi Pal**, Subhendu Dhibar, Ritam Mukherjee, Subham Bhattacharjee, Partha Pratim Ray, Bidyut Saha, Materials Advances, 4 (2023) 3628-3635.
  
- [5] Novel technique for fabrication of n-type crystalline silicon selective emitter for solar cell processing.  
**Baishakhi Pal**, Soma Ray, Utpal Gangopadhyay, Partha Pratim Ray, Materials Research Express, 6 (2019) 75523.
  
- [6] Exploration of semiconducting properties of Zn (II)-and Cd (II)-based coordination polymers with dicarboxylate of a chair-type backbone.  
Akhtaruzzaman, **Baishakhi Pal**, Samim Khan, Basudeb Dutta, Sanobar Naaz, Suwendu Maity, Prasanta Ghosh, Partha Pratim Ray, Mohammad Hedayetullah Mir, CrystEngComm, 23 (2021) 7525-7533.
  
- [7] An experimental approach to ensure energy quenching and fluorescence resonance energy transfer of excitons from P3HT to CuInSe<sub>2</sub>.  
Animesh Biswas, **Baishakhi Pal**, Mainak Das, Ramjan Sk, Animesh Layek, Partha Pratim Ray, Materials Letters, 338 (2023) 134066.

- [8] Utilization of counter anions for charge transportation in the electrical device fabrication of Zn (II) metal-organic frameworks.  
Krishna Sundar Das, **Baishakhi Pal**, Sayan Saha, Sohel Akhtar, Avik De, Partha Pratim Ray, Raju Mondal, Dalton Transactions, 49 (2020) 17005-17016.
- [9] Findings of inhomogeneity in barrier height of Schottky junction Al/rGO-SnO<sub>2</sub> having anomaly in theoretical and experimental value of Richardson constant: A Gaussian approach.  
Pubali Das, **Baishakhi Pal**, Mrinmay Das, Sayantan Sil, Dhananjoy Das, Animesh Layek, Partha Pratim Ray, Results in Physics, 42 (2022) 105996.
- [10] Improved charge transport properties of graphene incorporated tin oxide based Schottky diode over pure one.  
Pubali Das, **Baishakhi Pal**, Joydeep Datta, Mrinmay Das, Sayantan Sil, Partha Pratim Ray, Journal of Physics and Chemistry of Solids, 148 (2021) 109706.
- [11] Exploring a supramolecular gel to *in-situ* crystal fabrication from the low molecular weight gelators: a crystal engineering approach towards microelectronic device application.  
Subhendu Dhibar, **Baishakhi Pal**, Kripasindhu Karmakar, Sandip Kundu, Subham Bhattacharjee, Rupam Sahoo, SK Meheubub Rahaman, Dhananjay Dey, Partha Pratim Ray, Bidyut Saha, ChemistrySelect, 8 (2023) e202204214.
- [12] A 5-aminoisophthalic acid low molecular weight gelator based novel semiconducting supramolecular Zn (ii)-metallogel: unlocking an efficient Schottky barrier diode for microelectronics.  
Subhendu Dhibar, **Baishakhi Pal**, Kripasindhu Karmakar, Sanjay Roy, Sk Abdul Hafiz, Arpita Roy, Subham Bhattacharjee, Soumya Jyoti Ray, Partha Pratim Ray, Bidyut Saha, Nanoscale Advances, 5 (2023) 6714-6723.
- [13] Exploitation of Structure-Property Relationships towards Multi-Dimensional Applications of a Paddle-Wheel Cu (II) Compound.  
Basudeb Dutta, **Baishakhi Pal**, Sunanda Dey, Suvendu Maity, Partha Pratim Ray, Mohammad Hedayetullah Mir, European Journal of Inorganic Chemistry, 2022 (2022) e202100904.
- [14] Effect of graphene on improved photosensitivity of MoS<sub>2</sub>-graphene composite based Schottky diode.  
Soumi Halder, **Baishakhi Pal**, Arka Dey, Sayantan Sil, Pubali Das, Animesh Biswas, Partha Pratim Ray, Materials Research Bulletin, 118 (2019) 110507.

- [15] Fabrication of Cu (II) based halobenzoate appended ladder polymers with efficient charge transport properties.  
Sakhiul Islam, **Baishakhi Pal**, Samim Khan, Suwendu Maity, Sanobar Naaz, Prasanta Ghosh, Partha Pratim Ray, Mohammad Hedayetullah Mir, CrystEngComm, 22 (2020) 6720-6726.
- [16] Ni (II) and Zn (II)-metallogel-based anti-bacterial scaffolds for fabricating light-responsive junction-type semiconducting diodes with non-ohmic conduction mechanism.  
Gerald Lepcha, **Baishakhi Pal**, Santanu Majumdar, Kazi Tawsif Ahmed, Indrajit Pal, Swadesh Ranjan Biswas, Partha Pratim Ray, Biswajit Dey, Materials Advances, 4 (2023) 2595-2603.
- [17] Establishment of different aliphatic amines-based rapid self-healing Mg (OH) 2 metallogels: exploring the morphology, rheology and intriguing semiconducting Schottky diode characteristics.  
Santanu Majumdar, **Baishakhi Pal**, Gerald Lepcha, Krishna Sundar Das, Indrajit Pal, Partha Pratim Ray, Biswajit Dey, New Journal of Chemistry, 47 (2023) 4752-4760.
- [18] A croconate-directed supramolecular self-healable Cd (ii)-metallogel with dispersed 2D-nanosheets of hexagonal boron nitride: A comparative outcome of the charge-transport phenomena and non-linear rectifying behaviour of semiconducting diodes.  
Santanu Majumdar, **Baishakhi Pal**, Rajib Sahu, Krishna Sundar Das, Partha Pratim Ray, Biswajit Dey, Dalton Transactions, 51 (2022) 9007-9016.
- [19] Effect of induced charges on the performance of different dielectric layers of c-Si solar cell by experimental and theoretical approach.  
Soma Ray, **Baishakhi Pal**, Hemanta Ghosh, Suchismita Mitra, Anup Kumar Mondal, Chandan Banerjee, Hiranmoy Saha, Utpal Gangopadhyay, Silicon, 12 (2020) 2601-2609.
- [20] Design of Dual Purpose Fe-metallogel for Magnetic Refrigeration and Fabrication of Schottky Barrier Diode.  
Sayan Saha, **Baishakhi Pal**, Krishna Sundar Das, Pradeepta Kumar Ghose, Avik Ghosh, Avik De, Abhijit Kumar Das, Pratim Partha Ray, Raju Mondal, ChemistrySelect, 7 (2022) e202203307.
- [21] Optical Nonlinearity of Semiconducting Cd (II) Metallogel in the Femtosecond Regime with Two-, Three-, and Four-Photon Absorption.  
Tara Singha, **Baishakhi Pal**, Santanu Majumdar, Gerald Lepcha, Indrajit Pal, Partha Pratim Ray, Biswajit Dey, Prasanta Kumar Datta, ACS Applied Optical Materials, 2 (2024) 474-484.

- [22] A Nd6 molecular butterfly: a unique all-in-one material for SMM, MCE and maiden photosensitized opto-electronic device fabrication.  
Krishna Sundar Das, Sayan Saha, **Baishakhi Pal**, Amit Adhikary, Shruti Moorthy, Sukhen Bala, Soheli Akhtar, Pradeepta Kumar Ghose, Saurabh Kumar Singh, Partha Pratim Ray, Dalton Transactions, 51 (2022) 1617-1633.
- [23] Suberic Acid-Based Supramolecular Metallogels of Ni (II), Zn (II), and Cd (II) for Anti-Pathogenic Activity and Semiconducting Diode Fabrication.  
Gerald Lepcha, Santanu Majumdar, **Baishakhi Pal**, Kazi Tawsif Ahmed, Indrajit Pal, Biswarup Satpati, Swadesh Ranjan Biswas, Partha Pratim Ray, Biswajit Dey, Langmuir, 39 (2023) 7469-7483.
- [24] Potential impact of annealed cobalt-sulfide on current rectification of ITO/CoS<sub>2</sub>/Al Schottky device: Structural, optical, electrical, and magnetic characterizations.  
Pubali Das, Jitendra Saha, Satyendra PrakashPal, **Baishakhi Pal**, Animesh Layek, Partha Pratim Ray, Journal of Physics and Chemistry of Solids, 188 (2024) 111922.
- [25] Exploration of temperature dependent dielectric relaxation and correlated barrier hopping (CBH) conduction mechanism of hydrothermally synthesized CuO nanoflakes.  
Rajkumar Jana, Joydeep Datta, Sayantan Sil, Arka Dey, **Baishakhi Pal**, Animesh Biswas, Partha Pratim Ray, Materials Research Express, 6 (2019) 1050d1.
- [26] Unveiling the Semiconducting Diode Property through Current Density-Voltage Features with Effective Interface Mobility and Conductivity of Nitroterephthalic Acid-Directed Supramolecular Co (II)/Cu (II) Metallogels.  
Indrajit Pal, Animesh Biswas, Santanu Majumdar, Gerald Lepcha, **Baishakhi Pal**, Partha Pratim Ray, Biswajit Dey, ACS Applied Engineering Materials, 1 (2023) 3005-3015.



➤ Conference Proceedings

- [1] Texturization of multi crystalline silicon without conventional alkaline and acidic solution for solar cell processing.  
**Baishakhi Pal**, Soma Ray, Sukhendu Jana, Sayan Das, Utpal Gangopadhyay, Partha Pratim Ray, Materials Today: Proceedings, 4 (2017) 12684-12688.
- [2] A Comparative Study of SiO<sub>2</sub>: TiO<sub>2</sub> Composite and SiO<sub>2</sub> Film by Sol-Gel Method for Solar Cell Application.  
 Kausturi Chatterjee, Soma Ray, **BaishakhiPal**, Kalyan Adhikary, Utpal Gangopadhyay, Ratan Mandal, The Physics of Semiconductor Devices: Proceedings of IWPSD 2017, (2019) 341-347.
- [3] Fabrication of Nanowire on micro Textured Crystalline Silicon Wafer Before and After Diffusion Process: A comparative study of solar cell performance.  
 Soma Ray, Sugato Ghosh, Hemanta Ghosh, Suchismita Mitra, Chandan Banerjee, Anup Kumar Mondal, Hiranmoy Saha, Sukhendu Jana, Sayan Das, **Baishakhi Pal**, Materials Today: Proceedings, 4 (2017) 12678-12683.

\*\*\*

## List of Conferences, Symposiums & Short-Term Courses Attended

- [1] Presented a Poster entitled **“Texturization of Multi Crystalline Silicon without Conventional Alkaline and Acidic Solution for Solar Cell Processing”** in the **“2<sup>nd</sup> International Conference on Solar Energy Photovoltaic”** – organised by School of Electronics Engineering, KIIT University, Bhubaneswar; during 17<sup>th</sup> December – 19<sup>th</sup> December, 2016.
  
- [2] Presented a Paper entitled **“Selected Alternative Nano and Micro Textured Silicon: A Novel Technique for Selective Emitter Formation for Solar Cell Processing”** in the **“Fourth International Symposium on Semiconductor Materials and Devices (ISSMD)”** – organised at the School of Materials Science and Nanotechnology, Jadavpur University, Kolkata; during 8<sup>th</sup> March – 10<sup>th</sup> March, 2017.
  
- [3] Presented a Paper entitled **“Improvement of Tin-Oxide (SnO<sub>2</sub>) based Schottky Diode using Graphene over pure one”** in the **“International Conference on Current Trends in Materials Science and Engineering (CTMSE 2021)”** – organised by IEM, Kolkata; during 11<sup>th</sup> March – 13<sup>th</sup> March, 2021”.
  
- [4] Participated in online short-term course titled **“Advanced Materials for Environmental Sensors”** – organised by Dept. of Metallurgy Engineering and Material Science, IIT Indore; during 7<sup>th</sup> March – 12<sup>th</sup> March, 2022.

\*\*\*

## List of Workshops & Hands-on Training Programme Attended

- [1] One-week hands-on Training programme on “**Fabrication and Characterization of Advanced Photovoltaic Devices**” – organised by Dept. of Physics, IEST Shibpur; supported by DST-IEST Solar PV hub; during 12<sup>th</sup> December – 18<sup>th</sup> December, 2022.
- [2] Presented a Poster entitled “**Novel Technique for Fabrication of n-type Crystalline Silicon Selective Emitter Solar Cell**” in the “**XIX International Workshop on the Physics of Semiconductor Devices (IWPSD)**” – jointly organised by Solid State Physics Laboratory, Delhi, DRDO & Indian Institute of Technology Delhi, New Delhi; during 11<sup>th</sup> December – 15<sup>th</sup> December, 2017.
- [3] One Day Workshop on “**Intellectual Property Rights on Innovation**” – jointly organised by Maulana Abul Kalam Azad University of Technology, West Bengal & Meghnad Saha Institute of Technology, Kolkata; on 15<sup>th</sup> September, 2017.

Baishakhi Pal  
15/05/2024

\*\*\*



# Publications, Conferences & Workshop Certificates

---



Contents lists available at ScienceDirect

## Materials Science in Semiconductor Processing

journal homepage: [www.elsevier.com/locate/mssp](http://www.elsevier.com/locate/mssp)

## Improvement of charge kinetics of MoS<sub>2</sub> nano-petal based Schottky device by incorporation of W: A comparative study of structural, optical, and electrical properties

Baishakhi Pal<sup>a</sup>, Pubali Das<sup>a</sup>, Joydeep Datta<sup>a,b</sup>, Utpal Gangopadhyay<sup>c</sup>, Partha Pratim Ray<sup>a,\*</sup><sup>a</sup> Department of Physics, Jadavpur University, Kolkata, 700032, India<sup>b</sup> Department of Physics, Techno India University, Kolkata, 700091, India<sup>c</sup> Meghal Saha Institute of Technology, Kolkata, 700150, India

## ARTICLE INFO

## Keywords:

MoS<sub>2</sub> and MoWS<sub>2</sub> nanocomposites  
Schottky diode  
Current density-Voltage  
Charge transport parameters  
Metal semiconductor junction  
Impedance spectroscopy analysis

## ABSTRACT

Molybdenum Tungsten Di-Sulphide is a semiconducting alloy of different TMD (transition metal dichalcogenide) materials that has enormous tunable structural, optical, and electrical attributes. In this research, we have performed the hydrothermal synthesis of Mo<sub>1-x</sub>W<sub>x</sub>S<sub>2</sub> nanocomposites with different molar concentration of tungsten (i.e.  $x = 0, 0.1, 0.2, 0.3$ ) and fabricated Al/Mo<sub>1-x</sub>W<sub>x</sub>S<sub>2</sub>/TiO structured Schottky Barrier diodes. Characterization of their structural, optical, and charge transport attributes are compared. In this alloy formation, the amount of W (tungsten) concentration has a great impact on the particle size of composites. The transportation of charges via the metal-semiconductor junction is the basis for the superiority of thin film semiconductor devices like the Schottky diode. The diode parameters as well as charge transfer characteristics were analyzed by Impedance Spectroscopy and the theory of SCLC (space charge limited current). The calculated mobility and transit time for the Mo<sub>0.8</sub>W<sub>0.2</sub>S<sub>2</sub> device are  $5.65 \times 10^{-4} \text{ m}^2 \text{ V}^{-1} \text{ s}^{-1}$  and 1.59 ns respectively. These results are better than the rest of the devices. Dramatic conductivity enhancement for the Mo<sub>0.8</sub>W<sub>0.2</sub>S<sub>2</sub> based Schottky device is observed. As a result, this work not only investigates Al/MoWS<sub>2</sub> interface in detail but also explains the faster and better charge transport of the Mo<sub>0.8</sub>W<sub>0.2</sub>S<sub>2</sub> based device from a structural perspective.

## 1. Introduction

Many 2D and 3D materials have been tremendously explored in recent years due to their distinctive traits illustrating considerable optical characteristics along with incredibly quick recovery times [1], mechanical flexibility [2], substantially greater modulation depths [3], and even high electrical conductivity [4]. The distinct properties of 2D and 3D materials turn them very appealing to use in optoelectronic devices. Among these materials, one of the varieties of 2D material, transition metal dichalcogenides (TMDs) are like MX<sub>2</sub> form, M denotes Mo and W type transition metal, and X indicates S, Se, Te type dichalcogenide. They have a vast quantity of applications in capacitors, electrochemical devices, solid lubricants, electronic and photo-sensing components like ultrasensitive and ultrasensitive photodetector that are very thin, flexible, and almost transparent [5–10].

Currently, alloying different TMD materials are highly exciting because of aspects like greater thermal stability, extended optical

absorption [11], and an elevated layer-dependent feature [12–14]. TMD alloy development can activate the inert basal planes of TMD materials [15]. Furthermore, doping heavy atoms makes electron injection easier. The quantity of electrons injected is determined by the level of doping. Tungsten (W) is a transition metal with the same physical and chemical characteristics as Mo and high electron density. Furthermore, WS<sub>2</sub> has a comparable crystal structure and lattice constants to MoS<sub>2</sub> [16]. As a result, we may hypothesize that even after being doped with W, the crystal structure of MoS<sub>2</sub> can remain stable.

MoS<sub>2</sub> and WS<sub>2</sub> together yield a mixed TMDs compound with the chemical formula Mo<sub>1-x</sub>W<sub>x</sub>S<sub>2</sub>. Such promising substances (MoWS<sub>2</sub>) have substantial performance enhancements, especially to their structural characteristics and band gap tunability [17] because the dimensions of the constituent elements differ intrinsically. WS<sub>2</sub>/MoS<sub>2</sub> composite comprised of two S layers with a sandwiched W/Mo layer in between (S–W–S or S–Mo–S) by Vander Walls interactions [18–20]. Despite the fact that a lot of studies have been undertaken for the

\* Corresponding author.

E-mail addresses: [parthap.ray@jadavpuruniversity.in](mailto:parthap.ray@jadavpuruniversity.in), [parthapray@yahoo.com](mailto:parthapray@yahoo.com) (P.P. Ray).<https://doi.org/10.1016/j.mssp.2023.107535>Received 11 February 2023; Received in revised form 2 April 2023; Accepted 14 April 2023  
1369-8001/© 2023 Elsevier Ltd. All rights reserved.



## Investigating charge transportation and photo-responsive outcome of a Schottky diode fabricated by 2-amino terephthalic acid directed supramolecular Mn(II)-metallogel

Baishakhi Pal<sup>a</sup>, Santanu Majumdar<sup>b</sup>, Krishna Sundar Das<sup>c</sup>, Gerald Lepcha<sup>b</sup>, Indrajit Pal<sup>b</sup>, Partha Pratim Ray<sup>a,\*</sup>, Biswajit Dey<sup>b,\*\*</sup>

<sup>a</sup> Department of Physics, Jadavpur University, Kolkata, 700032, India

<sup>b</sup> Department of Chemistry, Visva Bharati University, Santiniketan, 731235, India

<sup>c</sup> School of Chemical Sciences, Indian Association for the Cultivation of Science, Jadavpur, Kolkata, West Bengal, 700032, India

### ARTICLE INFO

#### Keywords:

Supramolecular Mn(II) metallogel

LMWG

FESEM

Rheology

Semiconducting features

Schottky diode device

### ABSTRACT

This study investigates a supramolecular metallogel formed using an ultrasonication technique and employing manganese acetate tetrahydrate as a metal salt, 2-amino terephthalic acid (ATA) as an organic gelator, and N,N'-dimethyl formamide and dimethyl sulfoxide as mixed solvents. The mechanical toughness and viscoelastic parameters of the metallogel material were well demonstrated by rheology-based experimental values of storage and loss moduli with rotational frequency, shear strain, and shear stress of the Mn(II)-metallogel (Mn-ATA). The microstructural analysis along with chemical composition were shown using field emission scanning electron microscopy and energy dispersive X-ray analysis-based elemental research. Analysis of the infrared spectrum aided in determining how Mn-ATA was formed. Electrospray ionization mass investigation of Mn-ATA demonstrated the existence of several metallogel components and their engagement in producing the metallogel structure. Different diode parameters (i.e. photosensitivity, photoconductivity sensitivity, responsivity, specific detectivity, ideality factor, barrier height, and series resistance) were measured, revealing the semiconducting property of the metallogel. The current-voltage characteristics of a Mn-ATA-based thin-film type metal-semiconductor junction device demonstrated non-linear rectifying behavior, indicating Schottky diode behavior with dominating electronic-charge transport features. The device displayed an improved rectifying property under illumination, which also implied higher conductivity. The device's measured conductivity in the low-voltage domain (equivalent to ohmic behavior) was  $1.03 \times 10^{-5}$  and  $4.12 \times 10^{-5} \text{ Sm}^{-1}$  under darkness and illumination, respectively, implying photo-responsive behavior.

### 1. Introduction

Molecular self-assembly [1], a fundamental theme of supramolecular chemistry, is increasingly important in the material and technological fields. Supramolecular gels [2] are the fascinating result of a molecular self-assembly process. Gelator and solvent molecules are the two main constituents for fabrication of a supramolecular gel system [3]. Several polar and non-polar solvents [4–6] including water, N,N'-dimethyl formamide (DMF), dimethyl sulfoxide (DMSO), tetrahydrofuran, toluene, dichloromethane, acetone, ethanol, methanol, acetonitrile and carbon tetrachloride are immobilized within the chemical components

based on the gelator types during gel formation. In addition to the use of different polymeric gelators [7],  $\pi$ -gelators [8], and oligomeric gelators [9], low molecular-weight gelators (LMWGs) are a specific form of gelators that are widely recognized for obtaining supramolecular-type soft gel systems [3]. The LMWGs use distinct types of non-covalent interactions to generate a stable gel, and the LMWG-directed quasi-solid viscoelastic gel is usually referred to as supramolecular material [10]. Due to the wide range of applications in diverse areas, academic to industrial, research in the field of gelation technology is quickly expanding. Supramolecular gels have numerous potential applications from material science to biological fields including catalytic activity [11],

\* Corresponding author.

\*\* Corresponding author.

E-mail addresses: [parthap.ray@jadavpuruniversity.in](mailto:parthap.ray@jadavpuruniversity.in) (P.P. Ray), [biswajit.dey@visva-bharati.ac.in](mailto:biswajit.dey@visva-bharati.ac.in), [bdeychem@gmail.com](mailto:bdeychem@gmail.com) (B. Dey).

<https://doi.org/10.1016/j.jpcs.2023.111612>

Received 3 May 2023; Received in revised form 16 August 2023; Accepted 17 August 2023

Available online 19 August 2023

0022-3697/© 2023 Elsevier Ltd. All rights reserved.





Cite this: *Dalton Trans.*, 2024, **53**, 7912

## Comparative outcomes of the voltage-dependent current density, charge transportation and rectification ratio of electronic devices fabricated using mechanically flexible supramolecular networks†

Baishakhi Pal,<sup>a</sup> Santanu Majumdar,<sup>b</sup> Indrajit Pal,<sup>b</sup> Gerald Lepcha,<sup>b</sup> Amiya Dey,<sup>b</sup> Partha Pratim Ray <sup>\*a</sup> and Biswajit Dey <sup>\*b</sup>

In this study, we report the synthetic method of two distinct supramolecular metallogels, namely Mn-BDA and Cd-BDA, using Mn(II) acetate tetrahydrate, Cd(II) acetate dihydrate and butane-1,4-dicarboxylic acid (BDA). DMF, a polar aprotic solvent, was immobilized in both metallogel-networks for their synthesis. The metallogelation of Mn-BDA was successfully attained through the instant mixing of a Mn(II)-source and BDA in DMF solvent media. By applying ultrasonication, a Cd-BDA metallogel was prepared. The stoichiometry of gel-forming components concerning metal salts and the LMWG are accountable to obtain respective stable metallogels. Rheological parameters such as storage modulus ( $G'$ ) and loss modulus ( $G''$ ) explored the mechanical flexibility of the synthesized metallogels through amplitude and angular frequency sweep experiments. Both the metallogels possess significant mechanical stability, which was determined by monitoring diverse gel-to-sol transition shear strain values ( $\gamma\%$ ). Distinctive morphological visualizations of both of these metallogels (i.e., Mn-BDA and Cd-BDA) were made via field emission scanning electron microscopic (FESEM) studies, demonstrating a fibrous inter-connected network with a hierarchical self-assembled arrangement for Mn(II)-based metallogels and a typical stacked-flake-like association with hierarchical motifs for Cd(II)-based metallogels. EDAX elemental mapping substantiated the presence of metallogel-forming agents such as individual metal acetate salts, BDA acting as a low-molecular weight gelator, and gel-immobilized solvents such as DMF. Furthermore, Fourier transform infrared spectroscopy and ESI-mass spectroscopy were performed for both these supramolecular metallogels. FT-IR spectroscopic and ESI-mass spectroscopic results clearly substantiate the possible non-covalent supramolecular interactions among basic molecular repeating moieties, i.e., butane-1,4-dicarboxylic acid (the low-molecular weight gelator), individual metal salts and gel-immobilized polar aprotic solvent DMF for the construction of distinct stable supramolecular metallogel-systems. The semiconducting property of the fabricated metallogels was investigated. Two Schottky diodes (SDs) composed of ITO/Cd-BDA/Al and ITO/Mn-BDA/Al in a sandwich pattern with Al serving as the metal electrode were fabricated. Both these metallogel-based devices effectively offer significant semiconducting diode features with non-linear  $J-V$  characteristics. The non-ohmic conduction protocol of the fabricated metallogel-based devices was explored. Mn-BDA and Cd-BDA metallogel-based fabricated devices have rectification ratios of 6.67 and 23.50, respectively. The gel-based diode performances were examined by observing the voltage-dependent current density, charge transportation and rectification ratio.

Received 8th February 2024,  
Accepted 4th April 2024

DOI: 10.1039/d4dt00383g

rsc.li/dalton

<sup>a</sup>Department of Physics, Jadavpur University, Kolkata 700032, India.

E-mail: parthap.ray@jadavpuruniversity.in

<sup>b</sup>Department of Chemistry, Visva-Bharati University, Santiniketan 731235, India.

E-mail: bdeychem@gmail.com, biswajit.dey@visva-bharati.ac.in;

Tel: +91 9433868381

† Electronic supplementary information (ESI) available. See DOI: <https://doi.org/10.1039/d4dt00383g>

## 1. Introduction

Natural gels are highly valued in science and technology.<sup>1</sup> Gel is the gift of serendipity acquired through chemical interactions.<sup>2,3</sup> Gels can be primarily identified using the inversion vial test of soft-scaffolds, in which the inversion stabilities of semi-solid materials against gravity are being





Cite this: *Mater. Adv.*, 2023, 4, 3628

# A semiconducting supramolecular novel Ni(II)-metallogel derived from 5-aminoisophthalic acid low molecular weight gelator: an efficient Schottky barrier diode application†

Baishakhi Pal,<sup>‡a</sup> Subhendu Dhibar,<sup>‡\*b</sup> Ritam Mukherjee,<sup>b</sup> Subham Bhattacharjee,<sup>c</sup> Partha Pratim Ray<sup>‡\*a</sup> and Bidyut Saha<sup>‡\*b</sup>

An outstanding approach for the development of a supramolecular metallogel with nickel(II) ion and 5-aminoisophthalic acid as a gelator (LMWG) in DMF medium has been accomplished at room temperature. Rheological studies of the supramolecular Ni(II)-metallogel established the mechanical compactness of the gel material. FESEM microstructural study and EDX elemental mapping showed flake-like morphological patterns and major chemical constituents of the Ni(II)-metallogel. The possible metallogel formation approach has been examined using FT-IR spectroscopic study. Moreover, the supramolecular Ni(II)-metallogel assemblies show electrical conductivity in metal-semiconductor (MS) junction electronic devices. The metallogel based thin film device shows an electrical conductivity of  $1.53 \times 10^{-5} \text{ S m}^{-1}$ . Semiconductor properties such as Schottky barrier diode nature of the synthesized Ni(II)-metallogel based devices were explored.

Received 22nd May 2023,  
Accepted 16th July 2023  
DOI: 10.1039/d3ma00260h  
rsc.li/materials-advances

## 1. Introduction

Gels are often thought to consist of an elastic cross-linked network containing a trapped liquid.<sup>1</sup> Gels are ubiquitous in daily life; notable examples are hair gels, toothpaste, and soft contact lenses. The field of materials science and its associated industrial applications are constantly being reinforced by molecular self-assembly, one of the main branches of supramolecular chemistry.<sup>2</sup> The spontaneous self-assembly of molecules produces three-dimensional frameworks known as supramolecular gels.<sup>3</sup> The gelators and solvent molecules, which are immobilised by the gelator molecules in the 3D soft gel scaffolds, are the two principal elements making up the supramolecular gel.<sup>4</sup> The vial inversion test, which demonstrates that a vial of gel remains stable against gravity, provides the most direct primary evidence of gel formation.<sup>5</sup> The organic

and/or inorganic gelators trap various solvents, such as water ( $\text{H}_2\text{O}$ ),<sup>6</sup> acetonitrile ( $\text{H}_3\text{C}-\text{C}\equiv\text{N}$ ),<sup>7</sup> ethanol ( $\text{CH}_3\text{CH}_2\text{OH}$ ),<sup>8</sup> methanol ( $\text{CH}_3\text{OH}$ ),<sup>9</sup> dichloromethane ( $\text{CH}_2\text{Cl}_2$ ),<sup>10</sup> deuterated dichloromethane ( $\text{CD}_2\text{Cl}_2$ ),<sup>11</sup> 1,2-dichlorobenzene ( $\text{C}_6\text{H}_4\text{Cl}_2$ ),<sup>12</sup> acetone ( $\text{CH}_3\text{COCH}_3$ ),<sup>13</sup> carbon tetrachloride ( $\text{CCl}_4$ ),<sup>14</sup> DMF ( $[(\text{CH}_3)_2\text{NC}(\text{O})\text{H}]$ ),<sup>15</sup> tetrahydrofuran ( $[(\text{CH}_2)_4\text{O}]$ ),<sup>16</sup> dimethyl sulfoxide ( $\text{C}_2\text{H}_6\text{OS}$ ),<sup>17</sup> and toluene ( $\text{C}_6\text{H}_5\text{CH}_3$ ),<sup>18</sup> to create three-dimensional gel structures.<sup>19</sup> Polymers, such as polyester, poly(ethylene glycol), polyolefins, polycaprolactones, and polycarbonates, often serve as gelators to produce a variety of stable gel compositions.<sup>20</sup> However, low molecular weight gelators (LMWGs), which have molecular weights under 3000, have a strong capacity in supramolecular gel formation through the immobilization of solvent molecules.<sup>21,22</sup> Literature is full with various low molecular weight gelators, such as alkenes,<sup>23</sup> amides,<sup>24</sup> modified amino acids,<sup>25</sup> urea,<sup>26</sup> peptides,<sup>27</sup> sugars,<sup>28</sup> and dendrimers,<sup>29</sup> which have wonderful gelation properties in the presence of different solvent molecules. Supramolecular gel formation is the output of intriguing non-covalent interactions, including hydrogen bonds,<sup>30</sup> electrostatic interactions,<sup>31</sup> hydrophobic<sup>32</sup> and hydrophilic forces,<sup>33</sup> van der Waals forces,<sup>30</sup> and aryl-system-based interactions.<sup>34</sup> Supramolecular gels have become a vital area in materials science owing to their numerous applications in both the academic and industrial arena, such as catalysis,<sup>35</sup> lithography,<sup>36</sup> opto-electronic devices,<sup>37</sup> electrochemical devices,<sup>38</sup> chemo-sensors,<sup>39</sup> cell culture,<sup>40</sup> drug delivery,<sup>41</sup> tissue engineering,<sup>42</sup> and semiconductors.<sup>15</sup>

<sup>a</sup> Department of Physics, Jadavpur University, Jadavpur, Kolkata-700032, India. E-mail: parthap.ray@jadavpuruniversity.in; Tel: +91 3324572844

<sup>b</sup> Colloid Chemistry Laboratory, Department of Chemistry, The University of Burdwan, Golapbag, Burdwan-713104, West Bengal, India. E-mail: sdhibar@scholar.buruniv.ac.in, bsaha@chem.buruniv.ac.in; Tel: +91 7001575909, +91 9476341691

<sup>c</sup> Department of Chemistry, Kazi Nazrul University, Asansol-713303, West Bengal, India

† Electronic supplementary information (ESI) available. See DOI: <https://doi.org/10.1039/d3ma00260h>

‡ BP and SD should be treated as joint first authors



## Materials Research Express



## PAPER

## Novel technique for fabrication of n-type crystalline silicon selective emitter for solar cell processing

RECEIVED  
16 March 2019REVISED  
3 April 2019ACCEPTED FOR PUBLICATION  
12 April 2019PUBLISHED  
24 April 2019Baishakhi Pal<sup>1,2</sup>, Soma Ray<sup>2,3</sup>, Utpal Gangopadhyay<sup>2</sup> and Partha Pratim Ray<sup>1</sup><sup>1</sup> Department of Physics, Jadavpur University, Kolkata-700032, West Bengal, India<sup>2</sup> Center of Advanced Research in Renewable Energy and Sensor Technology, Meghnad Saha Institute of Technology, TIG, Kolkata-700150, West Bengal, India<sup>3</sup> Centre of Excellence for Green Energy and Sensor Systems, IEST, Shibpur, Howrah-711103, IndiaE-mail: [utpal\\_ganguly@yahoo.com](mailto:utpal_ganguly@yahoo.com)**Keywords:** crystalline silicon, selective emitter, sheet resistance, diffusion, BSF, junction depth, peak doping concentration

## Abstract

A new way of realizing crystalline silicon selective emitter by simultaneous formation of front side selective emitter as well as rear back surface field (BSF) layer in rear side diffusion step has been presented in this work. In this paper, we have demonstrated a novel technique to achieve a selective emitter having a highly diffused region with lower sheet resistance around  $30\text{--}32\ \Omega\ \text{sq}^{-1}$  along with peak doping concentration  $7.34 \times 10^{19}\ \text{atoms cm}^{-3}$ , junction depth around  $0.97\ \mu\text{m}$  and lightly diffused region with higher sheet resistance around  $78\text{--}80\ \Omega\ \text{sq}^{-1}$  along with peak doping concentration  $4.57 \times 10^{19}\ \text{atoms cm}^{-3}$ , junction depth around  $0.64\ \mu\text{m}$ . These results show that selective emitter has been formed in single diffusion process without any extra heat treatment and chemical etching process, thus this process becomes cost effective.

## 1. Introduction

High efficiency crystalline silicon solar cells require a good emitter design where contact resistance and surface recombination velocity both will be minimum i.e. emitter design should be able to collect all light generated carriers with less surface recombination and good metal contacts with low contact resistance. Fulfilling these two requirements at the same time is not possible in homogeneous doping emitter.

Selective emitter structure is of great importance because of its better blue response in short wavelength region and thus enhanced light-to-electricity conversion in that region. It solves the problem of trade-off between surface recombination velocity and contact resistance. The illuminated emitter surface where light falls and carriers generated are collected is lightly doped to reduce the surface recombination velocity which leads to increase in both open circuit voltage ( $V_{oc}$ ) and short circuit current density ( $J_{sc}$ ), and the non-illuminated emitter surface beneath the metal finger contact is highly doped to decrease the contact resistance, which improves the fill factor [1].

Many selective emitter solar cell fabrication processes involve double diffusion steps; however the major difficulty associated with this process is the alignment-accuracy of the front side metal grid with the highly doped emitter surface at the time of contact formation. The double diffusion technique with photolithography is used to form high efficiency solar cells but this is very costly method [2, 3].

Industrial selective emitter solar cell can be formed by the coating of phosphorus containing metal paste by screen printing in the selected portion of the emitter of a p-type crystalline silicon substrate. This process is well-matched with common mass production technique where silver paste is used to form the front contact by screen printing. This phosphorus contained metal paste worked as a source of direct diffusion by which the coated layer covered region becomes heavily doped, and gas-phase out diffusion by which other region becomes lightly doped into the substrate. This forms the highly doped area and the lightly doped area at the same time. But to obtain target doping, concentration management is necessary for uniform diffusion [4–6].

Issue 42, 2021



From the journal:  
**CrystEngComm**

## Exploration of semiconducting properties of Zn(II)- and Cd(II)-based coordination polymers with dicarboxylate of a chair-type backbone†

Akhtaruzzaman,<sup>a</sup> Baishakhi Pal,<sup>b</sup> Samim Khan, <sup>a</sup> Basudeb Dutta, <sup>a</sup> Sanobar Naaz,<sup>a</sup> Suvendu Maity,<sup>c</sup> Prasanta Ghosh, <sup>d</sup> Partha Pratim Ray<sup>\*b</sup> and Mohammad Hedayetullah Mir <sup>\*a</sup>



Materials Letters

Volume 338, 1 May 2023, 134066



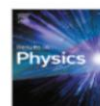
## An experimental approach to ensure energy quenching and fluorescence resonance energy transfer of excitons from P3HT to CuInSe<sub>2</sub>

Animesh Biswas<sup>a,b</sup>, Baishakhi Pal<sup>a</sup>, Mainak Das<sup>a</sup>, Ramjan Sk<sup>a</sup>, Animesh Layek<sup>a</sup> , Partha Pratim Ray<sup>a</sup>





Results in Physics  
Volume 42, November 2022, 105996



## Findings of inhomogeneity in barrier height of Schottky junction Al/rGO-SnO<sub>2</sub> having anomaly in theoretical and experimental value of Richardson constant: A Gaussian approach

Pubali Das <sup>a</sup>, Baishakhi Pal <sup>a</sup>, Mrinmay Das <sup>a b c</sup>, Sayantan Sil <sup>a d</sup>, Dhananjoy Das <sup>a</sup>, Animesh Layek <sup>a</sup>, Partha Pratim Ray <sup>a</sup>



Journal of Physics and Chemistry of Solids  
Volume 148, January 2021, 109706



## Improved charge transport properties of graphene incorporated tin oxide based Schottky diode over pure one

Pubali Das, Baishakhi Pal, Joydeep Datta, Mrinmay Das, Sayantan Sil, Partha Pratim Ray


ChemistrySelect


Chemistry  
Europe  
European Chemical  
Societies Publishing

Research Article


## Exploring a supramolecular gel to *in-situ* crystal fabrication from the low molecular weight gelators: a crystal engineering approach towards microelectronic device application


Dr. Subhendu Dhibar , Baishakhi Pal, Kripasindhu Karmakar, Sandip Kundu, Dr. Subham Bhattacharjee, Rupam Sahoo, SK. Mehebab Rahaman, Dr. Dhananjay Dey , Prof. Dr. Partha Pratim Ray , Prof. Dr. Bidvut Saha





[View PDF Version](#)
[Previous Article](#)
[Next Article](#)


 Open Access Article


 This Open Access Article is licensed under a [Creative Commons Attribution-Non Commercial 3.0 Unported Licence](#)


DOI: [10.1039/D3NA00671A](https://doi.org/10.1039/D3NA00671A) (Paper) *Nanoscale Adv.*, 2023, 5, 6714-6723

## A 5-aminoisophthalic acid low molecular weight gelator based novel semiconducting supramolecular Zn(II)-metallogel: unlocking an efficient Schottky barrier diode for microelectronics<sup>†</sup>

Subhendu Dhibar <sup>a,†</sup>, Baishakhi Pal <sup>b</sup>, Kripasindhu Karmakar <sup>ab,†</sup>, Sanjay Roy <sup>bc</sup>, Sk Abdul Hafiz <sup>d</sup>, Arpita Roy <sup>e</sup>, Subham Bhattacharjee <sup>d</sup>, Soumya Jyoti Ray <sup>bc</sup>, Partha Pratim Ray <sup>ab,†</sup> and Bidyut Saha <sup>ab,†</sup>



**EurJIC**  
European Journal of Inorganic Chemistry




**Chemistry Europe**  
European Chemical Societies Publishing

Research Article


## Exploitation of Structure-Property Relationships towards Multi-Dimensional Applications of a Paddle-Wheel Cu(II) Compound

Dr. Basudeb Dutta, Baishakhi Pal, Dr. Sunanda Dey, Dr. Suwendu Maity, Dr. Partha Pratim Ray✉, Dr. Mohammad Hedayetullah Mir✉





**Materials Research Bulletin**

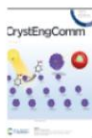
Volume 118, October 2019, 110507



## Effect of graphene on improved photosensitivity of MoS<sub>2</sub>-graphene composite based Schottky diode

Soumi Halder <sup>a</sup>, Baishakhi Pal <sup>a</sup>, Arka Dey <sup>ab</sup>, Sayantan Sil <sup>a</sup>, Pubali Das <sup>a</sup>, Animesh Biswas <sup>ac</sup>, Partha Pratim Ray <sup>a</sup>  

Issue 40, 2020

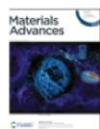


From the journal:  
**CrystEngComm**

## Fabrication of Cu(II) based halobenzoate appended ladder polymers with efficient charge transport properties†

[Sakhiul Islam](#),<sup>a</sup> [Baishakhi Pal](#),<sup>id</sup> <sup>b</sup> [Samim Khan](#),<sup>id</sup> <sup>a</sup> [Suvendu Maity](#),<sup>c</sup> [Sanobar Naaz](#),<sup>a</sup> [Prasanta Ghosh](#),<sup>id</sup> <sup>d</sup> [Partha Pratim Ray](#),<sup>id</sup> <sup>\*b</sup> and [Mohammad Hedayetullah Mir](#),<sup>id</sup> <sup>\*a</sup>

Issue 12, 2023



From the journal:  
**Materials Advances**

## Ni(II) and Zn(II)-metallogel-based anti-bacterial scaffolds for fabricating light-responsive junction-type semiconducting diodes with non-ohmic conduction mechanism†

[Gerald Lepcha](#),<sup>a</sup> [Baishakhi Pal](#),<sup>b</sup> [Santanu Majumdar](#),<sup>a</sup> [Kazi Tawsif Ahmed](#),<sup>c</sup> [Indrajit Pal](#),<sup>a</sup> [Swadesh Ranjan Biswas](#),<sup>c</sup> [Partha Pratim Ray](#),<sup>id</sup> <sup>\*b</sup> and [Biswajit Dey](#),<sup>id</sup> <sup>\*a</sup>

Issue 10, 2023



From the journal:  
**New Journal of Chemistry**

## Establishment of different aliphatic amines-based rapid self-healing Mg(OH)<sub>2</sub> metallogels: exploring the morphology, rheology and intriguing semiconducting Schottky diode characteristics†

[Santanu Majumdar](#),<sup>a</sup> [Baishakhi Pal](#),<sup>b</sup> [Gerald Lepcha](#),<sup>a</sup> [Krishna Sundar Das](#),<sup>c</sup> [Indrajit Pal](#),<sup>a</sup> [Partha Pratim Ray](#),<sup>id</sup> <sup>\*b</sup> and [Biswajit Dey](#),<sup>id</sup> <sup>\*a</sup>



Issue 23, 2022



From the journal:  
**Dalton Transactions**

## A croconate-directed supramolecular self-healable Cd(II)-metallogel with dispersed 2D-nanosheets of hexagonal boron nitride: a comparative outcome of the charge-transport phenomena and non-linear rectifying behaviour of semiconducting diodes†

[Santanu Majumdar](#),<sup>a</sup> [Baishakhi Pal](#),<sup>b</sup> [Rajib Sahu](#),<sup>c</sup> [Krishna Sundar Das](#),<sup>d</sup> [Partha Pratim Ray](#)<sup>\*b</sup> and [Biswajit Dey](#) <sup>\*c</sup>

## Effect of Induced Charges on the Performance of Different Dielectric Layers of c-Si Solar Cell by Experimental and Theoretical Approach

Original Paper | Published: 02 January 2020

Volume 12, pages 2601–2609, (2020)



[Soma Ray](#), [Baishakhi Pal](#), [Hemanta Ghosh](#), [Suchismita Mitra](#), [Anup Kumar Mondal](#), [Chandan Banerjee](#),  
[Hiranmoy Saha](#) & [Utpal Gangopadhyay](#)

**ChemistrySelect**

**Chemistry  
Europe**  
European Chemical  
Societies Publishing

Research Article

## Design of Dual Purpose Fe-metallogel for Magnetic Refrigeration and Fabrication of Schottky Barrier Diode

[Sayan Saha](#), [Baisakhi Pal](#), [Krishna Sundar Das](#), [Pradeepta Kumar Ghose](#), [Avik Ghosh](#), [Avik De](#),  
[Abhijit Kumar Das](#), [Partha Pratim Ray](#) [Raju Mondal](#)

## Optical Nonlinearity of Semiconducting Cd(II) Metallogel in the Femtosecond Regime with Two-, Three-, and Four-Photon Absorption

Tara Singha, Baishakhi Pal, Santanu Majumdar, Gerald Lepcha, Indrajit Pal, Partha Pratim Ray\*, Biswajit Dey\*, and Prasanta Kumar Datta\*

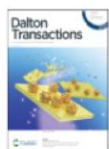
**Cite this:** *ACS Appl. Opt. Mater.* 2024, 2, 3, 474–484

Publication Date: March 7, 2024

<https://doi.org/10.1021/acsaom.4c00007>

Copyright © 2024 American Chemical Society

Issue 4, 2022



From the journal:

**Dalton Transactions**

## A Nd<sub>6</sub> molecular butterfly: a unique all-in-one material for SMM, MCE and maiden photosensitized opto-electronic device fabrication†

Krishna Sundar Das,<sup>† a</sup> Sayan Saha,<sup>† a</sup> Baishakhi Pal,<sup>b</sup> Amit Adhikary,<sup>id a</sup> Shruti Moorthy,<sup>c</sup> Sukhen Bala,<sup>a</sup> Sohel Akhtar,<sup>id</sup>

<sup>a</sup> Pradeepta Kumar Ghose,<sup>d</sup> Saurabh Kumar Singh,<sup>id \*c</sup> Partha Pratim Ray,<sup>\*b</sup> and Raju Mondal<sup>id \*a</sup>

## Suberic Acid-Based Supramolecular Metallogels of Ni(II), Zn(II), and Cd(II) for Anti-Pathogenic Activity and Semiconducting Diode Fabrication

Gerald Lepcha, Santanu Majumdar, Baishakhi Pal, Kazi Tawsif Ahmed, Indrajit Pal, Biswarup Satpati, Swadesh Ranjan Biswas Partha Pratim Ray\*, and Biswajit Dey\*

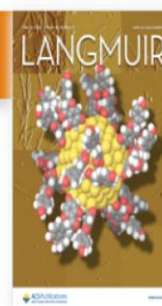
**Cite this:** *Langmuir* 2023, 39, 21, 7469–7483

Publication Date: May 16, 2023

<https://doi.org/10.1021/acs.langmuir.3c00765>

Copyright © 2023 American Chemical Society

[request reuse permissions](#)



Langmuir





# Potential impact of annealed cobalt-sulfide on current rectification of ITO/CoS<sub>2</sub>/Al Schottky device: Structural, optical, electrical, and magnetic characterizations

Pubali Das<sup>a</sup>, Jitendra Saha<sup>a</sup>, Satyendra Prakash Pal<sup>b</sup>, Baishakhi Pal<sup>a</sup>, Animesh Layek<sup>a</sup> , Partha Pratim Ray<sup>a</sup>

## Materials Research Express

### PAPER

## Exploration of temperature dependent dielectric relaxation and correlated barrier hopping (CBH) conduction mechanism of hydrothermally synthesized CuO nanoflakes

Rajkumar Jana<sup>1</sup>, Joydeep Datta<sup>1</sup>, Sayantan Sil<sup>1</sup>, Arka Dey<sup>1</sup> , Baishakhi Pal<sup>1</sup>, Animesh Biswas<sup>1,2</sup> and Partha Pratim Ray<sup>1</sup>

Published 18 September 2019 • © 2019 IOP Publishing Ltd

[Materials Research Express](#), Volume 6, Number 10

Citation Rajkumar Jana et al 2019 *Mater. Res. Express* 6 1050d1

DOI 10.1088/2053-1591/ab41d7



ACS Publications  
Most Trusted. Most Cited. Most Read.

## Unveiling the Semiconducting Diode Property through Current Density–Voltage Features with Effective Interface Mobility and Conductivity of Nitroterephthalic Acid-Directed Supramolecular Co(II)/Cu(II) Metallogels

Indrajit Pal, Animesh Biswas, Santanu Majumdar, Gerald Lepcha, Baishakhi Pal, Partha Pratim Ray\*, and Biswajit Dey\*

Cite this: *ACS Appl. Eng. Mater.* 2023, 1, 11, 3005–3015



Publication Date: October 26, 2023 ✓

<https://doi.org/10.1021/acsaenm.3c00481>

Copyright © 2023 American Chemical Society



# Texturization of Multi Crystalline Silicon without Conventional Alkaline and Acidic Solution for Solar Cell Processing

Baishakhi Pal<sup>a, b</sup>  , Soma Ray<sup>a</sup>, Sukhendu Jana<sup>a</sup>, Sayan Das<sup>a</sup>, Utpal Gangopadhyay<sup>a</sup>, Partha Pratim Ray<sup>b</sup>

## A Comparative Study of SiO<sub>2</sub>:TiO<sub>2</sub> Composite and SiO<sub>2</sub> Film by Sol-Gel Method for Solar Cell Application

Conference paper | First Online: 01 February 2019  
pp 341–347 |



**The Physics of Semiconductor Devices**  
(IWPSD 2017)

Kausturi Chatterjee , Soma Ray, Baishakhi Pal, Kalyan Adhikary, Utpal Gangopadhyay & Ratan Mandal



Available online at [www.sciencedirect.com](http://www.sciencedirect.com)

ScienceDirect

Materials Today: Proceedings 4 (2017) 12678–12683

**materialstoday:**  
PROCEEDINGS

[www.materialstoday.com/proceedings](http://www.materialstoday.com/proceedings)

ICSEP 2016

## Fabrication of Nanowire on micro Textured Crystalline Silicon Wafer Before and After Diffusion Process: A comparative study of solar cell performance

Soma Ray<sup>1,2,a\*</sup>, Sugato Ghosh<sup>2</sup>, Hemanta Ghosh<sup>2</sup>, Suchismita Mitra<sup>2</sup>, Chandan Banerjee<sup>3</sup>, Anup Kumar Mondal<sup>2</sup>, Hiranmoy Saha<sup>2</sup>, Sukhendu Jana<sup>1,2</sup>, Sayan Das<sup>1,2</sup>, Baishakhi Pal<sup>1</sup>, Utpal Gangopadhyay<sup>1</sup>









## CERTIFICATE OF PARTICIPATION

This is to certify that      *Ms. Baishakhi Pal*  
 from      Meghnad Saha Institute of Technology

has presented a paper / participated in the International Symposium on Semiconductor Materials and Devices (ISSMD 2017), organized at the School of Materials Science and Nanotechnology, Jadavpur University, Kolkata, West Bengal, INDIA during March 8-10, 2017.



*Prof. K. K. Chattopadhyay*  
 Convener, ISSMD 2017



**XIX International Workshop on The Physics of Semiconductor Devices**

Jointly Organized by

**Solid State Physics Laboratory, Delhi**  
**Defence Research & Development Organisation**

and

**Indian Institute of Technology Delhi, New Delhi**


**December 11-15, 2017**


**CERTIFICATE**

This is to certify that Ms. Baishakhi Pal

of Meghnad Saha Institute of Technology

has presented a Poster in the IWPSD-2017 field at Indian Institute of Technology, New Delhi during December 11-15, 2017.

  
(D.S. Rawal)  
Secretary, IWPSD 2017  
Solid State Physics Laboratory, Delhi

  
(Rajesh K. Sharma)  
Chairman, IWPSD 2017  
Solid State Physics Laboratory, Delhi





# QIP CENTER INDIAN INSTITUTE OF TECHNOLOGY INDORE



## Participation Certificate

This is to certify that Ms. Baishakhi Pal has participated in online short-term course titled "*Advanced Materials for Environmental Sensors*" conducted as a part of quality improvement program, organized by the Department of Metallurgy Engineering and Materials Science, IIT Indore from 07/03/2022 to 12/03/2022.

Dr. Ajay Kumar Kushwaha  
**Course Coordinator**

Dr. Surya Prakash  
**Coordinator, QIP**

CURRENT TRENDS IN MATERIALS SCIENCE AND ENGINEERING 2021

Certificate



THIS IS PRESENTED TO

Baishakhi Pal

Jadavpur University

FOR PRESENTING THE PAPER ENTITLED

*Improvement of Tin-Oxide (SnO<sub>2</sub>) based Schottky Diode using Graphene over pure one*

IN INTERNATIONAL CONFERENCE ON CURRENT TRENDS IN MATERIALS SCIENCE AND ENGINEERING (CTMSE 2021)  
ORGANIZED BY INSTITUTE OF ENGINEERING & MANAGEMENT, SALT LAKE DURING 11th TO 13th MARCH, 2021

  
DR. SATYAJIT CHAKRABARTI  
PATRON



  
ARUN KUMAR BAR  
CHAIR



  
RANABIR BANIK  
CONVENER



  
DR. SASWATI BARMAN  
CONVENER







One-week Hands-On Training programme on  
**“Fabrication and Characterization of Advanced  
Photovoltaic Devices”**

Under  
DST-STUTI Program of Indian Institute of Technology (ISM) Dhanbad-826004  
Funded By: Department of Science & Technology (DST), Govt. of India

Organised by  
Department of Physics, Indian Institute of Engineering Science & Technology (IIEST), Shibpur  
Supported by  
DST-IIEST Solar PV hub




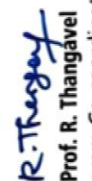


**12<sup>th</sup> – 18<sup>th</sup> Dec. 2022**



# Certificate

## of Participation

This is to certify that Prof./Dr./Mr./Ms. *Baishakhi Pal*.....of  
*Dept. of Physics, Jadavpur University*.... has participated in the one-week hands-on Training programme  
on “Fabrication and Characterization of Advanced Photovoltaic Devices” from 12th – 18th December 2022 organised  
by Department of Physics, Indian Institute of Engineering Science & Technology (IIEST), Shibpur under the aegis of  
DST-STUTI programme of Indian Institute of Technology (ISM) Dhanbad-826004, funded by the Department of Science  
and Technology (DST), Government of India.

 <b>Prof. Sagar</b> Coordinator: DST-STUTI Project IIT (ISM) Dhanbad	 <b>Prof. Ravi K. Gangwar</b> Co-coordinator: DST-STUTI Project IIT (ISM), Dhanbad	 <b>Shailendra</b> <b>Prof. S. K. Sharma</b> Program Coordinator Department of Physics IIT (ISM) Dhanbad	 <b>R. Thangavel</b> <b>Prof. R. Thangavel</b> Program Co-coordinator Department of Physics IIT (ISM) Dhanbad	 <b>Dr. Syed Minhaz Hossain</b> Program Coordinator Department of Physics IIEST, Shibpur, W.B.	 <b>Dr. Mojammeel Haque Mondal</b> Co-coordinator: Department of Physics IIEST, Shibpur, W.B.
---	---	--	--	---	--